APPLICATION OF LASERS IN ATOMIC NUCLEI RESEARCH

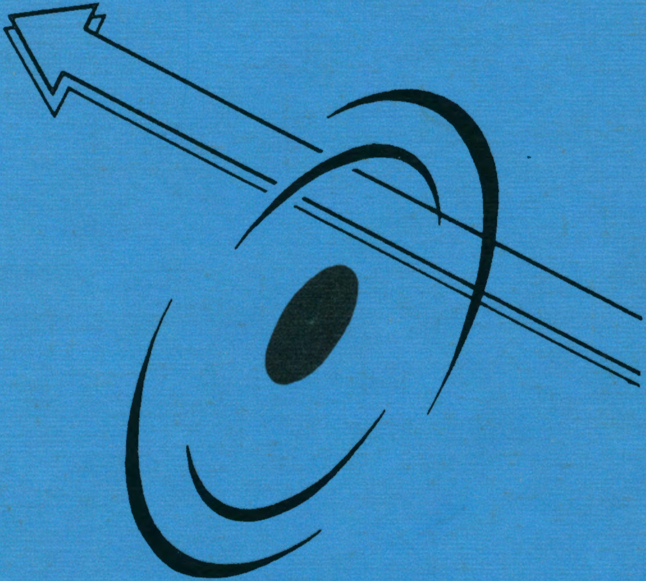

ПРИМЕНЕНИЕ ЛАЗЕРОВ В ИССЛЕДОВАНИИ АТОМНЫХ ЯДЕР

JOINT INSTITUTE FOR NUCLEAR RESEARCH

APPLICATION OF LASERS IN ATOMIC NUCLEI RESEARCH

4th International Workshop
LASER SPECTROSCOPY ON BEAMS OF RADIOACTIVE NUCLEI

Poznan, Poland, May 24 - 27, 1999

Dubna 2000

PREFACE

In accordance with the plan of the international collaboration between the Flerov Laboratory of Nuclear Reactions (Joint Institute for Nuclear Research, Dubna, Russia) – the Institute of Physics (Adam Mickiewicz University, Poznan, Poland) – and Heavy Ion Laboratory (Warsaw University, Warszawa, Poland), the 4th Workshop on the Application of Laser in Atomic Nuclei Research was held in Morasko (vicinity of Poznan) on May 24 – 27, 1999. Several different fields of the nuclear structure investigations of radioactive nuclei, using laser radiation, were discussed at this Workshop. The scientific programme of the Workshop covered the following main topics:

- Trends in research using beams of radioactive nuclei
- Laser spectroscopy on beams of fission fragments
- Study of nuclear structure by off- and on-line laser methods
- Charge distribution, nuclear moments and deformation
- Hyperfine magnetic anomaly
- Properties of atoms and nuclei
- Traps, sources and spectrometric methods.
- Experimental laser methods and applied research.

The programme of the Workshop also included a trip to Warsaw (May 27 – 29, 1999). The participants of the Workshop visited the Laboratory of Heavy Ions of Warsaw University where they acquainted themselves with the heavy ion cyclotron U-200P and its physical setups. The scientific programme and results of investigation with the use of the U-200P were presented.

The working language of the Workshop was English.

Scientists from 11 countries participated in the Workshop, from scientific centres of Leuven (Belgium), Sofia (Bulgaria), Prague (Czech Republic), Jyväskylä (Finland), Caen, Orsay (France), Mainz (Germany), Tokyo (Japan), Warsaw, Poznan, Kielce (Poland), Moscow, St.-Petersburg, Dubna (Russia), Karlstadt (Sweden), Birmingham, Manchester (UK).

Organizing Committee:

Prof.Z.Blaszczak *(Poznan, Poland)* – **Chairman**
Dr.B.Markov *(Dubna, Russia)* – **Scientific Secretary**
Prof.J.Dembczynski *(Poznan, Poland)*
Prof.W.Nawricik *(Poznan, Poland)*
Prof.S.Chojnacki *(Warsaw, Poland)*
Prof.A.Kopystynska *(Warsaw, Poland)*
Prof.Yu.Gangrsky *(Dubna, Russia)*
Prof.Yu.Penionzhkevich *(Dubna, Russia)*

Organizers: Institute of Physics, Adam Mickiewicz University, Poznan, Poland
Flerov Laboratory of Nuclear Reactions JINR, Dubna, Russia

ISBN — 5-85165-567-4

IV INTERNATIONAL WORKSHOP

LASER SPECTROSCOPY ON BEAMS OF RADIOACTIVE NUCLEI

MAY 24-27,1999,
POZNAN, POLAND

ORGANIZERS:
Institute of Physics,
Adam Mickiewicz University,
Poznan, Poland
Flerov Laboratory of Nuclear Reactions,
JINR, Dubna, Russia

CONTENTS

WELCOME ADDRESS

Ladies and Gentlemen,

It is my great honour and pleasure to welcome all the guests and participants of our regular Workshop in Poznan. I am doing this not only in my name but also on behalf of the whole Organizing Committee. I am pleased to see among us Professor Penionzhkevich - head of the Department of Exotic Nuclei Investigation at the Flerov Laboratory of Nuclear Reaction at the Joint Institute for Nuclear Research in Dubna, Professor Yu.P. Gangrsky, head of the Laboratory of Nuclear Structure Investigation by Laser Spectroscopy at the same Institute, Professor J. Dembczynski, Dean of the Faculty of Technical Physics at Poznan University of Technology and at present the rector-elect of this University, Professor W. Nawrocik - Dean of the Faculty of Physics of Adam Mickiewicz University, who is the host of our Workshop and many other distinguished guests, who honoured the opening of the conference with their presence.

It happened that a few weeks ago we celebrated the 80th anniversary of our University. In this time the University has developed from a small college to one of the greatest science and cultural centres. The recollection of this event directs me to the history of our conferences. The idea was born in Dubna, where the first conference took place; the subsequent conferences were organised in Poznan. The people most devotedly engaged in starting the conferences here were: our friends from Dubna Professor Gangrsky and Dr Markov, and, from our side, our Dean Professor Nawrocik and myself. Let me remind you of the titles of these conferences, shown in Figure 1. Each time the conference grew in status and in the number of participants from an increasing number of countries. At this conference, which will be the last in this century and in this millennium as well, you will meet over 60 participants from 11 countries.

This fourth Workshop, which is the third one taking place in Poznan, is devoted to the problems related to the Laser Spectroscopy of Radioactive Nuclei. One of these problems is the experiments on beams of accelerated radioactive nuclei. This is a very interesting field of nuclear physics; it is now being developed in many science centres. A number of radioactive beam factories are being operated or in progress now. At the Flerov Laboratory of the Joint Institute for Nuclear Research a project named DRIBS (Dubna Radioactive Ion BeamS) has been proposed. The project including the production of two kinds of the exotic radioactive beam – light neutron-rich nuclei and fission fragments. A heavy ion cyclotron and an electron accelerator-microtron, will be used for this purpose. Several reports concerning this project are to be presented at our Workshop. These reports deal with the obtaining of beam of radioactive nuclei and different experimental methods for their study. The laser spectroscopy method is the most promising for the study of such nuclei. It allows one to determine the size and the shape of the studied nuclei and the nucleon configurations of the ground or isomeric states. This is a very important source of information about nucleon interaction in nuclei far from β-stability. I hope that discussion of the presented reports will be useful in selecting of the most suitable techniques and in planning future experiments.

Let me wish you successful and fruitful discussions and many interesting contacts. The weather is beautiful and we hope that it will be the case during the whole conference; the organisers will also do their best to make sure you never regret coming here.

I also hope that you will enjoy it so much that in the next two years we will meet again at the subsequent 5th Workshop, which as I suppose will also take place in Poznan (in Morasko) under the proposed title: "New Results and Perspectives of Atomic Nuclei Investigations by Laser Spectroscopy".

Let me ask Prof. Nawrocik to officially declare the conference open.

Professor Z. Blaszczak
Chairman of the Organizing Committee

Dubna – Poznan International Workshop

I. **Laser Spectroscopy of Atomic Nuclei**
Dubna, December 18–20,1990

II. **Charge and Nucleon Radii of Exotic Nuclei**
Poznan, Poland, May 29–31,1995

III. **Hyperfine Structure and Nuclear Moments of Exotic Nuclei by Laser Spectroscopy**
Poznan, Poland, February 3–5,1997

IV. **Laser Spectroscopy on Beams of Radioactive Nuclei**
— Poznan,Poland, May 24–27, 1999

Fig.1

Low-Energy Fission-Fragment Beams in the DRIBs Project

Yu.E. Penionzhkevich
Flerov Laboratory of Nuclear Reactions, Joint Institute for Nuclear Research, Dubna

The Dubna radioactive beam factory (DRIBs) [1] will make use of two possibilities for producing secondary beams of radioactive nuclei (Fig. 1). During the first phase of the project (Phase I) the possibility for obtaining radioactive nuclei in fragmentation reactions of stable nuclei, accelerated by the cyclotron U400M to intermediate energies (~50 MeV/A), will be realized. The fragmentation products, obtained in a special ion source, will be converted into single-charged ions, which after transportation to the second cyclotron (U400) will be accelerated up to energies of ~20-25 MeV/A. This method will make it possible to obtain mainly beams of light radioactive nuclei with $Z \leq 30$ with intensities up to 10^8 pps (e.g.,nuclei such as ^{6}He). In the second phase of the project (Phase II) it is supposed to produce and accelerate radioactive neutron-rich nuclei in the mass region $80 \leq A \leq 140$. This mass region corresponds to the fragments of low-energy fission of heavy nuclei. For this reason use will be made of the photofission of ^{238}U. The γ-quanta will be produced by the electron accelerator (the microtron MT-25), where the electron beam with an intensity of about 20 μA has an energy of 25 MeV. With the help of a special converter the electron beam is transformed into a beam of γ-quanta with an energy of up to 25 MeV and a flux of 10^{14} s^{-1}. This beam, focused into a narrow angle, will fall onto a ^{238}U-target weighing 100 g. It is well known that the photofission cross section has a maximum corresponding to the giant dipole resonance at an energy of the γ-quanta equal to E_γ = 13.5–14 MeV [2], see Fig. 2. This brings forth an increase of the photofission probability. The yield of the fission fragments will increase as a result of the interactions of the secondary neutrons (γn and fission neutrons) with the U-target. When the mentioned above parameters of the beam and target are realized, one can get as much as 10^{11} fission fragments/second. Taking into account the widths of the mass and charge distributions of the fragments, the yields of definite fission fragments can be estimated. In Table 1 the yields estimated in this way are presented for the Kr (Z = 36) and Xe isotopes (Z = 54).

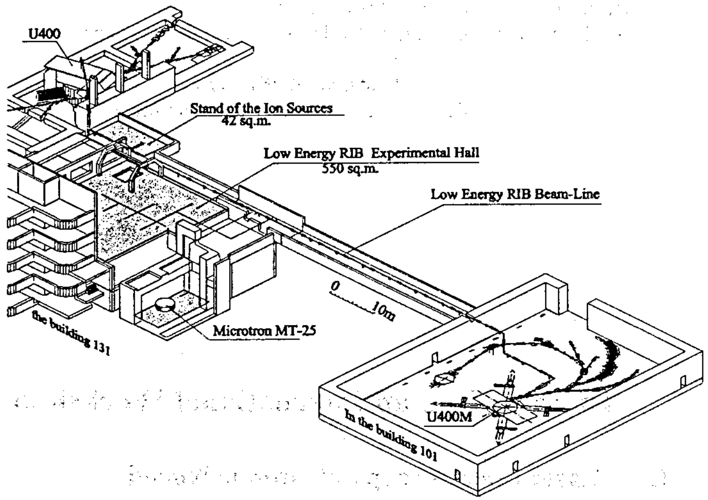

Fig. 1. Layout of the Dubna Radioactive Ion Beams facility (DRIBs).

Table 1

Z	A	$T_{1/2}$ [s]	Y(A) %	Y(A,Z) [s^{-1}]
36	90	32.3	4.5	$4.5 \cdot 10^9$
	91	8.6	5.0	$4.4 \cdot 10^9$
	92	1.8	5.5	$3.6 \cdot 10^9$
	93	1.3	5.8	$2.4 \cdot 10^9$
	94	0.2	6.0	$1.0 \cdot 10^9$
	95	0.8	5.9	$2.5 \cdot 10^8$
54	140	13.6	5.7	$4.4 \cdot 10^9$
	141	1.7	5.8	$3.9 \cdot 10^9$
	142	1.2	6.0	$3.1 \cdot 10^9$
	143	0.3	5.9	$1.4 \cdot 10^9$
	144	1.2	5.8	$3.8 \cdot 10^8$
	145	0.9	5.7	$0.7 \cdot 10^8$

From the Table it follows that when the efficiency of the ion source and the transport system amounts to some 20-30 % it is possible to obtain beams of fission fragments in the region of Kr and Xe with an intensity of up to 10^9 s^{-1}. Simultaneously with the fragments situated close to the maxima of the mass distribution (A = 90 and 130), asymmetric fission fragments are formed with a rather high yield. These are neutron-rich nuclei, which are of interest in connection with the studies of the structure of exotic nuclei. In Table 2 the yields are presented of the isotopes of Ni to Ba relative to the total number of fission fragments (10^{11} s^{-1}). Presented are also the yields of the last known isotopes and the isotopes with binding energy of the neutron B_n = 2.5 MeV. From the Table follows that for the isotopes situated at the "tails" of the fragment mass distribution (for instance, for ^{77}Ni, ^{78}Ni) the yields are 10^5–10^3 s^{-1}. This allows producing them in sufficiently large amounts to permit precise measurement of the characteristics of their decay. The problem lies only in the possibility to realize a relatively fast ion source having a diffusion time for these elements not longer than 0.1- 0.2 s. The obtained ions, corresponding to the exotic nuclei with energies up to 10 keV, will be

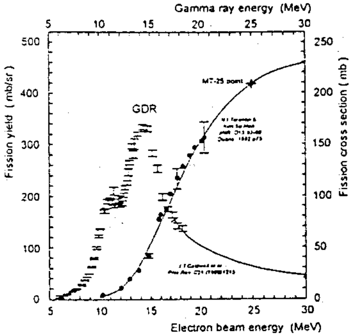

Fig. 2. Dependence of the ^{238}U fission cross section on the gamma-quanta energy and the fission fragment yield taken from works indicated in the figure.

TABLE 2

Fission fragments ^{238}U (γ,f)

E_{exit}=15MeV, $N_{tot}\approx10^{11}c^{-1}$

Isotope	Last stabl isotope	first β-n	Last isotope	Y=10^{-8}	B_n=2,5Mev	B_n=0
$_{28}$Ni	^{64}Ni	^{73}Ni $8\cdot10^{-8}$ 0,49c	^{74}Ni 10^{-7} (1.1c)	^{75}Ni (0.23c)	^{77}Ni $5\cdot10^{-5}$ (0,10c)	^{81}Ni
$_{30}$Zn	^{70}Zn	^{78}Zn $5\cdot10^{-5}$ 2.0c	^{81}Zn $3\cdot10^{-7}$ 0,29c	^{82}Zn (0.13c)	^{79}Zn $1.5\cdot10^{-5}$ (0.31c)	^{87}Zn
$_{32}$Ge	^{76}Ge	^{83}Ge $1.7\cdot10^{-4}$ 1.9c	^{85}Ge $5\cdot10^{-5}$ 0,53c	^{88}Ge (0.15c)	^{85}Ge $2.5\cdot10^{-5}$ (0,25c)	^{97}Ge
$_{34}$Se	^{82}Se	^{87}Se $6,7\cdot10^{-3}$	^{91}Se $1,4\cdot10^{-4}$ (0,27c)	^{94}Se	^{93}Se $6\cdot10^{-7}$ (0,10c)	^{103}Se
$_{36}$Kr	^{86}Kr	^{92}Kr $1.7\cdot10^{-2}$ 0,36c	^{95}Kr $1,5\cdot10^{-3}$ (0,78c)	^{99}Kr	^{99}Kr 10^{-8}	^{109}Kr
$_{37}$Rb	^{87}Rb	^{91}Rb $5,6\cdot10^{-2}$ 58,2c	^{102}Rb 10^{-9} 0,037c	^{101}Rb	^{102}Rb 10^{-9} 0.037c	^{110}Rb
$_{39}$Y	^{89}Y	^{97}Y $4,9\cdot10^{-2}$ 3,7c	^{102}Y $2,5\cdot10^{-3}$ 0.30c	^{106}Y (0.009c)	^{110}Y 10^{-10}	^{120}Y
$_{40}$Zr	^{96}Zr	^{103}Zr $8\cdot10^{-3}$ 1.3c	^{105}Zr$2.2\cdot10^{-3}$ 1,0c	^{111}Zr	^{113}Zr 10^{-10}	^{123}Zr
$_{42}$Mo	^{100}Mo	^{109}Mo $3\cdot10^{-3}$ 1.4c	^{110}Mo $8\cdot10^{-3}$ 0.30c	^{115}Mo	^{117}Mo 10^{-10}	^{125}Mo
$_{44}$Ru	^{104}Ru	^{113}Ru $5\cdot10^{-3}$ 3.0c	^{115}Ru $3\cdot10^{-4}$ 0,74c	^{122}Ru	^{125}Ru 10^{-12}	^{131}Ru
$_{46}$Pd	^{110}Pd	^{119}Pd $0.8\cdot10^{-3}$ 1,8c	^{120}Pd $0.5\cdot10^{-3}$	^{127}Pd	^{129}Pd 10^{-11}	^{137}Pd
$_{48}$Cd	^{116}Cd	^{127}Cd $5\cdot10^{-6}$ 0.57c	^{130}Cd 10^{-7} 0,19c	^{131}Cd	^{131}Cd 10^{-8}	^{139}Cd
$_{50}$Sn	^{124}Sn	^{133}Sn $1.5\cdot10^{-3}$ 1,47c	^{134}Sn $2\cdot10^{-3}$ 1.05c	^{139}Sn	^{133}Sn $1.5\cdot10^{-3}$ 1.47c	^{145}Sn
$_{52}$Te	^{130}Te	^{136}Te $1.3\cdot10^{-2}$ 19.0c	^{138}Te $2\cdot10^{-3}$ 1.4c	^{145}Te	^{143}Te 10^{-6}	^{153}Te
$_{54}$Xe	^{136}Xe	^{141}Xe $1.2\cdot10^{-2}$ 1.72c	^{145}Xe $4\cdot10^{-4}$ 0,9c	^{148}Xe	^{149}Xe 10^{-8}	^{159}Xe
$_{56}$Ba	^{138}Ba	^{146}Ba $8\cdot10^{-3}$ 2,0c	^{150}Ba 10^{-4} 0,30c	^{153}Ba (0.20c)	^{155}Ba 10^{-10}	^{165}Ba

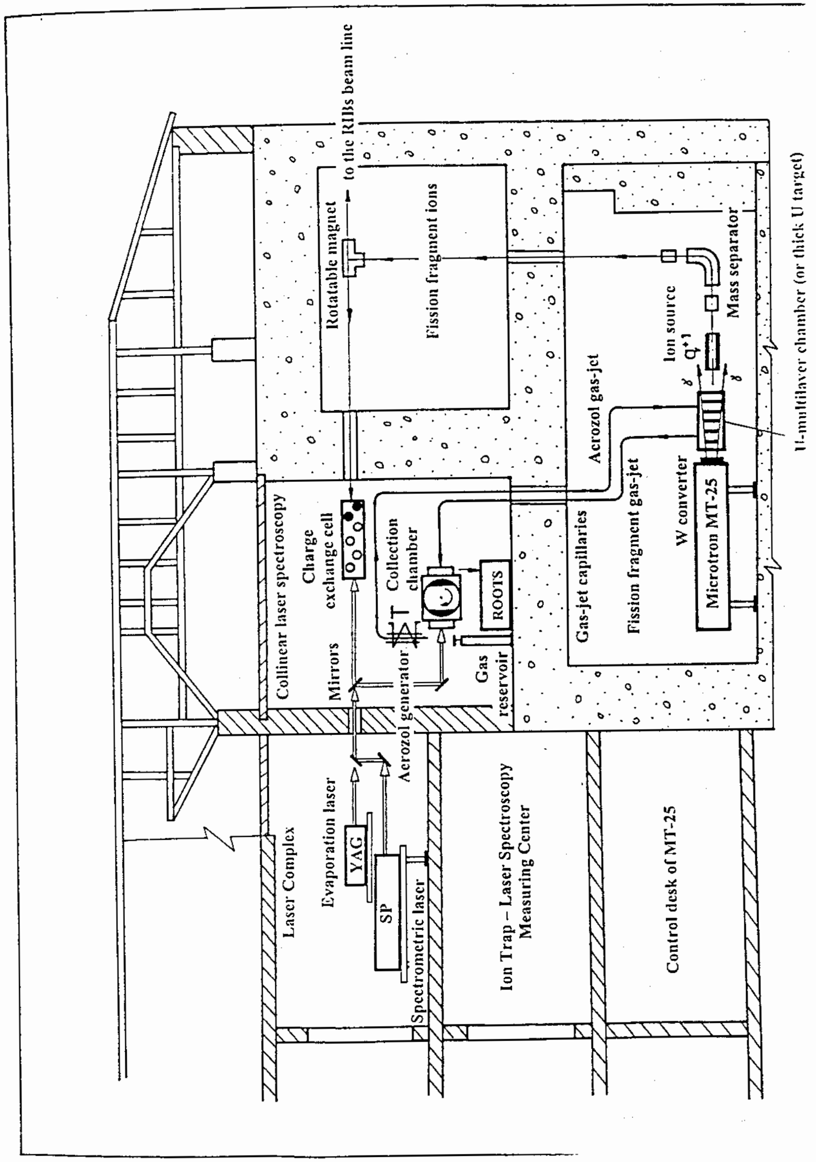

Fig. 3. A schematic view of LERIS.

transported to a special experimental hall, where investigations will be carried out with low energy radioactive nuclear beams. Low energy radioactive beams of light elements, obtained in fragmentation reactions at the U400M cyclotron, also will be transported to the same area. In Fig. 3, the layout of the low energy radioactive beam laboratory is presented (LERIS). In this laboratory investigations of the properties of exotic nuclei will be performed in the following directions:

1. Nuclear Structure

The data on the structure of neutron-rich nuclei with $30 \leq Z \leq 60$ is rather scarce in spite of the fact that many interesting features have been predicted for them - new deformation regions, inversion of the energy levels, change of the sign of the deformation when going from neutron-deficient to neutron-rich nuclei [3], shape isomerism [4], etc. Fig. 4 presents the systematics of the low-energy levels of the Sn isotopes. A sharp change in the energy is observed in the transition to the neutron-rich isotopes. Thus for the 2^+ states of the isotopes $^{120-130}$Sn this value amounts to ~1.2 MeV, while for the isotope ^{132}Sn it is already about 4 MeV. This can be explained by different factors, including the deformation close to the closed shell N = 82. In the given project it is suggested to study energy level schemes using 4π-γ-spectroscopy (gamma-balls), the deformation and the root-mean-square radius – using the methods of collinear laser spectroscopy [5]. From this point of view interesting are also nuclei with neutron magic numbers, e.g., N = 82, such as ^{131}In, ^{130}Cd and ^{129}Ag, which will also be formed with yields sufficient to allow investigating them with the above-mentioned methods.

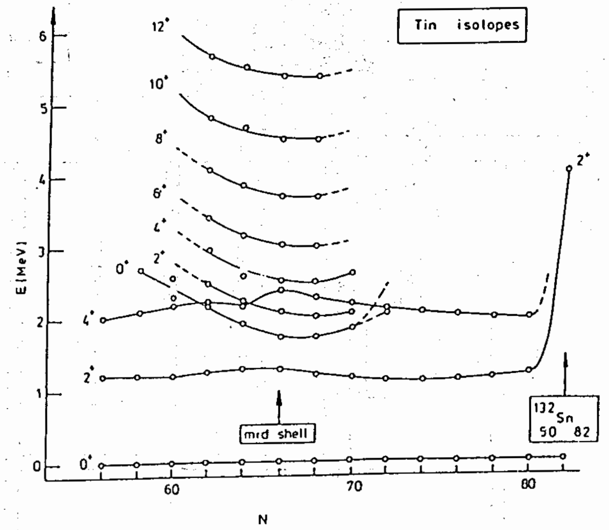

Fig. 4. The gamma-quanta energies (E) for different Sn-isotopes (A).

As has been mentioned in some articles [e.g. 6] because of the large deformation of the fission fragments, high spin isomers can be formed. It is interesting to study isomers such as ^{99m}Nb (I=5$^+$), ^{125m}Cd (I=11/2$^+$), ^{128m}In (I=8$^-$), ^{130m}In (I=10$^-$), ^{131m}Sn (I=11/2$^-$), ^{131m}Sn (I=19/2$^-$) and others. In Table 3 presented are isomers, which may be expected to have high yield in

TABLE 3

Fission fragments isomers

Nb	I=1/2$^-$	^{100}Nb – 3.0 c, ^{102}Nb – 4.3 c, ^{104}Nb – 0.88 c.
	I=5$^+$	^{97}Nb – 60 c, ^{99}Nb – 2.6 m.
Ag	I=1/2$^+$	^{111}Ag – 65 c, ^{113}Ag – 69 c, ^{115}Ag – 18 c, ^{117}Ag – 5.3 c.
Cd	I=11/2$^-$	^{119}Cd – 2.2 m; ^{121}Cd – 8.3 m, ^{123}Cd – 1.8 m, ^{125}Cd – 0.25 m.
In	I=1/2$^-$	^{121}In – 3.8 m, ^{123}In – 47 c, ^{125}In – 12 c, ^{127}In – 3.7 c, ^{129}In – 1.2 c, ^{131}In – 0.27 c.
	I=8$^-$	^{116}In – 2.2 c, ^{118}In – 8.5 c, ^{120}In – 47 c, ^{122}In – 10.8 c, ^{124}In – 3.4 c, ^{126}In – 1.5 c, ^{128}In – 0.8 c, ^{130}In – 0.5 c (I-10$^-$)
Sn	I=11/2$^-$	^{129}Sn – 7.5 m, ^{131}Sn – 63 c,
	I=7$^-$	^{128}Sn – 6.5 c, ^{130}Sn – 1.7 m.
Sb	I=19/2$^-$	^{129}Sb – 18 m, ^{131}Sb – 17 m.
Te	I=11/2$^-$	^{133}Te – 55.4 v

photofission reactions. It is of additional interest within the DRIBs project also to produce isomeric beams.

Large are the perspectives of studying oriented nuclei using the methods of low-temperature nuclear orientation [7]. These methods allow high precision determination of the quadrupole moments of nuclei, including those of isomers. For odd-neutron nuclei the LMR-method has proven to be highly efficient [8]. It should be also mentioned that the low-temperature nuclear orientation method could be used for the production of polarized beams of fission fragments.

It is interesting to study also the neutron decay of fission fragments. Because of the relatively high β-decay energy of neutron-rich nuclei in this mass region, possible are β-delayed 2n- and 3n-decay modes of nuclei such as ^{100,102}Rb, $^{131-133}$Cd, $^{135-137}$Sn, etc. By investigating the correlation between the two neutrons emitted in the decay of such nuclei it is possible to look for possible di-neutron configurations in these nuclei. Estimation shows that for neutron-rich fission fragments exotic decay modes such as cluster decay are also energetically possible. Moreover, after β-decay (for these nuclei $Q_\beta \geq 15$ MeV) the excitation of giant resonances at energies $E_{GR} \geq 15$ MeV is also possible.

Thus the beams of fission fragments open new perspectives in the investigation of neutron-rich nuclei with Z in the range $30 < Z < 60$, which are practically very weakly studied.

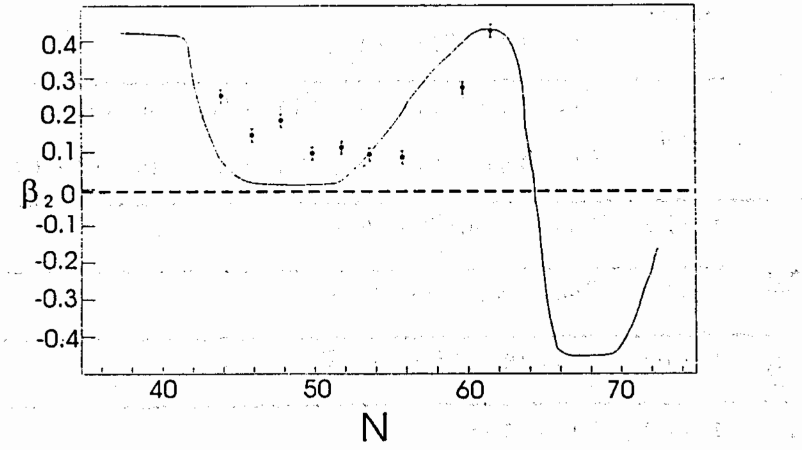

Fig. 5. The dependence of β_2 on the neutron number of Zr isotopes.

Low energy beams of fission fragments are expected to be very useful for high precision measurements of nuclear masses. The exact determination of the mass excess of nuclei far from the line of β-stability is a very important issue of nuclear physics. On the basis of the mass values conclusions can be drawn about the stability of nuclei close to the nucleon driplines as well as about the location of the driplines themselves. The particles of low energy could be used in special high-frequency traps [8]. Also, the nuclei stored in such traps can be used for the determination of the charge radii and quadrupole moments using the methods of nuclear spectroscopy. Fig. 5 presents the quadrupole deformation of different Zr isotopes. The experimental points obtained by means of nuclear spectroscopic methods are for isotopes up to ^{101}Zr. It can be seen that for the two neutron-rich isotopes ^{100,101}Zr the value of the deformation

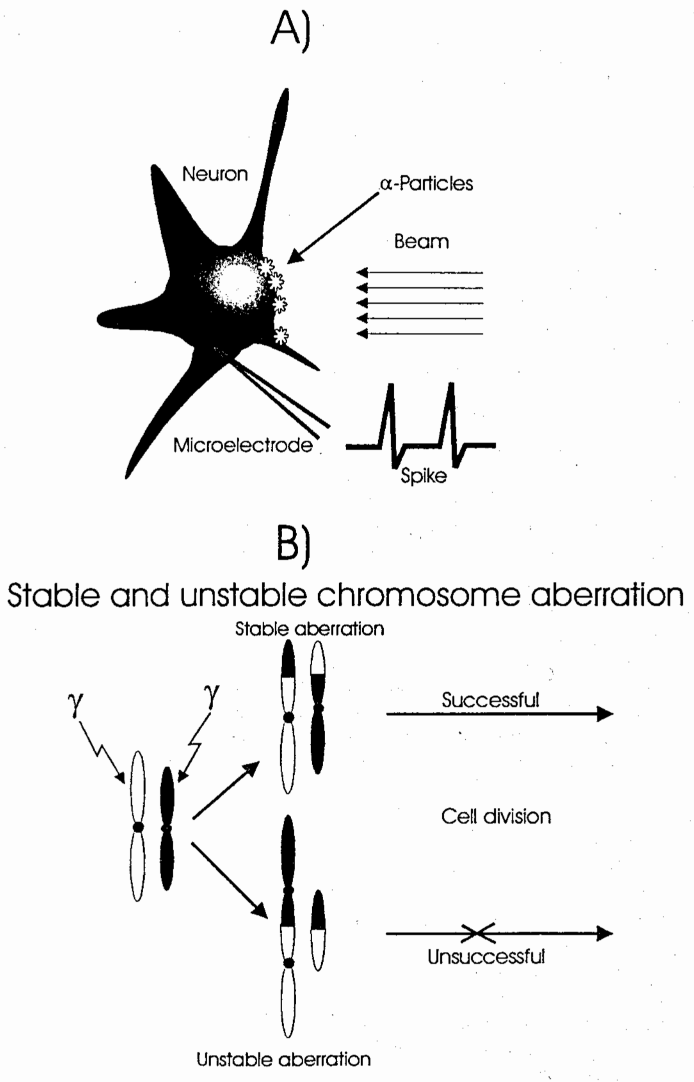

Fig. 6.

rapidly increases up to $\beta \approx 0.4$. The theoretical calculations within the shell model predict for the Zr isotopes with A > 101 an abrupt change in the deformation and, moreover, a change in its sign. In order to reveal this interesting effect it is necessary to investigate all Zr isotopes including ^{106}Zr. All of them are produced with a rather high yield as fission fragments.

2. Applied research with low-energy fission-fragment beams

When using low-energy radioactive beams for investigations in the field of condensed matter physics and biology, we should stress on one very important advantage, namely, that they can be implanted in the studied object without causing its radiation damage, as is usually the case in the interaction of high-energy beams, where a large part of the imported energy is deposited in the end of the Bragg curve.

In the investigation of the structure of a crystal, the implanted radioactive nuclei emitting penetrating radiation (e.g., γ-radiation) can experience the blocking effect inside the crystal lattice [9]. This radiation can be measured with special position-sensitive detectors, which allows determining with high resolution the structure of the crystal and its changes as a result of the radiation effects.

The use of low-energy radioactive beams opens new perspectives in radiobiological investigations. The usual methods of studying neurons and neuron meshes consist of exciting and measuring the signals using special microelements. In the case of implantation of a radioactive nucleus in the region of the studied neuron the latter is subjected to excitation by the radiation, e.g., by α-particles emitted by the implanted nucleus. Such a method allows excitation of a definite group of neurons without affecting or destroying the adjacent regions of biological tissues (Fig. 6a).

A fundamental problem of biology is the investigation of chromosomal aberrations, which can bring forth different illnesses, including oncological ones. Fig. 6b shows a scheme of the interaction of the radiation with the chromosomes [10]. The chromosomes fission into two types and further they form new chromosomes. At this, stable and unstable aberrations can be realized. The unstable aberrations can lead to the creation of new degenerated cells, which are the cause of different illnesses at a genetic level. The modeling of such processes can be carried out efficiently by implanting radioactive nuclei in the region of the investigated cells.

References:
1. Yu.Ts.Oganessian. Brief description of the Dubna radioactive Ion Beams Project "DRIBs". Dubna, 1998
2. J.T.Caldwall et al., Phys. Rev. C21, 1215 (1980)
3. J.L.Wood et al., Phys. Reports 102, no. 3-4 (1992)
4. K.Neergard et al., Nucl. Phys. A262, 61 (1976)
5. Yu.P.Gangrsky. Particle and Nuclei 23, 1616 (1992)
6. H.Kudo et al., Proc. of the VI Int. School-Seminar on heavy Ion Physics, Dubna 1997, ed. Yu.ts.Oganessian & R.Kalpakchieva, World Scientific (1998), p. 675
7. Proceedings of the Int. Workshop on Symmetry and Spin, Prague 1998, Ed. M.Finger, Czech J. Phys. 49 (1999)
8. N.hermanspahn et al., Acta Physica Polonica B27, 357 (1996)
9. M.Morjean et al., Proc. of the VI Int. School-Seminar on heavy Ion Physics, Dubna 1997, ed. Yu.ts.Oganessian & R.Kalpakchieva, World Scientific (1998), p. 683
10. E.A.Krasavin, S.Kozulek. mutagenetic influence of radiation with different linear energy transfer. Moscow, Energoizdat 1991(in Russian)

CHARGE RADII OF NUCLEI NEAR CLOSED NEUTRON SHELLS

Yu.P.Gangrsky, S.G.Zemlyanoi, B.N.Markov, L.M.Melnikova
Joint Institute for Nuclear Research, Dubna, Russia
K.P.Marinova
K.Okhridsky State University, Sofia, Bulgaria

The experimental values of charge radii differences for the nuclei close to magic neutron numbers are presented. These values are obtained from the isotopic shifts of the optical lines by the high resolution laser spectroscopy methods. The systematics of the charge radii differences for the nuclei near the closed neutron shells and the comparision with the droplet model calculation are discussed.

INTRODUCTION

1999 is the 50-years jubilee of the shell model. This model was proposed by M.Goeppert-Mayer and H.Jensen in 1949 and it was the big achievement in nuclear physic. Being sed on very simple assumptions and requiring a minimum of calculations, it provides a satisfactory description of a number of nuclear properties – the binding energies, spins and parities of the ground states and the energy spectra of the lowest excited states. It also forms the starting point for more refined theories of the nuclear structure.

The main peculiarity of the shell model is the existence of the so-called magic numbers (2, 8, 20, 28, 50, 82, 126), which distinguish nuclei with particulary stable proton and neutron configurations. The nuclei containing the magic number of protonsor or neurtons are the most stable and compact, their shape is close to spherical. In the present report are discussed the space distribution of an electrical charge and its parameter (charge radius) in the nuclei around the neutron magic number.

CHARGE RADII of NUCLEI

The distribution of an electrical charge in a nucleus as radial and azimutal, is one of its major characteristics. It depends on the internucleon interactions in a nucleus and consequently serves one of the sources of the information about the nuclear forces. The spatial distribution of an electrical charge is represented complex enough and is described by a number of the parameters. One of them, describing the linear sizes of a nucleus, is a mean-square charge radius MSCR, which is defined by the expression:

$$\langle r^2 \rangle = \frac{\int \rho(r) r^4 dr}{\int \rho(r) r^2 dr}, \qquad (1)$$

where ρ (r) - the density of an electrical charge on the distance r from the centre of a nucleus. The concrete expression for $<r^2>$ depends on a kind of the distribution of the charge in the nucleus. For the nucleus with the sharp border and the homogeneous distribution of the charge (rectangular distribution)

$$\langle r^2\rangle = \frac{3}{5}R^2, \tag{2}$$

where R – the radius of a nucleus. In a case of Fermi distribution of a charge (constant density at the centre and smooth recession on border) [1]:

$$\langle r^2\rangle = \frac{3}{5}c^2 + \frac{7}{5\pi^2}a^2, \tag{3}$$

where c – half-density radius ($\rho(c) = 0.5\rho_0$, ρ_0 - the density of a charge at the centre of a nucleus), and a - parameter of a surface layer (distance, on which density of a charge decreases from $0.9\rho_0$ up to $0.1\rho_0$). If all electrical charge is concentrated on a surface of a nucleus, than obviously, $<r^2> = R^2$

At the constant volume, the least value of MSCR appears at the nuclei having the spherical shape. Any deviations from sphere (the appearence of the nuclei deformation) results in the increase of MSCR. This increase of MSCR is defined by the expression [2]:

$$\Delta\langle r^2\rangle = \frac{5}{4\pi}\langle r^2\rangle_0 \sum_i \Delta\langle\beta_i^2\rangle, \tag{4}$$

where $<r^2>_0$ - MSCR of the spherical nucleus, β_i- the deformation parameters of the various orders (quadrupole β_2, octupole β_3,etc.).

The received by experience value of MSCR allows to find, how the sizes and shape of a nucleus vari with the change of its nucleon structure (for example, with growth of the neutrons number, the excitation energy or the angular momentum). The purpose of the given paper was to research the change of MSCR in the isotopes of the same element near the closed neutron shells. The measurements of the MSCR differences in the nucleus with the neutron magic numbers (28, 50 or 82) and having one or two neutrons more or less, (at the crossing of the closed shells) were performed.

EXPERIMENTAL METHODS of the MSCR DETERMINATION

The experimental methods of the MSCR determination (and also the other parameters describing the spatial distribution of an electrical charge in a nucleus) are based on the electromagnetic interaction of a "test" particles with the nucleus. The results of the measurements will be the most certain at the use of such "test" particles, which undergo only the electromagnetic interaction, for example, electron or muon. These particles are used in two kinds of experiments:

1. Elastic or inelastic scattering on the nuclei.
2. Precise measurement of the stationary states energies in the bound systems – electron (or muon) - nucleus.

The level energies of these systems (for example, atoms) depend, among other factors, on the final sizes of a nucleus [3]. The energy shift in comparison with a point nucleus is most significant for s-states (the orbital moment l = 0). As is known the point nuclei do not exist in the nature and the theoretical calculation of atomic levels with such nuclei is unsufficiently exact. Therefore the shifts of the levels for various isotopes of the same element are compared in a practice. Thus by the experience, compare not the energies of the levels, but the wave-lengths of the radiation transitions between the levels, one of which is sensitive to the spatial distribution of an electrical charge of a nucleus (s-level), and another is not present. In such a way determine the MSCR differences for the whole set of the compared isotopes. Usually the absolute value of MSCR is known for one or several isotopes (they are obtained from measurements of the elastic scattering of electron or of the muon levels spectra). Therefore the measured values of the MSCR differences allow to determine the absolute values of MSCR for all set of isotopes.

Firsly, such values of the MSCR differences were obtained by the analysis of the atomic or ionic optical spectra. The use in the last years of lasers with the scanned wave-length has raised these measurements on a new step. The unique properties of laser radiation (its intensity and monochromacity, small angular spread) have allowed to essentially improve the accuracy and the sensitivity of the measurements. The main feature of the experiments with the use of the lasers is that the energies of the optical transitions are not measured, but are determined by the wave-lengths of the laser radiation, at which the resonances of the excitation of the atomic levels are observed. Thus the resonant wave-lengths are determined with the high accuracy, and the moments of the resonance appearance are fixed by various manners. These manners include the measurements of the resonant laser fluorescence, the multistep ionization of the atoms or the anisotropy of the polarized nuclei radiation. The block-diagram of the experimental set-up based on the method of the resonant laser fluorescence is presented in Fig. 1. This set-up was created at the Laboratory of Nuclear Reactions JINR and during a number of years was used for the measurement of the nuclear MSCR for a wide set of the elements [4]. This set-up includes the argon-ion pumping laser, the dye laser for the generation of the radiation with the chosen wave-length and the set of the devices for the stabilization, the calibration and the registration of the laser radiation. The use for the atomization of the powerful pulse laser has allowed to carry out the measurements with the refractory elements and their compounds [5].

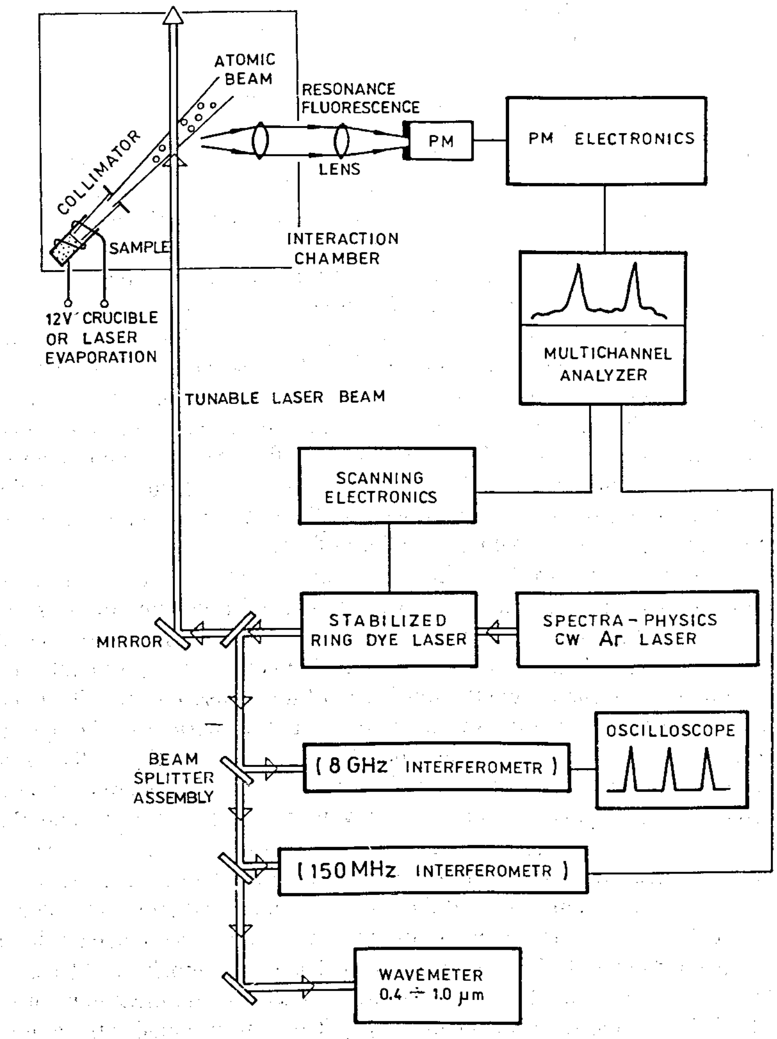

Fig. 1. The block diagram of the experimental set-up

RESULTS of the MEASUREMENTS

On the described set-up, the measurements of the MSCR differences and of the nuclear multipole moments of the long isotope chains of a wide set of elements (from Na up to U) were carried out. Some number of these chains crosses the closed neutron shells (Ti [6], Zr [7], Ce, Nd, Sm [8]). The characteristics of these chains (the range of the mass numbers and the neutron numbers, and also the wave-lengths of the laser radiation used for the excitation of atomic levels) are presented in Tabl. 1. In this table the measured differences of the resonant frequencies appropriate to the excitation of atoms with the magic neutron number nuclei and distinguished from them on one or two neutrons (isotopic shifts) are presented also. The way of the determination of the MSCR differences from the measured isotopic shifts is described in detail [8].]. For the majority of isotopic chains the measurement of the isotopic shifts is carried out for the whole set of the wave-lengths, that increased essentially the accuracy and reliability of the received results.

The received in such a way values of MSCR differences of nuclei with the magic neutron number and distinguished from them on one or two neutrons are presented in Tabl. 2. For the completeness of a picture the known data from the other sources are added (they are collected in the reviews [9-10]), and also the absolute values of MSCR of the nuclei with the magic neutron numbers are included [11-12].

The examples of the dependences of the MSCR differences on number of the neutrons in the nucleus at the crossing of the neutron closed shells are showed in Fig. 2. For comparison the results of the droplet model calculation are presented also (they are discussed below).

DISCUSSION of the RESULTS

From Table 2 and Fif. 2 it is visible that the character of the MSCR dependence on the neutron number changes essentially at the crossing of the closed shell: the weak growth or even the fall of MSCR at $N < N_{mag}$. is replaced by its strong increase at $N > N_{mag}$. Such break in dependence $<r^2>$ on N is expressed most sharply at $N_{mag} = 28$ and 50. The nuclei with such number of neutrons have the least values of MSCR in all chain of isotopes. At every N_{mag} the values $<r^2>$ are identical practically for all elements in a wide range Z, as is visible in Fig. 3 on an example of the nuclei with the neutron number near N = 82.

The growth of MSCR at addition of the neutrons depends on the change of its volume and shape:

$$\Delta\langle r^2\rangle = \Delta\langle r^2\rangle_V + \Delta\langle r^2\rangle_\beta, \qquad (5)$$

where $<r^2>_v$ and $<r^2>_\beta$ - the changes of MSCR, induced by the change of the nuclear volume and shape. The volume of the nucleus is determined by the number of the nucleons, however the growth of MSCR with the increase of only the numbers of the neutrons is occured more slowly, than under the known law connecting the radius of a

TABLE 1

ISOTOPIC SHIFTS OF THE OPTICAL LINES IN THE ATOMIC SPECTRA OF STUDIED NUCLEI

Element	$N_1 - N_2$	λ nm	$\Delta\nu^{N.N-2}$ MHz	$\Delta\nu^{N.N-1}$ MHz	$\Delta\nu^{N.N+1}$ MHz	$\Delta\nu^{N.N+2}$ MHz
Ti	22-28	588.0	846(5)	402(5)		
		588.9	1417(9)	668(11)		
		591.9	839(10)	403(10)		
		592.2	1664(11)	787(9)		
		593.8	1401(10)	661(9)		
		586.6	1670(10)	787(9)		
		594.2	1678(9)	788(6)		
		598.1	1667(5)	784(6)		
Zr	50-56	573.6			-97(7)	-237(2)
		579.8			-93(4)	-222(2)
		588.6				-226(1)
Ce	78-84	577.3	175(9)			-1740(10)
		577.4	-32(9)			-1365(6)
		578.9	192(7)			-1946(10)
		580.4	177(6)			-1217(9)
Nd	82-90	572.9				574(3)
		581.4				-1456(5)
Sm	82-92	574.6				-2804(1)(3)*
		577.9				-1030(15)*

*$\Delta\nu^{N,N+4}$

TABLE 2

CHARGE RADII DIFFERENCE OF THE NUCLEI DISTINGVISHED ON ONE OR TWO NEUTRONS

N	Nuclei	$< r^2 >^N$ fm^2	$< r^2 >^{N-2,N}$ fm^2	$< r^2 >^{N+2,N}$ fm^2	$< r^2 >^{N-1,N}$ fm^2	$< r^2 >^{N+1,N}$ fm^2
20	^{38}Ar	3.4020(20)	-0.082(26)	0.169(32)	-0,081(17)	0.044(12)
	^{39}K	3.4367(22)		0.112(37)	-0.056(44)	0.021(19)
	^{40}Ca	3.4827(17)		0.215(5)	-0.127(16)	0.0032(25)
28	^{47}K	3.4551(26)	0.046(12)		0,015(12)	
	^{48}Ca	3.4831(17)	0.145(18)	0.295(48)	0.009(10)	
	^{50}Ti	3.5760(30)	0.165(17)		0.031(13)	
	^{52}Cr	3.6550(26)	0.073(22)	0.159(40)		0.062(18)
50	^{86}Kr	4,1840(20)	0.042(12)	0.282(53)	0,009(11)	0.125(26)
	^{87}Rb	4,1990(20)	0.033(60)	0.283(57)	0.025(34)	0.127(41)
	^{88}Sr	4.2036(58)	0,050(8)	0.277(12)	0.007(4)	0.124(5)
	^{90}Zr	4.2733(20)		0.224(26)		0.137(16)
82	^{136}Xe	4.7908(20)	-0.052(12)	0.254(20)		0.105(10)
	^{137}Cs	4.8085(70)	-0.057(7)	0.270(50)	-0.064(10)	0.117(20)
	^{138}Ba	4,8348(7)	-0.034(4)	0.269(15)	-0.066(5)	0.119(8)
	^{139}La	4.8550(10)	-0.055(27)		-0,080(10)	
	^{140}Ce	4.8773(14)	-0.020(4)	0,265(12)		
	^{142}Nd	4.9145(32)	-0.019(12)	0.269(26)	-0.059(12)	0.118(12)
	^{144}Sm	4.94900(14)	-0.006(5)	0,261(20)	-0.038(10)	0.115(7)
	^{145}Eu	4.9798(116)	-0,026(5)	0,250(14)	-0.048(6)	0.114(7)
	^{147}Tb			0,207(11)		0.084(9)
	^{148}Dy	5.0462(235)	-0.013(2)	0,243(22)		
126	^{206}Hg	5.4799(19)	-0.107(5)		-0.071(5)	
	^{207}Tl	5.4895(32)	-0.103(10)			0.099(15)
	^{208}Pb	5.5071(8)	-0.109(3)	0,195(3)	-0.068(3)	0.087(2)
	^{212}Rn		-0.110(10)		-0.082(8)	
	^{213}Fr		-0.099(3)		-0.064(3)	
	^{214}Rn		-0.091(15)		-0.061(8)	

nucleus R and its mass number A:

$$R = r_0 A^{1/3}, \qquad (6)$$

where is usually accepted $r_0 = 1.2$ fm. Thus the growth of MSCR at the increase of the nucleon number on the ΔA is defined by expression:

$$\Delta\langle r^2\rangle_V = 0{,}576(\Delta A)A^{-1/3}. \qquad (7)$$

The slower growth of the charge radius in comparison with expression (7) is explained, apparently, by that the added neutrons are placed mainly on a surface of a nucleus. Such change of MSCR can be described on the basis of various models distinguished by a choice of the nucleon interaction potential in the nucleus. One of the most widespread is a droplet model [14,15]. From the calculation on this model it follows, that for nuclei near the closed neutron shells 50 and 82 the increase of MSCR at the pair neutrons addition is 0.12 fm^2, that is twice less than follows from expression (7). The droplet model dependence $\langle r^2\rangle_v$ on N is given in Fig. 2 and its strong difference from the experimental data is visible: instead of the smooth dependence the break is always observed at $N = N_{mag}$.

One of the reasons of this distinction is the change of the nuclei shape with growth of the neutron number. At the magic neutron number the shape of the nucleus is closest to spherical, and at the change N the deviations from this shape are observed. These deviations are described by the deformation parameters of the various orders. The most essential of them is the quadrupole deformation, at which the nucleus gets the shape close to a prolate or oblate ellipsoid. This deformation includes a statical part and dynamic one, growing out of zero fluctuations of the nuclear surface.

In case of the even-even nuclei the value of deformation parameters β can be obtained from the reduced probabilities of the electric quadrupole transitions between the first level 2^+ and the ground state 0^+ - B(E2):

$$\beta = \frac{4\pi}{3ZR^2}\sqrt{B(E2)}. \qquad (8)$$

The collection of the experimental values β, obtained in such a way, is presented in review [16]. At the absence of experimental values β the empirical ones were used obtained from the dependence of the deformation parameter on the neutron number in the nucleus [17]. Using these values β and the expression (4) it is possible to determine the MSCR change at the transition from the spherical nucleus with the magic neutrons number N to the nuclei with N + 2 and N - 2. The values of the deformation parameters of the considered nuclei and the MSCR changes, induced by them, are presented in Tabl. 3. It is visible, that the obtained values $\langle r^2\rangle_\beta$ are rather

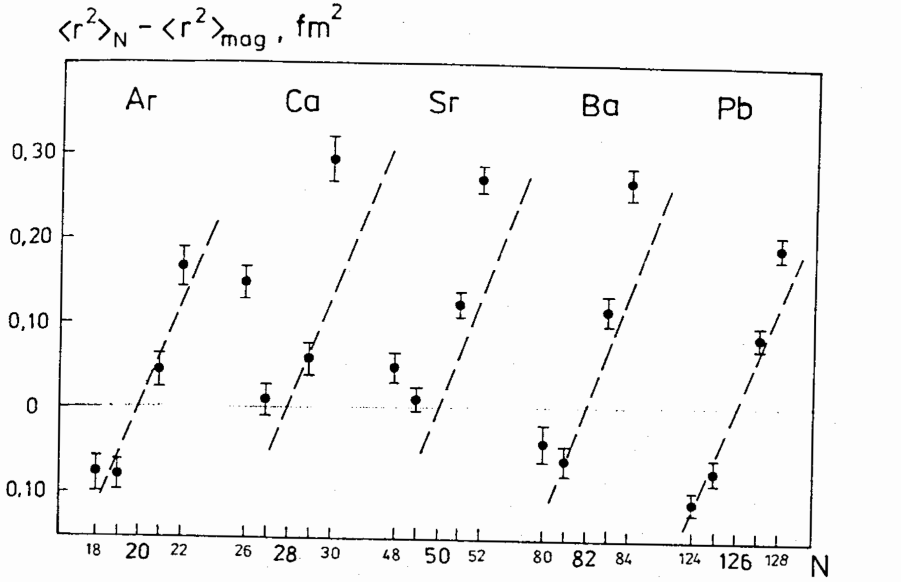

Fig. 2. The dependence of the MSCR differences of nuclei with the closed neutron shell and distinguished from them on one or two neutrons on the neutron number in the nuclei. The dotted line are the droplet model calculations.

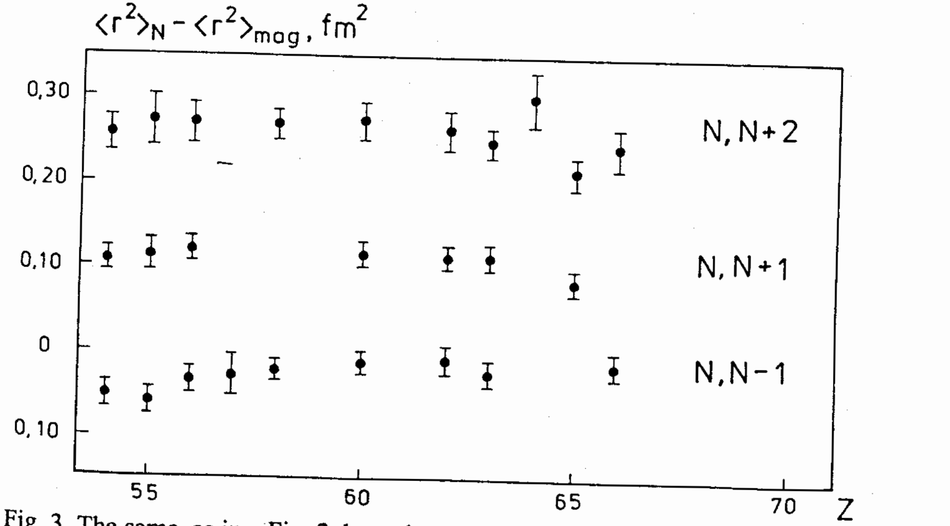

Fig. 3. The same, as in Fig. 2,dependence, but on atomic number of an element Z at N = 82.

TABLE 3

CHANGE OF MSCR, INDUCED BY THE QUADRUPOLE DEFORMATION OF NUCLEI

$N = N_{mag.}$			$N_1 = N_{mag.} - 2$		$N_2 = N_{mag.} + 2$	
$N_{mag.}$	Nuclei	$\beta(N_{mag.})$	$\beta(N_1)$	$\Delta < r^2 >^{N,N_1}$ fm^2	$\beta(N_2)$	$\Delta < r^2 >^{N,N_2}$ fm^2
20	^{38}Ar	0.162(6)	0.273(16)	0.223(10)	0.251(15)	0.169(40)
	^{40}Ca	0.122(10)			0.247(10)	0.226(40)
28	^{48}Ca	0.101(17)	0.152(5)	0.062(20)	0.240(20)	0.220(60)
	^{50}Ti	0.166(11)	0.269(7)	0.228(45)		
	^{52}Cr	0.224(5)	0.293(8)	0.189(37)	0.250(6)	0.065(27)
50	^{86}Kr	0.145(6)	0.149(4)	0.008(16)	0.18(2)*	0.070(60)
	^{88}Sr	0.117(3)	0,128(10)	0.019(22)	0.120(19)	0.005(30)
	^{90}Zr	0.091(4)	0.12(2)*	0.041(30)	0.103(4)	0.017(11)
	^{92}Mo	0.106(3)	0.14(2)	0.060(40)	0.151(2)	0.079(22)
82	^{136}Xe	0.086(19)	0.120(10)	0.064(40)	0.11(2)*	0.100(70)
	^{138}Ba	0.092(2)	0.124(8)	0.063(21)	0.15(2)*	0.110(60)
	^{140}Ce	0.101(1)	0.127(7)	0.056(18)	0.124(2)	0.049(8)
	^{142}Nd	0.093(1)	0.123(10)*	0.063(20)	0,131(4)	0.083(15)
	^{144}Sm	0.088(1)	0,127(10)*	0.086(20)	0,125(10)	0.084(20)
126	^{206}Hg	0,040(10)	0.069(1)	0.063(21)		
	^{208}Pb	0.023(3)	0.054(3)	0.065(10)	0.050(10)*	0.045(15)

* empical values

insignificant and, as a rule, cannot explain the observed deviations $<r^2>$ from the smooth dependence on the neutron number in a nucleus (Fig.2). The inclusion of the higher order deformations does not improve practically a situation. The octupole deformation parameters (collected in the review [18]) in the nuclei near the magic neutron numbers are of the same order, as the quadrupole deformation parameters and their changes are even less. The gexadecapole deformation, as a rule, is much less than these two previous ones. Therefore it is possible to believe that the dependence of the nuclei volume and, hence, $<r^2>_v$ is not the smooth function of the neutron number in the nuclei near the closed shells, and the change $<r^2>_v$ depends on quantum numbers of a neutrons and on the degree of shell filling.

It is interesting to look for the change $<r^2>_v$ at crossing the various closed neutron shells. These values $<r^2>_v$ can be obtained as the difference between the experimental values of the MSCR changes and the corrections on the change of the quadrupole deformation presented in Tabl. 3:

$$\Delta\langle r^2\rangle_V = \Delta\langle r^2\rangle_{exp} - \Delta\langle r^2\rangle_\beta . \qquad (9)$$

The obtained in such a way values $<r^2>_v$ are shown in Fig. 4. It is visible, that the values $\Delta<r^2>_v$ differ near the different magic neutron numbers, and also the values $\Delta<r^2>_v$ at $N_{mag.}$ + 2 are more than at N_{mag} - 2. It means, that volume of a nucleus grows much faster at the beginning of a neutron shell filling than at its end. However this difference decreases with the raising Z and N of the nucleus, and for isotopes Hg and Pb vanishes practically. But in the light nuclei (Ar and Ca) the picture is opposite: $\Delta<r^2>_v$ is more at the end of the shell than at its beginning.

Another possibility of the explanation of the observed $<r^2>$ dependence at the crossing of the neutron closed shell is a thickness of the surface layer (skin thickness) in the nucleus. As is well known from elastic electron scattering experiments, the nuclear charge distribution has a rather diffuse surface region. The parameter defining this region (a) is included in the expression (3) for the MSCR. It was observed that the scin thickness exhibits pronounced shell effect [20]. Its value is much less at the end of the shell than at the beginning.

All considered cases of the MSCR change are concerned to the nuclei near the valley of β-stability. For the nuclei far from this valley there can be of other character of the MSCR change at the crossing of the closed neutron shell. The indication on it serves a chain of the neutron-rich Na isotopes, in which the sharp increase of MSCR was observed at the transition from the nucleus ^{30}Na (N = 19) to ^{31}Na (N = 20) [21]. Such jump of MSCR can mean that the Na nuclei at the access of the magic neutron number (N = 20) become not spherical, as in all considered above cases, but strongly deformed. Therefore it is very interesing to measure the charge radii of the nuclei with the magic neutron number, but situated far from the valley of β-stability.

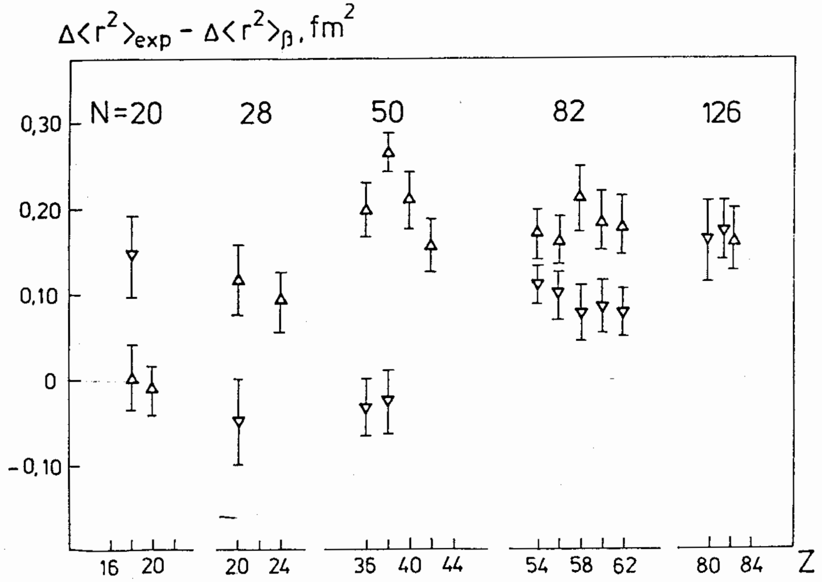

Fig. 4. The dependence of experimental values of the MSCR differences after the deduction of the correction on the change quadrupole deformation of a nucleus on atomic number Z.

Δ – $\Delta\langle r^2\rangle_V^{N,N-2}$

∇ – $\Delta\langle r^2\rangle_V^{N,N+2}$.

In conclusion it is possible to note, that the charge radii reflect a lot of the details of the nuclear structure: the deformations of the various orders, the nucleon configuration, the degree of the neutron shell filling. Therefore their measurements are the valuable source of the information about these nuclear characteristics.

REFERENCES

1. Barret R.C., Jackson D.F. – Nuclear sizes and structure, Clarendon Press, Oxford, 1972.
2. Bohr A., Mottelson B. – Nuclear structure, V.1, Benjamin, N.Y., 1969..
3. King W.H. - Isotope Shift in Atomic Spectra, Plenum, N.Y., 1984.
4. Gangrsky Yu.P., Marinova K.P., Markov B.N., e.a. // Izv. AN, ser. phys., 1985, V.49, P. 2261.
5. Gangrsky Yu.P., Zemlyanoi S.G., Izosimov I.N. e.a. // PTE, 1990, №1, P.168.
6. Gangrsky Yu.P., Marinova K.P., Zemlyanoi S.G. e.a. // J. Phys. B, 1995, V.28, P.957.
7. Gangrsky Yu.P., Zemlyanoi S.G., Kolesnikov N.N. e.a. // Yadernaya Physica, 1989, V.50, P.1217.
8. Borisov S.K., Gangrsky Yu.P., Hradecni Ch. e.a. // JETP, 1987, V.93, P. 1545.
9. Aufmuth P., Heulig K., Steudel A. // ADNDT, 1987, V.37, P.445.
10. Otten E.W. - Treatise on Heavy-Ion Science, Plenum, N.Y.,1989, V.8, P.517.
11. Angeli I. // Acta Phys. Hung., 1991, V.69, P.233.
12. Nadjakov E.G., Marinova K.P., Gangrsky Yu. P. // ADNDT, 1994, V.56, P.133.
13. Fricke G., Bernhardt C., Heulig K. e.a. // ADNDT, 1995, V.60, P.177.
14. Myers W.D. - Droplet Model of the Nucleus, IFI Plenum, N.Y ., 1977.
15. Myers W.D., Schmidt K. // Nucl. Phys. A, 1983, V.410, P.61.
16. Raman S., Malarkey C.H., Milner W.T. e.a. // ADNDT, 1987, V.36, P.1.
17. Raman S., Nestor C.W., Kanane S., Bhate K.H. // ADNDT, 1988, V.38, P.1.
18. Spear R.H. // ADNDT, 1989, V.42, P.55.
19. Gangrsky Yu.P. // Particle and Nuclei, 1992, V.23, P.1616.
20. Friedrich J., Voegler N. // Nucl. Phys. A, 1982, V.373, P.192.
21. Touchard F., Serre J.V., Buttgenbach S. e.a. // Phys. Rev. C, 1982, V.25, P.2756.

X-Ray Spectroscopy of Exotic Radioactive Beams at RIKEN

M. Wakasugi

RI Beam Factory Project Office, RIKEN, Wako, Saitama 351-0198, Japan

Abstract. We will construct the electron-RI collider (double storage ring: DSR) at RIKEN Radioactive Isotope Beam Factory (RIBF). Accelerator complex including the DSR is called MUSES (Multi-USe Experimental Storage rings). The DSR is a new type of storage ring. One ring of the DSR is for RI (heavy ion) beams, and another ring accepts not only heavy ion beams but also an electron beam. In this paper, we present outline of the RIBF project and one of unique experiments, which is the X-ray spectroscopy of RI beams, planned at the DSR.

OUTLINE OF RIBF PROJECT

The Radioactive Isotope Beam Factory (RIBF) is an expansion of the existing heavy ion accelerators facility at RIKEN[1]. The construction of the RIBF is separated into two phases. The first phase consisting of an intermediate ring cyclotron (IRC), a superconducting ring cyclotron (SRC), two RI beam separators (Big RIPS) and some experimental halls has been started from this year. The second phase is named MUSES (Multi-USe Experimental Storage rings) project[2]. The MUSES is an accelerators complex consisting of an accumulator cooler ring[3] (ACR), a booster synchrotron ring[4] (BSR), a 300-MeV electron linac[5] (e-linac) and double storage rings[6] (DSR). Figure 1 shows a plan view of the RIBF. Heavy ion beams from the RRC (Riken Ring Cyclotron K=540) are boosted up to 400A MeV for light ions and more than 100A MeV for heavy ions by the IRC (K=950) and the SRC (K=2500). With this beam energy, we can produce RI beams for all elements using projectile-fragmentation process. Details of the SRC and the IRC are described elsewhere[7,8].

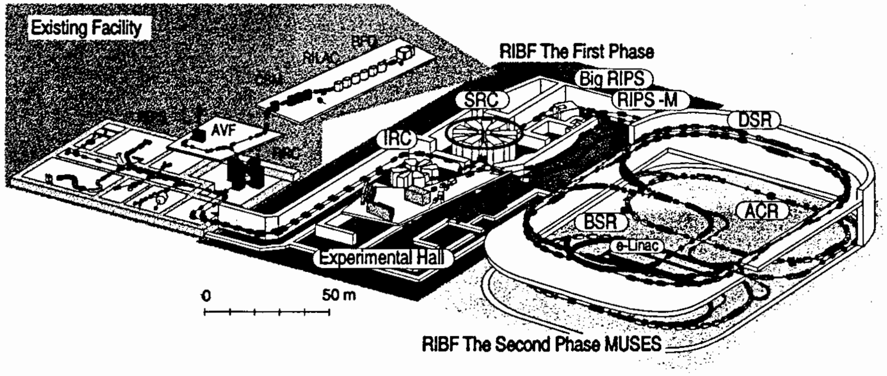

FIGURE 1. Plan view of the RIBF at RIKEN.

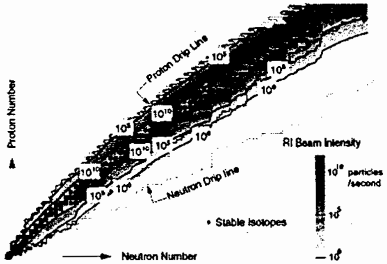

FIGURE 2. Estimated RI beam intensity from the Big RIPS. The intensity of the primary beam is assumed to be 1 pμA. The primary beam energy and target thickness are optimized in this calculation.

RI Beam Separators

At the downstream of the SRC, we construct three RI beam separators. Two separators (Big RIPS) provide RI beams for the experimental halls, and another (RIPS-M) for the MUSES system. The primary beam is supplied for three separators with time sharing technique (see Fig. 4). A pulse beam with the beam intensity of 100 particles μA (pμA) is supplied for RIPS-M, and the maximum duty factor is 10^{-3} (the beam duration of 30 μsec and the interval of 30 msec). DC beams with the intensity of 1 pμA are supplied for the Big RIPS. RI beam intensity from the Big RIPS estimated using the computer code INTENSITY2[9] is shown in Fig. 2. About 3000 radioactive isotopes including about 1000 new isotopes can be used for experiments. The RIPS-M used for the MUSES has a momentum acceptance of ±2.5 % and an angular acceptance of ±10 mrad. The momentum spread of the RI beams from the RIPS-M is expected to be ±0.5 %. Since this value is too large from the cooling time in the ACR point of view, we place debunchers at about 80-m downstream of the RIPS-M. The momentum spread is reduced to ±0.15 % by the debunchers. The maximum RF voltage required here is totally 4.23 MV[10].

Accumulator Cooler Ring (ACR)

Figure 3 shows schematic view of the MUSES system. The RI beams are injected into the ACR by means of a multi-turns injection method (about 30 turns per one injection). Injected RI beam is stacked by controlling the supplied RF voltage and the frequency in the ACR. During RF stacking process, the beam is cooled down in both the transverse and the longitudinal directions by combination of a stochastic cooling[11] and an electron cooling methods[12]. A cycle of the injection, i.e. the multi-turns injection, the RF stacking and the cooling, is repeated until that the number of stored particles reaches to the equilibrium number which depends on the lifetime of the RI and the space charge limit. This cycle is shown in Fig. 4(b). The combination of the stochastic cooling and the electron cooling makes the cooling time shorter than that for the case of only the electron cooling. The cooling time is, roughly speaking, less than 1 sec for all RI beam in our estimation. If we do not need the cooling, only the stacking process takes about 30 msec. This is why the maximum

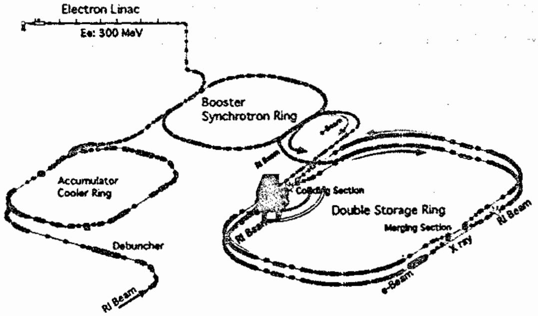

FIGURE 3. Schematic view of the MUSES system.

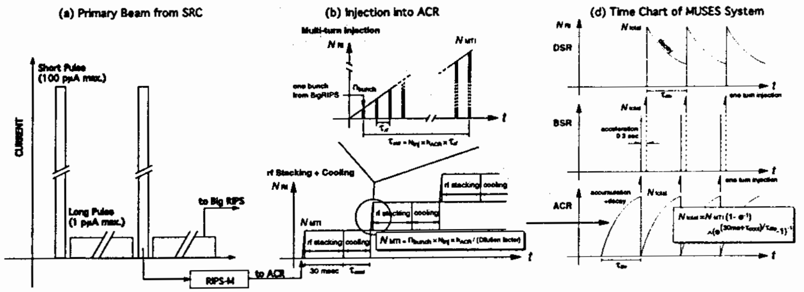

FIGURE 4. Time charts of ion beam in the MUSES system. (a) indicates the time sharing of the primary beam from the SRC, (b) the injection cycles, and (c) the time charts of the ACR-BSR-DSR complex.

duty factor of primary beam for the RIPS-M is 10^{-3}. Details of the ACR, the injection system and the cooling devices installed in the ACR are described in Refs. 3, 10, 11 and 12. The ACR itself is not only a cooling device but also an experimental device. We provide an electron cooler, schottky devices, four dispersive positions in arcs section (the maximum dispersion is 4.52 m), two achromatic straight sections where internal targets can be placed, etc. in the ACR so that the ACR is responsible to various experiments. Some experiments have been already proposed at the ACR, and they are presented elsewhere.

Booster Synchrotron Ring (BSR)

The cooled RI beam is extracted from the ACR and injected into the BSR to boost up to the required energy, and the beam is immediately transported to the DSR as shown in the time chart of Fig. 4(c). The BSR has a circumference of 179.7 m, the maximum magnetic rigidity of 14.6 Tm, a repetition rate of 1 Hz and the acceleration time of 0.3 sec. The ion beams can be accelerated up to 1.4 GeV for proton and 0.8A GeV for uranium. Relatively wide range of RF frequency of 25-53 MHz is required to boost up to the maximum energy[13]. Two kinds of extraction methods are provided[14], which are a fast (one turn) extraction and a slow extraction using 1/3 resonance technique. The fast extraction is for transporting the beams to the DSR, and the slow extraction is used for experiments at the experimental halls. The BSR can accept not only ion beams coming from the ACR but also an electron beam from the e-linac. The electron beam can be accelerated from 300 MeV up to required energy, the maximum energy is 4.8 GeV. Depending on the use of the electron beam at the DSR, either the single bunch or the full bunch operation mode is chosen in the BSR. Corresponding to that, the operation mode of the e-linac is also changed to the short pulse mode (1-nsec pulse length, 1-A peak current) or the long pule mode (5 μsec, 100 mA).

Double Storage Rings (DSR)

As shown in Fig. 3, the DSR is a new type of experimental storage ring that consists of vertically stacked two rings which are called e-ring and I-ring, respectively. It has a circumference of 269.5 m and two colliding points in long straight sections which are called the colliding section and the merging section, respectively. The colliding section is for nearly head-on colliding experiments and the crossing angle is 20 mrad. The RI-electron collision experiment is planned at the colliding section. On the other hand, the merging section with the crossing angle of 175 mrad is for the ion-ion merging experiments. In this section, we can make low energy collision experiments such as a fusion reaction. In this straight section, the RI-X-ray colliding section is also provided. An undulator is installed as a source of high-brilliant X ray in this section. Details of this experiment is described later. The DSR has different operation modes corresponding to different types of collision experiments. There are the colliding mode and the merging mode for the RI (ion) beams. For the electron beam, we have the small emittance operation mode required to produce high-brilliant X ray, and the large emittance operation mode is also required to get larger luminosity for the RI-electron collision experiment. According to requirements for the small emittance mode, a double bend achromatic (DBA) lattice is adopted in the arc sections, and the emittance of order of 10^{-9} mrad is presently designed. On the other hand, the emittance for the large emittance mode is designed to be about 10^{-6} mrad. Specifications of the ion and the electron beams for each operation mode are summarized in Table I, and details of design of the DSR is described in Refs.6 and 15.

TABLE I. Specifications of the ion and the electron beams in the presently designed DSR

	e-Ring		I-Ring	
	Large emittance mode	Small emittance mode	Colliding mode	Merging mode
Harmonic No.	450	450	48	48
Momentum compaction	0.042	0.0014	0.039	0.039
Betatron tune ν_x/ν_y	6.754/8.164	16.046/9.106	6.235/5.018	5.637/5.732
Emittance $\varepsilon_x/\varepsilon_y$ (πμmrad)	0.97/0.01 at GeV	0.0016/0.0047 at 1 GeV	1.0/1.0 typical	1.0/1.0 typical
Betatron function β_x/β_y (m)	0.02/0.02 [a]		0.1/0.1 [a]	0.6/0.6 [b]
Natural chromaticity ξ_x/ξ_y	-37.7/-90.7	-29.7/-34.7	-62.7/-47.6	-11.4/-10.3
Momentum spread ($10^4\Delta E/E$)	2.64 at 1 GeV	2.74 at 1 GeV		
Radiation loss (keV/turn)	10.6 at 1 GeV	10.6 at 1 GeV		

[a] at the colliding point.
[b] at the merging point.

RI-X-RAY COLLISION EXPERIMENT

The purpose of this experiment is to determine the mean square nuclear charge radii $<r^2>$ and the electromagnetic moment by means of isotope shift measurements in the 2S-2P atomic transitions of the Li-like RI ions[16,17]. We provide an undulator and an X-ray spectrometer as a monochromatic X-ray source in the e-ring of the DSR. The advantage of this experiment is that this method can be applied to small number of RI's stored in the DSR because the atomic transition has much bigger cross section compared with nuclear reactions.

According to the multi-configulation Dirac-Fock calculation[18], the excitation energy of $2S\text{-}2P_{1/2}$ (D1) transition has less than 300 eV for all element. X ray in this energy region is easy to produced at the DSR. The isotope shift in this transition is expected to be larger than the other charge states. Because of simple electronic structure, calculation for nuclear effects in the isotope shift is possible with high accuracy. These are why we choose the Li-like charge state as a target of this experiment. The problem is that we have to make RI ions having three electrons. Figure 5 shows the production rate of the Li-like RI beam from the RIPS-M. Because of required ion beam energy for the projectile-fragment reaction, the Li-like ions can be produced for elements of Z>36. So this experiment is mainly applied to heavier elements.

Requirements for RI beam and X ray

We wish to derive the $<r^2>$ values with the error of less than 5 % from the isotope shifts. The requirement for RI beams is that the momentum spread ΔP/P should be 10^{-4} - 10^{-3} for Z=40 - 92. This beam is provided in two ways: one is the use of the RI beam cooled by the ACR (storage mode), and another way is that the RI beam is directly transported from the RIPS-M to the DSR after momentum selection by slits at the RIPS-M (direct mode). Both ways have advantages and disadvantages. Former way is useful for RI's having relatively long lifetime because of the cooling time at the ACR, and latter way is useful for RI's having shorter lifetime and large production rate. Depending on the lifetime and the production rate, we can choose either way. On the other hand, requirements for the X ray are follows. The X-ray energy is 30 - 800

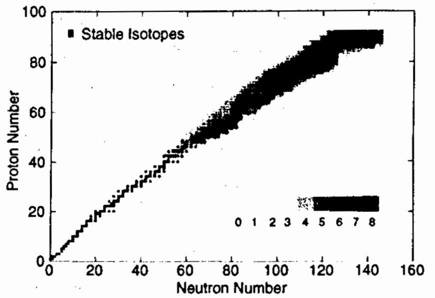

FIGURE 5. Production rate of Li-like RI beams. Conditions such as the primary beam energy, target thickness, etc.,are optimized to produce Li-like RI ions. The primary beam intensity is assumed to be 1 pμA.

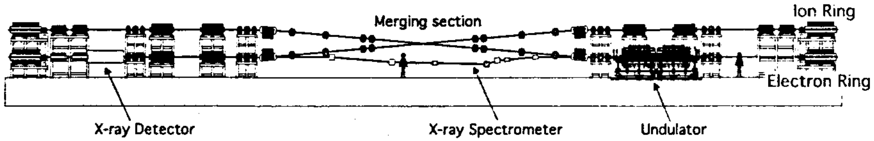

FIGURE 6. Experimental setup of the RI-X-ray collision experiment at the DSR.

eV to excite the D1 transition of Z>40 elements, and the energy resolution is about $\Delta E_x/E_x=10^{-4}$. The X ray intensity should be at least 10^{12} photons/sec/0.01%b.w. at the RI-X-ray colliding section.

Experimental setup

Figure 6 shows experimental setup installed near merging section in the DSR. This consists of an undulator, an X-ray spectrometer and a fluorescence X-ray detector. High-brilliant X ray is produced by the undulator, its energy resolution is reduced to 10^{-4} by the X-ray spectrometer, and the X ray injected again into the DSR collides with RI ions at the detector position (RI-X-ray colliding section). The resonance energy of the D1 transition is shifted due to the Doppler effect. Calibration of the resonance energy is performed in two ways. One is the velocity measurement using schottky signals in the ring. Another way is that the measurement is repeated for RI beams propagating in both parallel and antiparallel directions to the X ray beam. From measured two Doppler shifted resonance energy of E_p and E_{ap}, we can derive true resonance energy E_0 as

$$E_0 = \sqrt{E_p E_{ap}} \;, \tag{1}$$

independently of the ion beam velocity.

The Undulator and the Photon Flux

Presently designed undulator is the Apple-II type of undulator[19] so that it is possible to scan not only the energy but also the polarization. The length of a period is 3 cm, which consists of 16 permanent magnets of Nd-Fe-B, and the total length is 4.8 m including 160 periods. The tunable range of gap width is 20 - 27 mm, corresponding to the bending factor K of 0.712 - 0.35. Required X ray energy range is covered by changing both the gap width and the electron beam energy from 0.3 GeV to 1.7 GeV. Figure 7 shows calculated photon flux from the undulator at the electron beam current of 500 mA. Assuming the transmission efficiency of the X-ray spectrometer $\varepsilon_{spt}=10^{-3}$, the intensity of X-ray at the colliding section exceeds the minimum intensity required from the experiment. In this case, quality of the electron beam in the DSR is important. As shown in Table I, the electron beam emittance in the small emittance mode is order of 10^{-9} mrad and the beam size at the undulator section is about 100 μm. This can produce high brilliant X ray as shown in Fig. 12. The specifications for the small emittance mode is the same like the third generation synchrotron light source. In such machine, instability of the electron beam is always big problem especially at lower energy. The instability is caused by the ring broadband impedance and the narrowband impedance at the high-Q cavities. We are now investigating the instability[20] and designing the vacuum tube and cavities of the DSR.

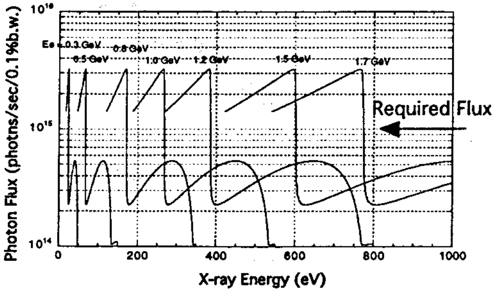

FIGURE 7. Calculated X-ray flux from the presently designed undulator.

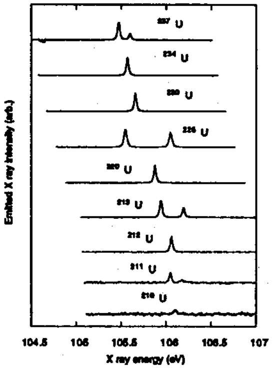

FIGURE 8. Expected spectrum for uranium isotopes for the storage mode. The following conditions are assumed: the ion beam energy of 500A MeV, the momentum spread of 0.1 %, the beam size of 2 mm in diameter, the X-ray energy resolution of 10^{-4}, the photon flux of 10^{12} photons/sec/0.01%b.w., and the cross section 2×10^{-13} cm^2.

Simulations

Taking into account expected conditions of the RI beams and the X ray mentioned above, we have simulated the expected fluorescence spectrum and results for uranium isotopes are shown in Fig. 8. The bottom spectrum is for ^{210}U which is close to the proton dripline, and about 80 ions of ^{210}U are stored in the DSR. In this simulation study, we tried to decrease the number of stored particles in the DSR, and it is found that only one ion stored in the DSR is enough to make isotope shift measurements. Assuming the maximum measurement time of 1 month and averaged counting rate of noise of 0.01 counts per second, we tried to find the lower limit of the number of particles for this experiment. This simulation results that the required minimum number of ions passing through the RI-X-ray colliding section in unit time is 10^4 ions/sec for this experiment. Figure 9 shows the number of ions passing through the RI-X-ray colliding section in unit time for both

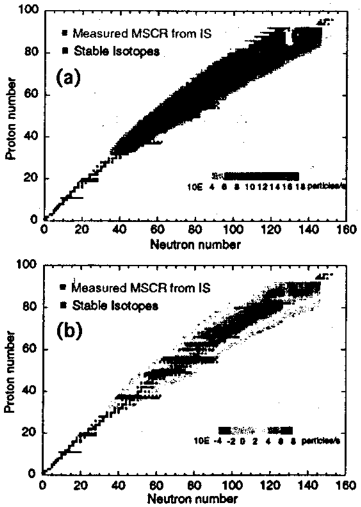

FIGURE 9. Number of ions passing through the RI-X-ray colliding section in unit time. (a) is for the storage mode and (b) is for the direct mode.

the storage mode and the direct mode described above. Especially, the direct mode is useful for isotopes located at unstable valley around N=130, because these isotopes have short lifetime and large production rate. The total number of isotopes having more than 10^4 ions/sec is about 1900 isotopes.

CONCLUDING REMARKS

In the MUSES project, we will construct two storage rings: the ACR and the DSR. The DSR is a unique storage ring because not only the RI beams but also the electron beams can be stored at the same time. This allow us to perform new type of collision experiments such as the RI-electron collision and the RI-X-ray collision. According to many requirements of various experiments, the DSR has been designed to be a highly potential machine.

With respect to measurement of the mean square nuclear charge radii, the RI-X-ray collision experiment further expands the boundary of the limit of the measurement. The measurements for RI's having the lifetime of order of 1 μsec is possible using the direct mode. Totally, we can make measurements for about 1900 isotopes with Z>36. The key of this experiment is the production of the intense monochromatic X ray,i.e. providing a large-current small-emittance electron beam in the DSR. The details of design of the accelerator system and the detector system are in progress.

REFERENCES

1. Yano Y., et al., Proc. of PAC97, 930 (1998).
2. Katayama T., Nucl. Phys. A626, 545c (1997).
3. Ohtomo K., et al., Proc. of PAC97, 1072 (1998).
4. Ohkawa T., et al., Proc. of PAC97, 1024 (1998).
5. Kamino Y., et al., Proc. of EPAC98, 722 (1998).
6. Inabe N., et al., Proc. of PAC97, 1400 (1998).
7. Goto A., et al., Proc. of 16th Cyclotron and Their Applications, to be published.
8. Kawaguchi T., et al., Proc. of PAC97, 3419 (1998).
9. Winger J.A., et al., Nucl. Instrum. Meth., B70, 380 (1992).
10. Ohtomo K., et al., Proc. of EPAC98, 2126 (1998).
11. Inabe N., et al., Proc. of EPAC98, 1037 (1998).
12. Watanabe I., et al., Proc. of EPAC98, 2258 (1998).
13. Watanabe I., et al., Proc. of EPAC98, 1823 (1998).
14. Ohkawa T., et al., Proc. of EPAC98, 2123 (1998).
15. Inabe N., et al., Proc. of EPAC98, 897 (1998).
16. Tanihata I., Nucl. Phys. A588, 253c (1995).
17. Wakasugi M., et al., Proc. of EPAC96, 611 (1997).
18. Cheng K.T., et al., Atom. Data Nucl. Data Tables 24, 111 (1979).
19. Wakasugi M., et al., Proc. of PAC97, 3521 (1998).
20. Wakasugi M., et al., Proc. of EPAC98, 1017 (1998).

Resonant ionization spectroscopy on secondary beams, recent results on Ir isotopes

D. Verney, F. Le Blanc, J. Obert, J. Oms, J.C. Putaux,
B. Roussière and J. Sauvage
Institut de Physique Nucléaire, IN2P3-CNRS, 91406 Orsay Cedex, France
J. Pinard and L. Cabaret
Laboratoire Aimé Cotton, CNRS, 91405 Orsay Cedex, France
G. Huber and V. Sebastian
Institut für Physik der Universität Mainz, 55099 Mainz, Germany
J.E. Crawford and J.K.P. Lee
Physics Department, McGill University, H3A2T8 Montréal, Canada
J. Genevey and F. Ibrahim [1]
Institut des Sciences Nucléaires, IN2P3-CNRS, 38026 Grenoble Cedex, France
G. Le Scornet and D. Lunney
CSNSM, IN2P3-CNRS, 91405 Orsay Cedex, France
and ISOLDE collaboration
CERN, 1211 Genève 23, Switzerland

Abstract. Laser spectroscopy measurements have been performed on neutron-deficient iridium isotopes. The hyperfine structure and isotope shift of the optical Ir I transition $5d^7 6s^2\ {}^4F_{9/2} \rightarrow 5d^7 6s6p\ {}^6F_{11/2}$ have been studied for the $^{182-189}$Ir, ^{186}Ir^m and ^{191,193}Ir isotopes. The nuclear magnetic and quadrupole moments were obtained from the hyperfine splitting measurements and the changes of the mean square charge radii from the isotope shift measurements. A large deformation change between ^{187}Ir and ^{186}Ir and between ^{186}Ir^m and ^{186}Ir^g has been observed. The experimental magnetic moments are compared to those calculated in the framework of a rotor+quasiparticle model, which allows the determination or confirmation of the labels of the quasi-particle proton states.

Introduction

The dipole magnetic and quadrupole electrostatic moments of nuclei, and the variation of the nuclear radii along isotopic series provide fundamental information for any attempt to analyse nuclear shapes in terms of nuclear structure. The possibility to determine these quantities from hyperfine spectra and isotope shift measurements turns laser spectroscopy into a very efficient tool for the investigation of nuclear properties.

Neutron deficient iridium isotopes belong to a transitional mass region situated between the well-deformed rare-earth nuclei, and the spherical doubly-magic ^{208}Pb. Important variations of the mean square charge radius between neighbouring isotopes have been pointed out in this region first in Hg [1,2] and later on in Au [3-5,9] and Pt [6,7,10]. They were interpreted as shape transitions and deformation changes. Similar variations were also studied between ground and isomeric states for instance in ^{185}Hg [8], ^{184}Au [9] and ^{183}Pt [10] which were associated with shape or deformation coexistences.

The striking point emerging from this important sum of studies is the role that a few

---

[1] Permanent address : Institut de Physique Nucléaire, IN2P3-CNRS, 91406 Orsay Cedex, France

specific single-particle states seems to play on the deformation of the whole nucleus. This has provided part of the motivation for the study of the neutron deficient iridium isotopes by laser spectroscopy. Moreover, a recent quadrupole-interaction-resolved NMR on Ir oriented nuclei experiment [11] has shown that the deformation of $^{186}\mathrm{Ir}^{g}$ is larger than the deformation of $^{186}\mathrm{Ir}^{m}$. The β deformation parameter can be determined more directly from the measurement of the change in the mean square charge radius. Furthermore, its sign can be extracted from the analysis of the spectroscopic quadrupole moment. And at last, the value of the magnetic moment is a precious clue for the determination or confirmation of the nuclear state configuration.

Experimental procedure

The COMPLIS experimental setup (figure 1) installed at the ISOLDE facility at CERN is based on Resonant Ionization Spectroscopy technique [12]. The iridium isotopes are obtained as β-decay descendants of mercury isotopes. These ones are produced by bombarding a molten lead target with the 1 GeV staggered proton beam delivered by the PS-Booster [13], and are then extracted under 60 kV from the ion source. After mass separation through the General Purpose Separator, the Hg^+ ions are guided by a series of electrostatic quadrupoles and deflectors, then are slowed down to 1 keV and focused with a retardation lens in order to be collected in the first atomic layers of a graphite substrate.

After a waiting time defined in order to optimize the amount of the grand grand daughters of the Hg atoms, Ir atoms are desorbed by a strongly focused Nd:YAG laser beam and, after a $10\mu s$ migration time, are then ionized in three steps at the crossing point of three laser beams. The ions created are accelerated with the same retardation lens system towards the emergent beam line of COMPLIS. They are finally detected using microchannel plates and mass identified with their time of flight.

The hyperfine spectroscopic information is provided on the first excitation step at 351.7 nm ($5d^7 6s^2\ {}^4F_{9/2} \to 5d^7 6s6p\ {}^6F_{11/2}$) : allowed atomic transitions are induced between the hyperfine levels for the resonant frequency values when scanning the frequency of the light emission of a single-mode pulsed dye laser [14]. This single mode source is realized by inserting a supplementary dye flow cell pumped by a Nd:YAG pulsed beam inside the cavity of a cw single mode dye laser of the commercial type "Coherent 599" (see figure 2). The resulting beam is then amplified outside the cavity and frequency doubled in an ADP nonlinear crystal. For operation at about 700 nm the dye used was DCM solved in DMSO for the intra cavity dye jet, the intra and extra cavity dye cells. Transitions to the second excitation step and then to the ionization continuum are induced respectively by the frequency doubled radiation and the radiation of a pulsed dye laser of a commercial type "Lambdaphysik" (see figure 2).

The pumping Nd:YAG pulse rate is 10 Hz. Optical delays are introduced on the path of the ionization beams in order for them to cross synchronously.

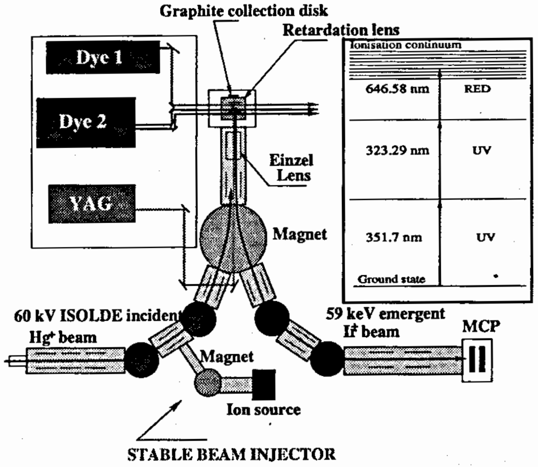

Figure 1: COMPLIS experimental setup. The insert shows the ionization scheme.

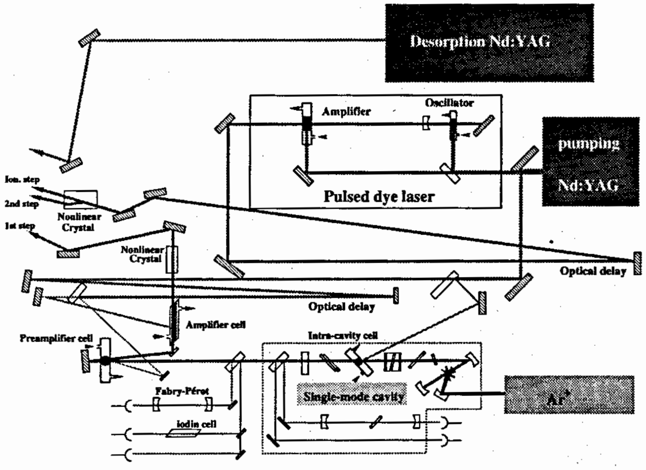

Figure 2: COMPLIS laser system.

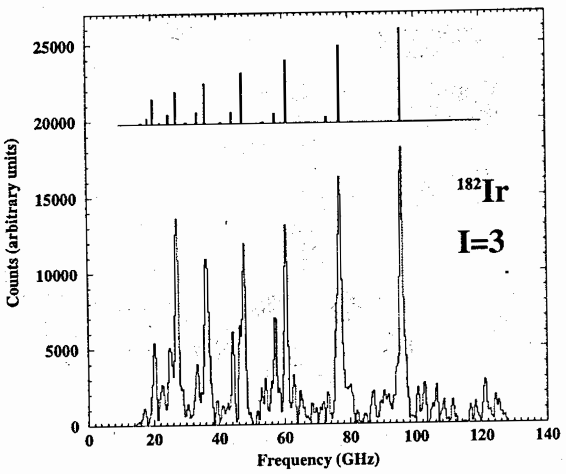

Figure 3: ^{182}Ir hyperfine experimental spectrum. In the upper part is drawn the theoretical spectrum reconstructed with the extracted hyperfine constants A, A', B, B'.

Results and discussion

Nuclear moments

The A and B hyperfine constants were extracted from the experimental spectra. The hyperfine spectrum of ^{182}Ir which is the lightest isotope that we measured is shown as an example on figure 3. The magnetic dipole moments were calculated with :

$$A = \frac{\mu_I \overline{H_0}}{IJ} ,$$

where the magnetic field $\overline{H_0}$ created by the electrons at the nucleus has been evaluated from the very accurate values of A=0.05752131(7) and μ_I=0.1507(6) known for the stable ^{191}Ir [15,16]. The spectroscopic quadrupole moments were deduced from the B hyperfine constant using :

$$B = e\, Q_S\, \overline{\Phi_{JJ}}(0) ,$$

where the gradient of the electric field $\overline{\Phi_{JJ}}(0)$ created by the electrons at the nucleus has been extracted from the B=0.4712046(6) and Q_S=0.816(9) values given in [15,17] for ^{191}Ir.

The values obtained for the moments are reported in Table 1 and compared to those available in literature. The signs of the magnetic moments for $^{182-189}$Ir and ^{186}Ir^m could be assigned for the first time.

Table 1: Magnetic and quadrupole moment values for Ir isotopes from COMPLIS experiment as compared to values available in literature.

		COMPLIS		LITERATURE[18]	
A	I	$\mu_I(\mu_N)$	Q_S(b)	$\mu_I(\mu_N)$	Q_S(b)
193	$3/2^+$	+0.1658(76)	+0.750(69)	+0.1637(6)	+0.751(9)
191	$3/2^+$			+0.1507(6)	+0.816(9)
189	$3/2^+$	+0.145(7)	+0.87(7)	0.13(4)	+0.878(10)[11]
188	1^-	+0.31(1)	+0.47(5)	0.302(10)	+0.484(6)[11]
187	$3/2^+$	+0.171(10)	+0.88(10)		+0.941(11)[11]
186^g	5^+	+3.69(15)	−2.6(9)	3.88(5)	−2.548(31)[11]
186^m	2^-	−0.634(29)	+1.5(1)	0.638(8)[19]	+1.456(17)[11]
185	$5/2^-$	+2.55(7)	−1.8(6)	2.605(13)	−2.06(14)
184	5^-	+0.690(32)	+2.6(4)	0.696(5)	+2.1(3)
183	$5/2^-$	+2.36(8)	−1.9(6)		
182	3^+	+2.64(19)	−1.7(5)	2.28(8)	

Table 2: Experimental magnetic moments and rotor+quasiparticle model calculation results for neutron-deficient iridium isotopes.

A	I	μ_{exp} (μ_N)	β	state K[Nn$_z\Lambda$]	μ_{calc} (0.6g$_{s,free}$)	μ_{calc} (g$_{s,free}$)
193	$3/2^+$	+0.1637(6)	0.110	3/2 [402]	+0.51	−0.12
			0.213	3/2 [402]	+0.49	−0.14
191	$3/2^+$	+0.1507(6)	0.112	3/2 [402]	+0.51	−0.11
			0.217	3/2 [402]	+0.48	−0.16
189	$3/2^+$	+0.144(7)	0.115	3/2 [402]	+0.51	−0.10
			0.210	3/2 [402]	+0.48	−0.15
187	$3/2^+$	+0.17(1)	0.217	3/2 [402]	+0.48	−0.16
186^m	2^-	−0.63(3)		$\pi 3/2[402] \otimes \nu 7/2[503]$[24]	−0.71[23]	−0.49[23]
186^g	5^+	+3.69(15)		$\pi 1/2[541] \otimes \nu 1/2[?]$[24]		
185	$5/2^-$	+2.55(7)	0.251	1/2 [541]	+1.98	+1.31
183	$5/2^-$	+2.36(8)	0.267	1/2 [541]	+1.89	+1.26

Theoretical treatment

A very first step towards an interpretation of the experimental results is done by comparing the experimental magnetic moments to those calculated using an axial rotor+quasiparticle model.

In this approach, single-particle states ψ of the core are first calculated with the Constraint Hartree-Fock method [20] using the Skyrme III effective nuclear interaction and a BCS treatment for the pairing. Axial symmetry is assumed and these states are calculated self-consistently as a function of the deformation by minimizing $\langle H\rangle + f(\langle Q\rangle)$: the total hamiltonian $\langle H\rangle$ and an additive term which depends on the quadrupole moment and corresponds to a constraint.

On a second step, in the framework of a rotor+quasiparticle model [21], the resulting ψ wave functions located at ±5 MeV around the Fermi level are used in order to diagonalize the total hamiltonian including the Coriolis interaction term. During the procedure, the experimental dependence on the core angular momentum R of the moment of in-

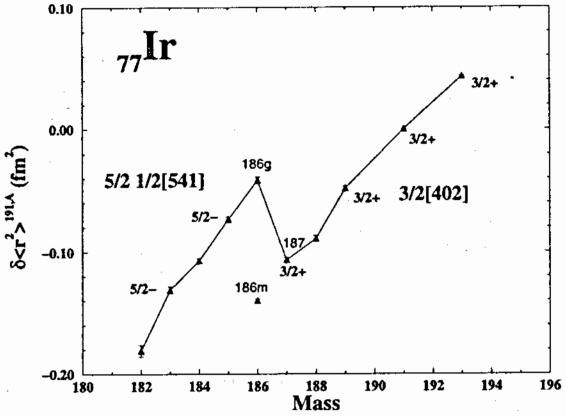

Figure 4: Preliminary curve of the mean square charge radius variations of neutron-deficient iridium isotopes from isotope shift measurements. The F atomic factor was evaluated using the $\lambda^{191-193}$ given in [25]

ertia $\Im(R)$ is implemented. The eigenstates Ψ obtained correspond to the core-coupled quasiparticle states. The BCS treatment of the pairing leads to a distribution of the probability of occupation of these quasiparticle states around the Fermi level which means that a Ψ wave function describe the A−1 or the A+1 nucleus, depending on its energy position as respect to the Fermi level. At last, the magnetic moments are calculated using the Ψ states and g_R=Z/A [22].

Preliminary discussion

In table 2 are presented the results of the calculations which were performed so far. The labels of the proton state indicated correspond to the main component of the quasiparticle states coupled to the even-even cores : ^{192,190,188,186,184,182}Os.

The rather satisfactory agreement obtained between the experimental moments with those calculated confirms the labels of the proton state for the odd-mass iridium isotopes. From the $\pi \otimes \nu$ configurations proposed for ^{186}Ir^g and ^{186}Ir^m in references [23,24], we can underline a change in the label of the proton state which is identified as π 3/2 3/2 [402] from ^{193}Ir to ^{186}Ir^m and π 5/2 1/2 [541] from ^{186}Ir^g to ^{182}Ir.

In figure 4 is shown the preliminary curve of the mean square charge radius variations along the iridium isotopes series. We made a crude approximation for the F atomic factor by extracting it from the value of the nuclear parameter $\lambda^{191-193}$ given in [25] and using our result for the isotope shift $\delta\nu^{191-193} = -2.00(1)$GHz. The error which is made should affect the slope without questionning the two following remarks : first, the mean

square charge radii decrease regularly except for a sudden breaking up between ^{187}Ir and ^{186}Ir^g and second, an important difference between the radii of ^{186}Ir^g and ^{186}Ir^m exists. As already suggested in [11], this should reflect the change of the proton state we underlined above and the role played by the π 1/2$^-$[541] proton state coming from the $\pi h_{9/2}$ orbital.

The very important point in an immediate future will be to extract the $\langle\beta^2\rangle^{1/2}$ deformation parameters from the $\delta\langle r_c^2\rangle$ values as soon as a reliable value for F, which is being calculated using the MCDF method, is available. These values would then be used in order to fix the constraint in the calculations of the quasiparticle states, which in turn could lead to a better understanding of the K mixing in these states.

[1] J. Bonn *et al.*, Phys. Lett. **38B**, 308 (1972).
[2] G. Ulm *et al.*, Z. Phys. A **325**, 247 (1986).
[3] K. Wallmeroth *et al.*, Nucl. Phys. **A493**,224 (1989).
[4] G. Savard *et al.*, Nucl. Phys. **A512**, 241 (1990).
[5] G. Passler *et al.*, Nucl. Phys. **A580**, 173 (1994).
[6] H.T. Duong *et al.*, Phys. Lett. B **217**, 401 (1989).
[7] T. Hilberath *et al.*, Z. Phys. A **342**, 1 (1992).
[8] P. Dabkiewicz *et al.*, Phys. Lett. **82B**, 199 (1979).
[9] F. Le Blanc *et al.*, Phys. Rev Lett. **79**, 2213 (1997).
[10] F. Le Blanc *et al.*, Phys. Rev. C, in press (1999).
[11] G. Seewald *et al.*, Phys. Rev. Let. **77**, 5016 (1996).
[12] G.S. Hurst *et al.*, Rev. Mod. Phys. **51**, 767 (1979).
[13] J. Lettry *et al.*, Nucl. Inst. and Meth. **B126**, 170 (1997).
[14] J. Pinard and S. Liberman, Opt. Comm. **20**, 334 (1977).
[15] S. Büttgenbach *et al.*, Z. Phys. **A286**, 333 (1978).
[16] K.H. Burger *et al.*, Phys. Lett. **140B**, 17 (1984).
[17] Y. Tanaka *et al.*, Phys. Rev. C **29**, 1830.
[18] *Table of Isotopes*, eighth edition, Eds R.B. Firestone and V.S. Shirley, New York : John Wiley and Sons Inc., 1996.
[19] R. Eder *et al.*, Hyp. Int. **59**, 83 (1990).
[20] H. Flocard *et al.*, Nucl. Phys. **A203**, 433 (1973).
[21] M. Meyer *et al.*, Nucl. Phys. **A316**, 93 (1979).
[22] J. Libert *et al.*, Phys. Rev. **C25**, 586 (1982).
[23] C. Ekström *et al.*, Phys. Scr. **14**, 199 (1976).
[24] A. Ben Braham *et al.*, Nucl. Phys. **A533**, 113 (1991).
[25] G. Sawatzky and R. Winkler, Z. Phys. **D14**, 9 (1989).

LASER SPECTROSCOPY ON THE BEAMS OF FISSION FRAGMENTS

Yu.P.Gangrsky, D.V.Karaivanov, K.P.Marinova, B.N.Markov, G.V.Mishinsky,
S.G.Zemlyanoi and V.I.Zhemenik

Laboratory of Nuclear Reactions, JINR, Dubna , Russia

1. Introduction

The new project "Dubna Radioactive Ion Beams" ("DRIBs") is in the stage of realization now at Flerov Laboratory of Nuclear Reactions (JINR). According to the project a wide range of neutron-rich isotopes of different elements can be produced in photofission ^{235}U(γ,f)-reaction. Uranium target will be irradiated by the bremstrallung with maximum energy of 25 MeV on the electron beam with intensity of 20 μA of the MT-25 microtron. The total fragments yield from 100g U-target can be of the order of 10^{11} s^{-1}. One of the programs which can be proposed for the study of nuclei properties and of the nuclear reactions mechanism in the frame of this project and discussed here is the laser spectroscopy investigation of the structure of neutron-rich nuclei.

2. Laser spectroscopy and neutron-rich nuclei

The laser spectroscopy methods are very sensitive and precise tools for nuclear structure investigations. They allow one to determine an important nuclear parameters (spin I, magnetic dipole moment μ, electric quadrupole moment Q, changes in mean square charge radii of nuclei $\delta\langle r^2\rangle$ for a long chains of isotopes in ground and isomer states. Moreover it is possible to determine as mean squared deformation parameter of nuclei $\langle\beta_2^2\rangle$ (from the $\delta\langle r^2\rangle$-value), as well as mean deformation parameter itself $\langle\beta_2\rangle$, including its sign (from Q-value) and thus determine the shape of nuclei (oblate or prolate). The $\langle\beta_2^2\rangle$ - value is sensitive to the sum of static and dynamic (including zero-point vibration) deformation, while the latter one is sensitive just to the static deformation. All these nuclear quantities can be helpful in understanding of nuclear shape evolution, of the role and interplay of single-particle and collective effects in nuclei.

From the point of view of nuclear structure investigations by laser spectroscopy traditionally interesting regions of nuclei are that, where well deformed nuclei can be found (rare-earth elements region - for example [4]), or their deformation drastically changes (shape transitions, shapes coexistence Hg, Au, Pt-nuclei - for instance [4, 10]), or regions around nuclear shells closure. In another words,it is regions of nuclei where some peculiarities in behavior of nuclear shape and size can be observed and explanations of them are good testing points of all theoretical models of nucleus. Some of these regions are well investigated already. But, as was mentioned above, neutron-rich fission fragments of the elements from Zn (Z = 30) to Ce (Z = 58) will be produced at DRIBs facility with sufficiently high yields for laser spectroscopy experiments. And it opens a new perspectives for investigation of nuclear structure in new regions of exotic nuclei. For example, the most interesting from nuclear point of view nuclei are expected to be obtained with the following yield (at total beam intensity 10^{11} s^{-1}): ^{80}Zn -10^5 s^{-1}, ^{81}Ga - 3·10^6 s^{-1}, ^{100}Zr - 10^9 s^{-1}, ^{104}Zr - 5·10^7 s^{-1}, ^{131}In - 10^8 s^{-1}, ^{132}Sn - 5·10^8 s^{-1} (see Fig.1). Two peculiarities of the neutron-rich fission fragments are very important: low neutron binding energy (< 5 MeV) and high β–decay energy (> 5 MeV).

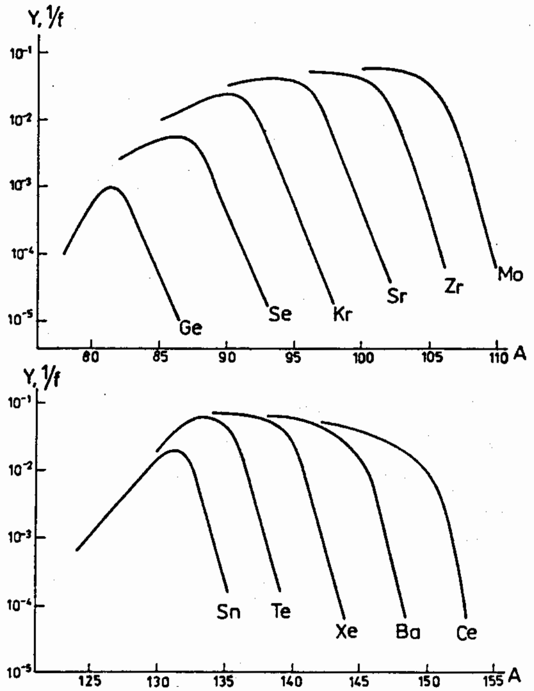

Fig.1. The yields of isotopes, obtained as fission fragments

These lead to a completely new situation in the decay characteristics and level properties of the fission fragments compared to those of the nuclei from the β-stability valley. Some special features must be mentioned, which are a consequence of the abnormal ratio of neutron to proton number: i) the character of the nucleon interactions may be drastically changed and ii) the neutrons start to fill orbits in a crucial new order. This finds its expression in the appearance of new neutron and/or proton magic numbers and new regions of strong deformation. The radical changes not only in nuclear shape but also in the whole nucleon coupling scheme are of great physical interest. Information about such an unusual behavior of nuclei can be obtained by laser spectroscopic measurements of the single and collective nuclear parameters in the following regions:

- Neutron-rich nuclei around neutron shell closures (N = 50 and N = 82). Let us remember that a "strange" behavior has already been observed at the shell closure N = 20 for the neutron-rich ^{31}Na and ^{32}Mg which, in spite of our conventional ideas, are strongly deformed. The expected region of interest around neutron magic numbers 50 and 82 are,e.g.,Zn- and Ga-isotopes with A = 79-83 and the Ag-, Cd- and In-isotopes with A = 128-132. Especially interesting **is to determine shape of** double magic nucleus ^{132}Sn and of nuclei around it. The are among the fission fragments produced at DRIBS-facility.

- Deformed neutron-rich nuclei with $N > 60$ and $Z = 36$ (Kr) to 46 (Pd). In the well-investigated shape transition regions the trends of the changes of the quadrupole deformation β_2 are very different for different Z. A drastic jump in β_2 beyond $N = 88$ and for proton number around $Z = 64$ (e.g.,Sm, Eu, Gd isotopes at $N = 90$) is observed at the beginning of the deformation region. An analogous effect is seen at its end (e.g.,Hg isotopes around $N = 100$). On the contrary, for other isotopes(e.g., Ba, Hf) the N-dependence of β_2 is very smooth. However, the deformation region between $N = 60$ and 82 for neutron rich nuclei (e.g.,^{39}Y – ^{42}Mo) remains still poorly investigated. There exist several theoretical models which predict interesting properties of nuclei in this region. According to some of them [1] around the middle of the region ($N \approx 66$) a sign change of the quadrupole deformation parameter, i.e.,a transition from prolate to oblate nuclear shape, is to be expected. One of the most interesting seems to be Zr- isotopes in which a shape transition is predicted at different neutron numbers by different theories (see Fig.2).

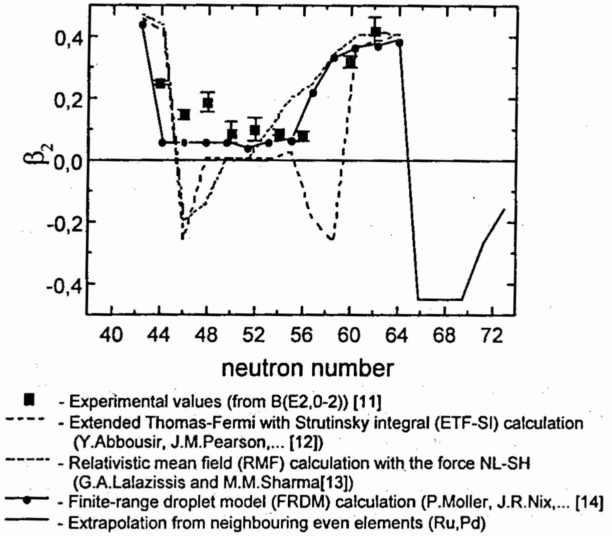

Fig.2. Quadrupole deformation in Zr nuclei

3. Experimental methods

The method of the laser excited resonance fluorescence in an atomic beam has been developed in the FLNR in two variants relative to the atomic beam source (electrically heated oven and pulsed laser evaporation) [2,3] and has already demonstrated its merits in an off-line modification in the field of many stable and long-lived isotopes: Na; Ti; Zr; the rare-earths - La, Ce, Nd, Sm, Eu and Gd; U and Am. On the basis of existing laser spectroscopy setups of different types in FLNR and our experience in this field, two laser spectroscopic methods can be proposed for the DRIBS-facility.

3.1 *Collinear laser spectroscopy as described, e.g., in [4].* The on-line mass-separator included in the DRIBS-project is very suitable for an application of the laser spectroscopic methods. The ion source with uranium target is also a part of the different systems at the DRIBS-facility. Both will be in a process of built-up. In the standard optical-detection scheme the laser-excited optical fluorescence is registered. This technique can be applied for beams with intensity usually exceeding 10^6 s^{-1} (Fig.3.). Some modifications of this technique providing a detection efficiency superior to the simple fluorescence detection and, consequently higher sensitivity, are necessary for the beams with lower intensity. They take advantage of coincidence detection of fluorescence signal with incoming beam particles (atoms or ions) [9] or the state selective ionization followed by ion counting [5], state selective atomization followed by atom counting [6] or, in the cases of short-lived isotopes, by detecting the radioactive decay. In some favorable cases a detection limit of about 100 s^{-1} can be reached.

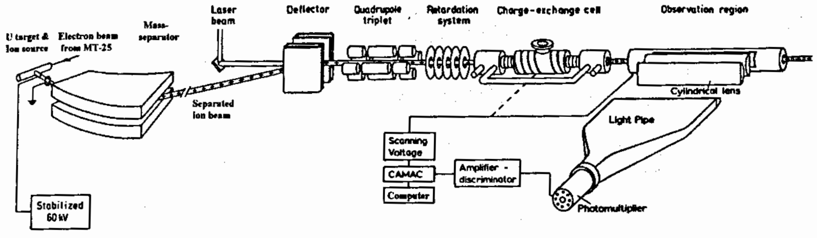

Fig.3. Standard on-line setup for collinear laser spectroscopy

The mass separators with fission fragments usually use surface ionization or plasma ion sources. Technical limits connected to the heating required for an efficient release make this type of ion sources unsuitable for the most refractory elements or for elements with high ionization potential (e.g.,Zr, Mo, Kr, Xe). The intensity produced by these ion sources is too small to form beams for any kind of laser spectroscopy experiments. Also, for the refractory elements the delay times in the source volume are too high [7] and total separation times of less than several minutes are hard to achieve, making it impossible to study nuclei with shorter lifetimes. The second method we propose avoids these problems and permits to obtain high intensity beams of such elements.

3.2. On-line laser spectroscopy with Ar-jet tranportation and laser desorption of the fission fragments. To explain the measuring procedures, we briefly describe the principle of the experiment (Fig.4). Recoils of fission fragments from multilayer uranium target (each layer about 15 mg/cm^2, layer distance ≈ 2.5 cm, up to 10 layers in the target) are stopped in a chamber with buffer gas (Ar with pressure of about 1 bar) containing aerosols and transported through a long capillary to the measuring vacuum chamber with differential pumping. There they are collected onto a rotating disk. The time of collection depends on the half-live of the investigated nuclides. Finally, after rotating the disk on 180° , the fission fragments are desorped by a high power pulsed Nd:YAG laser to form an atomic beam. Then the standard laser spectroscopy methods on collimated atomic or ion beams can be applied, provided beams of an intensity exceeding 10^7 s^{-1} are available. For isotopes with lower gain, the detection sensitivity can be enhanced by the well-known method of resonance ionization [8] or collinear spectroscopy. The method of the aerosol transport of nuclear reaction products was developed in the FLNR, JINR and was used for different experimental investigations, e.g. in radiochemistry. From the point of view of the planed laser spectroscopic experiments, the parameters of the aerosol transport system are highly promising. With transport velocity of 20 m/s, transport times less than 0, 5 s are needed for distances $\leq$ 10 m. Thus, for the refractory elements this technique is faster and essentially simpler than collinear laser spectroscopy with standard ion source (see 3.1).

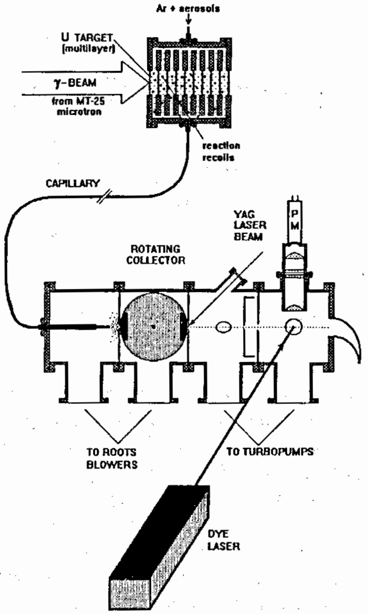

Fig.4. On-line laser spectroscopy setup with Ar-jet and laser desorption

Some combination of both method proposed is also possible. To investigate, for instance,Zr-isotopes it is not necessary to get these isotopes from the ion source directly. It is possible to obtain Zr-isotopes as daughter nuclei after radioactive decay of Rb-isotopes (Rb→Sr→Y→Zr). Rubidium ions easy to obtain in traditional type ion sources. After mass-separation and transportation Rb ions will be implanted in the rotating disk. After some time of collection and waiting for decay into Zr-isotopes, they will be desorped by Nd:YAG laser to obtain pulsed beams of Zr atoms (or ions). This idea is realized in COMPLIS setup at ISOLDE (CERN) [10]. Then again standard laser spectroscopy methods (collinear spectroscopy, resonance ionization spectroscopy, orthogonal fluorescent spectroscopy) can be applied.

4. Optical properties and possible measurements

Obviously, the nuclides of interest, from the nuclear point of view, could be a subject of laser spectroscopy investigations if they possess suitable optical qualities. Using appropriately chosen laser spectroscopy techniques and optical transitions, high-accuracy data on $\delta\langle r^2\rangle$ and on the nuclear moments for extended chains of isotopes and isomers of many elements have been obtained. But in the Z-region of the fission fragments at the DRIBS-facility ($30 \leq Z \leq 58$) only few long isotopic chains (Kr, Rb, Sr, In, Xe, Cs and Ba) including short-lived neutron-rich isotopes in ground and isomer states have been investigated by optical methods and the corresponding nuclear information has been obtained.

The accuracy with which changes in mean square charge radii $\delta\langle r^2\rangle$ can be derived from the measured isotope shifts (IS) is determined by i) the error of the measurements; ii) the uncertainty in the mass shift (MS) due to estimate of the specific mass shift (SMS); iii) the uncertainty in the interpretation of the electronic configuration involved in a particular transition (configuration mixing); iv) the error in determination of the electronic factor E, which is a link between the optical and nuclear parameters [4]. The investigation of the optical IS in light elements is subject to two major difficulties: the field shift (FS) is small compared to the mass shift (MS) and the specific MS is hard to allow for. In many cases the observed IS is very small as a result of a mutual compensation of the always positive normal MS and a negative SMS. For the medium-Z elements the contribution of the FS to the observed isotope shifts is more essential: the MS and the FS are roughly from the same order. The FS is larger than the MS in favorably chosen lines, that is, lines involving transitions of electrons to or from low s-states provided the $\delta\langle r^2\rangle$-values are not extremely small as in the case just below the closed neutron shell (N = 28, 50 and 82). Under these conditions extremely high experimental precision and resolution are necessary. In addition, laser spectroscopy experiences serious difficulties since most of these elements do not have resonance lines in the visible region.

After a detailed view on the optical properties of the above-discussed elements the following peculiarities of their optical properties should be emphasized:

- Most transitions from the ground state are in the UV region and frequency doubling or work with short lived dyes, e.g.,stilbene, is necessary.
- Access to the visible region is offered in most cases by transitions from high-lying metastable states of the neutral atoms and ions.
- There is relatively poor experimental information about the IS in different optical transition in this Z-region.
- Conclusions about the possible values of the field shift (FS) and specific mass shift (SMS) may be drawn only on the basis of the atomic state configuration under the assumption it is a pure configuration. FS can be only observed in transitions with $\Delta|\psi(0)|^2 \neq 0$. These comprise not only lines with *s*-electrons jump (or to a much smaller extend $p_{1/2}$-electrons jump) but also transitions in which the screening of the inner closed *s*-electron shell is changed. Only small SMS occurs in $ns^2 - nsnp$ or $ns - np$ transitions with absolute value seldom larger than the normal MS.

As is pointed out above, the most interesting cases for study are the neutron-rich isotopes of Zn, Ga, Cd, Ag,and In around the shell closure $N = 82$ and these of Y, Zr, Nb, Tc,and Mo from the deformation region $N \geq 60$. Some favorable optical transitions for the neutral atoms and/or single ions of these elements are present in Table 1.

Table 1. List of some favorable transitions for the elements with Z between 30 and 58 suitable for laser spectroscopy investigations. The metastable states of the optical transitions are marked with $^{m)}$. BE - binding energy of the metastable state (the values for which charge exchange with alkali vapor can provide access to the corresponding metastable states are marked with *. IS_{exp} - measured IS for $\delta A = 2$; FS - field shift, SMS – specific mass shift (l – large, s – small, ? – unknown), CL – collinear laser spectroscopy (in different variants), ON/OFF - on-line or off -line measurements possible.

Z el.	λ, nm	Transition	lower state E, cm^{-1}	BE, eV	IS_{exp}, MHz	FS/SMS	exp. method
30 ZnI	308.6	$4s^2 - 4s4p$	ground			l/s	CL, Ar-jet
	472.2	$4p - 5s$	32501 $^{m)}$	5.4*		l/s	CL
ZnII	589.4	$3d^{10}4p - 3d^9 4s^2$	48481		2700	l/l	
31 GaI	287.4	$4s^2 4p - 4s^2 4d$	ground			s/l	CL, Ar-jet
	417.2	$4s^2 4p - 4s^2 5s$	826			l/s	
	639,7	$4s^2 5s - 4s^2 6p$	24789		150	l/s	
	641.3	$4s^2 5s - 4s^2 6p$	24789		143	l/s	
32 GeI	303.9	$4p^2 - 4p5s$	ground		15		CL, Ar-jet
	306,7	$4p^2 - 4p5d$	16367 $^{m)}$	5,8*		s/l	CL
	422.6	$4p^2 - 4p5s$	16367 $^{m)}$	5,8*	-63	l/?	CL
33 AsI	197.3	$4p^3 - 4p^2 5s$	ground			l/?	
	537.2	$4p^2 5s - 4p^2 5p$	53136	3,2*		l/s	
AsII	600.2	$4p5p - 4p5s$	101088			l/s	
34 SeI	196.1	$4p^4 - 4p^3 5s$	ground			l/?	
	207.6	$4p^4 - 4p^3 5s$	ground			l/?	
	537.1	$4p^3 5s - 4p^3 5p$	50997			l/s	
35 BrI	150	$4p^5 - 4p^4 5s$	ground			l/?	
39 YI	297,5	$4d5s^2 - 4d^2 5p$	ground			l/l	CL, Ar-jet
	619.2	$5s^2 - 5s5p$	ground			l/l	CL, Ar-jet
	546.8	$4d^2 5s - 4d^2 5p$	33608 $^{m)}$	4.6*		l/s	CL
40 ZrI	573.6	$5s^2 - 5s5p$	ground		-237	l/s	CL, Ar-jet
	507.8	$4d^3 5s - 4d^3 5p$	11641 $^{m)}$	5.15*		l/s	CL
	516.1	$4d^3 5s - 4d^3 5p$	11956 $^{m)}$	5.45*		l/s	CL
41 NbI	353.5	$4d^4 5s - 4d^3 5s5p$	ground			?/l	CL, Ar-jet
	556.3	$4d^3 5s^2 - 4d^4 5p$	10238 $^{m)}$	5.5*		l/l	CL
42 MoI	300.2	$4d^5 5s - 4d^4 5s5p$	ground			?/l	CL, Ar-jet
	550.6	$4d^5 5s - 4d^5 5p$	10768 $^{m)}$	5.67*	-190	l/s	CL
	575.1	$4d^4 5s^2 - 4d^5 5s$	11454 $^{m)}$	5.77*	-600	l/l	CL
43 TcI	592,5	$4d^5 6s^2 - 4d^5 6s6p$	ground			l/s	CL, Ar-jet
TcII	229.8	$4d^5 5s - 4d^5 5p$	ground			l/s	CL
44 RuI	287,5	$4d^6 5s^2 - 4d^6 5s5p$	ground			l/s	CL, Ar-jet
45 RhI	271.7	$4d^8 5p - 4d^8 5s$	ground			l/s	CL, Ar-jet
	568,6	$4d^8 5s - 4d^8 5p$	13521 $^{m)}$	5.8*		l/s	CL
	580,7	$4d^7 5s^2 - 4d^8 5p$	14788 $^{m)}$	5.6*		l/l	CL
46 PdI	276.3	$4d^{10} - 4d^9 5p$	ground			?/l	CL, Ar-jet
47 AgI	338.3	$4d^{10} 5s - 4d^{10} 5p$	ground		450	l/s	OFF, ON
48 CdI	326,1	$5s^2 - 5s5p$	ground		-300	l/s	OFF
49 In	410.4	$5p – 6s$	ground				ON
	451,1	$5p – 6s$	2213				ON
50 Sn	452.5	$5p^2 - 5p6s$	17163 $^{m)}$	5.2			ON
	563,2	$5p^2 - 5p6s$	17163 $^{m)}$	5.2			ON
51 SbI	<231	$5s^2 5p^3 - 5s^2 5p^2 6s$	ground			l/?	
52 TeI	<226	$5s^2 4p^4 - 5s^2 4p^3 6s$	ground			l/?	
TeII	575.6	Unknown	82744				
53 I-I	<183	$5s^2 5p^5 - 5s^2 5p^4 nd$	ground			?/l	
	558.6	$5p^4 6s - 5p^4 6p$	54633	3,8*		l/s	
	576.4	$5p^4 6s - 5p^4 6p$	54633	3.8*			
I-II	<123	$5s^2 5p^4 - 5s^2 5p^3 ns$	ground			l/?	
	577,5	$5s^2 5p^5 - 5s^2 5p^3 6p$	81915			l/?	
57 LaI	550,6	$5d6s^2 - 5d6s6p$	ground			l/s	CL, Ar-jet
	574.1	$5d^2 6s - 5d^2 6p$	2668			l/s	
	565.7	$5d^2 6s - 5d^2 6p$	9719	4,4*		l/s	CL
LaII	580.8	$5d^2 - 4f5d$	ground			l/l	CL
58 CeI	577.4	$4f5d6s^2 - 4f5d6s6p$	ground		-1743	l/s	CL, Ar-jet
CeII	287.2	$5d^2 6s - 5d^2 6p$	ground	1.2		l/s	CL
	286.3	$5d^2 6s - 5d^2 6p$	ground	1,3		l/s	CL

It can be noted that the optical properties of the elements in Table 1 do not pose any restrictions relative to the laser spectroscopy application. The best candidates for future investigations seem to be Zr, Mo (method 3.2) and Zn, Ag, Cd,and In (method 3.1). This is related to the possibility of extracting the electronic factor and the specific MS, e.g.,by using the available values of the mean square charge radii for more than three isotopes from X-ray measurements on muonic atoms and/or the high accuracy optical information about these parameters.

References:

1. *P. Möller and J. R. Nix, ADNDT (1981)*
2. *Yu. P. Gangrsky, S. G. Zemlyanoi et al., Sov. Phys. JETF **67** (1988) 1089*
3. *Yu. P. Gangrsky, K. P. Marinova et al., Izv. Acad. Sc. USSR, ser. phys. **49** (1985) 2261*
4. *E. W. Otten, Treatise on Heavy Ion Science **8** (1989) 517*
5. *R. Neugart, W. Klempt and K. Wendt, Nucl. Instr. Meth. **B17** (1986) 35*
6. *L. Vermeeren, P. Lievens and R. E. Silverans, Hyp. Int. **61** (1990) 1399*
7. *V. Panteleev (private communication)*
8. *V. N. Fedoseyev, V. S. Lethokov et al., Opt. Commun. **52** (1984) 24*
9. *D. A. Eastham, P. M. Walker, J. R. H. Smith, J. A. R. Griffit et al., J. Phys. **G12** (1986) 205*
10. *F. Le Blanc, D. Lunney, J. Obert et al., Phys. Rev. **C60** (1999) 054310*
11. *S. Raman, C.H. Malarkey, W. T. Milner et al., At. Data Nucl. Data Tables **36** (1987) 1*
12. *Y. Amboussir, J. M. Pearson et al., Nucl. Phys. **A549** (1992) 155*
13. *G. A. Lalazissis, M. M Sharma, Nucl.Phys. **A586** (1995) 201*
14. *P. Moeller, J. R. Nix, W. D. Myers and W. I. Swiatecki, At. Data Nucl. Data Tables (1995)*

Laser spectroscopy at an ion guide based on-line isotope separator

P. Dendooven[3], D.M. Benton[2], J. Billowes[1], P. Campbell[1], E.C.A. Cochrane[2], J.L. Cooke[2],
T.G. Cooper[1], D.E. Evans[2], D.H. Forest[2], I.S. Grant[1], J.A.R. Griffith[2], A. Honkanen[3],
M. Huhta[3], J. Huikari[3], A. Jokinen[3], J. Kilgallon[1], V.S. Kolhinen[3], J.M.G. Levins[1],
A. Nieminen[3], M. Oinonen[3], M.R. Pearson[1], H. Penttilä[3], K. Peräjärvi[3], J.R. Persson[2],
D.S. Richardson[2], G. Tungate[2], P.D. Wheeler[1], G. Yeandle[1], L. Zybert[2] and J. Äystö[3]

[1]*Schuster Laboratory, University of Manchester, Manchester M13 9PL, United Kingdom*
[2]*School of Physics and Astronomy, University of Birmingham, Edgbaston, Birmingham B15 2TT, United Kingdom*
[3]*Department of Physics, University of Jyväskylä, PO Box 35 (Y5), 40351 Jyväskylä, Finland*

Abstract

During the implementation of a collinear laser spectroscopy apparatus at the Jyväskylä IGISOL facility some problems and phenomena specifically related to the ion guide technique were encountered. These are the large beam energy spread under normal operating conditions, the population of metastable ionic states and the need to perform on-line calibration measurements. Nevertheless, on-line laser spectroscopy of refractory elements is now possible for the first time. The manipulation of the ion beam in a gas-filled radiofrequency quadrupole will result in a large increase in sensitivity for laser spectroscopy measurements.

Introduction

Laser spectroscopic studies have been performed at on-line isotope separator (ISOL) facilities for over twenty years [1,2]. Up to a few years ago, access to many nuclear systems was severely hindered by the release time and chemical selectivity of the ion sources used. In particular, on-line laser spectroscopy of refractory elements (e.g.,Zr, Mo, Hf and W) was impossible due to the low productions efficiencies for these elements.

The Ion Guide Isotope Separator On-Line (IGISOL) technique, whose development started in the early 1980s at the University of Jyväskylä, offers a fast (~1 ms) and chemically non-selective method for producing singly charged radioactive ion beams. Due to these characteristics, an IGISOL facility can deliver beams which are unavailable at other types of ISOL facility. A detailed description of the IGISOL technique can be found in [3] and references therein. More recent developments at the Jyväskylä IGISOL are described in [4, 5, 6, 7].

In 1993, the construction of a collinear laser spectroscopy beam line by groups from the Universities of Birmingham and Manchester at the Jyväskylä IGISOL facility was started.

The laser spectroscopy apparatus is largely configured in the manner in which is was previously used at Daresbury [8]. In 1994, off-line laser spectroscopy with beams from a discharge ion source was started. On-line work with radioactive beams was started in 1995. In 1996, the feasibility of on-line laser spectroscopy at an IGISOL was demonstrated by measurements on ^{140,142,144}Ba produced with the fission ion guide [9,10]. The first on-line laser spectroscopy of a refractory element with any method (^{88}Zr produced in the ^{89}Y(p,2n) reaction) was performed in 1997 [11]. Laser spectroscopy on a series of Hf isotopes was performed in 1998 and 1999 [11,12] The results of these studies are presented in another contribution to this Workshop [13].

In this contribution, we describe the IGISOL-related problems and phenomena which were encountered and studied in the course of the development of laser spectroscopy at the Jyväskylä IGISOL facility.

Off-line beams for set-up and calibration

Most of the results of laser spectroscopy are derived from the change of a certain quantity between isotopes. A stable isotope is usually chosen as reference mark. High quality data can only be obtained if all measurements, including the reference measurement, are made under exactly the same experimental conditions. Usually, the ion source of an ISOL facility can deliver off-line beams of stable isotopes from the element whose radioactive isotopes are being studied. These stable beams can then also be used for tuning the equipment.

Due to the nature of its operating principle, the ion guide does not provide beams off-line, i.e., in the absence of the ionising effect of the cyclotron beam. In order to provide these, a discharge ion source was developed in which an electrical discharge is struck between two pointed electrodes placed in the helium-filled ion guide chamber [14]. Strong beams of He^+ are easily produced. Beams of other gases can be created by mixing a small amount of these gases with the helium. In addition, this source can produce beams of the cathode material of the discharge electrodes, mainly due to sputtering. For elements from which no electrode can be made, beams are produced by coating the tip of the electrode with a suitable substance containing the element of interest.

Beams from the discharge ion source have been used for testing and tuning purposes. However, since the properties of these beams are not exactly the same as those of the on-line beams of radioactive ions, on-line fine tuning and especially on-line calibration has proven to be necessary.

Beam energy spread

Under normal operating conditions, i.e.,a high skimmer voltage (several 100 V), the IGISOL beam has a rather poor quality. This fact was already observed early on in the ion guide development by measuring the mass resolving power as a function of the skimmer voltage (see, e.g., [15]). Using collinear laser spectroscopy, direct beam energy distribution measurements are possible. Such measurements performed using the discharge ion source show a beam energy spread (FWHM) of up to 100 eV [16]. This energy spread is caused by the collision of the ions accelerated by the skimmer voltage with the neutral helium gas. However, since the mass-separated yield increases with skimmer voltage (saturating at ~500 V), the use of a high skimmer voltage is preferred for nuclear spectroscopy experiments. This mode of operation cannot be used for laser spectroscopy since the Doppler broadening of the resonance spectrum prohibits high-resolution spectroscopy. Therefore, laser spectroscopy has so far been performed at low skimmer voltages (< 20 V) for which the beam energy spread is only a few eV. Much to our surprise we have noticed a local maximum in yield at such low skimmer voltages, especially when using high cyclotron beam currents. Under these conditions, an ion guide efficiency of up to more than 50 % of the optimum has been reached. This phenomenon is described in more detail elsewhere [3,17,18].

Metastable populations

It was noticed that the laser spectroscopy sensitivity (expressed,e.g.,as the number of beam ions needed per count in the resonance spectrum) for the refractory elements hafnium and zirconium is much smaller in on-line measurements on radioactive isotopes than in off-line measurements. This is attributed to the fact that the hafnium and zirconium ions created in on-line conditions (in a nuclear reaction) are predominantly (~90-95 %) in ionic metastable states, with only a small fraction in the ionic ground state to which the laser spectroscopy is tuned. This explanation is supported by off-line measurements using the discharge source to create beams of Hf^+ ions (Figure 1). The data show that the ground state population decreases and the metastable population increases for increasing helium pressure inside the discharge source. It is also worth noting that the population of levels with an excitation energy as high as 3.5 eV has been observed, clearly showing the non-thermal distribution of the level population. The same phenomenon has been observed for zirconium ions. Because in on-line conditions a helium pressure of 100-200 mbar is needed to stop the recoiling nuclear reaction products, we have not been able to avoid this problem of a small ground-state population.

Attempts to de-excite the metastable states by mixing N_2, H_2 or Ne with the helium gas were not successful.

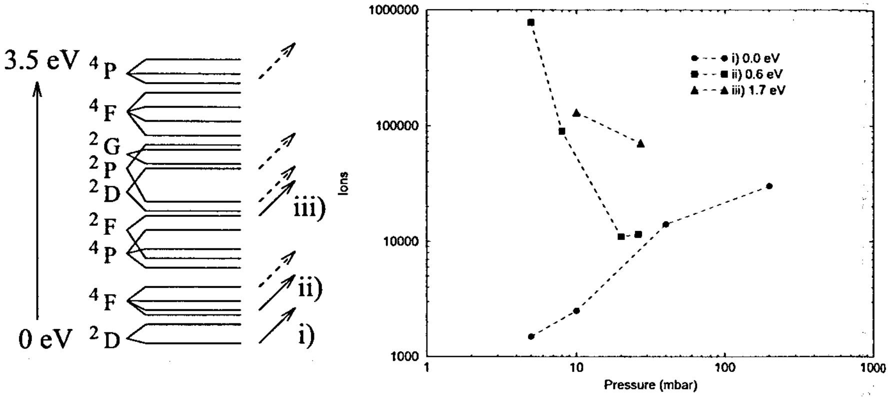

Figure 1. Metastable state population of Hf^+ ions. On the left hand side, the level scheme of Hf^+ is shown. The arrows indicate levels in which population of the beam ions has been observed. The figure on the right-hand side shows, for the levels indicated with solid arrows, the number of ions needed to produce one detected photon in the laser resonance spectrum as a function of helium pressure inside the ion guide chamber. The photon detection efficiency is 1 in 500. All points were measured with the off-line discharge ion source, except the point at 200 mbar which was measured on-line.

The ion beam cooler

Presently, a longitudinal Penning trap is being installed after the IGISOL separation magnet in order to obtain isobaric mass separation and thus mono-isotopic beams. Optimum performance of this Penning trap requires special preparation of the IGISOL beam: its energy spread is too large and the continuous IGISOL beam does not match the bunched operation of the Penning trap. This beam preparation is performed by the so-called ion beam cooler, installed between the separation magnet and the Penning trap. In the ion beam cooler, the beam is decelerated, thermalised in a gas-filled radiofrequency quadrupole and reaccelerated. The longitudinal segmentation of the radiofrequency quadrupole structure allows bunching of the ion beam (by using appropriate voltage barriers) in order to match its time structure with the operation of the Penning trap. The ion beam cooler/Penning trap project is described in more detail in [19]. At the time of this writing (September 1999), successful tests of the ion beam cooler have been performed (see [20] for details). It should be mentioned that laser spectroscopy has been invaluable as a beam diagnostics tool in these new developments.

Collinear laser spectroscopy will benefit from the cooled beams by at least one order of magnitude in sensitivity. The reasons for this are:

(1) the improved emittance of the ion beam allows a much larger fraction of the ions to be simultaneously brought into resonance with a narrow bandwidth and small size laser beam. A significant increase in signal and a reduction in scattered light background are consequently obtained.

(2) the IGISOL can be operated for maximum ion yield without affecting the energy spread of the ion beam after the RFQ cooler.

(3) since the cooled ion beam properties (precise energy and emittance) are decoupled from the IGISOL operating conditions, an isotope can be measured without the necessity of a calibration measurement on a known isotope simultaneously produced in the nuclear reaction under the same IGISOL conditions. The cyclotron beam energy can thus be chosen to optimise the production of a single reaction channel and significantly less time is needed for calibration runs.

(4) the bunching of the beam results in a small duty cycle (reducing the non-beam related background by the same factor) without loss of intensity.

(5) the storage of the ions in the ion beam cooler allows the manipulation of the ionic level population in order to put the ions in the level most favourable for laser spectroscopy. An example of this is the depopulation of the metastable states for hafnium and zirconium ions.

Summary

The successful implementation of collinear laser spectroscopy at the Jyväskylä IGISOL facility has made laser spectroscopy of refractory and very short-lived isotopes possible. In order to keep the beam energy spread small, we have been forced to operate the ion guide under different operating parameters, revealing interesting new features of the ion guide technique. Laser spectroscopy has proved to be a very valuable tool for beam diagnostics. By early 2000, beams from the ion beam cooler will be transported to the laser spectroscopy beam line, increasing the sensitivity of the measurements by a large factor.

References

1 E.W. Otten, *Treatise on Heavy-Ion Science* vol. 8, Ed. D.A. Bromley (Plenum, New York, 1989) p. 515

2 J. Billowes and P. Campbell, J. Phys. G: Nucl. Part. Phys. 21 (1995) 707

3 P. Dendooven, Nucl. Instrum. Meth. Phys. Res. B 126 (1997) 182

4 H. Penttilä, P. Dendooven, A. Honkanen, M. Huhta, P.P. Jauho, A. Jokinen, G. Lhersonneau, M. Oinonen, J.-M. Parmonen, K. Peräjärvi and J. Äystö, Nucl. Instrum. Meth. Phys. Res. B 126 (1997) 213

5 P. Dendooven, R. Béraud, E. Chabanat, A. Emsallem, A. Honkanen, M. Huhta, W. Jicheng, A. Jokinen, G. Lhersonneau, M. Oinonen, H. Penttilä, K. Peräjärvi and J. Äystö, Nucl. Instrum. Meth. Phys. Res. A 408 (1998) 530

6 P. Dendooven, S. Hankonen, A. Honkanen, M. Huhta, J. Huikari, A. Jokinen, V.S. Kolhinen, G. Lhersonneau, A. Nieminen, M. Oinonen, H. Penttilä, K. Peräjärvi, J.C. Wang and J. Äystö,Nuclear Fission and Fission-Product Spectroscopy: Second International Workshop, 22 Apr-25 Apr,1998, Seyssins, France, AIP Conference Proceedings 447, Ed. G. Fioni, H. Faust, S. Oberstedt and F.-J. Hambsch (The American Institute of Physics, Woodbury, New York, 1998) p.135–142

7 M. Oinonen, R. Béraud, G. Canchel, E. Chabanat, P. Dendooven, A. Emsallem, S. Hankonen, A. Honkanen, J. Huikari, A. Jokinen, G. Lhersonneau, C. Miehé, A. Nieminen, Y. Novikov, H. Penttilä, K. Peräjärvi, A. Popov, D.M. Seliverstov, J.C. Wang and J. Äystö, Nucl. Instrum. Meth. Phys. Res. A 416 (1998) 485

8 D.A. Eastham et al., Opt. Comm. 60 (1986) 293-295

9 J. Billowes, P. Campbell, E.C.A. Cochrane, J.L. Cooke, P. Dendooven, D.E. Evans, I.S. Grant, J.A.R. Griffith, A. Honkanen, M. Huhta, J.M.G. Levins, E. Liukkonen, M. Oinonen, M.R. Pearson, H. Penttilä, J.R. Persson, D.S. Richardson, G. Tungate, P. Wheeler, L. Zybert and J. Äystö, Nucl. Instrum. Meth. Phys. Res. B 126 (1997) 416

10 J.L. Cooke, J. Billowes, P. Campbell, E.C.A. Cochrane, T.G. Cooper, P. Dendooven, D.E. Evans, J.A.R. Griffith, I.S. Grant, A. Honkanen, M. Huhta, J.M.G. Levins, M. Oinonen, M.R. Pearson, H. Penttilä, J.R. Persson, D.S. Richardson, G. Tungate, P.D. Wheeler, L. Zybert and J. Äystö, J. Phys. G: Nucl. Part. Phys. 23 (1997) L97

11 P. Campbell, D.M. Benton, J. Billowes, P. Dendooven, D.E. Evans, D.H. Forest, I.S. Grant, J.A.R. Griffith, A. Honkanen, A. Jokinen, J.M.G. Levins, M. Oinonen, H. Penttilä, K. Peräjärvi, D.S. Richardson, G. Tungate, G. Yeandle and J. Äystö,Exotic Nuclei and Atomic Masses ENAM 98, 23 Jun-27 Jun,1998, Bellaire, Michigan, USA, AIP Conference Proceedings 455, Ed. B.M. Sherril, D.J. Morrissey and C.N. Davids (American Institute of Physics, Woodbury, New York, 1998) p.72–77

12 J.M.G. Levins, D.M. Benton, J. Billowes, P. Campbell, T.G. Cooper, P. Dendooven, D.E. Evans, D.H. Forest, I.S. Grant, J.A.R. Griffith, J. Huikari, A. Jokinen, K. Peräjärvi, G. Tungate, G. Yeandle and J. Äystö, Phys. Rev. Lett. 82 (1999) 2476

13 P. Campbell, D.M. Benton, J. Billowes, P. Dendooven, D.E. Evans, D.H. Forest, I.S. Grant, J.A.R. Griffith, A. Honkanen, A. Jokinen, J.M.G. Levins, M. Oinonen, H. Penttilä, K. Peräjärvi, D.S. Richardson, G. Tungate, G. Yeandle and J. Äystö, contribution to these proceedings.

14 E. Ollikainen, M. Huhta, A. Honkanen, M. Oinonen, J.M. Parmonen, J. Äystö, JYFL Annual Report 1993, Department of Physics, University of Jyväskylä, p. 45

15 P. Taskinen, H. Penttilä, J. Äystö, P. Dendooven, P. Jauho, A. Jokinen and M. Yoshii, Nucl. Instrum. Meth. Phys. Res. A 281 (1989) 539

16 J.R. Persson, E.C.A. Cochrane, J.L. Cooke, D.E. Evans, J.A.R. Griffith, G. Tungate, L. Zybert, J. Billowes, P. Campbell, T. Cooper, I.S. Grant, J. Kilgallon, P. Wheeler, P. Dendooven, A. Honkanen, M. Huhta, M. Oinonen, J.M. Parmonen and J. Äystö, JYFL Annual Report 1995, Department of Physics, University of Jyväskylä, p. 31

17 P. Dendooven, A. Honkanen, M. Huhta, M. Oinonen, J.-M. Parmonen, H. Penttilä, J. Persson, A. Popov and J. Äystö, JYFL Annual Report 1995, Department of Physics, University of Jyväskylä, p. 18

18 P. Dendooven, A. Honkanen, A. Jokinen, M. Oinonen, H. Penttilä, K. Peräjärvi and J. Äystö, JYFL Annual Report 1997, Department of Physics, University of Jyväskylä, p. 12

19 A. Jokinen, J. Äystö, P. Dendooven, V.S. Kolhinen, J. Huikari, A. Nieminen and K. Peräjärvi,Exotic Nuclei and Atomic Masses ENAM 98, 23 Jun-27 Jun,1998, Bellaire, Michigan, USA, AIP Conference Proceedings 455, Ed. B.M. Sherril, D.J. Morrissey and C.N. Davids (American Institute of Physics, Woodbury, New York, 1998) p.981–984

20 A. Nieminen, J. Huikari, A. Jokinen, J. Äystö, J. Billowes, P. Campbell, E.C.A. Cochrane and the EXOTRAPS collaboration, *An Ion Beam Cooler for Collinear Laser Spectroscopy*, in: Proceedings of the First Euroconference on Atomic Physics at Accelerators (APAC 99): Laser Spectroscopy and Applications, Mainz and Budenheim, Germany, 19-24 September 1999 (to be published)

On–line Laser Spectroscopy of Refractory Radioisotopes at the JYFL IGISOL facility

P. Campbell[a], D.M. Benton[b], J. Billowes[a], P. Dendooven[c], D.E. Evans[b], D.H. Forest[b], I.S. Grant[a], J.A.R. Griffith[b], A. Honkanen[c], M. Huhta[c], A. Jokinen[c], J.M.G. Levins[a], M. Oinonen[c], H. Penttilä[c], K. Peräjärvi[c], D.S. Richardson[b], G. Tungate[b], G. Yeandle[a] and J. Äystö[c]

[a]Schuster Laboratory, University of Manchester, Manchester M13 9PL, U.K.
[b]Department of Physics and Space Research, University of Birmingham, Birmingham B15 2TT, U.K.
[c]Accelerator Laboratory, University of Jyväskylä, Jyväskylä SF–403 51, Finland

Abstract. The laser–IGISOL programme at JYFL has realized the first ever on–line observation of collinear laser induced resonance fluorescence from ions of refractory elements. The measurements of radioactive isotope in the zirconium and hafnium systems demonstrate that the properties of IGISOL produced ion beams can be made suitable for precise and efficient laser spectroscopy.

INTRODUCTION

The vast majority of the short–lived radioisotopes that have been studied have been done so using the collinear ion–laser beam technique (or hybrids thereof) [1,2]. This work, based at on–line isotope separator facilities, has previously been hindered by the release times and chemical selectivity of the production ion sources used. Entire regions of the known nuclear landscape, such as the refractory and platinum–like elements; Zr, Mo, Hf, W, etc., have not been optically studied due to their cripplingly low production efficiencies from conventional ion sources.

On–line measurements in refractory systems have now been made using the non–conventional IGISOL (ion guide isotope separator on–line) facility as the primary production platform [3]. The IGISOL, developed at the University of Jyväskylä, Finland, offers a fast, ~1ms, and chemically nonselective method for producing singly charged ionic species from the products of nuclear reactions [4]. An extremely sensitive, ion coincidence based, variant of the standard collinear technique has been applied to specially prepared IGISOL beams [5] to achieve the first measurements on radioactive isotopes in the systems of zirconium and hafnium.

EXPERIMENTAL DETAILS

The preparation of the IGISOL for laser spectroscopy is described in detail elsewhere in these proceedings [5]. Following mass selection the prepared ion beam is transported ~15m to an enclosed building housing the laser facility. Figure 1 shows details of the laser–ion beam interaction region which is located 1.5m upstream of the laser entrance window.

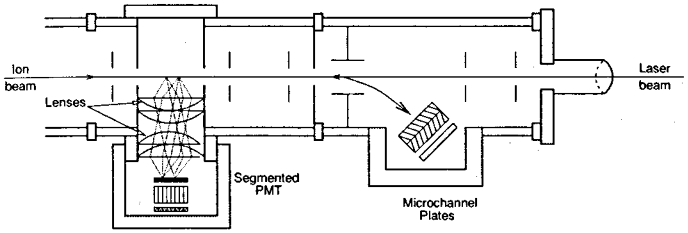

FIGURE 1. The laser–ion interaction region.

The shaping of the ion beam is controlled by three electrostatic quadrupole elements along its transport path. The focusing can be optimized such that a narrow, ~10mm^2, low divergence, ~1 mrad half angle, ion beam is delivered to the interaction region. An 18mm length of the laser–ion beam overlapped region is imaged, via Fresnel lenses (for visible emissions) or a quartet of fused silica lenses (for UV emissions), onto the sensitive region of a photomultiplier (PMT). The interaction region is insulated from the rest of the grounded beamline and held at a desired potential. The change in potential on entering the interaction region allows resonances to be Doppler tuned and prevents fluorescent losses from optical pumping. Downstream of the imaged region the ion beam is deflected onto a double stack of normally facing microchannel plates. During experimental scans only those photons detected in coincidence with an ion arrival are accepted as candidate events and efficient rejection of laser and other photon background is achieved [6].

A further improvement on background rejection is obtained by use of a position sensitive PMT. Position information on the origin of the fluorescent ion can then be used to narrow the photon–ion coincidence time window to a level that corresponds to the resolution limit of the apparatus. For this work a 16 fold segmented Hamamatsu R5900P–03–L16 photomultiplier was used and an aberration limited spatial resolution of 2–3mm was achieved.

Laser quality light from 300nm – 700nm is generated by two Spectra Physics 380D dye lasers, one of which is equipped with a purpose built intracavity frequency doubler. The work reported utilized 301nm and 327nm light produced by $LiIO_3$ doubling of the R6G and R640 dyes respectively. Although provision exists for operating fast collinear *atom* spectroscopy [6], ionic systems are logistically preferred and frequency extensions below 300nm are under development. Laser stabilization, to an effective linewidth of ~3MHz, is achieved by active locking of the cavity to absorption lines of I_2 or Te_2.

^{88}Zr

A beam of 8,000 s^{-1} ^{88}Zr was produced from the $^{89}Y(p,2n)^{88}Zr$ reaction at an energy of 25MeV (achieved using a primary beam, of 50MeV H_2^+ at ~8pμA). The yield of ^{88}Zr was calibrated using known cross sections and scaled from directly measured (γ–counted) ^{89}Y and ^{89}Zr isomer production. The total intensity at mass A = 88 was 12,000 ions s^{-1}. Figure 2 shows the tagged photons counted using an ordinary, nonsegmented, PMT in 5.25 hours as function of total acceleration voltage. The laser power used, ~2mW, resulted in some power broadening and a total linewidth (FWHM) of 10V was measured. The laser frequency, 327nm in the harmonic, was locked to an I_2 resonance at 15261.20cm^{-1} and a total acceleration of 37,110.3V was required to bring the system to resonance on the d^2s $^4F_{3/2}$ – dsp $^4F_{5/2}$ transition.

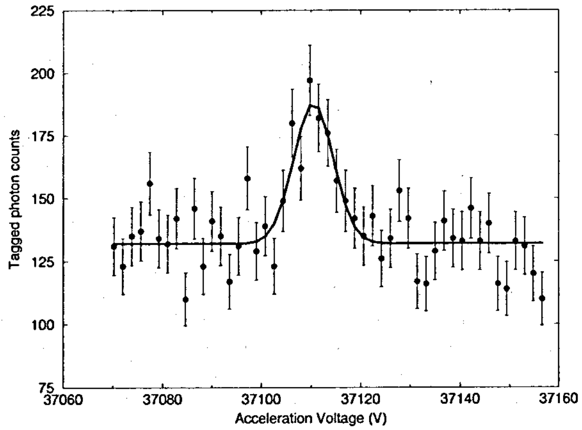

FIGURE 2. Resonance fluorescence spectra for ^{88}Zr.

The observed fluorescent efficiency was reduced by a factor of 20 compared to a low–temperature, off–line production of an even Zr isotope. This loss results from the population of metastable ionic levels during on–line production and is observed to increase with increasing ion guide pressure [5]. The on–line pressure, 220mbar, was selected to optimize production efficiency with respect to contaminant levels (the contaminant levels increase at lower pressure due to the reduction in gas cooling of the guide).

During this dedicated run no other Zr isotope was produced at a spectroscopically measurable rate and no calibration of the ^{88}Zr resonance position was achieved. The enforced inclusion of the full separator potential uncertainty, ~0.1%, dominates the assigned error. The measurement of an isotope shift would typically reduce this error by more than an order of magnitude.

The neutron deficient hafnium isotopes

Unlike the lighter Group IVb elements, the hafnium ion has a ds^2 ground state configuration. The oscillator strength for ds^2 – dsp transitions is notably stronger than that of d^2s – dsp transitions (such as that studied in Zr) and a factor of four less laser power is required to provide optimum signal to background. The use of the position sensitive photomultiplier further provides an increase in signal to background of ~5 and a comparison of the Hf resonance shown below in fig. 3 to that of Zr (in fig. 2) clearly demonstrates the improvement in background rejection.

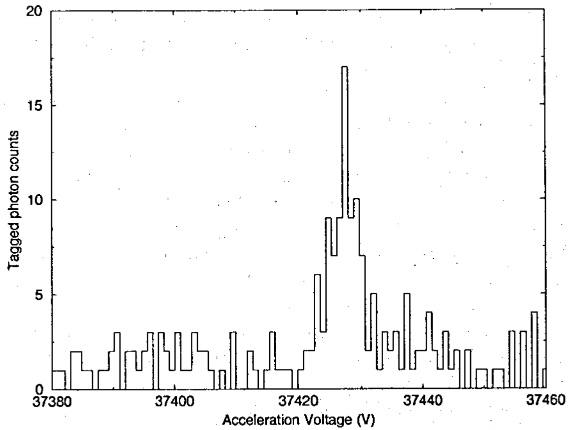

FIGURE 3. Resonance fluorescence spectra for ^{174}Hf.

The ^{174}Hf spectrum shown in figure 3 was obtained in 100 minutes using ~3000 ions s^{-1} produced from the $^{175}Lu(p,2n)^{174}Hf$ reaction at 25MeV proton beam en-

TABLE 1. Measured Hf isotope shifts and charge radii

Mass A	Spin	Isotope Shift $\delta\nu^{178,A}$ (MHz)	$\delta\langle r^2\rangle^{178,A}$ fm^2
170	0^+	-10180(30)	-0.466(7)
171g	$7/2^+$	-7522(12)	-0.344(5)
171m	$1/2^-$	-7515(19)	-0.344(6)
172	0^+	-6632(10)	-0.302(5)
173	$1/2^-$	-5017(7)	-0.228(4)
174	0^+	-3704.3(31)	-0.168(3)
176	0^+	-1868.1(20)	-0.084(2)
177	$7/2^-$	-1337.4(18)	-0.061(1)
179	$9/2^+$	790.8(19)	0.036(1)
180	0^+	2149.2(15)	0.098(2)

TABLE 2. The odd–N moments

Mass A	Spin	μ_I n.m	Q_s barns
171g	$7/2^+$	-0.674(12)	+3.463(27)
171m	$1/2^-$	+0.526(16)	—
173	$1/2^-$	+0.502(7)	—

ergy. The spectrum shows the acceleration voltage required to bring the ionic ensemble to resonance with a doubled laser frequency of fundamental 16579.2883 cm^{-1} exciting the ds^2 $^2D_{3/2}$ – dsp $^2D_{5/2}$ transition.

Primary proton beam energies of 20, 30, 40 and 55 MeV have been used during further, Lu(p,xn) based, investigations on the hafnium system. Other reactions including Lu(d,xn) and Yb(α,xn) have also been studied and isotope shifts and hyperfine parameters have been measured for A = 170 – 174 and 176 – 178. The measured isotope shifts are shown in table 1. Measurable systematic shifts between the same resonance peaks were observed during the initial period of each run. The cause of these temporary ~3V shifts is unclear but appears to be related to initially changing plasma conditions within the IGISOL. The resonance positions observed once the drifting has ceased (~ 2 hours from start) have however been demonstrated to be reproduceable between different energies and different beam–target combinations. Further long term (over 10 hours) total acceleration energy drifts are far smaller, $\leq$1V maximum, than these initial changes. Simultaneous measurements of more than one isotope, which provides isotope shift measurements which are unaffected by such total energy changes, have been made for all systems except ^{170}Hf.

The magnetic moments and quadrupole moments of the odd–N ^{171g}Hf, ^{171m}Hf and ^{173}Hf isotopes have been determined and are shown in table 2. The extraction used hyperfine parameters scaled from ^{177,179}Hf and assumed no hyperfine anomaly. The existence of an isomer in the A = 171 system (the 30s ^{171m}Hf) was demonstrated during yield tests at the IGISOL prior to the spectroscopic investigation [7]. A simultaneous fit to four partial scans of the compound ^{171}Hf structure is shown in figure 4. The relative peak intensities and hyperfine parameters are constrained to be identical for all scans.

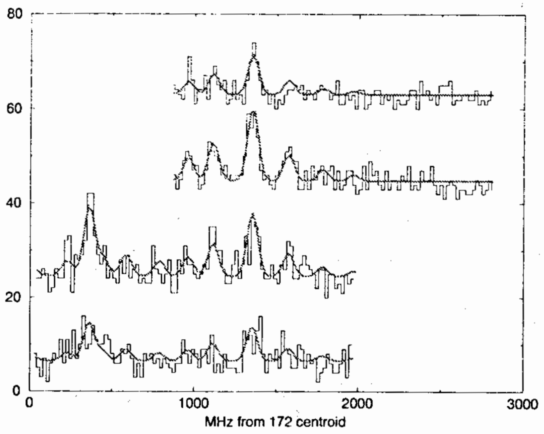

FIGURE 4. Fits to the compound structure of the ^{171}Hf ground state and isomer (the spectra are displaced for clarity).

DISCUSSION AND FUTURE WORK

Extracted $\delta\langle r^2\rangle$ for Zr and Hf are shown in figs. 5 & 6. Respectively the $\langle r^2\rangle$ extraction use the atomic parameters given in [8] for Zr and those of Zimmermann et al. [9] for Hf. The single ^{88}Zr measurement requires on–line calibration or an absolute frequency determination before meaningful nuclear structural data can be extracted. Nevertheless the data at present already shows the behaviour observed on crossing other magic shell closures. The detail of the trend, and further measurements in the system, will be explored in the immediate future at JYFL.

The Hf measurements accurately and substantially extend the knowledge of the charge radial trends in this chain. Figure 6 shows the trend of the measured $\langle r^2\rangle$ compared to that estimated from the droplet model [10] including theoretical estimates of β_2 [11]. The course of the charge radius near–perfectly corresponds to that of the prediction with even small details of the structure well reproduced. It must however be noted that a sizable discrepancy, ~35%, exists between different optical (and nonoptical) evaluations of $\delta\langle r^2\rangle$ in this chain [12]. Although agreement with predicted trends cannot on its own support a particular evaluation, use of the Zimmermann et al. [9] calibration of the hafnium atomic parameters is seen to result in consistency between optical, nonoptical and theoretical descriptions of the charge radius and is favoured in this work.

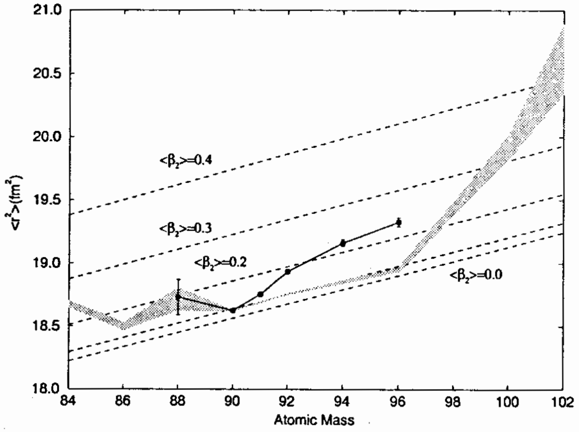

FIGURE 5. The optically measured Zr mean square charge radius (solid line and points) compared to the deformation trends inferred from B(E2) values (shaded region). The data are normalised to the measured $\langle r^2 \rangle$ of ^{90}Zr.

Many points of interest are apparent in figure 6. The level of agreement between the theoretical and experimental course of the charge radius is unique to this system. The agreement persists at the ~5% level in β_2 which is far better than the level to which the model may be considered reliable. Such behaviour might well be expected in a region of very strong static deformation but a significant vibrational character is known to exist in the hafnium ground states. For example the negative isomer shift of the ^{178m2}Hf isomer [12] indicates that a large increase in nuclear rigidity can still be obtained from a reduction in the nuclear pairing. A behaviour related to such an increase in rigidity would normally be observed in the odd–even staggering (OES) of the radius. In Hf, however, the OES is suppressed and at A = 171 and 173 inverted compared to other isotope chains. Static deformation effects thus clearly dominate the course of the Hf charge radius and further excellent agreement is observed between the charge radial trends and other measures of nuclear deformation [3] (such as B(E2) and Q_s whose relation to the charge radius can only be accurately compared in the limit of dominating static deformation).

Further measurements and extensions to the data are required. A remeasurement of the 175 system, which has been reported to have a large normal OES [13], will be attempted at JYFL. The substantial experimental data base, which these future measurements hope to provide, is an essential platform from which an investigation of the high–K isomeric systems in Hf can be performed. The case of A = 178, for which the ground and $I^\pi = 16^+$ isomeric state have been studied, is of long standing interest [12]. At the IGISOL direct access to both the $I^\pi = 8^-$ and $I^\pi = 16^+$ isomers in ^{178}Hf can be achieved. Primary yield tests for isomeric Hf production have been completed [7] and the necessary spectroscopic sensitivity has been achieved. An experimental resolution of the rôle of pairing in the course of the charge radius, which the high–K measurements should help to clarify, can only be achieved by the fullest investigation of this region.

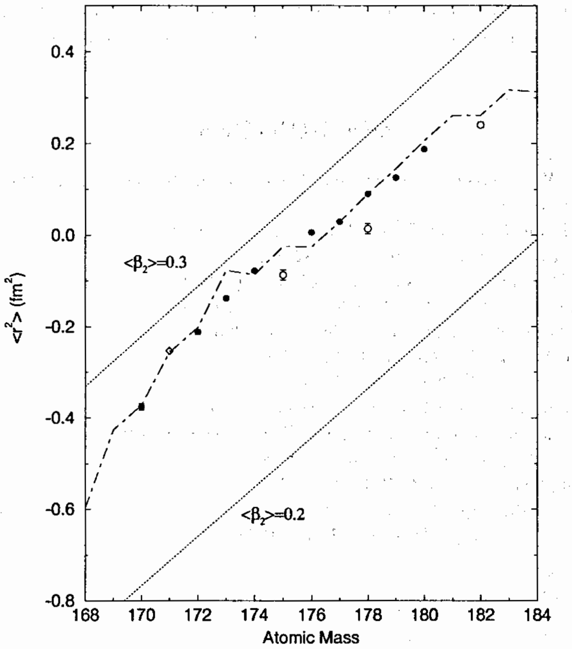

FIGURE 6. The predicted and measured Hf mean square charge radius (see text for details). The presentation is normalized at ^{178}Hf and the scale is arbitrarily placed. Results from other work (open circles) for ^{175}Hf, ^{178m2}Hf and ^{182}Hf are taken from refs. [13], [12] and [14] respectively.

Investigations into the systems of Zr and Hf continue at JYFL. As outlined above, the continued studies of Hf will be directed at the high spin isomers as well as the lower lying states. With respect to the Zr system, the IGISOL readily produces sizeable beams of neutron-rich species (produced by fission) and spectroscopic investigation of the rapidly changing and varied nuclear structure in this region will be attempted. It is hoped that these cases, and all other future work, will be greatly assisted by the successful installation of an on-line ion beam cooler [5].

An on-line ion beam cooler will be commissioned at the JYFL IGISOL during late 1999. At 100% transmission an operational cooler will realistically provide two orders of magnitude improvement in laser spectroscopic sensitivity [5] but will also vitally decouple the properties of the cooled beam from those of the IGISOL. The experimental difficulties experienced with changing ion guide plasma conditions and systematic uncertainties, previously encountered in Zr and Hf, will be removed. Metastable ionic populations may also be depopulated by the addition of partial pressures of molecular gases to the He in the cooler and the containment time (bunching) of the device can be optimised to provide maximum ionic ground state population.

REFERENCES

1. Otten E. W. *Treatise on Heavy-Ion Science 8* ed. Bromley D. A., Plenum Press, New York (1988)
2. Billowes J. and Campbell P. *J. Phys.* **G21** 707 (1995)
3. Levins J.M.G. et al. *Phys. Rev. Lett.* **82** 2476 (1999)
4. Taskinen P. et al. *Nucl. Inst. Meth.* **A281** 539 (1989)
5. Dendooven P. et al. *Contribution to these proceedings*
6. Eastham D. A. et al. *Opt. Comm.* **60** 1583 (1986)
7. Campbell P. et al. *J. Phys.* **G23** 1141 (1997)
8. Campbell P. et al. *J. Phys.* **B30** 4783 (1997)
9. Zimmermann D. et al. *Phys. Rev.* **A50** 1112 (1994)
10. Myers W. D. and Schmidt K. H. *Nucl. Phys.* **A410** 61 (1983)
11. Möller P. et al. *At. Nuc. Data Tables* **59** 185 (1995)
12. Boos et al. *Phys. Rev. Lett* **72** 2689 (1994)
13. Jin W. G. et al. *Phys. Rev.* **C55** 1545 (1997)
14. Anastassov A. et al. *Z. Phys.* **A348** 177 (1994)

HIGH RESOLUTION LASER SPECTROSCOPY AT THE UNIVERSITY OF BIRMINGHAM

E.C.A. Cochrane, D.M. Benton, D.H. Forest, J.A.R. Griffith,
J.K. Tasker and G. Tungate.

School of Physics and Astronomy, The University of Birmingham,
Edgbaston, Birmingham, B15 2TT, USA

Abstract

High resolution crossed beam laser spectroscopy has been successfully employed at the University of Birmingham for over 20 years, with isotope shifts and hyperfine structure of a variety of elements measured. A brief review of this work is given together with examples of recent spectra obtained for lanthanum, vanadium, manganese, iron and cerium. The effect of extra laser cavity modes on the data obtained is also discussed together with calibration etalon drift.

1. Introduction

Many techniques currently exist for measuring the hyperfine structure and isotope shifts that occur in spectral lines due to the interaction between the atomic electrons and nucleus. In recent years the highest quality data has been obtained using narrow line width lasers to resonantly excite atomic electrons, resulting in highly resolved spectra from which hyperfine structure parameters and optical isotope shifts can be extracted.

One such technique is crossed beam resonance fluorescence spectroscopy, where a highly collimated beam of atoms is met at right angles by a tunable laser beam and the resonantly scattered photons detected perpendicularly to both. This is performed at the University of Birmingham with good quality spectra recorded for a variety of stable or long-lived atoms, including refractory elements such as vanadium [1] and reactive species such as cerium [2]. With frequency doubling measurements have also been made in the UV region of the spectrum.

These experiments are described here together with methods for eliminating spurious laser modes and the effect of calibration etalon drift. The high precision and good sensitivity which can be achieved using this technique are illustrated throughout in spectra recently obtained.

2. Experimental Apparatus

A beam of atoms is created by placing a small sample of the element under investigation into an oven situated at the bottom of an evacuated chamber, know as the atomic beam unit (ABU), shown in figure 1. The oven is a narrow bore tantalum tube through which a high current is passed, raising its temperature and heating the sample inside.

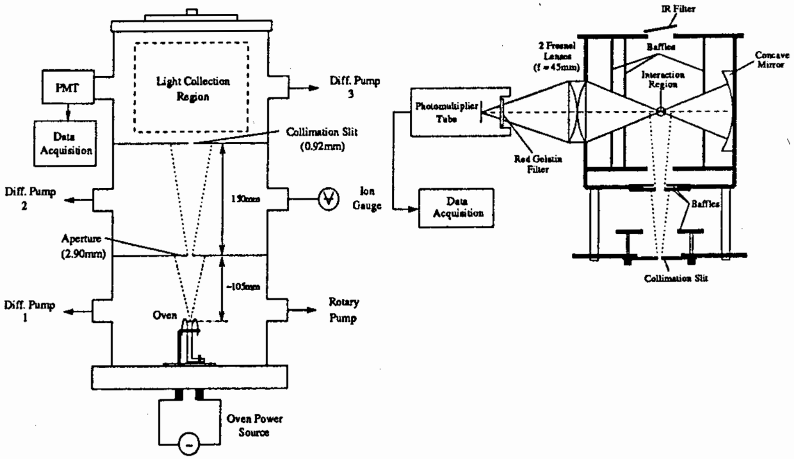

Figure 1: Diagrams of the atomic beam unit (ABU) and light collection region (LCR).

The atoms emerging from the oven are highly collimated to form a narrow beam in the light collection region (LCR), figure 1, where they are resonantly excited by light from a tunable dye laser. The scattered photons are then detected perpendicularly to both beams, as described above, with an EMI 9489B photomultiplier tube.

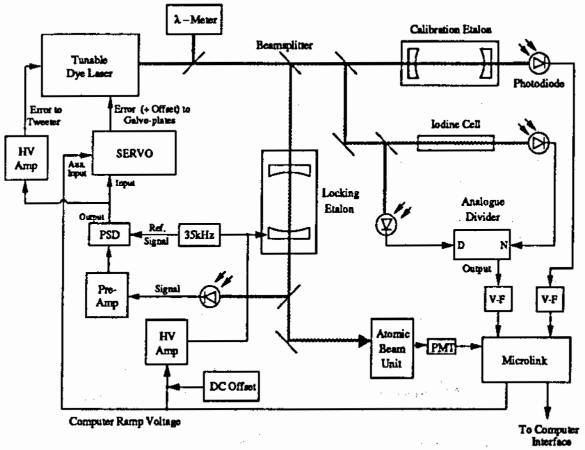

Figure 2: Schematic diagram of the optical system showing the locking electronics and active filtering system.

A schematic diagram of the optical system used is shown in figure 2. A Lexel 3500 Argon-ion laser is used to pump a Spectra Physics 380A ring cavity tunable dye laser providing narrow line width tunable laser light. The wavelength of the dye laser output is measured to 0.005nm using a wavelength-meter, with a more accurate value obtained from a molecular iodine absorption trace.

The laser cavity is stabilised by locking its output to the transmission peak of the *locking* etalon, a temperature stabilised Burleigh confocal etalon (CFT 25, FSR = 3GHz). Frequency scans are then taken by applying a ramp voltage to a piezo-mounted mirror in the etalon cavity, where the laser tracks the transmission peak. The probe beam sent to the ABU is also taken from the output beam of this etalon. The etalon then acts as an active filter for the laser light, stopping weak side modes that can exist in the dye laser output reaching the ABU and resulting in spurious spectral lines. The reason for implementing this active filtering system is apparent in figure 3 which shows the spectra taken for the naturally abundant lanthanum isotopes, ^{139}La (99.91%) and ^{138}La (0.09%), before and after the filtering system was introduced [3].

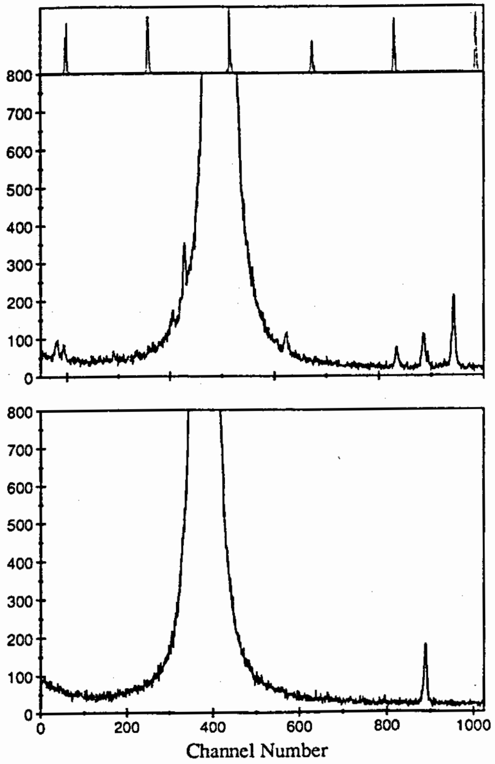

Figure 3: Natural lanthanum spectra taken at $\lambda = 593.068$nm [3] before the active filtering system was used (middle), where each spurious peak is an integral number of laser cavity modes from the ^{139}La spectral lines, and after these modes had been eliminated (bottom). The signal from the calibration etalon (299.63MHz) is shown along the top.

Laser scans of around 3GHz in length are taken and the absolute frequency of the laser varied to include all of the spectral lines present. The transmission peaks of a temperature stabilised confocal *calibration* etalon, (Tropel 216B, FSR = 299.63(1)MHz [6]), are recorded alongside the atomic spectra in order to calibrate the scans taken. Both the laser scans and the subsequent data acquisition are controlled by an Archimedes A5000 computer connected to the electronics system through an IEEE-488 Microlink interface.

In order to produce a tunable source of UV light, a $LiIO_3$ nonlinear crystal can be placed inside the dye laser cavity. In such cases the UV output is taken directly to the ABU and the fundamental beam is used to scan, stabilise and calibrate the laser, as described above.

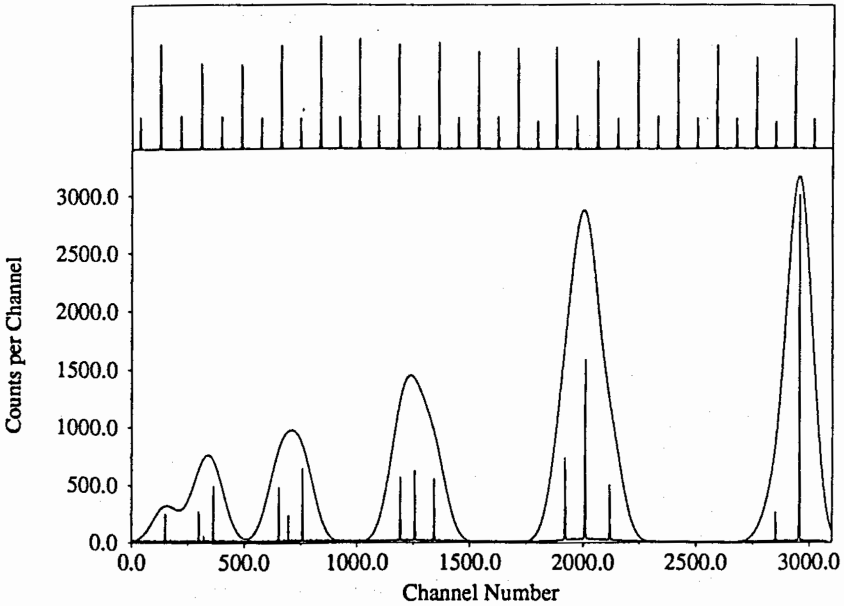

Figure 4: ^{55}Mn hyperfine structure (FWHM ~10MHz) in the $\lambda = 543.255$nm transition measured using crossed beam laser spectroscopy. Also shown is a simulation of how this transition would appear with Doppler broadened line widths. The signal from the calibration etalon (299.63MHz) is shown along the top.

3. Examples of Data Obtained

Highly resolved spectra can be taken using crossed beam laser spectroscopy, with line widths of the order of 10MHz easily achieved in Birmingham. This is illustrated in a spectra taken for ^{55}Mn, figure 4, which shows the spectra recorded for a highly collimated beam of manganese atoms, situated on a Doppler broadened pedestal, together with a simulation of the same spectra with Doppler broadened linewidths [4]. Both the pedestal, thought to be due to diffuse gas in the light collection region, and the simulation clearly shows that without a reduction in Doppler broadening the hyperfine lines present would not be resolved.

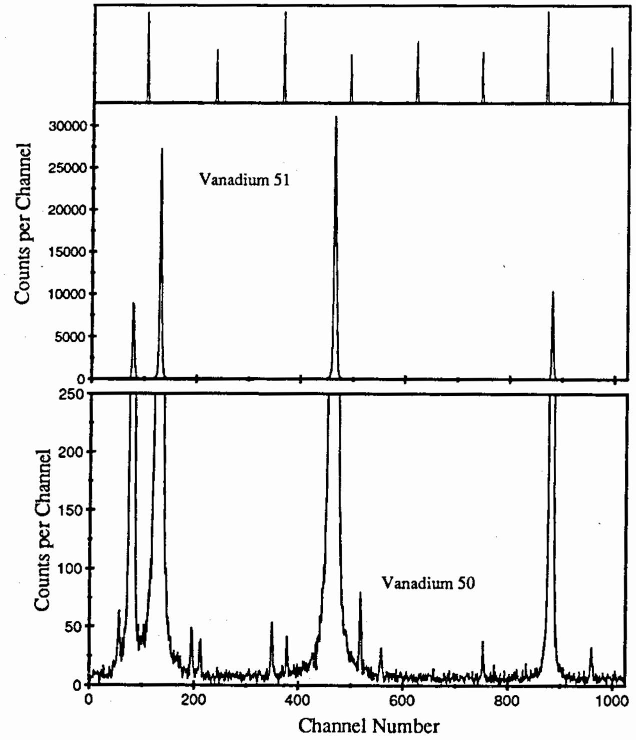

Figure 5: Example of ^{51}V hyperfine structure peaks (FWHM ~8MHz) in the λ = 624.310nm transition together with an expanded scale showing the weakly abundant ^{50}V peaks. The signal from the calibration etalon (299.63MHz) is shown along the top.

This resolution, and the high sensitivity that can be achieved, is also demonstrated in spectra taken for samples of natural vanadium [1] and cerium [2], figures 5 and 6 respectively. Both elements, like lanthanum, have weakly abundant isotopes which require very good signal to noise ratios in order to be observed. This is particularly true in the case of vanadium, where the high spin of the weakly abundant ^{50}V isotope ($I^{\pi} = 6^{+}$, 0.25%)

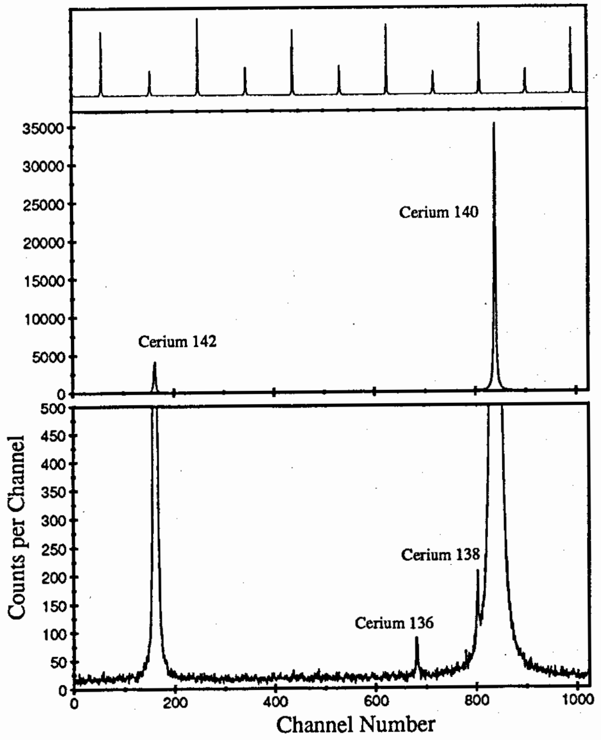

Figure 6: Weak ^{136}Ce (0.19%) and ^{138}Ce (0.25%) peaks resolved from those belonging to the more abundant ^{140}Ce (88.45%) and ^{142}Ce (11.11%) isotopes (FWHM ~10MHz) in the λ = 592.631nm transition. The signal from the calibration etalon (299.63MHz) is shown along the top.

means that its fine structure line is split into many components which lie within a forest of stronger ^{51}V ($I^{\pi} = \frac{7}{2}^{+}$, 99.75%) lines.

Recently UV transitions have been studied using intra-cavity frequency doubling and an example of one such transition, taken for atomic iron, is given in figure 7. Here all of the naturally abundant isotopes are visible, although the natural line width of this transition, ~30MHz, means that only two of the three ^{57}Fe hyperfine lines can be observed.

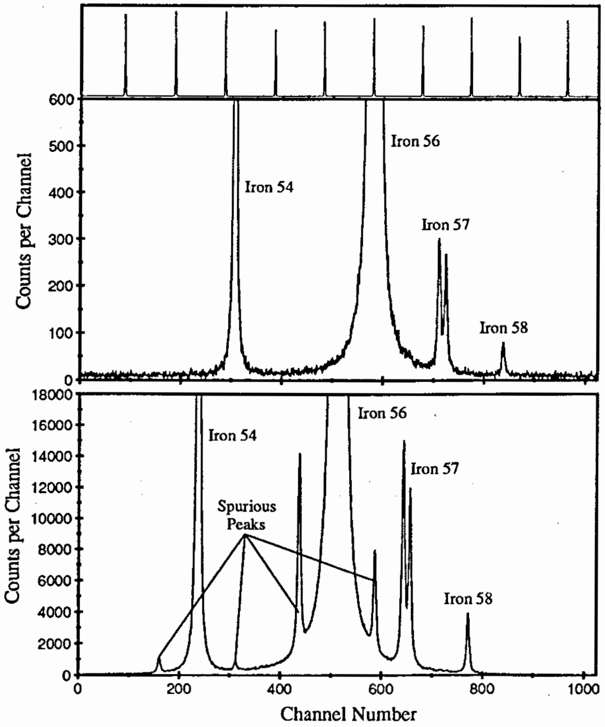

Figure 7: Scan showing the spectral structure of the naturally abundant iron isotopes in the $\lambda = 305.909$nm transition (middle) together with data recorded for the same transition showing spurious spectral lines ~460MHz from the large atomic peaks (bottom). The signal from the calibration etalon (299.63MHz) is shown along the top.

3.1. Spurious Peaks in UV Transitions

During experiments to measure the UV lines in iron, it was found some atomic spectra contained several spurious lines, as shown in figure 7. These were not limited to particular transitions, with the extra peaks appearing in one set of data and then disappearing in later measurements of the same transition. After investigations it was concluded that as similar peaks appeared in the fundamental output which, together with the spurious UV lines, were an integral number of laser cavity modes (~230MHz) from the real peaks, then these UV lines were caused by spurious modes resulting from sum-mixing effects between the main dye laser modes and its weaker side modes. This is shown in figure 8 where the fundamental output from two confocal etalons was recorded alongside the $\lambda = 319.323$nm iron transition. Although no techniques have been developed to filter out these extra UV modes, they can be eliminated by careful laser alignment.

4. Data Analysis

In order to determine the frequency per channel across each scan, and thus evaluate optical isotope shifts and the splitting of the hyperfine components, a quadratic fit to the calibration etalon peak positions is used. The effect of a quadratic calibration compared to that of a linear calibration is small, usually lying within experimental uncertainties, although it can lead to more accurate values for the hyperfine coefficients. Note that for UV transitions the frequency per channel of the atomic spectra is twice that given by the calibration markers, which are recorded using the fundamental output of the laser.

A fitting routine, using a least square fit of the hyperfine multiplet to the measured splitting, is then used to find the $A(J)$ and $B(J)$ coefficients where appropriate. This program also gives the weighted centroid of hyperfine spectra allowing the isotope shifts to be determined.

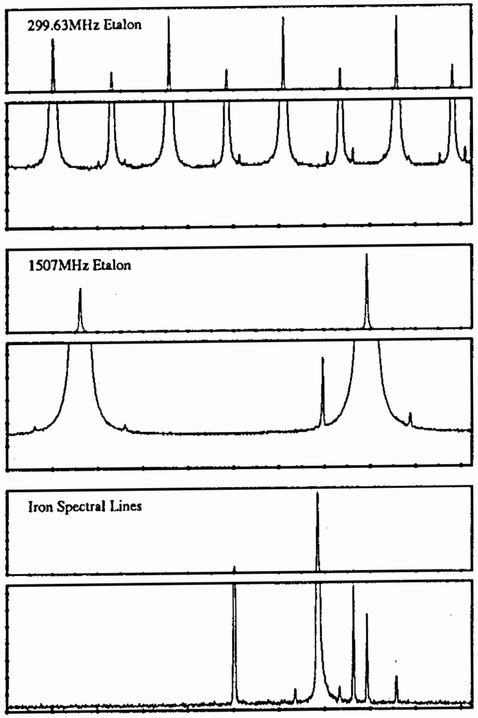

Figure 8: The weak dye laser side modes are visible here in the transmission spectra of its fundamental output through two confocal etalons of FSR 299.63MHz (top trace) and 1507MHz (middle trace). The 319.323nm iron spectra containing spurious UV lines recorded alongside the etalon traces is also shown here (bottom trace). In this case all of the spurious peaks are ~230MHz from the main lines.

4.1. Calibration Etalon Drift

Although the calibration etalon is sealed in a temperature-stabilised enclosure, its transmission peaks are observed to drift in absolute frequency. This drift can be measured relative to a given atomic peak over a series of scans and is found to be approximately linear in time with values ranging from $0.03\mathrm{MHz\,s}^{-1}$ to $-0.03\mathrm{MHz\,s}^{-1}$. This means that for scans taken over 1024 channels, with a dwell time of 0.1s per channel, the etalon can drift by as much as 3MHz, expanding or contracting the scans by this amount.

Although this effect is small in most cases, for well separated atomic peaks it can cause a significant error in the splittings calculated if no corrections are made. For example, in the 625.857nm transition in ^{51}V, the drift of the etalon caused the hyperfine peaks separated by 3006.0(4)MHz to be measured as 3008.1(4)MHz apart, leading to larger errors in the hyperfine coefficients evaluated. Therefore the etalon drift is corrected for in each individual scan taken by calculating the time separating each spectral line and evaluating the drift rate from a series of measurements.

5. Examples of Final Results

The high quality spectra that can be taken with the equipment in Birmingham, together with quadratic fits to the calibration markers and correcting for the etalon drift, leads to accurate results for both optical isotope shifts and the hyperfine $A(J)$ and $B(J)$ coefficients. This is illustrated in the data given below for the lower state $A(J)$ and $B(J)$ coefficients of the first metastable states in vanadium [1] and the optical isotope shifts recently measured for cerium [2].

State (a^6D_J)	Energy (cm^{-1})	$A(J)^*$ (MHz)	$A(J)^\dagger$ (MHz)	$B(J)^*$ (MHz)	$B(J)^\dagger$ (MHz)
$a^6D_{1/2}$	2112.32	751.47(25)	751.4778(28)	0.0	0.0
$a^6D_{3/2}$	2153.20	405.57(15)	405.6038(12)	−8.1(11)	−8.107(12)
$a^6D_{5/2}$	2220.13	373.47(9)	373.5180(10)	−5.5(14)	−5.459(25)
$a^6D_{7/2}$	2311.37	382.34(8)	382.3670(10)	1.9(17)	2.268(29)
$a^6D_{9/2}$	2424.89	406.83(5)	406.8513(16)	14.4(17)	14.324(65)

Table 1: Lower state $A(J)$ and $B(J)$ hyperfine coefficients of the first metastable states in ^{51}V measured here* [1] and compared to values recorded by Childs and Goodman† [7] using atomic beam magnetic resonance techniques.

Transition (nm)	A, A'	$\delta\nu^{A,A'}$ (MHz)
590.067	142,140	−1808.4(4)
591.012	142,140	−1869.5(2)
	140,136	376.9(3)
602.420	142,140	−960.7(1)
602.424	142,140	−2168.5(5)
592.631	142,140	−2169.3(2)
	140,138	119.4(2)
	140,136	517.3(5)
592.835	142,140	−2018.2(2)
	140,138	138.8(4)
	140,136	540.3(6)

Table 2: Optical isotopes shifts between the naturally abundant cerium isotopes recently measured in Birmingham [2]

6. Conclusion

Crossed beam spectroscopy has been used in Birmingham for many years enabling spectra to be taken for stable and long-lived isotopes with high resolution and good sensitivity. This in turn has lead to accurate values for optical isotope shifts and hyperfine coefficients, with this accuracy recently improved by using quadratic fits to the calibration markers and correcting for etalon drift. Measurements have been performed on refractory and reactive elements, and frequency doubling techniques have enabled experiments to be extended to UV transitions. This leaves open the possibility for future spectroscopic work on previously unstudied elements which are difficult to create into an atomic beam or which have transitions outside the visible region of the spectrum.

References

[1] E.C.A. Cochrane, D.M. Benton, D.H. Forest and J.A.R. Griffith *J. Phys. B* **31** (1998) 2203

[2] J.K. Tasker, *4th Year Project Report*, The University of Birmingham (1999)

[3] D.M. Benton, J.L. Cooke and J.A.R. Griffith *J. Phys. B* **27** (1994) 4365

[4] D.H. Forest *Doctoral Thesis* The University of Birmingham (1999)

[5] D.M. Benton, E.C.A. Cochrane and J.A.R. Griffith *J. Phys. B* **30** (1997) 5359

[6] R. New *Doctoral Thesis* The University of Birmingham (1979)

[7] Childs W J and Goodman L S 1967 *Phys. Rev.* **156** 64

Mass Selective Resonance Ionization Spectroscopy of Trans-Einsteinium Elements*)

H. Backe [1], *A. Dretzke* [1], *G. Gwinner* [3], *T. Kolb* [1], *W. Lauth* [1], *W. Ludolphs* [1], *R. Repnow* [3], *Th. Schütze* [1], *M. Sewtz* [1], *A. Steinhof* [1], *N. Trautmann* [2]

[1]Institut für Kernphysik, Universität Mainz, Germany
[2]Institut für Kernchemie, Universität Mainz, Germany
[3]Max Planck Institut für Kernphysik, Heidelberg, Germany

1. Introduction

The investigation of atomic, chemical and nuclear properties of new heavy elements requires ultrasensitive methods the development of which is a real experimental challenge. Concerning the atomic properties, the first ionization potentials of these elements are of particular interest. These have been determined in recent experiments off-line up to the element Es (Z=99) with small samples breaded in nuclear fission reactors employing the Resonance Ionization Mass Spectroscopy (RIMS) method [1], [2]. However, elements with charge numbers Z>100 can only be produced by nuclear fusion reactions with low production rates, sometimes only a few atoms per week [3], and very sensitive on-line methods are required to obtain the above mentioned properties. A very powerful on-line method is the RAdiation Detected Resonance Ionization Spectroscopy (RADRIS) in a buffer gas cell [4]. This has been demonstrated with isotope shift measurements at ^{240f,242f}Am fission isomers at production rates as low as about 10/s and half-lives as short as 1 ms. The RADRIS method relies on the radioactive decay detection of the nuclides in question which is not practicable if the half-lives of the nuclides are longer than about a few minutes. Because of this limitation the detection technique has been developed further. In the new apparatus the radioactive decay detection is replaced by a mass selective direct detection of the resonantly produced ions.

In this contribution a status report is given on an experiment with our Ion-Guide detected Resonance Ionization Spectroscopy (IGRIS) technique [5] aiming in a measurement of the first ionization potential of the element fermium (Z=100).

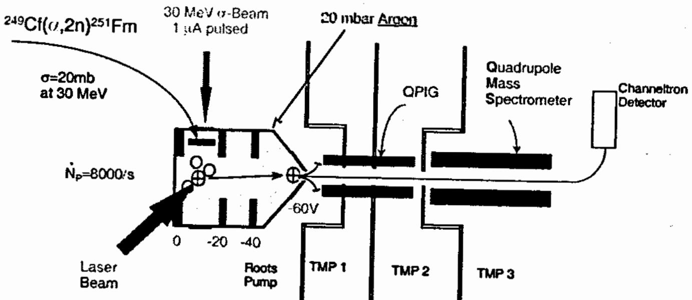

Figure 1: *Schematic experimental set-up for resonance ionization spectroscopy at ^{251}Fm.*

---

*)Supported by BMBF under contract 06MZ 863I9 (TP1).

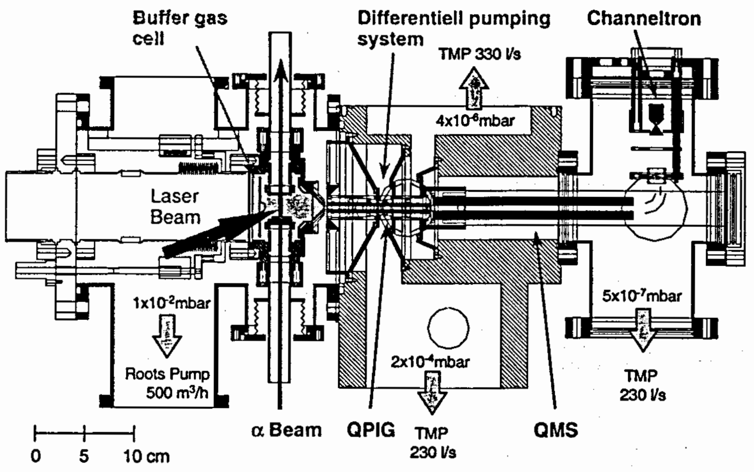

Figure 2: *Experimental set-up. The ^{249}Cf target is located just behind the entrance window of the buffer gas cell. Shown are also the α beam and the laser beam which enters from the top, the QPIG which transfers the ions through the apertures of the differential pumping system and the QMS. One roots pump and three turbo molecular pumps are sufficient to sustain a pressure in the analyzing section of $5 \cdot 10^{-7}$mbar.*

2. Principle of the experiment

The experimental setup is schematically shown in Fig. 1. A 30 MeV pulsed α beam from the Emperor tandem Van de Graaff accelerator at the Max-Planck-Institut für Kernphysik in Heidelberg enters the optical buffer gas cell through a thin 1.8 mg/cm^2 titanium window. Fermium will be produced via the ^{249}Cf(α,2n)^{251}Fm reaction with a cross-section of 20 mb. The ^{251}Fm ions recoiling out of the target come to rest in the 20 mbar argon buffer gas atmosphere as neutral or singly charged ions. At a beam current of 1 μA a stopping rate of about 8000/s is expected. The singly charged ions are removed by electric fields which guide the ions onto electrodes. A suitable timing, see Fig. 9a for illustration, assures that in the α-beam-off periods only neutral Fm atoms remain in the buffer gas. During the storage time of about 40 ms these atoms are illuminated by pulsed laser beams. The resonantly ionized atoms drift in a now altered electric guiding field toward the nozzle and are ejected with the buffer gas jet. A rf QuadruPole-Ion Guide (QPIG) transmits the ions through a differential pumping section into the Quadrupole Mass Spectrometer (QMS). Finally the ions are detected with a channeltron detector. The experimental set-up is shown in Fig. 2.

The optical spectroscopy of trans-einsteinium elements is hampered by the fact that no excited atomic levels are known for these elements. However, for a two step ionization scheme at least one intermediate level must be known, see Fig. 3 left. In order to find such a level the first excitation step should lead in a regime where the level density is relatively high while the second step ends up in the continuum.

The ionization potential is expected at an energy of 52,400 cm^{-1} [6], corresponding to 6.5 eV. If the photon energy of the first laser is about 34,000 cm^{-1} the level density should be high enough (10-20/cm^{-1}) to find an intermediate level. Once this level is known the ionization potential can be determined by tuning the energy of the second laser around the expected ionization limit.

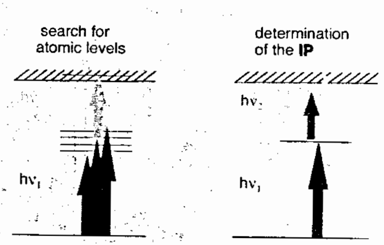

Figure 3: *Principle of the two step resonance ionization of fermium (Z=100).*

3. Electric field guidance

The optical gas cell is loaded during the beam on period with fusion products which are thermalized and partly (13%) neutralized in the buffer gas. Only this neutral part is suitable for resonance ionization spectroscopy. To remove the charged part electric fields are applied in a pulsed mode, see Fig. 4. After the clean up period only neutral reaction products remain stored in the buffer gas atmosphere where they are irradiated by laser light in the beam off period. During the resonance ionization the electric fields are switched in a way that resonantly ionized atoms, which drift along the field lines, are guided towards the nozzle. Both field configurations are shown in Fig. 5.

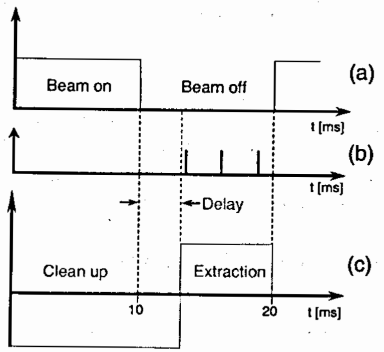

Figure 4: *Timing of beam pulses (a), laser pulses (b) and electric guiding fields (c).*

In the nozzle itself where the electric field has defocusing components, the friction force of the buffer gas jet predominates and the ions are extracted with the gas jet.

The electric field guidance of the ions inside the buffer gas cell signifies a major improvement of hitherto IGISOL-techniques [7]. The extraction time of the ions is no longer determined by the exchange time of the gas in the cell. For our apparatus, even at the low argon gas flow rate of 25,000 sccm/h through the nozzle of 1 mm diameter the extraction time does not exceed several milliseconds. The low gas flow rate brings about a very compact setup with a 500 m^3/h roots pump only, and three turbo molecular pumps (TMP).

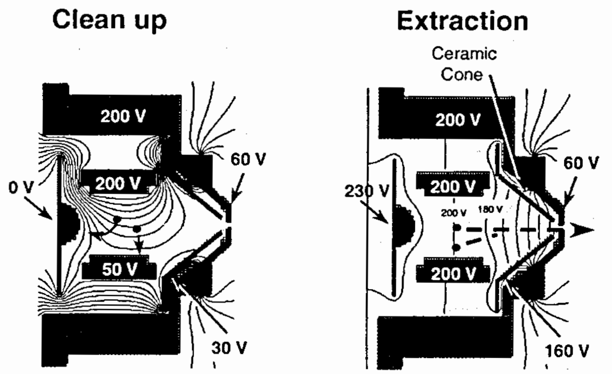

Figure 5: *Electric field configuration in the optical cell during the clean up and the extraction period.*

4. Determination of the transport time

The extraction time of the ions out of the optical cell has been determined with the daughter isotope Po ($t_{1/2}$ = 1.78 ms) recoiling out from a ^{223}Ra source after α decay of ^{219}Rn ($t_{1/2}$=3.96 s) and thermalizing in the buffer gas. A pulsed voltage is applied to the ^{223}Ra source as indicated in Fig. 6.

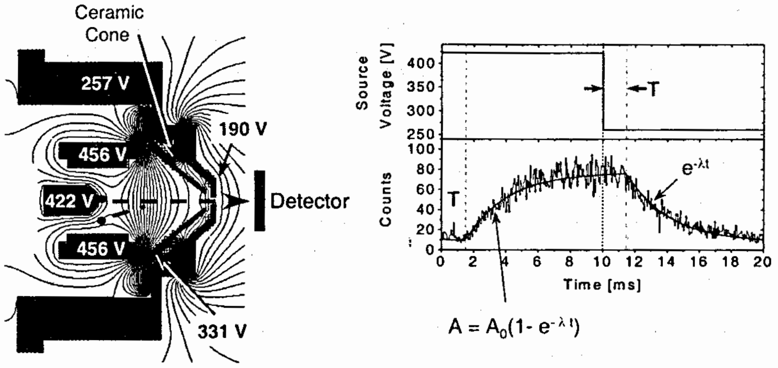

Figure 6: *Determination of the extraction time. The potential at the α source amounts to 422 V in the extraction phase, i. e. the time interval between 0 and 10 ms, and to 260 V between 10 ms and 20 ms. In this time interval no ions can leave the cell. The corresponding decay signal of ^{215}Po on the detector is shown on the right.*

The extracted ions were detected with a semiconductor detector which was placed in front of the nozzle. The energy resolution of the detector allowed to select the decay events of the short lived ^{215}Po isotopes. The delay between the switching time $t = 0$ ms and 10 ms and the on-set of the increase of the count rate and its exponential decay, respectively, is the extraction time of the ions which amounts to $T = 1.5$ ms.

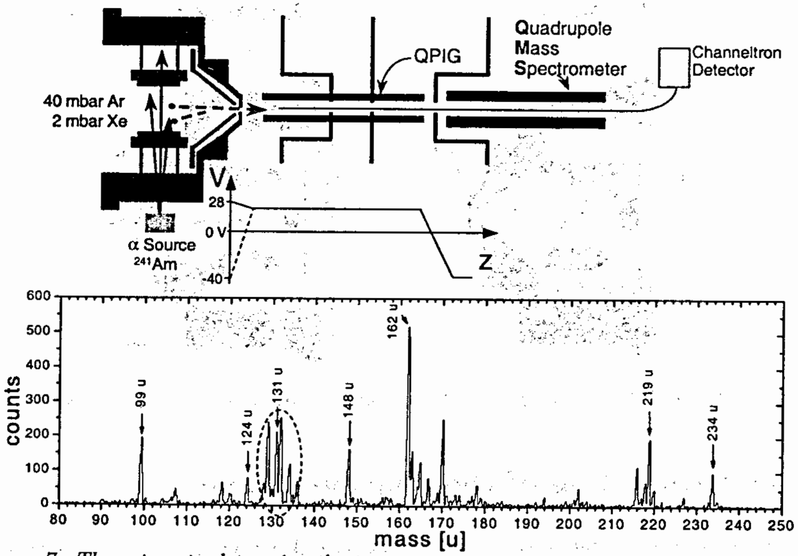

Figure 7: *The set-up to determine the transport time through the QPIG is shown above; a typical mass spectrum of the created ions, below.*

To determine the transport time of the ions through the QPIG a ^{241}Am α source was placed in front of the entrance foil of the optical cell, see Fig. 7. The α particles ionize inside the cell the Ar buffer gas atoms, admixed Xe atoms as well as gas impurities. The potential of the nozzle is periodically changed from 28 V to -40 V. At $V = 28$ V the ions are transported by a field gradient from the nozzle to the QMS. At $V = -40$ V all ions drift back onto the nozzle.

Typical time distributions are shown in Fig. 8. The mean transport time increases with increasing mass of the ions from 5 ms to more than 200 ms. The transport time of ^{131}Xe of 8 ms is exceptionally short. The reason is that Xe as a one atomic ion has a very good mobility. All other ions form rapidly long organic chains with hydrocarbon from the pumping oil. These large molecules consequently have a low mobility in buffer gas. To overcome this problem a fast transport of the ions inside the ion guide structure is required. Simulations of electric field gradients inside the QPIG show that the transport times can be reduced to about 100 μs.

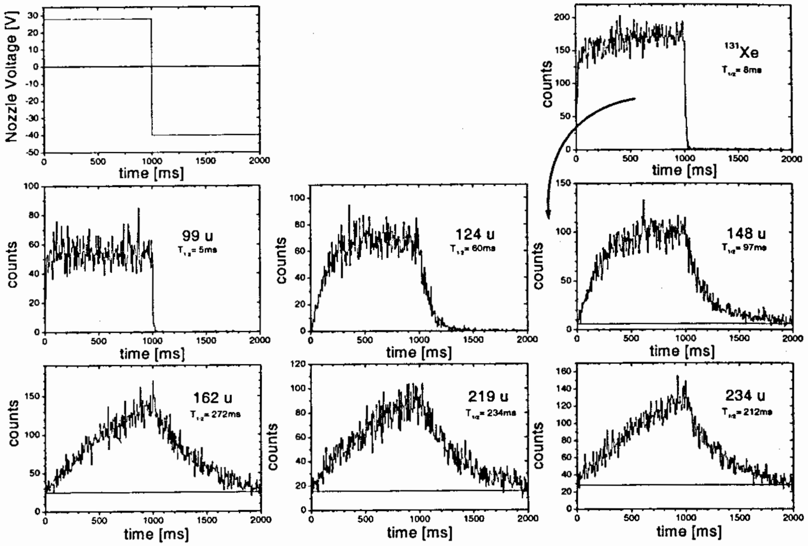

Figure 8: *Transport time through the ion guide. From the time distribution of ions after the change of the nozzle voltage at 1000 ms a mean transport time can be defined. It is given in the diagrams as the half life $T_{1/2}$.*

5. First on-line test experiments

Of crucial importance for the sensitivity is a low background count rate in the extraction period at the mass number A=251. A background may be caused by two different processes. On the one hand, neutral and relatively long living active complexes (atomic and molecular) can be created during the beam-on period. These complexes can ionize in collisions with the neutral Fm atoms yet during the extraction period. One example for these complexes is active nitrogen which is created in the plasma [8], [9]. On the other hand, γ-radiation due to activation processes by the primary beam in the gas cell or in the beam dump causes background in the channeltron detector.

To investigate these effects a 22 MeV d-beam at a mean ion current of 325 nA has been guided through the buffer gas cell filled with 21 mbar argon in which a dysprosium target, 90 μg/cm^2 on a 1.8 mg/cm^2 titanium backing, was located.

Electric fields have been applied inside the cell in a way that all created ions were removed as quick as possible during the beam-off period. The results are shown in Fig. 9b. The count rate in the channeltron detector during beam-on, $8.31 \cdot 10^{-2}$/ms, can mainly be attributed to γ background, $8.32 \cdot 10^{-2}$/ms, which originates from reactions of the primary beam in the gas cell and the beam dump, as already mentioned. After a delay time $t_d = 3$ ms the ion signal drops in the beam-off period to the background count rate of the channeltron detector, $1.30 \cdot 10^{-2}$/ms, from which $1.25 \cdot 10^{-2}$/ms is the γ-background-count-

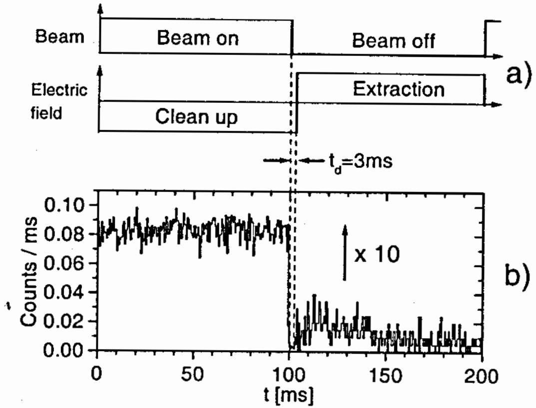

Figure 9: *Timing of pulsed beam and electric field configurations (a). Time resolved spectrum of the ion signal after optimization of the electric fields (b). Life-time 813 s.*

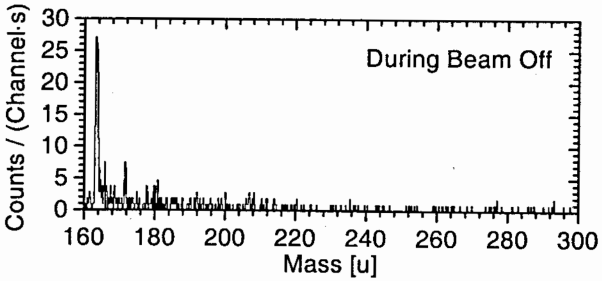

Figure 10: *Mass spectrum taken in the extraction period. With the calibration of 5 channels/u a background count rate of 0.9/s results at mass number 251.*

rate. The mass spectrum in the extraction period is shown in Fig. 10. The γ-background during the beam-off period has meanwhile been reduced by a factor 4.5 and is negligible for the planned experiment. This has been accomplished with a 2.5 cm thick lead shielding around the channeltron detector.

The ion signal in the beam-off period changes drastically when about 10% N_2 is added to the buffer gas, see Fig. 11. A strong ion signal is observed in the extraction period still a long time after the beam has been turned off. It can be described by the function $\dot{N} = N_0 e^{-t/\tau} \cdot \Theta(t-(100+t_d))$ with $\tau \sim 25$ ms, t_d=delay time, and $\Theta(t)$ the step function. The signal originates from ionization processes of gas impurities in collisions with active nitrogen. Therefore, any contamination of to the buffer gas with N_2 must be carefully avoided.

Further test experiments with Er beams, the chemical homologue of Fm, are underway to optimize the efficiency and the resonance ionization scheme.

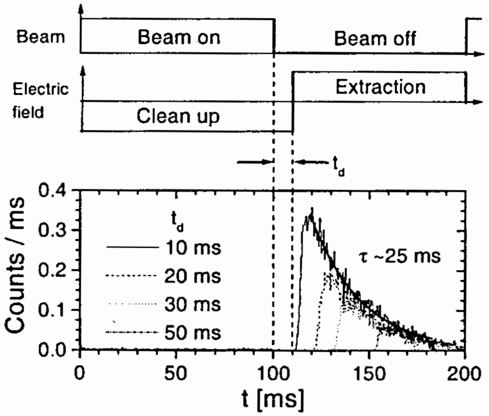

Figure 11: *Time resolved spectrum of the mass integrated ion signal with 10% N_2 admixture to the buffer gas.*

References

[1] J. R. Peterson et al., J. Alloys. Comp. 271-273 (1998) 876

[2] N. Erdmann et al., J. Alloys. Comp. 271-273 (1998) 837

[3] S. Hofmann et al., Z. Phys. A 354 (1996) 229

[4] H. Backe et al., Phys. Rev. Lett. 80 (1998) 920

[5] H. Backe et al., Nucl. Instr. and Meth. B 126 (1997) 384

[6] J. Sugar, J. Chem. Phys. 59 (2) (1973) 788

[7] P. Dendooven, Nucl. Instr. and Meth. B 126 (1997) 182

[8] R. J. Strutt et al., Proc. Roy. Soc. A 85 (1911) 223

[9] V. Lj. Marković et al., J. Phys. D: Appl. Phys. 27 (1994) 979

HYPERFINE STRUCTURE ANOMALY TO PROBE THE MAGNETIC PROPERTIES OF QUARKS AND NUCLEI

Takashi. T. Inamura*

Heavy Ion Laboratory, Warsaw University, Poland

Abstract

Magnetic hyperfine structure anomaly has been well known as an effect of finite nuclear magnetization since Bohr and Weisskopf theoretically pointed out in 1950. However, little effort has been made to explore the finite nuclear magnetization and the source of magnetization through this anomaly. Today it is commonly accepted that quarks confined in protons and neutrons are producing nuclear magnetization. This could be quantitatively studied by measuring the anomaly with a high precision.

1. Introduction

To study sub-nucleon degrees of freedom in atomic nuclei, basic ingredients here are: 1)Electromagnetic interactions, 2)Atomic electrons, and 3)Atomic nucleus. And I shall add spices, that is to say, quarks.

It is hard to believe that atomic nuclei are simply built of bound nucleons having the same identities as protons and neutrons always and everywhere inside the nucleus. As you all know, the neutron possesses a magnetic moment

$$\mu_n = -1.91314(4) \times 10^{-5}\mu_N, \tag{1}$$

where μ_N is the nuclear magneton that is given by $e\hbar/2M_p c$. This fact shows that the neutron has a structure made up of some charged entities, that is to say, quarks in current terms.

I have no doubt about the validity of the nuclear shell model from a usual nuclear physics viewpoint. But there is a limit of its validity when it comes to 1% accuracy, for instance, in describing nuclear magnetic moments or related quantities such as hyperfine structure anomaly. One could expect that the effects of quarks inside the nucleus manifest themselves in extremely accurate measurements of magnetic properties of the nucleus. The question is how to detect the loss of nucleon identities inside the nucleus.

---

*On leave of absence from RIKEN and JST in Japan.

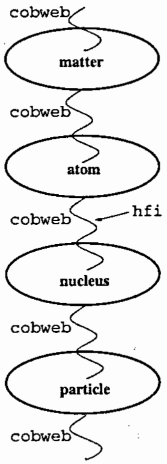

Figure 1: Separated layers of the physical world.

2. How to detect the loss of nucleon identities inside the nucleus

Before coming to this point I would like to travel a bit around the general aspect of physics.

We can divide the physical world into several layers (disciplines) which are autonomous, having their own entities like protons and neutrons in the nucleus layer.(See Fig.1.) One can happily live in individual layers, neglecting cobwebs (interactions) between neighbouring layers. However, once you are interested in the cobweb, you will never be happy, being confined in a given layer. I am such a guy who has been fascinated by one of the cobwebs, hyperfine interactions, from the nuclear physics side, otherwise I could have lived happily and slept in the nucleus layer. I believe that one of the cobwebs will lead us to a big discovery although they are so thin. (The interaction energy is so small that one can easily neglect it.)

To study the loss of nucleon identities inside the nucleus, I don't want to be so rude that I disturb the order of them in nature. I am just knocking at the door of the atomic electrons which always surveying the inside of the nucleus. It should be remarked that atomic electrons, particularly $s_{1/2}$ and $p_{1/2}$ electrons, are surveying the entire volume of the nucleus without our

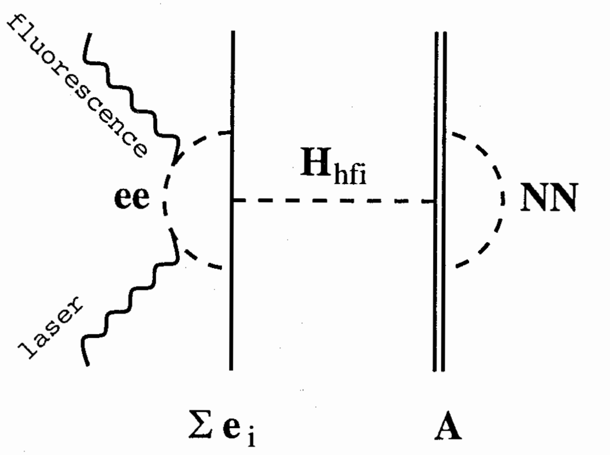

Figure 2: Feynman diagram of hyperfine interaction: e are atomic electrons, N nucleons, and A is the nucleus.

artificial interference by atom smashers (high-energy accelerators). They will answer about the effects of quark deconfinement. The knocking method best suited for this purpose is to measure the effects of the spatial distribution of nuclear magnetization, i.e., hyperfine structure (hfs) anomaly.

The total Hamiltonian H of a given atomic system is written as

$$H = H_{ee} + H_{NN} + H_{eA}, \qquad (2)$$

where e denotes atomic electrons, N nucleons, and A the nucleus. The last term is hyperfine interaction H_{hfi}. Figure 2 shows a Feynman diagram of hyperfine interactions. The Hamiltonian of hyperfine interactions to first order in v/c can be approximately given by

$$H_{hfi} = \int_{\tau_e}\int_{\tau_N} \frac{\rho_e(\mathbf{r}_e)\rho_N(\mathbf{r}_N)}{\mid \mathbf{r}_e - \mathbf{r}_N \mid} d\tau_e d\tau_N - \frac{1}{c^2}\int_{\tau_e}\int_{\tau_N} \frac{\mathbf{j}_e(\mathbf{r}_e)\mathbf{j}_N(\mathbf{r}_N)}{\mid \mathbf{r}_e - \mathbf{r}_N \mid} d\tau_e d\tau_N, \qquad (3)$$

where $\rho(\mathbf{r})$ and $\mathbf{j}(\mathbf{r})$ are charge and current densities, respectively. It should be stated that this Hamiltonian is an approximation, being independent of any model. Remember that "truth" in nature must be independent of the model. Charge and current densities may be neither uniform nor spherically symmetric. We may have to introduce a model to give these densities, whereupon the model will be tested by experimental observation.

Since Bohr and Weisskopf theoretically elucidated the effect of the finite size of the atomic nucleus on the magnetic dipole hyperfine interaction in 1950 [1], namely Bohr-Weisskopf effect (B-W effect) or hfs anomaly, the spatial distribution of nuclear magnetization (DNM) has attracted much interest among atomic and nuclear physicists [2, 3, 4, 5, 6]. Very recently, an experiment has been carried out in this direction by Mainz-Poznan-ISOLDE collaboration [6]. This work is a counterpart to our collaborative work on ISOLDE [5].

In 1960s the quark model shed new light on the nuclear magnetization, giving the anomalous magnetic moments of proton and neutron in a reasonable manner [7]. Experimentally speaking, however, little progress has been made in understanding the nuclear magnetization.

3. Sub-nucleon degrees of freedom in the nucleus

We need to know what constraints on the DNM, i.e., B-W effect will come from sub-nucleon degrees of freedom in the nucleus, whether pionic or quark, quantitatively. Then we could obtain the evidence for the sub-nucleon degrees of freedom in the nucleus.

In the interaction Hamiltonian, Eq. (3), nuclear charge and current densities, $\rho_N(\mathbf{r})$ and $\mathbf{j}_N(\mathbf{r})$, should depend on the sub-nucleon degrees of freedom. The B-W effect is expected to be rather sensitive to the current density. However, we must know how large the neglected terms in Eq. (3) are, that is to say, relativistic effects including retarded potentials, first of all.

It would also be important to consider the Breit-Rosenthal effect [8] when the sub-nucleon degrees of freedom are taken into account. This effect is coming from the finite distribution of nuclear charge.

4. Concluding remark

The hyperfine structure anomaly should play important role in studying the sub-nucleon degrees of freedom. To exploit that possibility, we have to open up a precision frontier by improving the present accuracy by two orders of magnitude. For instance, it would be a prerequisite to be able to measure the magnetic dipole hyperfine constant A in an accuracy of 10^{-8} systematically in a chain of isotopes.

Lastly, I would like to quote Aage Bohr's statement given at the beginning of his paper *On the hyperfine structure of deuterium* [9]:

The unexpected effects revealed by very accurate measurements of the hyperfine structure of hydrogen and deuterium have, as is well known, given rise to a re-examination of the consequences of quantum electrodynamics.
The same spirit is true of today.

References

[1] A. Bohr and V.F. Weiskopf, Phys. Rev. 77 (1950) 94.

[2] J. Eisinger and V. Jaccarino, *Proc. Intern. Conf. on Nuclear Sizes and Density Distributions held in Stanford, Dec. in 1957*; Rev. Mod. Phys. 30 (1958) 528.

[3] S. Büttgenbach, Hyp. Int. 20 (1984) 1.

[4] T.T. Inamura, *Symp. on Lasers in Nuclear Physics held in Osaka, Dec. 1987*, RCNP-P-95 (1988).

[5] H.T. Duong, C. Ekström, M. Gustafsson, T.T. Inamura, P. Juncar, P. Lievens, I. Lindgren, S. Matsuki, T. Murayama, R. Neugart. T. Nilsson, T. Nomura, M. Pellarin, S. Penselin, J. Persson, J. Pinard, I. Ragnarsson, O. Redi, H.H. Storke, J.L.Vialle, and the ISOLDE Collaboration, *Systematic measurements of Bohr-Weisskopf effect at ISOLDE*, CERN-ISOLDE proposal IS302 since 1987; Nucl. Instr. and Meth. A325 (1993) 465.

[6] N.J. Stone and J. Rikovska, *Proc. Intern. Conf. on On-line Nuclear Orientation held in Oxford, Sept. 1988*; Hyp. Int. 43 (1988) 37.

[7] K. Enders, E. Stachowska, G. Max, Ch. Zölch, U. Georg, J. Dembczynski, G. Werth, and the ISOLDE Collaboration, Phys. Rev. A 56 (1997) 265.

[8] M.A.B. Beg, B.W. Lee, and A. Paris, Phys. Rev. Lett. 13 (1964) 513.

[9] G. Breit and E. Rosenthal, Phys. Rev. 41 (1932) 459.

[10] A. Bohr, Phys. Rev. 73 (1948) 1109.

Extraction of hyperfine anomalies without values of the nuclear magnetic dipole moment

J. R. Persson
Department of Physics
University of Karlstad,
SE-651 88 Karlstad, Sweden
email:jonas.persson@kau.se

August 5, 1999

Abstract

A new method for extracting the hyperfine anomaly from experimental hyperfine structure constants is presented. Instead of independent high-precision measurements of the nuclear magnetic dipole moment, precise measurements of magnetic dipole hyperfine interaction constants for two atomic states and a theoretical analysis can be used. This can lead to the determination of hyperfine anomaly for radioactive isotopes where the nuclear magnetic dipole moment is not known with high accuracy. The determination can be done in two ways, either by using a known hyperfine anomaly as calibration or by an analysis of the hyperfine interaction. In addition improved values of the nuclear magnetic dipole moment ratio can be obtained, as well as information on the hyperfine interaction, i.e., core polarisation.

1. Introduction

The influence on the hyperfine structure(hfs) of the finite size of the nucleus was first considered by Bohr and Weisskopf [1]. They calculated the hyperfine interaction (hfi) of $s_{1/2}$ and $p_{1/2}$ electrons in the field of an extended nucleus, and showed that the magnetic dipole hfi constant a for an extended nucleus is generally smaller than that expected for a point nucleus. Isotopic variations of magnetic moments become larger than those in the point dipole interaction when there are different contributions to the hfs from the orbital and spin parts of the magnetisation in the case of extended nuclei. The fractional difference between the point nucleus magnetic dipole hfi constant and the constant obtained for the extended nuclear magnetisation is commonly referred to as the Bohr-Weisskopf (BW) effect [2]. The magnetic dipole hfi constant a can therefore be written as

$$a = a_{point}(1 + \epsilon_{BW}), \tag{1}$$

where ϵ_{BW} is the BW-effect, and a_{point} the a constant for a point nucleus. Because electronic wavefunctions cannot be calculated with high accuracy in complex atoms it is not always possible to determine ϵ_{BW} directly. The BW-effect is,as the isotope shift, dependent on both a nuclear part as well as an atomic part. The atomic part is essentially the electron density within the nucleus. The recent development in atomic structure calculations has made it possible to calculate the electron density with high accuracy [3]. The nuclear part, i.e., the distribution of nuclear magnetisation, can be calculated using different nuclear models [2, 4]. However, it is impossible to experimentally determine the BW-effect direct, only the difference of the BW-effect in two isotopes, the so-called hyperfine anomaly (hfa), can be determined experimentally. Therefore one compares the ratio of the measured hfs constants for two isotopes (or isomers) of the same element with the independently measured ratio of the nuclear magnetic dipole moments to extract the hfa, ${}^1\Delta^2$, for the isotopes 1 and 2, and a given atomic state:

$$1 + {}^1\Delta^2 = \frac{a^{(1)}}{a^{(2)}} \frac{\mu_I^{(2)}/I^{(2)}}{\mu_I^{(1)}/I^{(1)}} \approx 1 + \epsilon_{BW}^{(1)} - \epsilon_{BW}^{(2)} . \tag{2}$$

For electrons with a total angular momentum $j > 1/2$ the anomalies may be disregarded as the corresponding wavefunctions (electrondensities) vanish at the nucleus. If we study the hfa for different atomic states we find a variation of the values. We have a state dependent hfa, the differences in values in different states can be large.The reason for these differences is due to that the hfi consists of three parts[5, 6], orbital, spin-orbit and contact (spin) interaction. Only the contact interaction contributes to the hfa. Thus we can rewrite the general magnetic dipole hfi constant as

$$a = a_{nc} + a_c , \tag{3}$$

where a_c is the contribution due to the contact interaction of s and $p_{1/2}$ electrons, respectively, and a_{nc} is the contribution due to non-contact interactions. The experimentally determined hfa, which is defined with the total magnetic dipole hfi constant a, should then be rewritten to obtain the relative contribution to the hfa:

$${}^1\Delta^2_{exp} = {}^1\Delta^2_c \frac{a_c}{a} , \tag{4}$$

where ${}^1\Delta^2_c$ is the hfa due to the contact interaction, that is, for an s- or p-electron. One can show that a_c is proportional to $g_J - 1$ which gives an indication on the magnitude of $\frac{a_c}{a}$. So far we have only considered direct intercations between the electron and the nucleus, in order to get a complete picture we should include electron-electron interactions. One interaction which can influence the hfi constant is the polarisation of the electron core [5], which may give a substantial contribution to the experimental hfa [2]. Core polarisation can be seen as an excitation of a d-electron, which does not give any contribution to the anomaly, to an s-electron, which gives a large hfa. Since the hfa (${}^1\Delta^2_s$) is independent of n, it is possible to use the hfa to obtain values of the core polarisation [2,7].

2. Extraction of the Hyperfine anomaly

If we consider the hfa for two atomic states A and B in the isotopes 1 and 2 using equation (2), we have:

$$\frac{a_A^{(1)}}{a_A^{(2)}} \frac{g_I^{(2)}}{g_I^{(1)}} = 1 + {}^1\Delta^2_A$$

$$\frac{a_B^{(1)}}{a_B^{(2)}} \frac{g_I^{(2)}}{g_I^{(1)}} = 1 + {}^1\Delta^2_B . \tag{5}$$

Dividing these we get rid of the nuclear g_I factors:

$$\frac{a_A^{(1)}/a_A^{(2)}}{a_B^{(1)}/a_B^{(2)}} = \frac{1 + {}^1\Delta^2_A}{1 + {}^1\Delta^2_B} . \tag{6}$$

Assuming that only s-electrons give a contribution to the hfa in this case, we use eq.(4):

$$\frac{a_A^{(1)}/a_A^{(2)}}{a_B^{(1)}/a_B^{(2)}} \approx 1 + {}^1\Delta^2_s\left(\frac{a_s^A}{a^A} - \frac{a_s^B}{a^B}\right) . \tag{7}$$

The ratio between the two magnetic dipole hfi constant ratios for the two isotopes will be dependent only on the difference of the contact contributions of the two atomic states and the hfa for the s-electron. It should be noted that the ratio a_s/a is independent of isotopes. Once it is determined for one isotopic pair, the ratio can be used for all isotopic pairs, which is very useful in the study of hfa in radioactive isotopes. The ratio can be determined in two ways; either by making an analysis of the hfi and deducing a_s/a from the analysis, or by using a known hfa to obtain a_s/a for an atomic state.

3. Theoretical approach

The contact contributions a_s (and a_p) have to be evaluated separately by analysing the hfs. For more complex atoms with several open shells this is not a trivial task. The different contributions can only be obtained by performing an extended analysis of the hfs in several atomic states using the effective operator formalism [6]. This is, however, possible if a sufficient number of states have been measured and high-quality eigenvectors for the breakdown of LS-coupling are available. Further complications arise from the influence of core-polarisation [2] on the contact interactions, but it is still possible to do a full investigation of both the hfa and the core-polarisation by studying the experimental hfa [2]. This has been demonstrated in Eu [8], where a good consistency of Δ_s was obtained for a number of atomic states. Now it is possible to use the results from a careful analysis of the hfs to derive the hfa without exact values of the nuclear g_I factors.

Using the effective operator formalism [6], the hfi constants can be expressed as a linear combination of effective radial parameters a_l^{ij} and angular coefficients k_l^{ij},

$$a(J) = k_l^{01}a_l^{01} + k_l^{12}a_l^{12} + k_l^{10}a_l^{10} + k_s^{10}a_s^{10}, \tag{8}$$

where the indices stand for the rank in the spin and orbital spaces, respectively. The term of interest is $k_s^{10}a_s^{10}$ which is the contribution to the hyperfine interaction constant from the s electron, a_s. The angular term can be evaluated if the eigenvectors of the atomic state are known. The values of the effective radial parameters are obtained by a least-squares fit to experimental hfi constants. One should be aware of that the result from the analysis can be misleading especially if it is performed on a complex system. The best results should be obtained in atomic systems close to LS-coupling. Further complications arise in systems with a limited number of states, where a full analysis of the hfs can not be done. It must be emphasised that the influence of the contact interaction on the magnetic dipole hfi constant, that is the hfa, must be different between the two states used. If they are similar,the difference of a_s/a will be small and cause an extreme sensitivity to the values used. Therefore two states must have to be chosen carefully, to avoid this problem.

3.1 Example: Hyperfine anomaly in Nd and Gd

Over the years many investigations of the hfs have been carried out in the rare-earth (4f-shell) region [9], and a vast amount of hfi constants and isotope shift data has been obtained. One would expect that analysis of the hfi in this region is very difficult due to the large number of states. However, one finds that many states are very close to pure LS-coupling, especially the low-lying states. It is therefore relatively easy to

Table 1: Hyperfine interaction constants in Nd.

	$a\ ^{143}Nd/a\ ^{145}Nd$	k_s	a_s/a
$4f^45d6s\ ^7L_{11}$	1.610074(20)	0.0454545	0.45176
$4f^45d6s\ ^7L_5$	1.601299(55)	-0.0833333	-2.26981
$4f^45d6s\ ^7K_4$	1.598040(65)	-0.1	-3.21333

Table 2: Hyperfine anomaly and magnetic dipole ratios in Nd.

	$^{143}\Delta_s^{145}(\%)$	$\mu_I\ ^{143}Nd/\mu_I\ ^{145}Nd$
$4f^45d6s\ ^7L_{11}$		1.60860(3)
$4f^45d6s\ ^7L_5$	0.2013(57)	1.60871(6)
$4f^45d6s\ ^7K_4$	0.2055(68)	1.60853(7)
mean	0.2034(63)	1.60861(6)
ABMR[12]		1.626(12)
$4f^46s^2\ ^5I(mean)$[10]		1.60861(2)

perform an analysis. Even if the hfs has been well studied, the nuclear magnetic dipole moments are not always known to high accuracy.

3.1.1 Hyperfine anomaly in Nd

The hfs of Nd has been studied with high accuracy by Childs and Goodman [10] and Childs [11], in the $4f^46s^2\ ^5I_{4-8}$ and $4f^45d6s\ ^7L_{5-11}$, $^7K_4$ states with the ABMR and LRDR methods, respectively. The studied states have also been found to be close to LS-coupling, making an analysis of the hfi rather simple. The high accuracy of the hfi constants and that an analysis has been performed [11] make it possible to extract the hfa. It is important that the factor $(\frac{\alpha_s^A}{\alpha^A}-\frac{\alpha_s^B}{\alpha^B})$ attains a relatively large value. It is therefore important to choose the atomic states with great care, by studying the ratios of the α constants between the two stable isotopes ^{143}Nd and ^{145}Nd, we choose the $4f^45d6s\ ^7L_{11,5}$ and $4f^45d6s\ ^7K_4$ states for extraction of the hfa, and use $^7L_{11}$ as state A. The experimental a-constant ratios and contact contribution are given in table 1. The hfa for s-electrons are deduced and the result presented in table 2. The error of the hfa is only due to the experimental errors of the hfi constants, as the errors in the contact contribution are not known. The error in the hfa is therefore too small and should be about 4 times larger when the uncertainties of the contact contributions are known. Once the hfa is determined it is possible to use this result as a way of obtaining the ratio of the nuclear magnetic dipole moments. The nuclear magnetic dipole moment has been measured by Smith and Unsworth [12] and the ratio is given with the calculated ratio in table 2. We also note that the a-constants ratio in $4f^46s^2\ ^5I_{4-8}$ states, is the same as the "new" ratio, this is an indication that the hfa in these states are zero. This is not surprising, as the configuration does not contain an unpaired s-electron, thus having no contact interaction. This has also been found to be the case in other rare-earths. The difference between Smith and Unsworths experimental ratio and the calculated ratio could be due to systematic errors in the experiment.

3.1.2 Hyperfine anomaly in Gd

Precise studies of the hfs in Gd have been performed by Unsworth [13], who measured the ^9D term in the $4f^75d6s^2$ configuration, and Childs [14], who studied the $4f^75d^26s\ ^{11}F$ term. Unsworth [13] found that the contact interaction was very small, indicating that no core polarisation is present in the $4f^75d6s^2$ configuration. The same have also been found in other rare-earths and seem to be a general feature. In addition the $4f^75d6s^2\ ^9D$ states will have no hfa, something that can also be seen from the lack of J-dependence of the a-constant ratios for the two isotopes $^{155,157}Gd$. The levels $4f^75d^26s\ ^{11}F$ term is reported to be 98-99% pure L-S coupled states [15], it is thus possible to use pure L-S states in the analysis of the hfi [14]. In table 3 the a-constant ratios for the $^{11}F_{2,3,8}$ states are given together with the s-electron contact contribution. It is possible to derive the hfa; the result is given in table 4. The ratio of the nuclear magnetic dipole moments has also been extracted. The ratio obtained compares well with the ratio of the $4f^75d6s^2\ ^9D$ states, proving that the ratio is close to the actual ratio and that there is no hfa in these states. The ratio is also in agreement with the ENDOR measurement [16], but the experimental error is one order of magnitude larger than the derived error.

Table 3: Hyperfine interaction constants in Gd.

	$a\ ^{157}Gd/a\ ^{155}Gd$	k_s	a_s/a
$4f^75d^26s\ ^{11}F_2$	1.31320(5)	0.4	1.2294(36)
$4f^75d^26s\ ^{11}F_3$	1.31297(5)	0.25	1.0776(32)
$4f^75d^26s\ ^{11}F_8$	1.31262(5)	0.125	0.8222(25)

Table 4: Hyperfine anomaly and magnetic dipole ratios in Gd.

	$^{157}\Delta_s^{155}(\%)$	$\mu_I\ ^{155}Gd/\mu_I\ ^{157}Gd$
$4f^75d^26s\ ^{11}F_2$	0.108(18)	0.76249(24)
$4f^75d^26s\ ^{11}F_3$	0.104(28)	0.76250(24)
$4f^75d^26s\ ^{11}F_8$		0.76250(24)
mean	0.106(24)	0.76250(24)
ENDOR[16]		0.7633(45)
$4f^75d6s^2\ ^9D(mean)$[13]		0.76254(40)

4. Experimental approach

If the hfa has been determined for the s-or p- electron in an element it is possible to obtain a value for a_s/a in the atomic states from the experimental a-constants. By comparing two atomic states it is possible to obtain the factor $(\frac{a_s^A}{a^A}-\frac{a_s^B}{a^B})$, as mentioned earlier this factor is isotope independent, which makes it possible to use it to derive the hfa for an isotope where the nuclear magnetic dipole moment is not known with high accuracy. By using this method it is possible to obtain a better value for the nuclear magnetic dipole moment as the hfa is also determined. However, when the hfi constants have been obtaioned by laser spectroscopy, the errors may be too large. As a general rule the hfi constant should be known with a better accuracy than 10^{-3}. If the hfa is known for a linear combination of s-electron anomaly and p-electron anomaly, it is still possible to find general trends. As examples, to this method Eu and In are presented.

4.1. Europium

Europium has been subject to many investigations since the measurements of Schüler and Schmidt in 1935 [17]. In total the hfs has been determined in over 30 atomic states and 15 states in Eu^+. The high accuracy in some measurements has made it possible to determine the hfa. One problem with a complex atom like Eu is that the hfa is state dependent and has to be analysed to give the correct value[2]. A case study of the hfa was performed by Büttgenbach in his review article[2], he found the values -0.64(3)%,-0.66(3)% and -0.59(5)% depending on the states and experimental method used. The average value -0.64(4)% is probably a very good approximation, however the value obtained from Fabry-Perot measurements in the ion (-0.59(5)%) is probably too low. In the accurate measurements in an ion trap, by Becker et al. [18], an uncorrected value of -0.663(18)% was obtained for the hfa. The uncertainty in this value is mainly from the magnetic moment measurements [19], the difference from the value given by Büttgenbach is due to that the value has not been corrected for the noncontact part of the hfi constant.

Using the known hfa in combination with experimental data will give an estimate of the hfa. The unstable Eu isotopes have been studied using laser spectroscopy by Ahmad et al. [20]and by Dörschel et al. [21]. Recently a measurement was performed by Enders et al. [22, 23, 24] using a Paul ion trap, to obtain the hfi constants in the ground and first metastable states of Eu^+. The high precision values from the ion trap measurements cannot, at the time being, be used to extract the hfa as both values are too close to each other [25]. It turns out that it is only the values of Ahmad et al. [20] that is suitable to use. In their study of nuclear spins, moments and changes of the mean square charge radii, they used two atomic transitions 459.4 nm and 462.7 nm, connecting the atomic ground state ($4f^7 6s^2\ {}^8S_{7/2}$) with two excited states ($4f^7 6s6p\ {}^8P_{9/2,7/2}$). These transitions have been studied with higher accuracy by Zaal et al. [26], why a calibration of the hfa exists for the stable isotopes.

The hfs of the ground state was not resolved in the measurements [20] why the a-constants of the excited states are used. Using the measured a-constants for the ${}^8P_{9/2,7/2}$ states from [20] and eqn.(3) it is possible to deduce the hfa, for most unstable isotopes using the -0.64(4)% value for the hfa between the stable isotopes as a calibration. The result is presented in table 5. As can be seen the errors are larger than the actual values except for ${}^{149}Eu$ making it difficult to draw any deeper conclusions. There seems to be an odd-even staggering which changes sign at the N=82 neutron shell closure, but the uncertainties are too large to be able to be sure about this. The drastic change in nuclear magnetic dipole moment between N=88 (A=151) and N=90 (A=153) due to the shape transition is also reflected in the hfa. For the odd isotopes Asaga et al. [27] have done a theoretical study and calculated the BW-effect, thus making it possible to calculate the hfa. Since they addressed the question of the empirical Moskowitz-Lombardi formula [28]

$$\epsilon_{BW} = \frac{\alpha}{\mu_I} \tag{9}$$

the hfa has also been calculated using this formula. The result is presented in table 6. The constant α has been taken to be 0.015 n.m. It should be noted that this value of α is close to the value of Hg [28] and close to the values obtained for Ir [29, 30]and Au[31], however, the sign is different.

Clearly the theoretical calculations by Asaga et al.[27] manage to reproduce the trend of the hfa, even if the values are too small. It is also interesting to note that the empirical M-L formula is still valid for Eu and not only for elements around Z=80 (Ir,Au,Hg). However the change in sign of α is still not explained, but might be due to the electronic factor as well as a nuclear factor, why this should be studied further. There also seems to exist an odd-even staggering of the hfa in Eu, similar to what was found in Au[31].

4.2. Indium

The hfs of the stable In isotopes were studied by Eck and Kusch [32] and Eck, Lurio and Kusch [33] in 1957 using ABMR. They studied the hfs of the ${}^2P_{1/2}$ and ${}^2P_{3/2}$ states, deducing the a and a,b and c hfi constants, respectively. In combination with the high precision measurements of the nuclear magnetic dipole moment by Rice and Pound [34], the hfa was deduced and studied in [33]. The hfs in unstable In isotopes was studied by Eberz et al. [35] by the means of collinear fast-beam laser spectroscopy. They used two atomic transitions $5p\ {}^2P_{1/2} - 6s\ {}^2S_{1/2}$ and $5p\ {}^2P_{3/2} - 6s\ {}^2S_{1/2}$ to determine the nuclear magnetic dipole moment and the electric quadrupole moment as well as the isotope shift for the studied isotopes.

Table 5: Magnetic moments and hfa for Eu isotopes

A	I	μ_I	${}^A\Delta^{151}(\%)$
142	1	1.536(19)	-0.14(1.18)
142m	8	2.978(11)	-0.08(31)
143	5/2	3.673(8)	-0.06(17)
144	1	1.893(13)	-0.19(48)
145	5/2	3.993(7)	-0.08(15)
146	4	1.425(11)	0.12(50)
147	5/2	3.724(8)	-0.12(17)
148	5	2.340(10)	0.08(31)
149	5/2	3.565(6)	-0.19(16)
150	5	2.708(11)	0.08(28)
151	5/2	3.4717(6)	0.00
153	5/2	1.5330(8)	-0.64(29)

Table 6: Magnetic moments and hfa for odd Eu isotopes

A	μ_I	${}^A\Delta^{151}_{exp}(\%)$	${}^A\Delta^{151}_{Th.}(\%)$[27]	${}^A\Delta^{151}_{ML}(\%)$
145	3.993	-0.08(15)	0.021	0.056
147	3.724	-0.12(17)	0.010	0.029
149	3.565	-0.19(16)	0.007	0.011
151	3.4717	0.00	0.000	0.000
153	1.5330	-0.64(29)	-0.127	-0.546

By using the obtained a-constants in [35] it is possible to deduce the hfa. However, the hfa is not the pure one-electron anomaly, since the states involved originates from different electron ($s_{1/2}, p_{1/2} and p_{3/2}$). Eck, Lurio and Kusch [33], who studied the hfa before in the $5p\ {}^2P_{1/2,3/2}$ states solved this problem by using the difference between the ${}^1\Delta^2_{3/2} -{}^1 \Delta^2_{1/2}$ instead. This makes it easier to analyse the data as it is not necessary to take the electronic interaction between the $p_{1/2}$ and $p_{3/2}$ electrons into account. This means that we will have a calibration to the stable ^{113,115}In isotopes, if we use the ${}^2P$ states in the analysis.

The result is given in table 7, together with the nuclear magnetic dipole moments. The hfa is normalised to ^{115}In. Comparing the results of the hfa from the table (-0.0031(3)%) with the value obtained by Eck, Lurio and Kusch [33] (-0.003132(40) %) we find that they are in agreement with each other. This shows the validity of the method. One finds from the table that in most cases, the errors are larger than the actual value of the hfa, but it is still possible to see some trends. The most interesting results are in the I=8 and I=9/2 isotopes(isomers), where a clear trend is visible. The hfa attains quite large values when the magnetic dipole moment is small, and decreases when the dipole moment increases, inducating once again that the hfa is proportional to $1/\mu_I$

In In there are some interesting effects which will be studied in detail. The question of universiality of the ML-formula is still open, but the indications, we have, show that there seems to be more to it, than the eye can see.

Table 7: Hyperfine anomaly in In

Mass	*Spin*	*Dipolemoment*	*Hyperfineanomaly*(%)
108	2	4.935	−0.29(36)
108	7	4.561	−0.55(34)
111	9/2	5.503	−0.60(49)
112	4	5.277	−0.45(41)
113	9/2	5.5289	−0.0031(3)
114	5	4.653	0(0.42)
115	1/2	−0.24398	0.20(37)
115	9/2	5.5408	0
116	5	4.235	0.78(32)
116	8	3.215	0.0137(42)
117	1/2	−0.25174	−0.006(12)
117	9/2	5.519	−0.20(24)
118	5	4.231	0.36(37)
118	8	3.321	0.95(30)
119	9/2	5.515	0.31(21)
120	8	3.692	0.3(2.2)
121	9/2	5.502	0.14(28)
122	5	4.318	0.17(60)
122	8	3.781	0.10(40)
123	9/2	5.491	0.03(22)
124	8	3.888	0.38(66)
125	9/2	5.502	0.02(46)

5 Conclusion

A new method of extracting hfa is presented. The method is based on precision measurements of the magnetic dipole hfi constants, and atomic calculations or careful analysis of the hfs can provide values of the hfa without precise measurements of the nuclear g_I factor. This would be very useful in determining the hfa for unstable isotopes which is of interest from nuclear-structure viewpoint. Still the method is limited by the accuracy in the measurements of the magnetic dipole hfi constants, but the trends can be extracted and will probably serve as a first step in understanding the BW-effect.

References

[1] A. Bohr and V.F. Weisskopf, Phys. Rev. **77**, (1950) 94

[2] S. Büttgenbach, Hyperfine Int. **20**, (1984) 1

[3] M.G.H. Gustavsson and A.-M. Martensson-Pendrill, Advances in Quantum Chemistry, **30**, (1998) 343

[4] T. Fujita and A. Arima, Nucl. Phys. **A254**, (1975) 513

[5] I. Lindgren and J. Morrison, *Atomic Many-Body Theory* (Springer-Verlag, Berlin 1983)

[6] P.G.H. Sandars and J. Beck, Proc. R. Soc. London **A289**, 97 (1965)

[7] J.R. Persson, in manuscript, (1999)

[8] E.R. Eliel, K.A.H van Leeuwen and W. Hogervorst, Phys. Rev. **A22**, 1491 (1980)

[9] Pfeufer, Z. Phys **D4**, 351 (1987)

[10] W.J. Childs and L.S. Goodman, Phys. Rev. **A6**, (1972) 1772

[11] W.J. Childs, Phys. Rev. **A44**, (1991) 760

[12] K.F. Smith and P.J. Unsworth, Proc. Phys. Soc. (London) **86**, 1249 (1965)

[13] P.J. Unsworth, J. Phys. **B2**, 122 (1969)

[14] W.J. Childs, Phys. Rev. **A39**, (1989) 4956

[15] Atomic Energy Levels, the Rare Earth Elements. Natl. Bur. Stand. Ref. Data Ser., Natl. Bur. Stand. (U.S.) Circ. No. 60, edited by W.C. Martin, R.Zalubas and L.Hagen (U.S. GPO, Washington, D.C., 1978)

[16] J.M. Baker, G.M. Copland and B.M. Wanklyn, Proc. J. Phys. **C2**, (1969) 862

[17] H. Schüler and T. Schmidt, Z. Phys. **94**, (1935) 457

[18] O. Becker, K. Enders, G. Werth and J. Dembczynski, Phys. Rev. **A48**, (1993) 3546

[19] L. Evans, P.G.H. Sandars and G.K. Woodgate, Proc. R. Soc. London Ser. A **289**, (1965) 114

[20] S.A. Ahmad, W. Klempt, C. Ekström, R. Neugart, K. Wendt and ISOLDE Collaboration, Z. Phys. **A321**, (1985) 35

[21] K. Dörschel, W. Heddrich, H. Hühnermann, E.W. Peau, H. Wagner, G.D. Alkhazov, E. Ye. Berlovich, V.P. Denison, V.N. Panteleev and A.G. Polyakov, Z. Phys. **317**, (1984) 233

[22] K. Enders, O. Becker, L. Brand, J. Dembczynski, G. Marx, G. Revalde, P.B. Rao and G. Werth, Phys. Rev. **A52**, (1995) 4434

[23] K. Enders, E. Stachowska, G. Marx, Ch. Zölch, U. George, J. Dembczynski, G. Werth and the ISOLDE Collaboration, Phys. Rev. **A56**, (1997) 265

[24] K. Enders, E. Stachowska, G. Marx, Ch. Zölch, G. Revalde, J. Dembczynski, G. Werth and the ISOLDE, Z. Phys. **D42**, (1997) 171

[25] J.R. Persson, Euro. Phys. J. **A2**, 3 (1998)

[26] G.J. Zaal, W. Hogervorst, E.R. Eliel, K.A.H van Leeuwen and J. Blok, Z. Phys. **A290**, (1979) 339

[27] T. Asaga, T. Fujita and K. Ito, Z. Phys.**A359**, (1997) 237

[28] P.A. Moskowitz and M. Lombardi, Phys. Lett. **46B**, (1973) 334

[29] S. Büttgenbach,R. Dicke, H. Gebauer, R. Kuhnen and F. Träber, Z. Phys.**A286**, (1978) 333

[30] P.A. Moskowitz, Phys. Lett. **118B**, (1982) 29

[31] C. Ekström, L. Robertsson, S. Ingelman, G. Wannberg and I Ragnarsson, Nucl. Phys. **A348**, (1980) 25

[32] T.G. Eck and P. Kusch, Phys. Rev. **106**, 958 (1957)

[33] T.G. Eck, A. Lurio and P. Kusch, Phys. Rev. **106**, 954 (1957)

[34] M. Rice and R.V. Pound, Phys. Rev. **106**, 953 (1957)

[35] J. Eberz, U. Dinger, G.Huber, H. Lochmann, R. Menges, R. Neugart, R. Kirchner, O. Klepper, T. Kühl, D. Marx, G. Ulm, K. Wendt and the ISOLDE Collaboration, Nucl. Phys. **A464**, (1987) 9

SECOND-ORDER CORRECTIONS TO THE HYPERFINE SPLITTING OF THE $4f^76s^2$ $^8S_{7/2}$ AND $4f^76s6p$ $^6P_{5/2}$ STATES FOR 151,153 AND 155 EUROPIUM ISOTOPES

E.STACHOWSKA, J.DEMBCZYNSKI, J.RUCZKOWSKI, B.ARCIMOWICZ

Faculty of Atomic Physics, Poznan University of Technology, Piotrowo 3, 60-965
Poznan, Poland

YU.P.GANGRSKY, D.KARAIVANOV, K.P.MARINOVA, B.N.MARKOV and
S.G.ZEMLYANOI

Flerov Laboratory of Nuclear Reactions, JINR, Dubna, Russia

Abstract. More accurate values of the hfs constants of the $4f^76s6p$ $^6P_{5/2}$ excited state of the EuI spectrum for the ^{151,153,155}Eu and of the $4f^76s^2$ $^8S_{7/2}$ ground state for ^{155}Eu are reported. They were obtained correcting the experimental values to the second-order perturbation theory. In the calculations the influence of a larger number of states than in our previous work has been taken into account. The nuclear moments of the ^{155}Eu recalculated after the second-order corrections are: $\mu(155) = 1.5203(53)$ n.m. and $Q(155) = 2.495(21)$ b. The importance of correcting the experimental results was demonstrated. The hyperfine anomalies obtained with the corrected values of the magnetic dipole constants are: $^{151}\Delta^{153} = 0.76(5)$ and $^{153}\Delta^{155} = 0.25(35)$.

1. Introduction

The high-accuracy and high-sensitivity laser spectroscopic methods are an important source of information about nuclear moments (spin I, magnetic dipole moment μ, electric quadrupole moment Q) and changes in mean squared nuclear radii, $\delta\langle r^2\rangle$, for extended chains of isotopes in ground and isomer states. These quantities offer access to the basic nuclear single-particle (I, μ, the hyperfine anomaly along a chain of isotopes) and collective (Q, $\delta\langle r^2\rangle$) properties.

Eu has a long chain of long-lived radioactive isotopes (from a few days to a few years). From a spectroscopic point of view this makes them candidates for systematic hyperfine structure (hfs) investigations over many isotopes. Of particular interest among them is the isotope ^{155}Eu which is known to be strongly deformed (see e.g. [1]). In our previous works [2,3] experimental values of magnetic-dipole A- and electric quadrupole B-constants of the lower $4f^76s^2$ $^8S_{7/2}$ and upper $4f^76s6p$ $^6P_{5/2}$ states in the optical line with $\lambda = 564{,}58$ nm for ^{155}Eu have been reported for the first time. After corrections for second-order hyperfine structure perturbation more precise values of the hfs constants of the excited state of the transition have been obtained and the nuclear moments of ^{155}Eu have been estimate. In addition information on the hyperfine anomaly between the neighbouring isotopes ^{151,153}Eu and ^{153,155}Eu has been extracted. The present paper deals with a recalculation of the hfs constants and hf anomaly which is based on: i) the experimentally obtained values of the hfs intervals and ii) an improved calculation of the second-order effect taking into account the influence of a larger number of atomic states.

2. Experimental results

The experimental setup and procedure are already described in [2,3]. The hfs structures of ^{151,153,155}Eu were measured in the transition between the ground $4f^76s^2$ $^6P_{5/2}$ and the excited $4f^76s6p$ $^6P_{5/2}$ levels of the optical spectrum of EuI. The experimental values of the hfs intervals of the $4f^76s6p$ $^6P_{5/2}$ state for all investigated isotopes and of the $4f^76s^2$ $^8S_{7/2}$ state for ^{155}Eu are listed in Tables 1 and 2. The errors quoted correspond to one standard deviation of the spread between different spectra. The systematic error due to the uncertainty of the free spectral range of the frequency calibration interferometer is negligible small. From these values the magnetic dipole, A_{exp}, and electric quadrupole, B_{exp}, constants (see Table 3) for both levels of the transition were evaluated in a least-squares fitting procedure using the well known two-parametric Casimir formula. The experimental method used in the present work does not meet the standard of the more precise double rf-laser spectroscopy [4] and in the case of small hfs gives relative bad accuracy. For this reason the hfs constants of the $4f^76s^2$ $^8S_{7/2}$ state for the stable ^{151}Eu and ^{153}Eu are present in Table 3 with the more precise values from [4].

3. Second-order corrections

From earlier investigations of the hfs of Eu isotopes [5-7] it is known that the mixing of electronic states with different J quantum numbers may play an important role and usually cannot be neglected in the interpretation of hfs measurements. To take this into account the "repulsion effect" among hfs sublevels with the same quantum number F belonging to different levels, has been calculated using second-order perturbation theory.

In order to correct the hfs constants for the J off-diagonal hfs perturbations we have used the procedure described in [5-7]. The $4f^76s6p$ $^6P_{5/2}$ level exhibits only a slight amount of configuration interaction. This simplified greatly our hfs calculations for this levels. As the shift of the $4f^76s6p$ $^6P_{5/2}$ sublevels is mainly determined by the "repulsion" of the neighboring $4f^76s6p$ $^6P_{3/2,7/2}$, ^{10,8}P$_{7/2,9/2}$ levels, in our previous work [2] the influence of these levels has been firstly taken into account. In the present work four other levels are added (see Table 4). The contribution of these level to the second-order perturbations, as we have established, is not negligible. The eigenvector compositions of all levels in Table 4 were also analyzed [8]. The procedure of the calculations is described in [2,5-7].

Table 1. Experimental, δW_{exp}, and corrected, δW_{corr}, values of the hfs intervals of the $4f^76s6p$ $^6P_{5/2}$-state and their experimental statistical errors for ^{151}Eu and ^{153}Eu. Here $\Delta W = W(F-1) - W(F)$

	^{151}Eu				^{153}Eu			
F	ΔW_{exp}, MHz	error, MHz	correction, MHz	ΔW_{corr}, MHz	ΔW_{exp}, MHz	error, MHz	correction, MHz	ΔW_{corr}, MHz
5	3172.35	0.89	-7.9320	3164.42	1869.21	0.55	-1.5476	1867.66
4	2346.36	0.52	-2.5695	2343.79	997.31	0.58	-0.9418	996.37
3	1648.57	0.68	0.7560	1649.33	458.35	0.80	-0.0129	458.34
2	1044.91	0.70	1.9570	1046.87	166.06	0.68	0.5329	166.59
1	509.19	1.85	1.4500	510.64	42.76	0.90	0,4748	43.23

Table 2. The same as in Table 1 for the excited and the ground states of the investigated transition for ^{155}Eu

$4f^76s6p$ $^6P_{5/2}$- state					$4f^76s^2$ $^8S_{7/2}$ -state			
F	ΔW_{exp}, MHz	error, MHz	correction, MHz	ΔW_{corr}, MHz	F	ΔW_{exp}, MHz	error, MHz	correction, MHz
5	1879.07	0.71	-1.5218	1877.55	6	53.61	0.21	0.000162
4	989.44	0.66	-0.9471	988.49	5	44.27	0.47	0.000172
3	443.26	0.87	-0.0210	443.24	4	33.89	0.99	0.000163
2	153.12	2.85	0.5312	153.65	3	27.33	2.18	0.000138
1	33.10	0.63	0.4764	33.58	2	17.00	1.84	0.000100

Table 3. The experimental and corrected values of the hfs constants for the lower and upper levels of the optical transition with $\lambda = 564.58$ nm

	A_{exp}, MHz	A_{corr}, MHz	B_{exp}, MHz	B_{corr}, MHz	Ref.
$4f^76s^2$ $^8S_{7/2}$					
^{151}Eu	-20.0523(2)		-0.7012(12)		[4]
^{153}Eu	-8.8532(2)		-1.7852(35)		[4]
^{155}Eu	-8.78(3)	-8.78	-1.861(20)	-1.881(39)	this work
$4f^76s6p$ $^6P_{5/2}$					
^{151}Eu	-591.92(9)	-591.22	-354.58(97)	-346.72	this work
^{153}Eu	-263.19(9)	-263.02	-922.07(79)	-920.65	this work
^{155}Eu	-261.68(11)	-261.50	-951.18(1.0)	-949.68	this work

The energy shifts $\delta W(F)$ of the hfs sublevels were first determined and used to correct the measured hfs intervals. These corrections and the corresponding corrected hyperfine spacings are presented in Tables 1 and 2. Then the hfs constants A_{corr} and B_{corr} (presented in Table 3) were calculated by fitting to the corrected hfs intervals. The uncertainties of the corrected and the experimental constants have been assumed to be the same and include only the experimental statistical errors. An analogous procedure was used to take into account the possible influence of different J-levels on the hfs of the ground EuI state - $4f^76s^2$ $^8S_{7/2}$. The levels perturbing the $4f^76s6p$ $^6P_{5/2}$ state and $4f^76s^2$ $^8S_{7/2}$ state are listed in Table 4, column 1 and 2, respectively. For the $^6P_{5/2}$ level they are the neighbouring levels belonging to $4f^76s6p$ configuration. For the ground state the levels $4f^76s^2$ ^{6}P, ^{6}D have been taken into account. They have not been observed until now and in our calculations the predicted energy values obtained from fine structure analysis have been used. An example of their contribution to the intervals between various F-sublevels is presented in Table 2 for the case of ^{155}Eu. As can be seen, the second-order corrections for the ground state are very small; they are even an order of magnitude lower than the experimental uncertainties of the data obtained by the high accuracy method of magnetic resonance in an atomic beam [4]. This has to be expected since the atomic level which can mix the electronic states via the hfs interaction, as can be seen from Table 4, lie at very large distances from the ground level. Thus, the values of the hfs constants of this level remain unchanged for ^{151}Eu and ^{153}Eu. The hfs constants A_{corr} and B_{corr} shown in Table 3 for the ground state of ^{155}Eu as described in [3] are an indirect result of the evaluating procedure used to obtain more correct value for these constants.

Table 4. Levels taken into account in the calculations of the second-order correction to the hyperfine splitting intervals of the excited $^6P_{5/2}$ (left column)) and the ground $^8S_{7/2}$ (right column) of the investigated optical transition with λ = 564,58 nm

term	J	energy	term	J	energy
$z^{10}P$	3.5	14067.86	$4f^76s^2$ ^{6}P	2.5	25863
	4.5	14563.57	$4f^76s^2$ ^{6}P	3.5	26449
z^8P	2.5	15890.53	$4f^76s^2$ ^{6}D	4.5	32431
	3.5	15952.31	$4f^76s^2$ ^{6}D	2.5	33213
	4.5	16611.79	$4f^76s^2$ ^{6}D	3.5	33214
z^6P	3.5	17340.65			
	2.5	17707.42			
	1.5	17945.49			
y^8P	2.5	21444.58			
	3.5	21605.17			
	4.5	21761.26			

4. Discussion

From the corrected values of the hfs constants obtained in the present work the nuclear moments of ^{155}Eu can be estimated using the known magnetic and electric quadrupole moments of ^{153}Eu: $\mu = 1.5330(8)$ n.m. and $Q_s = 2.412(21)$ b [9]. For the electric quadrupole moment of ^{155}Eu we obtain $Q_s(155) = 2.495(21)$ b which coincides in the limit of the errors with our old value [3].

The situation with the magnetic dipole moment is in general different and more complicated. As known [10], the ratio of the hf coupling constant A for two isotopes is not exactly equal to the ratio of their gyromagnetic factors $g_I = \mu/I$ as a result of the finite extension of the nucleus and the distribution of nuclear magnetization. The effect is expressed in the hf anomaly $^1\Delta^2$ between two isotopes 1 and 2 which is generally small, at most a few percent:

$$^1\Delta^2 = 1- \frac{A(1)}{A(2)} \cdot \frac{g_I(2)}{g_I(1)} \,. \tag{1}$$

Because $s_{1/2}$ and $p_{1/2}$ electrons are the only ones with non-zero densities near the nucleus, they are the only ones that will be affected by the finite nuclear size [10]. Therefore, one could expect that the $^1\Delta^2$ is nearly zero for the EuI $^8S_{7/2}$ ground state with its paired s-electrons. For the investigated Eu isotopes with equal spins, $I = 5/2$, equation (1) can be expressed in the form:

$$^1\Delta^2 = 1- \frac{A(1,{}^6P_{5/2})}{A(2,{}^6P_{5/2})} \cdot \frac{A(2,{}^8S_{7/2})}{A(1,{}^8S_{7/2})} \,. \tag{2}$$

Thus, we estimate the magnetic moment of ^{155}Eu from the ratio of the magnetic dipole coupling constants for the ground state (see Table 3): $\mu(155) = 1.5203(53)$ n.m. Our experimental results are in good agreement with the first estimation of $\mu(155)$ and $Q_s(155)$ [1], they are, however, more precise than the earlier ones. It must be noted that in the limits of our experimental precision the $\mu(155)$-value is not affected by the second-order effects while the Q-value increases about 0.3% after the corrections.

Table 5. Ratios of the magnetic dipole coupling constants (experimental and corrected) of the investigated levels for 151,153 and 155 europium isotopes and the hf anomaly of the excited state according to equation (2). $A(151)$ and $A(153)$ values for the ground state have been taken from [4]

	$^8S_{7/2}$-state	$^6P_{5/2}$-state	Δ, %
$A(151)/A(153)_{\mathrm{exp}}$	2.26498(8)	2.24902(84)	0.70(5)
$A(151)/A(153)_{\mathrm{corr}}$	2.26498(8)	2.24781(84)	0.76(5)
$A(153)/A(155)_{\mathrm{exp}}$	1.0083(35)	1.00577(55)	0.25(35)
$A(153)/A(155)_{\mathrm{corr}}$	1.0083(35)	1.00581(55)	0.25(35)

Table 5 shows the hf anomalies $^{151}\Delta^{153}$ and $^{153}\Delta^{155}$ of the excited state of the investigated transition relative to the ground state according to equation (2). It is seen that the hf anomaly in the $^6P_{5/2}$ level is relatively large for the isotope pair ^{151,153}Eu. This is in agreement with the experimental results of other authors (see,e.g.,[11]) but does not correspond to the recent theoretical predictions of [12]. As about the hf anomaly for the isotope pair ^{153,155}Eu, it is in the limits of the errors, because of the relatively large experimental uncertainties of the magnetic dipole constant for the ground state of ^{155}Eu.

The anomaly $^{151}\Delta^{153}$ is of about three times larger than the $^{153}\Delta^{155}$ which qualitatively can be ascribed to the strong change of the nuclear shape between ^{151}Eu and ^{153}Eu.

In conclusion we emphasize the main results of the present work:

- the values of the corrected hf splitting constants for both levels of the investigated optical transition for ^{155}Eu are reevaluated and the nuclear moments μ and Q are deduced;
- more accurate values of the hfs constants of the excited state for the stable ^{151}Eu and ^{153}Eu are obtained taking into account the second-order effects from 10 neighboring levels;
- it is shown that the influence of the second-order perturbation on the ground state splitting is negligible;
- a non vanishing hyperfine anomaly between ^{151}Eu and ^{153}Eu and a tendency for an existence of hf anomaly between ^{153}Eu and ^{155}Eu is established.

Acknowledgement. The authors would like to thank the Alexander von Humboldt Foundation for providing financial support.

References

1. K. Doerschel, W.Heiddrich et al. : Z.Phys. **A317** (1984) 233
2. Yu. P. Gangrsky, D.V.Karaivanov et al. Acta Phys.Polonica **B30** (1999) 1415
3. Yu. P. Gangrsky, D.V.Karaivanov et al.: Eur.J.Phys. D (submitted)
4. P.G.H.Sandars, G.K.Woodgate, G.K.: Proc.R.Soc.London Ser. **A257** (1960) 269
5. O.Becker, K.Enders, et al.: Phys.Rev. **A48** (1993) 3546
6. K.Enders, O.Becker, L.Brand. et al.: Phys.Rev. **A52** (1995) 4434
7. K.Enders, E. Stachowska, G.Marx et al.: Z.Phys. **D42** (1997) 171
8. J.Dembczynski et al.: in preparation
9. Lederer, C.M., Shirley, V.S.: Tables of Isotopes (Wiley, New York,1978), 7th edn.
10. Buettgenbach, S.: Hyp.Interaction: **20** (1984) 1
11. Eliel, E.R., Van Leeuven K.A.H., Hogervorst, W.: Phys.Rev. **A22** (1980) 1491
12. Asaga, T., Fujita, T., Iti, K.: Z.Phys. **A359** (1997) 237

New energy levels in praseodymium

B. Furmann
Chair of Atomic Physics, Poznan University of Technology
Piotrowo 3, 60-965 Poznan, Poland

Abstract

A method of the identification of electronic levels based on the analysis of the hyperfine structure of spectral lines is described. After recording of the hyperfine structure of an unclassified spectral line with the method of the laser induced fluorescence in a hollow cathode discharge, the hyperfine structure constants have been evaluated, and compared to the values for the well-known or theoretically predicted levels. The results for the neutral and the singly ionised praseodymium are presented.

Introduction

The interaction between the nuclear spin and the electronic shells, the effect of which is the hyperfine structure of the spectral lines, has been used for many years in the studies of the properties of atomic nuclei. The analysis of the hyperfine splittings can, however, also be a convenient tool for identification of the electronic levels involved in unclassified spectral lines. The system of the hyperfine structure sublevels is a specific "fingerprint" characterising in a univocal manner an energy- level. The method of identification of the electronic levels on the ground of the analysis of the hyperfine structure is very convenient and in many cases irreplaceable in the case of the complex spectra of the rare earth elements. In the present work this method has been used for the spectrum of neutral and singly ionised praseodymium. The density of the spectrum (up to several lines per 1 cm^{-1}) makes the identification of the levels exclusively on the basis on the Ritz rule impossible. Also the method of identification based on the analysis of Zeeman effect or the analysis of the hyperfine structure, recorded with the use of high resolution spectral instruments proved very deceptive [1]. In this situation a method of recording the hyperfine structure is indispensable, which makes possible:

1. Separation between the lines occuring in the same spectral region,
2. Precise measurement of the hyperfine splitting.

The above conditions can be realised by the method of the laser induced fluorescence in a hollow cathode discharge.

Experimental setup

A scheme of the experimental setup is presented in fig.1. Source of praseodymium atoms and ions was a discharge in the hollow cathode. The wavelength of the laser was initially "tuned" to the wavelength of the investigated spectral line (with the use of the Lyot filter). Then the wavelength was tuned very precisely (with the use of the laser stabilisation system) over the range covering the hyperfine structure of the line.

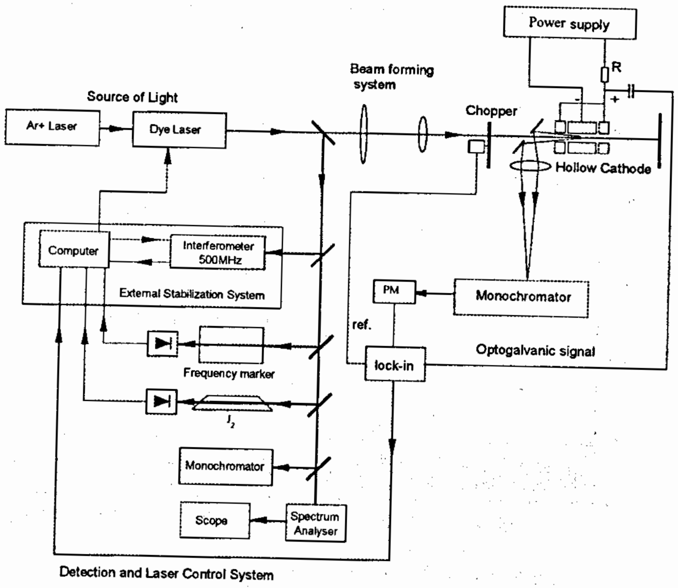

Fig.1. Experimental setup for registration of the hyperfine spectra of praseodymium by the method of laser induced fluorescence.(LIF)

When the wavelength attained the values corresponding to the transitions between hyperfine structure sublevels, absorption of the light assumed the resonance character. An increase of population of the upper level caused the respective increase of the intensity of the fluorescence. The above effect has been observed using intensity modulation of the laser light and testing, with the use of a lock-in amplifier, which of the emission spectral lines (selected by a monochromator) are modulated as a result, and then recording the variation of the fluorescence intensity at those lines. If the recorded hyperfine structure was identical at all the fluorescent lines, then those lines certainly involved the same upper level (i.e. followed the same absorption transition). In the other case individual fluorescence lines have been assigned - on the ground of the hyperfine structure analysis - to different absorption lines overlapping in the wavelength range covered by the laser light.

After the calculation (on the basis of the recorded spectra) of the A and B hyperfine structure constants and J quantum numbers of the upper and the lower level, the obtained values have been compared to the values for the well-known or theoretically predicted levels in praseodymium. If more than one possible level could be found within the experimental error, the measured fluorescence wavelengths, which should correspond to real transitions with participation of the found upper level, have been used for final identification. An examplary recorded spectrum of the hyperfine structure is presented in fig.2.

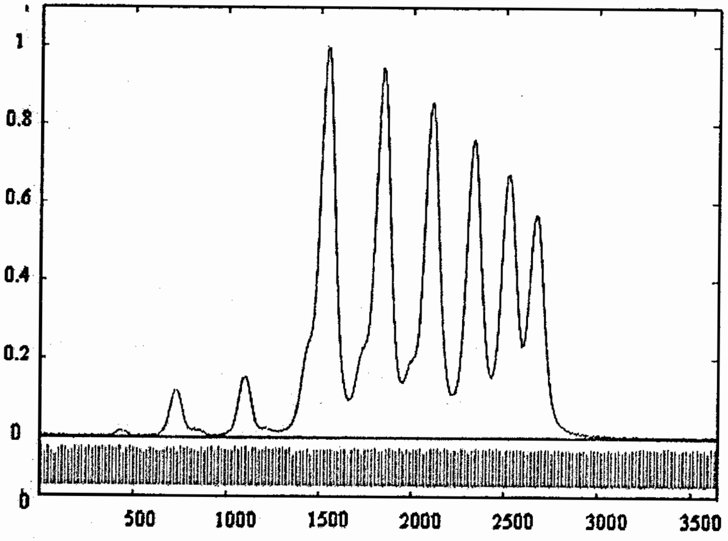

Fig.2. Hyperfine structure of the line in praseodymium recorded using the method of the laser induced fluorescence in a hollow cathode discharge

Experiment and results

In the first stage of investigations, the measurements of the hyperfine structure constants for some known electronic levels in singly ionised praseodymium have been performed. Those measurements were indispensable, since while in neutral praseodymium constants A and B for most of the levels were measured before, in some cases with the use of the resonance methods [2],[5]; in the case of praseodymium ion the previously measured constants showed too large experimental errors [1].

The main part of investigations was devoted to the identification of the levels. At first no special selection of the lines was applied and the hyperfine structure of all the unclassified lines in accessible spectral range was measured. After any new level was found with this method, other spectral lines involving this level were sought. In fig.3. a system of spectral lines involving the level E=28552.63 cm^{-1}, examined in this way, is presented as an example. With the above method a series of new levels in neutral praseodymium was found, however, those were mainly high-lying levels. Theoretical interpretation of the hyperfine structures constants of these levels was very difficult because of the strong configuration interaction in this region. Therefore in the next stage the effort was concentrated on the search for the theoretically predicted levels in PrI and PrII.

On the basis of theoretical expectations a computer simulation of the hyperfine structure of the line involving the levels under study; then, tuning the laser with the use of the Lyot filter, the predicted transition was sought and its hyperfine structure was recorded. An exemplary system of the lines involving the level E=10769.44 cm^{-1}, found in this way, is presented in fig.4. This method of searching for new levels proved effective in the cases of the levels, for which the error of the theoretical predictions did not exceeded 50cm^{-1} [4].

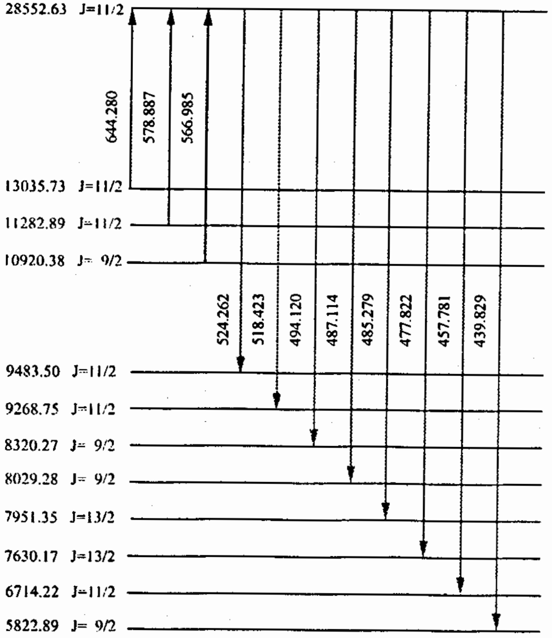

Fig.3. System of the levels and transitions obtained as the result of the identification of the new level E=28552.63 cm^{-1} in neutral praseodymium.

Conclusions

The identification of the energy levels based on the analysis of the hyperfine structure of the line recorded with the method of the laser induced fluorescence in a hollow cathode discharge led to the discovery of tens of new levels in praseodymium, from which more than ten were confirmed through the analysis of more than one line with their participation. In spite of certain difficulties, which occured when investigated transition connected two (lower and upper) new levels, the method should be regarded as very effective, though requiring a relatively complex experimental setup (altogether four ring dye lasers were used in order to cover a sufficiently broad spectral range).

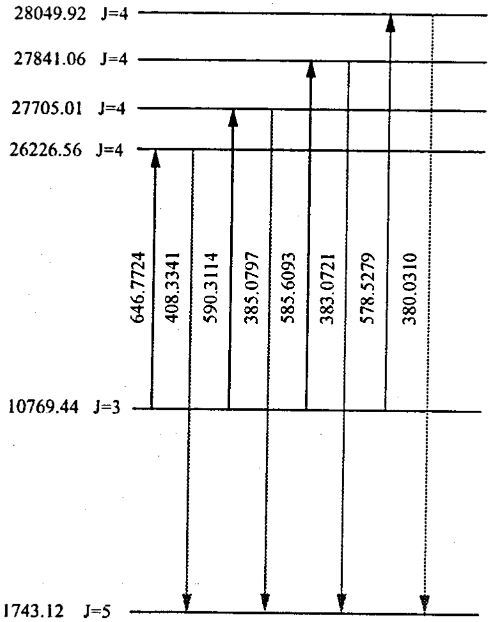

Fig.4. System of the levels and transitions obtained as the results of the identification of the new levels E=10769.44 cm^{-1} in singly ionised praseodymium.

References

[1] A.Ginibre, Physica Scripta 39, 1989,694-709

[2] A.Krzykowski, B.Furmann, D.Stefańska, A.Jarosz, A.Kajoch, Optics Comm. 140, 1997, 216-219

[3] W.F.Meggers, C.H.Corliss, B.F.Scribner, Table of spectra Line Intensities, Part I, Monograph 145, U.S.G.P.O. (National Bureau Standards, Washington, DC, 1975)

[4] J.Ruczkowski, B.Furmann, E.Stachowska, J.Dembczyński, "Hyperfine structure of odd configurations in praseodymium"- in preparation

[5] Childs W.J., Goodman L..S., Phys Rev. A24 1342 (1981).

HYPERFINE SPLITTING IN THE ATOMIC D$_2$ LINE AND THE QUADRUPOLE MOMENT OF ^{22}Na

Yu.P.Gangrsky, D.V.Karaivanov, K.P.Marinova, B.N.Markov,
L.M.Melnikova, G.V.Mishinsky, S.G.Zemlyanoi, V.I.Zhemenik

Flerov Laboratory of Nuclear Reactions, JINR, Dubna, Russia

Abstract. The hyperfine structure of the D$_2$ optical line in ^{22}Na has been investigated using high resolution laser spectroscopy of a well-collimated atomic beam. The hyperfine splitting constants A and B for the excited $3p\ ^2P_{3/2}$ level have been obtained. They are as follows: $A(22) = 7.31(4)$ MHz, and $B(22) = 4.71(28)$ MHz. With this data, using the high precision multiconfiguration Hartree-Fock calculations for the electric field gradient at the nucleus, the electric quadrupole moment of ^{22}Na has been deduced: $Q_s(22) = +\,0.185(11)$ b. The sign of $Q_s(22)$, determined for the first time, indicates a prolate nuclear deformation.

1. Introduction

In earlier systematic laser specroscopy study [1,2] of the nuclear properties over a long sodium isotope chain $^{21\text{-}31}$Na there is a lack of information about the electric quadrupole constant B, and respectively, about the nuclear quadrupole moments. Recently preliminary results on the absolute values of the quadrupole moments of some neutron–rich sodium isotopes ($^{26\text{-}31}$Na) and for the neutron-deficient ^{20}Na have been reported. They were obtained by β-radiation detected NMR [3,4]. Data on the electric quadrupole moment of the long-lived ^{22}Na, obtained by off-line laser specroscopy, have been published for the first time in our previous work [5].

The present talk is devoted to our precise study of the hf structure of ^{22}Na at the D$_2$ line which got us the chance:

i) to obtain high accuracy values of magnetic dipole, $A(22)$, and electric quadrupole, $B(22)$, coupling constants of the excited $3p\ ^2P_{3/2}$ state;
ii) to extract a reliable value of the electric quadrupole moment $Q_s(22)$ and thus to extend our knowledge on the nuclear deformation in the region of light deformed nuclei.

2. Experimental results

An off-line experimental method has been used, based on the detection of the laser-excited fluorescence in a well-collimated atomic beam. The experimental setup has been described in detail previously [5]. ^{22}Na ($T_{1/2} = 2.602$ years) was produced by the reaction ^{19}F(α,n) in a target of AlF$_3$. The sodium atoms were extracted from the target in the form of NaCl. NaCl water solution containing $2\cdot10^{13}$ atoms of ^{22}Na was dried on a tantalum foil. The heating of the sample in a Ta crucible to a temperature of about 600 – 700 °C resulted in thermal dissociation of the chloride and provided a stable atomic beam of ^{22}Na for about an hour. Care has been taken to minimize the abundance of the stable ^{23}Na by annealing the tantalum foil and crucible in a vacuum at $T \approx 1800$ °C for a several hours. Due to contamination of the target and of the used chemical reagents with the stable sodium isotope, the final ratio of ^{23}Na to ^{22}Na in the sample was about 150:1. In order to perform reliable measurements with the low abundant radioactive ^{22}Na great care has been taken to find an acceptable compromise between resolution and sensitivity. Numerous tests of the apparatus have been done with samples containing only the stable ^{23}Na in quantities down to 10^{13} atoms. In this way all the experimental conditions were optimized. In particular, an experimental FWHM of the detected resonance lines of about 20 - 23 MHz was established by reasonably limiting the residual Doppler broadening.

The large difference in the hf splittings of the lower and upper levels of the investigated D_2 sodium transition results in a typical flag-pattern spectrum: two narrow triplet groups defined by the small hf splitting of the excited $3p\ ^2P_{3/2}$ state are quite spaced because of the large splitting (1220 MHz) of the $3s\ ^2S_{1/2}$ ground state. In our measurements of the ^{22}Na hf splitting each group was recorded separately. Two samples of ^{22}Na were used, one for each hf splitting group, and for each of them more as 10 spectra were recorded with a sufficiently good signal to noise ratio.

The experimental values of the hfs intervals of the $3p\ ^2P_{3/2}$ state are listed in Tables 1. The errors quoted correspond to one standard deviation of the spread between different spectra. The systematic error due to the uncertainty of the free spectral range of the frequency calibration interferometer is negligible small. From these values the magnetic dipole, A, and electric quadrupole, B, constants of the $3p\ ^2P_{3/2}$ were evaluated in a least-squares fitting procedure using the well known two-parametric Casimir formula. They are:

$$A(22) = 7.31(4) \text{ MHz} \quad \text{and} \quad B(22) = 4.71(28) \text{ MHz}. \tag{1}$$

Table 1. Experimental, ΔW_{exp}, and calculated, ΔW_{cal}, values of the energy separation between the excited state hyperfine levels F and $F\text{-}1$ for ^{22}Na in D_2 line. Here $\delta = \Delta W_{\text{cal}} - \Delta W_{\text{exp}}$.

F	ΔW_{exp}, MHz	ΔW_{cal}, MHz	δ, MHz
4.5	36.62(35)	36.44	-0.18
3.5	23.79(19)	23.95	0.16
2.5	15.07(30)	14.75	-0.32

3. Quadrupole moment of ^{22}Na

The ^{22}Na isotope belongs to the region of well-deformed light nuclei. A large quadrupole deformation in this region has been deduced from the large matrix elements of the E2-intraband transitions [6]. The value of the hf constant B deduced in the present work offers an alternative and model-independent way to obtain an additional information about the nuclear deformation.

A review of the present status of our knowledge on quadrupole moments Q (see e.g. [7]) shows that the many Q moments of radioactive nuclei have been determined by optical methods as these methods are very sensitive and fast. The value for Q can be derived from the B factors of the hf splitting and electric field gradient d^2V/dz^2 at the nucleus :

$$Q = -B/(d^2V/dz^2)\,. \tag{2}$$

Recently d^2V/dz^2 for ^{23}Na was obtained from high-quality *ab initio* calculations of atomic (or molecular) system without any correction factors (see [8] and the references therein). These seem to be the most reliable calculations for the electric field gradient of ^{23}Na. Under the assumption that the electric field gradient at the nucleus is almost independent of the isotope, with d^2V/dz^2 from [8] and $B(22,\ ^2P_{3/2})$ from eq. (1),one obtains:

$$Q_s(22) = 0.0393(3)\cdot B(22,\ ^2P_{3/2}) = 0.185(11) \text{ b}. \tag{3}$$

The sign of $Q_s(22)$, determined for the first time, indicates a prolate nuclear deformation. An evaluation of the deformation parameter beta can be derived from the intrinsic quadrupole moment Q_0 which is related to the spectroscopic quadrupole moment Q_s via the well-known projection formula

$$Q_s = Q_0[I(2I-1)/(I+1)(2I+3)]. \tag{4}$$

For ^{22}Na with $I = 3$ the intrinsic quadrupole moment is $Q_0 = +0.444(26)$ b and hence $\beta_2 = 0.439(26)$. From the literature a value for the intrinsic quadrupole moment of ^{22}Na is known: $Q_0 = 0.50(1)$ b [6,9]. It is deduced from measurements of the rotational level lifetimes. The larger $Q_0(22)$ value can be due to the following reasons: i) our quadrupole moment takes into account only static deformation, while the results of [6,9] are also sensitive to zero point vibrations; ii) [6,9] contain a model dependence in the basic assumption about the nuclear shape assumed as rotational ellipsoid (as a matter of fact all Q_0 values and in particular formula (4) are model dependent as well); iii) in evaluating of the quadrupole moment the admixture of bands has been neglected in [6]. Having all this in mind, one could say that Q_0 value deduced in the present work is in a reasonable agreement with the results of [6].

Shell-model calculations show a remarkably close agreement with the experiment predicting a relatively large quadrupole deformation of ^{22}Na: the theoretical Q_0 values lie between those of [6] and of the present work. The collective effects which are described macroscopically by a deformation of the nucleus, are reproduced in the shell-model calculations by the coherent effect of the six valence nucleons - 3 protons and 3 neutrons.

The experimental results for the absolute values of β_2 in the Na region are given in Fig.1. These are: i) our β_2 values for ^{22}Na and ^{23}Na [5] and ii) the values estimated from the preliminary data [3,4] for ^{20}Na and $^{26\text{-}30}$Na which are more precise than the old results of Ref. [10]. For comparison Fig.1 shows also the N-dependence of the deformation parameter $|\beta_2|$ for the neighbouring nuclei $_{10}$Ne and $_{12}$Mg: for even-even isotopes they are deduced from $B(E2)$ measurements [12], for the odd-even - using the rotational level lifetimes given in [11]. It is seen, that $\beta_2(22)$ follows very well the general trend of $|\beta_2|$ versus N dependence for the investigated sodium isotopes.

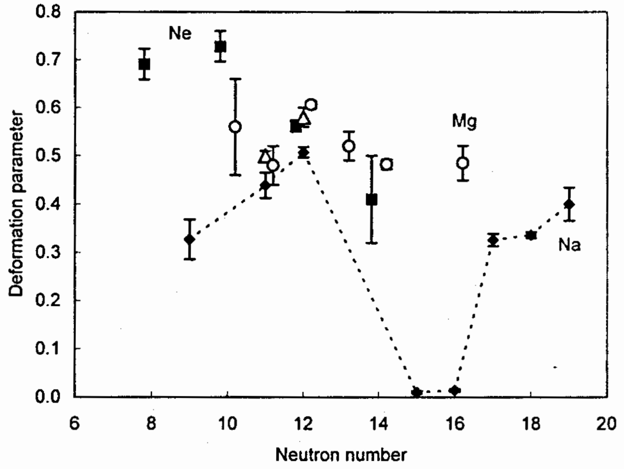

Fig. 1 Experimental deformation parameter $|\beta_2|$ of $_{11}$Na connected with dotted line to guide the eye. The gray triangles represent the nonoptical values of $|\beta_2|$ from [6] and [11] respectively. The $|\beta_2|$-values of the neighbouring $_{10}$Ne and $_{12}$Mg [11,12] isotopes are also presented for comparison.

References

1. G. Huber, C. Thibault, R.Klapisch et al.: Phys.Rev.Lett **34**, 1209 (1975)
2. G. Huber, F.Touchard, S. Büttgenbach et al.: Phys.Rev. **C18**, 2342 (1978)
3. W.Geithner, S.Kapperz, G.Katko et al.: Preprint CERN/ISC 97-29 (1997)
4. R.Neugart (private communication, 1999)
5. Yu.P.Gangrsky, D.V.Karaivanov, K.P.Marinova et al.: E.J.Phys. **A3**, 313 (1998)
6. R.M.Freeman, F.Haas, B.Heusch et al.: Phys.Rev. **C8**, 2182 (1973)
7. E.W.Otten: in: Treatise on heavy ion science (ed. D.A.Bromley) Plenum Press. **8**, 517 (1989)
8. D.Sundholm, J.Olsen: Phys.Rev.Lett. **68**, 927 (1992)
9. F.Haas, R.M. Freeman, J.F. Castillo, A. Gallmann: Phys.Rev. **C8**, 2169 (1973)
10. F.Touchard, J.M.Serre, S. Büttgenbach et al.: Phys.Rev. **C25**, 2756 (1982)
11. P.M.Endt: Nucl.Phys. **A521**, 1 (1990)
12. S.Raman, C.H.Malarkey et al.: At.Data Nucl.Data Tables **36**, 1 (1987)

HIGH RESOLUTION LASER SPECTROMETER

A. Kopystyńska

Institute of Experimental Physics, Faculty of Physics, Warsaw University, Poland

S. Chojnacki, T.T. Inamura[1], M. Kisieliński, M. Kowalczyk, E. Kulczycka, E. Wesołowski and S.G. Zemlyanoi[2]

Heavy Ion Laboratory, Warsaw University, Poland

Abstract

A high resolution laser spectrometer consists of a laser system, an atomic beam apparatus and a data acquisition system. At present the achieved spectral resolution is about 20 MHz.

1. Introduction

The high resolution laser spectrometer will be used to perform a systematic study of hyperfine structures and isotope shifts of stable and radioactive isotopes. From the hyperfine structure one can obtain nuclear spins I and moments (μ, Q, etc.) independently of the nuclear model; and similarly from the isotope shift, the differences in the mean square charge radii between two isotopes $\delta\langle r^2\rangle$. The experimental technique applied to this study is the laser-induced fluorescence of free atoms formed in an atomic beam.

2. Laser system

The laser system consists of a c.w. ring dye laser pumped with an argon ion laser. To study sodium the dye laser works with Rhodamine 6G. In a single mode operation the output power of the dye laser is about 400 mW and the linewidth is about 0.5 MHz. Intensity of the laser beam inter-

---

[1] RIKEN and JST, Japan.

[2] JINR, Flerov Laboratory of Nuclear Reactions, Dubna, Russia.

acting with atoms is attenuated by means of density filters to less than 1 mW. Laser light frequency is electronically tuned to the resonance and scanned through the hyperfine components of the atomic transitions of interest.

3. Atomic beam apparatus

The atomic beam is produced in an oven (Fig.1a), where a crucible containing the sample is placed. The crucible is heated by thermoelectron bombardment. The thermoelectrons are emitted from a wire and accelerated by 0.5 – 1 kV potential difference between the wire and the crucible. Thanks to the high-tension system the wire current intensity could be reduced to less than 100 A. As shown in Fig.1b an adjustable X – Y slit (4) defines the atomic beam divergence; the spherical mirror and two glass lenses collect fluorescence photons onto the entrance hole of a diaphragm placed in front of the photomultiplier.

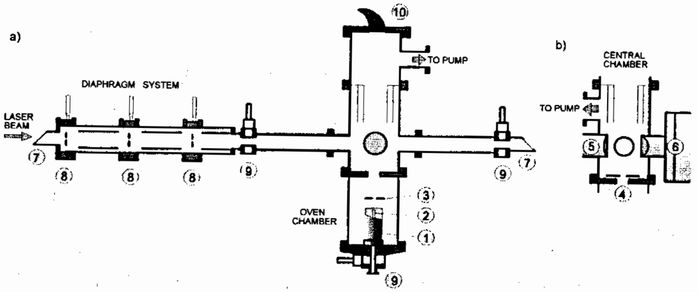

1. Oven housing, 2. Crucible, 3. Graphite diaphragm, 4. Adjustable slit, 5. Spherical mirror, 6. Photomultiplier, 7. Brewster window, 8. Diaphragm set-up (see Fig.2), 9. Valve, 10. Wood's horn

Fig.1. (a) Atomic beam apparatus cut in the plane of laser and atomic beams; (b) cut in the plane perpendicular to it.

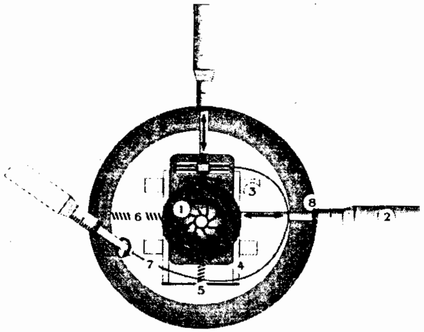

1. Iris diaphragm
2. Micrometer screw
3. Horizontal guide bars
4. Vertical guide bars
5. 6. Springs
7. String
8. Seals

Fig.2. Diaphragm set-up. Micrometer screws allow changing the position and diameter of the iris diaphragm under the vacuum.

Adding the diaphragm system (Figs. 1a and 2) completed the atomic beam apparatus, reducing the background significantly. The signal to noise ratio was improved by an order of magnitude compared with the previous measurements.

4. Data acquisition system

The data acquisition system consists of a photomultiplier EMI 9558A operating in a single-photon counting mode, a fast amplifier – discriminator and IBM PC compatible computer with a program simulating multichannel analyser.

5. Results

In order to determine the spectral resolution of the whole apparatus the hyperfine structure of the transition $3^2P_{3/2} \rightarrow 3^2S_{1/2}$ in ^{23}Na was measured. An excitation spectrum (Fig.3) was obtained by scanning the laser frequency in the adjustable range of about 3 GHz. An enlarged part of the spectrum corresponding to transitions between excited F' = 1, 2, 3 and ground F = 2 hyperfine states is shown in Fig.4 and to transitions between F' = 0, 1, 2 and F = 1 is shown in Fig.5. The experimental data are represented by dotted lines and solid curves are the results of fitting with purely Lorentzian shape components (dashed lines). The obtained hyperfine constants A and B for the $3^2P_{3/2}$ state are listed in Table 1 and compared to the recent measurements [2-4]. The spectral resolution achieved with our apparatus is about 20 MHz at present and can be still improved.

Table 1. Hyperfine constants A and B for the $3^2P_{3/2}$ state in ^{23}Na.

State	A (MHz)	B (MHz)	Reference
$3^2P_{3/2}$	18,61 ± 0,27	2,22 ± 0,50	This work
	18,62 ± 0,21	2,11 ± 0,21	[2]
	18,572 ± 0,024	2,723 ± 0,055	[3]
	18,534 ± 0,015	2,724 ± 0,030	[4]

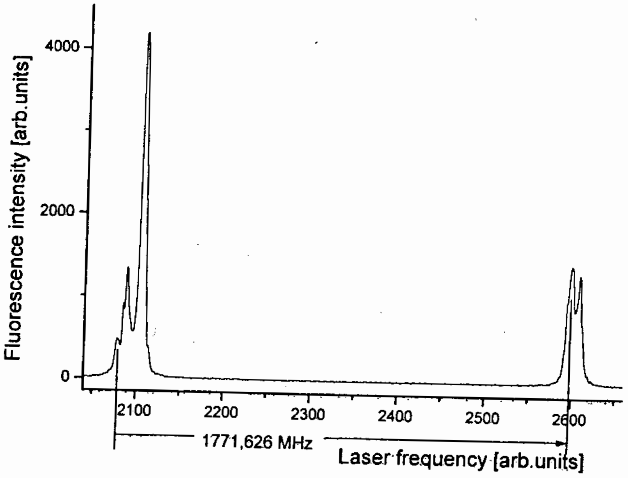

Fig.3. Hyperfine components of the $3^2P_{3/2} \rightarrow 3^2S_{1/2}$ transition in ^{23}Na. The hyperfine splitting of the ground state is taken from Ref. [1].

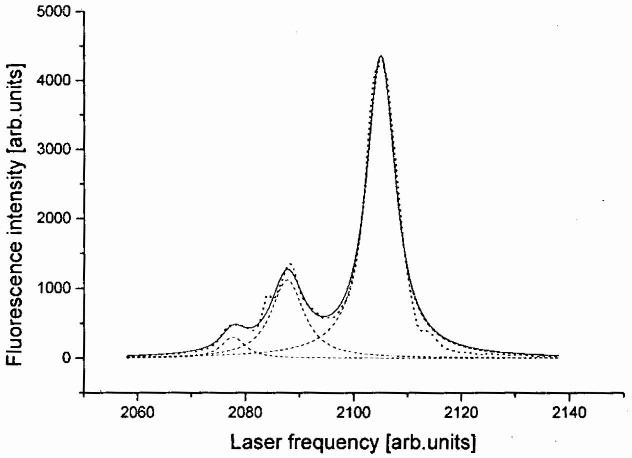

Fig.4. Enlarged part of the laser excited fluorescence spectrum corresponding to the F' = 1, 2, 3 → F = 2 transition.

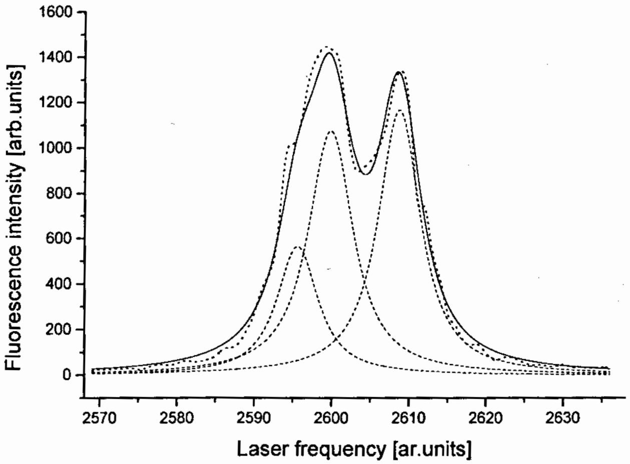

Fig.5. Enlarged part of the laser excited spectrum corresponding to the F' = 0, 1, 2 → F = 1 transition.

Acknowledgement

We would like to express our thanks to the technical staff of the HIL for their constant help. We are also grateful to Mr Dariusz Fabianowicz for his care of our laser system.

References

1. A.T. Ramsey, L.W. Anderson, J.Chem.Phys. **43**,191(1965).
2. W.A. van Wijngaarden, J.Li, Z.Phys. **D32**,67(1994).
3. Yu.P. Gangrsky, D.V. Karainov, K.P. Marinova, B.N. Markov, L.M. Melnikova, G.V. Mishinsky, S.G. Zemlyanoi, V.I. Zhemenik, Eur.Phys.J. **A3**,313(1998).
4. Wo Yei, A. Sieradzan, M.D. Havey, Phys.Rev. **A48**,1909(1993).

Nuclear Moments Measurements with Polarized Radioactive Nuclear Beams

K. Asahi, H. Ogawa, K. Sakai, A. Yoshimi, M. Tsuda, Y. Uchiyama,
T. Suzuki, K. Suzuki, N. Kurokawa, and M. Adachi
Department of Physics, Tokyo Institute of Technology
Oh-okayama 2-12-1, Meguro-ku, Tokyo 152-8551, Japan

A. Yoshida, S. Fukuda, M. Notani, T. Kubo, H. Okuno, H. Sato, and N. Fukunishi
Institute of Physical and Chemical Research (RIKEN)
Hirosawa 2-1, Wako-shi, Saitama 351-0198, Japan

N. Aoi, K. Yoneda, H. Iwasaki, N. Fukuda, and M. Ishihara
Department of Physics, The University of Tokyo
Hongo 7-3-1, Bunkyo-ku, Tokyo 113-0033, Japan

H. Izumi, H. Ueno, T. Shimoda, S. Tanimoto, and N. Takahashi
Department of Physics, Osaka University
Machikaneyama-cho, Toyonaka, Osaka 560-0043, Japan

H. Miyatake
Tanashi Brance, High Energy Accelerator Research Organization (KEK)
Midori-cho 3-2-1, Tanashi, Tokyo 188-8501, Japan

W.-D. Schmidt-Ott and M. Schaefer
Zweites Physikalisches Institut, Der Universitaet Goettingen
Bunsenstrasse 7-9, D-3400 Goettingen, Germany

The magnetic moments and the electric quadrupole moments were measured for several neutron-rich nuclei, by means of spin-polarized radioactive nuclear beams from the projectile fragmentation reaction at the intermediate energies. The results obtained, through the comparison with the standard shell model calculations, reveal intriguing anomalies which are considered to be characteristic of neutron-rich nuclei: The experimental magnetic moments obtained show remarkable deviations from calculations suggesting that the pairing energy in the effective two-body interactions between neutrons is much reduced in such neutron-rich nuclei. More drastically, the quadrupole moment results clearly show that the neutron effective charge is quenched as much as by 80 % in the neutron-rich B isotopes. The most recent result, that is for ^{18}N, indicates that the quenching develops gradually as N/Z increases.

1. Introduction

The projectile fragmentation reaction may be described in a simple-minded picture as a process in which a few nucleons are removed from a projectile nucleus when it collides with a target, with the remaining portion of the projectile keeping its original motion[1]. The resultant outgoing nucleus, called a projectile fragment, should show the linear momentum distribution which peaks at the velocity of the projectile with

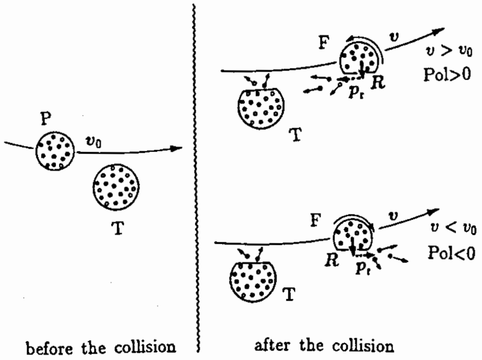

Figure 1: Predicted correlation between the fragment spin and linear momentum in a model of projectile fragmentation. A projectile P incident at a velocity v_0 is transmuted to a fragment F through removal of nucleons at the position $\boldsymbol{R}$. See text for further explanation.

a finite width given by the Fermi motion of nucleons in the projectile. Such a picture in fact explains rather well the observed fragment momentum distribution in the projectile fragmentation reaction at high and intermediate energies. Let us now apply the same consideration to the angular momentum of the fragment. Interestingly, we then are led to a prediction that the fragments are spin polarized provided they are selected in the outgoing momentum, as depicted in Fig. 1. The first experiment to test this idea was made at RIKEN[2], in which the existence of a substantial polarization was clearly proven true for ^{12}B fragments produced in the fragmentation of ^{14}N projectiles on a Au target at $E/A = 40$ MeV/u.The succeeding experiments with other fragments, projectiles, target, and incident energies have indicated that the polarization of the fragment spin is a rather general phenomenon common to this type of reaction[3–5].

We then started to take advantage of this finding as a method to produce spin polarized radioactive nuclear beams from the projectile fragmentation reaction. Using the polarized radioactive nuclear beams thus obtained, a series of experiments have been conducted: The magnetic moments μ of neutron-rich nuclei ^{14}B, ^{15}B, ^{17}B, ^{17}N, ^{18}N, ^{21}F have been measured using this method.[6–8] The electric qudrupole moments Q were measured for ^{14}B, ^{15}B,[9] and ^{18}N.[8] Isotopes on the proton-rich side have been studied by the Osaka-RIKEN-LBL group: They have determined μ moments for ^{9}C and ^{13}O, and the Q moments for ^{13}O.[10,11]

Below in this report we first outline the experimental procedures followed in the nuclear moments measurements with polarized radioactive nuclear beams, by taking a case of the most recent experiment on ^{18}N as an example. Then the experimental results obatined are presented, and the physical implications extracted from them

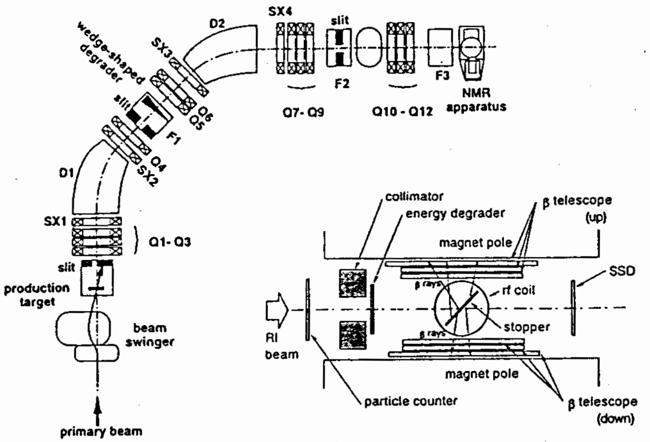

Figure 2: Typical arrangement for the nuclear moment experiment using a spin-polarized radioactive beam. The beam swinger, production target and fragment separator RIPS are indicated in a plan view, and the β-detected NMR setup installed at the collection point is detailed on the lower-right corner.

are discussed. Finally a comment is made on the discrepancy found between our results and the results from Leuven group for the magnetic moment and electric quadrupole moment of the ^{18}N ground state.

2. Experiment

The typical arrangement used in the nuclear moments measurements with polarized radioactive nuclear beams at RIKEN is shown in Fig. 2. A primary beam of energies around $E/A = 100$ MeV/u from the Ring Cyclotron is introduced into a target chamber through a beam swinger, so that fragments emitted from the target at finite angles are accepted by the fragment separator RIPS.[12] Fragments of the objective nuclide are isotope-separated and momentum-analyzed in RIPS, and finally focused on a collection point F3, at which a stopping material and a device for the β-detected NMR experiments are located. The polarization of fragments in the direction perpendicular to the reaction plane (referred to as the z-direction below) is preserved during the transportation through RIPS to the stopper, and held in the stopper under an applied static magnetic field $\boldsymbol{B}_0$ in the z-direction until the fragments decay by the β-ray emission. The β-ray angular distribution from a polarized nucleus is given as

$$W(\theta) = 1 + A_\beta P \cos\theta, \qquad (1)$$

where A_β and P denote the asymmetry parameter and the degree of polarization, respectively. A change in the up/down ratio $U/D \equiv W(0°)/W(180°) \approx 1 + 2A_\beta P$ of the β-ray intensities will give a good indication of the spin flip resulting from the nuclear magnetic resonace (NMR), which is incorporated in the present measurements as described in the following. An rf field $\boldsymbol{B}_1$ perpendicular to $\boldsymbol{B}_0$ is applied, with its frequency ν being swept over the range from $\nu_1 - \frac{1}{2}\Delta\nu$ to $\nu_1 + \frac{1}{2}\Delta\nu$. If the range include the Larmor frequency $\nu_L = \mu B_0/hI$, the nuclear spins are inverted (the adiabatic fast passage inversion; AFP) and the U/D ratio changes as $1 + 2A_\beta P \rightarrow 1 - 2A_\beta P$. Thus, the NMR is searched for by scanning the ν_1 value while monitoring the β-ray U/D ratio.

In the case of the ^{18}N experiment, the spin polarized beam of ^{18}N fragments was produced by the fragmentation of ^{22}Ne projectiles at $E/A = 110$ MeV/u on a ^{12}C target. The degree of polarization thus obtained was measured prior to the NMR search for μ measurement, by means of the adiabatic field rotation technique [13]. The best experimental conditions were searched for by changing the settings for the emission angle θ_L and momentum p, in order to optimize the figure of merit given by $F = P^2Y$, where P is the degree of polarization and Y the yield for the ^{18}N fragments. We thus obtained the ^{18}N polarization of $P = -(2.2 \pm 0.7)$ % with the settings $\theta_L = 2.5°$–$4.5°$ and $p = 8.07$–8.32 GeV/c. The β-NMR experiment was carried out for ^{18}N fragments implanted in a cooled Pt stopper. The resulting frequency spectrum at a temperature of 30 K is shown in Fig. 3. From the position of a dip observed in the spectrum the magnetic moment is determined as $|\mu(^{18}\mathrm{N})| = (0.3279 \pm 0.0017)\mu_N$.

We have also measured the electric quadrupole moment Q of the ^{18}N ground state. A single crystal of Mg was employed as a stopper, in which an electric field gradient eq is known to act on an implanted N atom [14–16]. In the spin $I = 1$ case, the quadrupole coupling between eq and Q causes the NMR line to split into two frequencies

$$\nu_\pm = \nu_L \pm \frac{3}{8}\nu_Q, \tag{2}$$

where $\nu_Q \equiv eqQ/h$. The measurement was made by applying the B_1 field having both the two frequency components in Eq. (2) with the ν_Q value being scanned. The result is shown in Fig. 3. From the observed dip the quadrupole coupling constant was determined as $|\nu_Q| = (73.2 \pm 1.8)$ kHz, from which the electric quadrupole moment $|Q| = (12.7 \pm 1.0)$ mb was deduced.

3 Results and discussion

Since the magnetic moment receives contributions with quite different respective weighting factors [namely, $g_s(\mathrm{p}) = 5.59$, $g_\ell(\mathrm{p}) = 1$, $g_s(\mathrm{n}) = -3.83$, and $g_\ell(\mathrm{n}) = 0$, if the free nucleon values are taken] from spin and orbital angular momenta of protons and neutrons, its value sensitively reflects the configurations of valence nucleons in a nucleus. Thus, with the help of full shell model calculations and, in some case, based on quite model-independent arguments, the microscopic structures of unstable nuclei may be investigated from the measured magnetic moments.

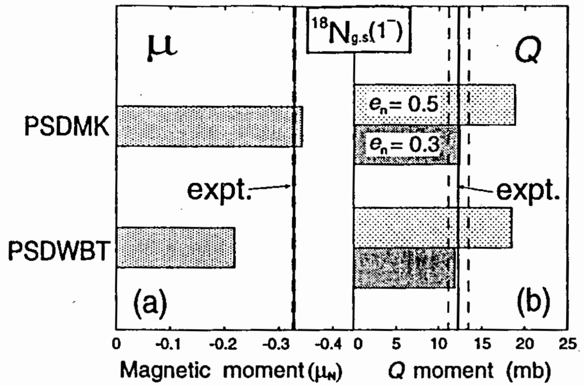

Figure 4: Comparisons of the experimental μ and Q values (expt.) for the ^{18}N ground state ($I^\pi = 1^-$) with shell-model calculations for the state $\psi(1^-)$, using two different effective interactions (PSDMK, PSDWBT). Broken lines accompanying the experimental line indicate the experimental error. In Q moment calculations the effective charge for neutrons was varied from $e_n = 0.3$ to 0.5, while that for protons was fixed at $e_p = 1.3$.

μ measurements for ^{15}B [6] and ^{17}B. [7] All these results for ^{17}N, ^{15}B and ^{17}B are well accounted for by assuming that the pairing energy for the sd neutrons is diminished by 30 %from ones usually employed in the region close to stability.

The electric quadrupole moments for ^{14}B and ^{15}B were determined.[9] Comparison with shell model calculations in the psd model space indicates that the E2 effective charge for the sd neutrons in these nuclei takes on anomalously small values, $e_{\mathrm{eff}} \approx 0.1e$, as compared to the standard value of $\approx 0.5e$ established in the region of stability.

The nucleus ^{18}N comprises 7 protons and 11 neutrons, with its low-lying states being described by a hole in the proton p shell and three particles in the neutron sd shell, relative to the ^{16}O core. In shell model calculations, there appear two $I^\pi = 1^-$ states in the lowest-energy region, whose wave functions are expressed as

$$\begin{aligned}\psi(1^-) &= \alpha|\pi(p_{1/2})_{-1}, \nu[(d_{5/2})_3]^{3/2^+}\rangle^{I^\pi=1^-} \\ &+ \beta|\pi(p_{1/2})_{-1}, \nu[(d_{5/2})_2^{2^+} s_{1/2}]^{3/2^+}\rangle^{I^\pi=1^-} + \cdots \end{aligned} \tag{3}$$

and

$$\begin{aligned}\psi'(1^-) &= \alpha'|\pi(p_{1/2})_{-1}, \nu[(d_{5/2})_2^{0^+} s_{1/2}]^{1/2^+}\rangle^{I^\pi=1^-} \\ &+ \beta'|\pi(p_{1/2})_{-1}, \nu[(d_{3/2})_2^{0^+} s_{1/2}]^{1/2^+}\rangle^{I^\pi=1^-} + \cdots. \end{aligned} \tag{4}$$

We note that $\psi(1^-)$ and $\psi'(1^-)$ correspond to the states $|\pi(p_{1/2})_{-1} \otimes {}^{19}\mathrm{O}(3/2^+)\rangle^{I^\pi=1^-}$ and $|\pi(p_{1/2})_{-1} \otimes {}^{19}\mathrm{O}(1/2^+)\rangle^{I^\pi=1^-}$, respectively, in a weak-coupling model in terms of

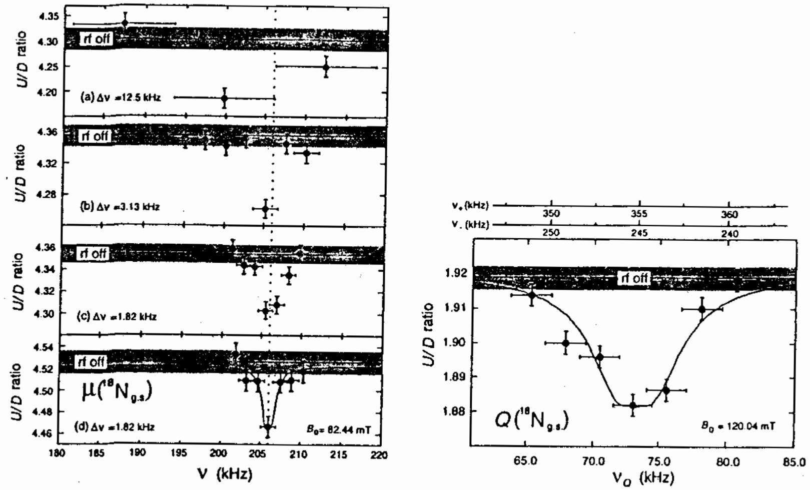

Figure 3: β-NMR spectra obtained for the determination of the magnetic moment (left) and electric quadrupole moment (right) for the ^{18}N ground state.

The magnetic moment of ^{14}B was determined to be $|\mu(^{14}\mathrm{B})| = 1.185\pm0.005\mu_{\mathrm{N}}$.[6] The *psd* space shell model calculations[17] show that the ground state of the odd-odd nucleus ^{14}B is dominated by two configurations $[\pi p_{3/2}, \nu s_{1/2}]^{J^\pi=2^-}$ and $[\pi p_{3/2}, \nu d_{5/2}]^{J^\pi=2^-}$. The diagonal matrix elements of $\hat{\mu}$ are much different for these two configurations $[\langle \pi p_{3/2}, \nu s_{1/2}|\hat{\mu}|\pi p_{3/2}, \nu s_{1/2}\rangle^{2^-} = +1.880\ \mu_{\mathrm{N}}$ and $\langle \pi p_{3/2}, \nu d_{5/2}|\hat{\mu}|\pi p_{3/2}, \nu d_{5/2}\rangle^{2^-} = -0.982\ \mu_{\mathrm{N}}]$, and therefore the μ value should represent a sensitive measure of the relative importance of these configurations. The experimental μ is substantially larger than the standard calculations, suggesting an underestimation of the $[\pi p_{3/2}, \nu s_{1/2}]^{J^\pi=2^-}$ component. Agreement is obtained when the single-particle energy ε for the $\nu s_{1/2}$ orbit is lowered by about 1 MeV from the standard value which is normally employed in calculations in the region of nuclei close to stability. A need for lowering ε in the region of neutron-rich nuclei was first pointed out based on theory in Ref. [18].

The result for ^{17}N was obtained as $|\mu(^{17}\mathrm{N})| = 0.352\pm0.002\mu_{\mathrm{N}}$.[7] The leading term in the $^{17}\mathrm{N}_{\mathrm{g.s.}}$ wave function is given by $\psi_0 = |\pi(p_{1/2})_{-1}, \nu[(sd)_2]^{0^+}\rangle^{J^\pi=1/2^-}$. Because of the $p_{1/2}$ character of proton in ψ_0, the only configurations which can admix with ψ_0 are those of a type, $\psi_2 = |\pi(p_{3/2})_{-1}, \nu[(sd)_2]^{2^+}\rangle^{J^\pi=1/2^-}$. From the experimental μ, the amount of the ψ_2 type admixture was determined in quite a model independent manner. The result, (5.6 ± 0.8) %, for the probability of the 2^+ configuration of the two *sd* neutrons is much larger compared to calculations with the PSDMK[19] and PSDWB[20] effective interactions. The same conclusion was obtained from the

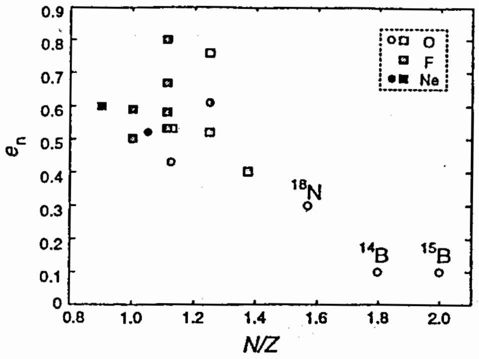

Figure 5: Empirical effective charge for neutrons in the *sd* orbits, extracted from the experimental static Q moments (circles) and E2 transition probabilities (boxes). The abscissa represents the N/Z ratio.

a proton hole coupled to the ^{19}O core. The observed magnetic moment,[8] $|\mu(^{18}\mathrm{N})| = (0.3279\pm0.0013)\mu_{\mathrm{N}}$, is very close to the calculated $|\mu|$ for $\psi(1^-)$ as shown in Fig. 4(a), while it is about five times smaller than $|\mu|$ values calculated for ψ', definitely excluding the wave function $\psi'(1^-)$ as the ground state.

The experimental electric quadrupole moment[8] is compared with the shell model calculations in Fig. 4(b). The calculated Q seem quite stable against the choice of the effective interaction, but they are substantially smaller than the experimental Q if the usually taken value of neutron effective charge, $e_{\mathrm{n}} \approx 0.5$, is employed. Since the proton contribution to the ^{18}N ground state Q-moment is very small ($Q_{\mathrm{p}} = 2.2-2.6$ mb is calculated with $e_{\mathrm{p}} = 1.3$), the smallness of $Q(^{18}\mathrm{N})$ implies that the neutron polarization charge should be smaller than assumed in the calculations. The agreement is obtained if $e_{\mathrm{n}} = 0.3$ is taken. In Fig. 5, where the experimental e_{n} values are plotted as a function of the N/Z ratio, one finds that the quenching of e_{n} develops gradually as N/Z increases.

In summary, we successfully carried out β-NMR measurements on magnetic moments and quadrupole moments of several neutron rich nuclei by means of spin polarized radioactive nuclear beams. The obtained results were compared with shell model calculations, and physical implications concerning the structures and interactions in neutron-rich nuclei were extracted from them. Finally, we note that the present results for μ and Q of $^{18}\mathrm{N}_{\mathrm{g.s.}}$ strikingly disagree with those reported by Leuven group[21,22]. They obtain from the Level Mixing Resonance (LMR) experiment a Q/μ ratio about 6 times larger, and from the LMR-NMR experiment a μ about 2.4 times smaller compared to the present results. The discrepancies are serious ones, and require to be solved in near futute. In this context, we like to point out a possibility of ascribing the dip observed in the LMR experiment to the effect of cross-polarization between the implanted ^{18}N spins and the host ^{25}Mg spins in the Mg stopper: The field strength for which the energy of the ^{18}N $m = 0 \leftrightarrow -1$ transition and that of the ^{25}Mg $m = +3/2 \leftrightarrow +1/2$ coincide is calculated as $B_{\mathrm{cross}} \approx 120$ mT.

This work was supported in part by a Grant-in-Aid in Scientific Research of the Japanese Ministry of Education, Science and Culture.

References

[1] A.S. Goldhaber, *Phys. Lett.* B **53**, 306 (1974).
[2] K. Asahi *et al.*, *Phys. Lett.* B **251**, 488 (1990).
[3] K. Asahi *et al.*, *Hyperfine Int.* **75**, 101 (1992).
[4] H. Okuno *et al.*, *Hyperfine Int.* **78**, 97 (1993).
[5] H. Okuno *et al.*, *Phys. Lett.* B **355**, 335 (1994).
[6] H. Okuno *et al.*, *Phys. Lett.* B **354**, 41 (1995).
[7] H. Ueno *et al.*, *Phys. Rev.* C **53**, 2142 (1996).
[8] H. Ogawa *et al.*, *Phys. Lett.* B **451**, 11 (1999).
[9] H. Izumi *et al.*, *Phys. Lett.* B **366**, 51 (1996).
[10] K. Matsuta *et al.*, *Hyperfine Int.* **97/98**, 519 (1996).
[11] K. Matsuta *et al.*, *Phys. Lett.* B **459**, 81 (1999).
[12] T. Kubo *et al.*, *Nucl. Instrum. Methods* B **70**, 309 (1992).
[13] H. Ogawa *et al.*, to be published.
[14] A. Kitagawa, K. Matsuta, Y. Nojiri, and T. Minamisono, *Hyperfine Int.* **60**, 869 (1990).
[15] T. Minamisono, T. Ohtsubo, K. Sato, S. Takeda, S. Fukuda, T. Izumikawa, M. Tanigaki, T. Miyake, T. Yamaguchi, N. Nakamura, H. Tanji, K. Matsuta, M. Fukuda, and Y. Nojiri, *Phys. Lett.* B **420**, 31 (1998).
[16] M. Tokman, D. Sundholm, P. Pyykkö, J. Olsen, *Chem. Phys. Lett.* **265**, 60 (1997).
[17] B.A. Brown, A. Etchegoyen, and B.D.M. Rae, Computer code OXBASH, *MSU Cyclotron Laboratory Report* No. 524 (1986).
[18] I. Talmi and I. Unna, *Phys. Rev. Lett.* **4**, 469 (1960).
[19] D.J. Millener and D. Kurath, *Nucl. Phys.* A **255**, 315 (1975).
[20] E.K. Warburton and B.A. Brown, *Phys. Rev.* C **46**, 923 (1992).
[21] G. Neyens, N. Coulier, S. Ternier, K. Vyvey, S. Michiels, R. Coussement, D.L. Balabanski, J.M. Casandjian, M. Chartier, D. Cortina-Gil, M. Lewitowicz, W. Mittig, A.N. Ostrowski, P. Roussel-Chomaz, N. Alamanos, and A. Lépine-Szily, *Phys. Lett.* B **393**, 36 (1997).
[22] G. Neyens *et al.*, *Phys. Rev. Lett.* **82**, 497 (1999).

SYSTEMATICS OF NUCLEAR CHARGE RADII

N.N.Kolesnikov
Moscow State University
Department of Physics

Now it is evident that the well-known formula for nuclear radii :

$$R = r_0 A^{1/3} \qquad (1)$$

is too rough to describe the existing experimental data. This was noted in a number of publication, and the correction to this formula were proposed /1-6/. In reality the sizes of nuclei depend not only on the total number of nucleons (A) but also on the relation between the number of protons (Z) and neutrons (N). Moreover a detailed analysis shows that the regular run of R as a function of Z and N breaks at the magic and submagic numbers of protons Z_m and neutrons N_m (note that this numbers are observed also as discontinuities in binding energies of protons and neutrons) . So we believe that instead of search for corrections to the formula (I) it is more constructive to accept from beginning that the nuclear radius is a function of both Z and N, and to look for it. The goal of this communication is to present the results of our analysis of different experimental data related to nuclear radii.

For determination of nuclear charge radii the electron scattering experiments, the spectra of muonic atom and optical measurements are usually used. The first two methods of investigation require at least tens milligrams of target material and so they are applicable practically only for stable nuclei. And so far only optical method was considered capable of measuring radii of unstable nuclei. Modern laser-spectroscopic technique have made it possible even for rather short-lived (up to ~ 1 s.) isotopes. However for light nuclei the application of this method is complicated not only for that nuclei whose mean-life is shorter than 1 second, but also for long-lived and stable nuclei due to uncertainty in evaluation of competing specific mass effect that gives for them a prevalent contribution to the isotopic shift in comparison with the volume (field) effect depending on the size of the nucleus.

In order to obtain the information about radii of such nuclei we will use the differences of the Coulomb energies and also the hypernuclear data.

COULOMB ENERGY AND NUCLEAR RADII OF 1P-SHELL NUCLEI

First of all we consider the nuclei of 1p-shell. For their description we will use the many-particle shell model. The energy of Coulomb interaction between nucleon (i) with isospin T(i) and nucleon (j) with isospin T(j) may be written in the form

$$V_{ij} = 1/4\,(1 + 2T_3(i))(\,1 + 2T_3(j))\,V(r_{ij}), \qquad (2)$$

where T_3 is +1/2 for proton and -1/2 for neutron.

If the self structure of the proton is taken into account then for Gaussian distribution of the charge

$$V(r) = e^2/r\,\Phi(r/r_p), \qquad (3)$$

where Φ is the error function and r_p is the root-mean-square (rms) radius of the proton.

It is natural to suppose that for all analogous states of 1p-shell isobars of given A (i.e. states of the same isomultiplet) the wave functions of the 1s-protons are identical. In this case the difference of the Coulomb energies ΔE_c between the states of two neighbouring isobar with the same isospin T consists of 2 parts: from the energy of interaction of the 1p-proton with all protons of 1s-shell ΔE_{sp} and the energy of interaction of all 1p-protons between them ΔE_{pp}.

The first part ΔE_{sp} is expressed through the Slaters integrals F_{sp} and G_{sp} :

$$\Delta Esp = (2F_{sp}^{(0)} - 1/3G_{sp}^{(1)})(Z-2). \qquad (4)$$

For calculation of ΔE_{pp} for the configuration $(1p)^n$ the wave functions of many-particle model with intermediate coupling /7/ $|(1p)^n, J, M, T, M_T>$ are expanded on the basic functions of LS-coupling $|(1p)^n[f],T,M_T,S,L,J>$:

$$|(1p)^n, J, M, T, M_T> \; = \; \Sigma\, C^J_{TSLf}\, |(1p)^n[f],T,M_T,S,L,J> \qquad (5)$$

that are eigenfunctions of operators T^2,T_3,S^2,S_z,L^2,L_z . The basic functions of LS-coupling according to Hund /8,9/ are constructed in the form of a linear combination of products of one-particles functions of nucleons. We suppose that the Hamiltonian is a sum :

$$H = \Sigma H_i + \Sigma U_{ij} + a\, \Sigma L_i S_i, \qquad (6)$$

where H_i is the one-particle Hamiltonian in oscillator model, the last term is the sum of spin-orbit interactions . The residual interaction U_{ij} contains all 4 types of exchange interaction (Majorana, Bartlet, Heisenberg, Wigner) with the weight coefficients fixed from the condition of best reproduction of nuclear spectra for 1p-shell nuclei , see /10/ and /11/. In calculation of differences of the Coulomb energies all many-particle matrix elements were reduced to one- or two-particles matrix elements according to paper /12-15/.

The supposition that the oscillator parameters a_s and a_p for 1s and 1p states are identical and that they are the same for all member of the isomultiplet pairs leads to the contradiction as it appears that the values of the parameter a obtained for the same nucleus from different isomultiplet pairs do not coincide. This was interpreted as an indication that the parameters a_p may be different from a_s and that they can change at the passage from one isobar to another (though the distribution of nucleons could be identical).

Therefore we accept that only parameters a_s are identical for all analogous states of fixed A and moreover that they are the same as for the ground state of the stable isobar, whereas a_p are not. The values of a_p found under this supposition are presented in Table 1 together with used for this experimental values taken from the tables of article /16/. As is seen the general tendency for a_p is a slight decrease with increase of Z and A. The calculations have shown that the correction to a_p due to the self structure of the proton is rather small (it leads to the diminution of a_p no more than 2-3%) and it decreases when A increases.

The effect of the exchange interaction in the total Coulomb energy is small too (it diminishes a_p by 10-15 % or less) and (similarly to the effect of the self-structure of the proton) it decreases with growth of A.. Therefore in our further analysis of the Coulomb energies of nuclei heavier than ${}^{16}O$ we will not take this two effects into account.

TABLE 1
PARAMETERS OF OSCILLATOR MODEL DENSITY FOR 1P-SHELL NUCLEI

Isobars	J^P, T	a (Fm)	a_p
${}^{6}He$	0+, 1	2,06	1,91
${}^{6}Li$		1,84	1,90
${}^{6}Be$			
${}^{7}Li$	3/2-,1/2	1,64	1,72
${}^{7}Be$			1,69
${}^{8}Li$	2+, 1	1,86	1,79
${}^{8}Be$		1,58	1,59
${}^{8}B$			1,56
${}^{9}Be$	3/2-, 1/2	1,78	1,72
${}^{9}B$			1,76
${}^{10}Be$	0+, 1	1,64	1,62
${}^{10}B$		1,62	1,66
${}^{10}C$			1,64
${}^{11}B$	3/2-, 1/2	1,54	1,61
${}^{11}C$			1,59
${}^{12}B$	3-, 1	1,62	1,66
${}^{12}C$		1,67	1,64
${}^{12}N$			1,57
${}^{13}C$	1/2-, 1/2	1,58	1,58
${}^{13}N$			1,61
${}^{14}C$	0+, 1	1,68	1,60
${}^{14}N$		1,66	1,65
${}^{14}O$			1,66
${}^{15}N$	1/2-, 1/2	1,66	1,79
${}^{15}O$			1,79

TABLE 2 . NUCLEAR RADII FROM HYPERNUCLEAR DATA

HYPERNUCLEUS	NUCLEUS-CORE	B_Λ (MeV)	$<r^2>^{1/2}$ from B_Λ	$<r^2>^{1/2}$ from μ-atoms
${}^{9}_{\Lambda}Li$	${}^{8}Li$	8,53(15)	2,12(1)	
${}^{9}_{\Lambda}Be$	${}^{8}Be$	6,71(4)	2,29(1)	
${}^{9}_{\Lambda}B$	${}^{8}B$	7,88(15)	2,30(1)	
${}^{10}_{\Lambda}Be$	${}^{9}Be$	9,11(22)	2,26(1)	2,43(8)
${}^{10}_{\Lambda}B$	${}^{9}B$	8,89(12)	2,32(1)	
${}^{11}_{\Lambda}B$	${}^{10}B$	10,24(5)	2,38(1)	2,45(12)
${}^{12}_{\Lambda}B$	${}^{11}B$	11,37(6)	2,37(1)	2,42(12)
${}^{12}_{\Lambda}C$	${}^{11}C$	10,76(14)	2,53(2)	
${}^{13}_{\Lambda}C$	${}^{12}C$	11,69(12)	2,46(1)	2,464(12)
${}^{14}_{\Lambda}C$	${}^{13}C$	12,17(33)	2,51(2)	2,44(3)
${}^{15}_{\Lambda}N$	${}^{14}N$	13,59(15)	2,57(1)	2,54(2)
${}^{16}_{\Lambda}O$	${}^{15}O$	13(2)	2,67(12)	

NUCLEAR RADII FROM COULOMB ENERGY FOR NUCLEI FROM OXIGEN TO CALCIUM

For nuclei heavier than 1p-shell nuclei another approach is used. The exchange Coulomb interaction is not taken into account and it is supposed that the distribution of the charge in the nucleus may be approximated by two-parameters Fermi distribution

$$\rho = \rho_0 \left(1 + \exp((r-R_0)/c)\right) \qquad (7)$$

with fixed parameter c = 0,56 Fm. For this density of charge the Coulomb energy was calculated numerically as function of R_0 for each isobar. By comparison of such calculated values of ΔE_c with corresponding experimental values, the rms radii of each of analogous states (related to the fixed A and T) may be expressed step by step trough the $<r^2>^{1/2}$ for one of them, for instance through the radius of the stable isobar. Moreover we assume it to be equal to the rms of the ground state of the stable isobar. This implies the supposition that there is no essential dependence of rms radius of a nucleus on the value of isospin T. The analysis of experimental data shows that the difference of the Coulomb energies for the states of different isospins remains practically the same for every pair of isobars . Moreover the values of $<r^2>^{1/2}$ found from differences of the Coulomb energies agree with all results obtained in electromagnetic (μ-atomic and optical) experiments for light (A< 40) isobaric pair : ^{28}Na- ^{28}Si; ^{27}Na- ^{27}Al; ^{26}Na- ^{26}Mg; ^{25}Na- ^{25}Mg; ^{24}Na- ^{24}Mg; ^{22}Ne- ^{22}Na; ^{21}Ne- ^{21}Na; ^{20}Ne- ^{20}Na /17,18/.
The values of $<r^2>^{1/2}$ calculated from Coulomb energies for elements from F to Ca are presented in fig.1 (together with experimental values marked by +). It is seen a regular change of rms radii with Z and N and a break at the submagic numbers Z=14 and N=14.
For estimation of $<r^2>^{1/2}$ were used besides experimental values of ΔE_c also the results of systematics. As was shown in /19/ the differences of energy of isomultiplet (analogous) states are regular function of Z and N in each of regions limited by (sub)magic numbers of protons Z_m and neutrons N_m (for considered region of nuclei Z_m and N_m are 8,14 20) and may be expressed with a good precision (maximal deviation from experiment 0,1 MeV) by the formula :

$$\Delta E_c = (aZ + b)/(cA + A_0)^{1/3} \qquad (8)$$

where a, b, c, A_0 are constant for each intermagic region (see /19/). The use of this results for ΔE_c allows one to enlarge the list of calculated values of nuclear radii.

NUCLEAR RADII FROM HYPERNUCLEAR DATA

In the frame of the two-body (Λ-particle + nucleonic core) model of hypernuclei it was shown that the binding energies of Λ- particle B_Λ are highly sensitive to the sizes of the nucleus-core /20/ and this allows to use the experimental values of B_Λ for the determination of nuclear radii. This implies the use of the realistic Λ-N potential that could describe well the hypernuclear experimental data. It is necessary also to bear in mind that the binding energy B_Λ depends on distribution not solely protons but all nucleons and therefore the confrontation of hypernuclear data with electromagnetic

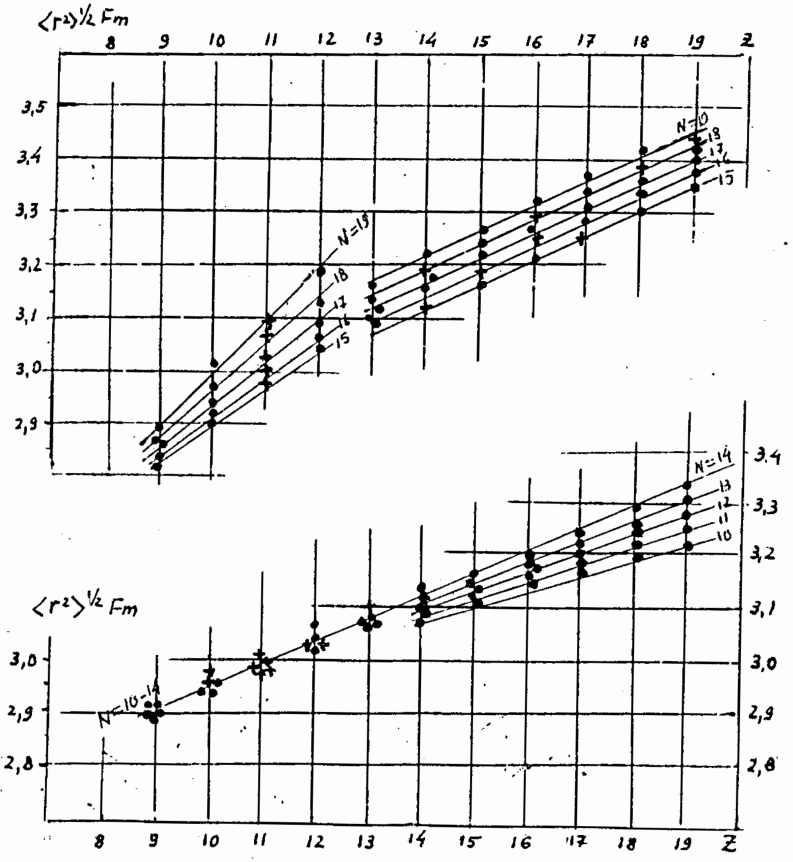

Fig.1. $<r^2>^{1/2}$ from differences of Coulomb energies of nuclei from O to Ca
+ -experimental value of $<r^2>^{1/2}$ from electromagnetic experiments

experiments allows to find separately the distribution of protons and distribution of neutrons. Note that a small effect may be due to the compressibility of a nucleonic core by the Λ-particle

The results of the calculation of the rms radii from hypernuclear data are presented in Table 2 in the column 4. In the brackets are given the limits of uncertainty due to the experimental errors in B_Λ. In the column 5 are presented for comparison the results obtained from electromagnetic measurements /17/. It is seen that the hypernuclear data agree generally with electromagnetic measurements except the case of ${}^{10}{}_{\Lambda}\mathrm{Be}$ where the used two-body model of this hypernucleus (instead of the cluster model) does not give the adequate description.

SYSTEMATICS OF CHARGE RADII FROM ELECTROMAGNETIC EXPERIMENTS

The most complete and reliable information about nuclear charge radii goes from the study of spectra of muonic atoms, scattering of electrons and from optical measurements. As is known the value of rms charge radius of a nucleus depends on the form of the distribution of the charge, so to be certain it is necessary to refer to the definite type of density of the charge. Our analysis supposes the Fermi type of density. The impute data were taken from the tables of experimental data summarized in articles /17/ and /18/.

As to the general situation with nuclear charge radii it is similar to that existing for binding energies of nuclei. There are two approaches to the problem of binding energies. One of them in the spirit of liquid drop model is based on the description of binding energies by smooth functions of nuclear coordinates (Z and N or their combination) with introduction of the shell-parity correction (method of shell-correction /21/). Another inspired by shell model divides all system of nuclei into region limited by magic (or submagic) numbers of proton and neutron and describes each of such region separately /22/.

For nuclear radii an approach similar to the first mentioned above alternative was used in a number of publications, for instance in /1-6/. Nevertheless the experimental values of rms have discontinuities at certain (magic) numbers of Z and N and it is difficult to describe with a good precision the dependence of $<r^2>^{1/2}$ on Z and N by a smooth function of Z and N even by addition of local correction. Therefore it is more realistic to divide all system of nuclei into intermagic regions and to describe them separately.. Our detailed analysis of experimental rms radii assured us that in each of such intermagic region the rms charge radii can be described with a good precision by linear functions of Z and N . This is seen in Fig.2 , where rms radius $<r^2>^{1/2}$ is presented versus number of protons Z and the experimental points related to the same number of neutron N are connected by the lines. The lines connecting the points corresponding to the fixed value of N are straight lines that break at certain numbers of protons, that can be interpreted as (sub)magic numbers Z_m. Moreover they are parallel and in certain limit (determined by magic numbers of neutrons N_m) equidistant. Therefore in every intermagic region with the magic numbers Z_0 and N_0 ($Z \geq Z_0$; $N \geq N_0$) the rms charge radii $<r^2>^{1/2}$ may be expressed by the formula :

$$<r^2>^{1/2} = R(Z) + D(N), \qquad (9)$$

where $R(Z) = R_0 + a(Z-Z_0)$ and $D(N) = b(N-N_0)$ (10)

$R_0 \equiv R(Z_0, N_0)$, Z_0 is for different regions Z_m = 20, 24, 28, 32, 36, 44, 50, 56, 68, 76, 82 and N_0 is N_m := 20, 24, 28, 32, 44, 50, 64, 70, 82, 90, 102, 108, 116, 126.

The parameters R_0 , a and b are for different regions equal :

$Z_0 = 20 \leq Z \leq 24$ $a = 0{,}0425$,
$N_0 = 20 \leq N \leq 24$, $R_0 = 3{,}48$, $b = 0{,}01$; $N_0 = 24 \leq N \leq 28$, $R_0 = 3{,}52$, $b = -0{,}01$;
$Z_0 = 24 \leq Z \leq 28$, $a = 0{,}025$,
$N_0 = 28 \leq N \leq 32$, $R_0 = 3{,}645$, $b = 0{,}02$; $N_0 = 32 \leq N \leq 44$, $R_0 = 3{,}725$, $b = 0{,}014$
$Z_0 = 28 \leq Z \leq 32$, $a = 0{,}04$,
$N_0 = 32 \leq N \leq 44$, $R_0 = 3{,}83$, $b = 0{,}008$
$Z_0 = 32 \leq Z \leq 36$, $a = 0{,}043$,
$N_0 = 44 \leq N \leq 50$, $R_0 = 4{,}06$, $b = 0{,}002$; $N_0 = 50 \leq N \leq 64$, $R_0 = 4{,}07$, $b = 0{,}014$
$Z_0 = 36 \leq Z \leq 44$, $a = 0{,}026$,
$N_0 = 44 \leq N \leq 50$, $R_0 = 4{,}18$, $b = -0{,}003$; $N_0 = 50 \leq N \leq 64$, $R_0 = 4{,}16$, $b = 0{,}0125$
$Z_0 = 44 \leq Z \leq 50$, $a = 0{,}0125$,
$N_0 = 50 \leq N \leq 64$, $R_0 = 4{,}365$, $b = 0{,}012$; $N_0 = 64 \leq N \leq 70$, $R_0 = 4{,}54$, $b = 0{,}005$
$N_0 = 70 \leq N \leq 82$, $R_0 = 4{,}57$, $b = 0{,}005$
$Z_0 = 50 \leq Z \leq 58$, $a = 0{,}026$,
$N_0 = 64 \leq N \leq 70$, $R_0 = 4{,}65$, $b = 0{,}001$; $N_0 = 70 \leq N \leq 82$, $R_0 = 4{,}88$, $b = 0{,}003$,
$N_0 = 82 \leq N \leq 94$, $R_0 = 4{,}68$, $b = 0{,}013$,
$Z_0 = 58 \leq Z \leq 68$, $a = 0{,}022$,
$N_0 = 70 \leq N \leq 82$, $R_0 = 4{,}86$, $b = 0{,}001$; $N_0 = 82 \leq N \leq 90$, $R_0 = 4{,}87$, $b = 0{,}009$,
$N_0 = 90 \leq N \leq 100$, $R_0 = 4{,}98$, $b = 0{,}006$,
$Z_0 = 68 \leq Z \leq 76$, $a = 0{,}008$,
$N_0 = 82 \leq N \leq 90$, $R_0 = 5{,}075$, $b = 0{,}011$; $N_0 = 89 \leq N \leq 112$, $R_0 = 5{,}16$, $b = 0{,}008$,

$N_0 = 108 \leq N \leq 116$, $R_0 = 5{,}39$, $b = 0{,}003$; $N_0 = 116 \leq N \leq 126$, $R_0 = 5{,}42$, $b = 0{,}0006$,
$N_0 = 126 \leq N$, $R_0 = 5{,}47$, $b = 0{,}001$.

For light nuclei $8 < Z < 20$ and $8 < N < 20$:
$Z_0 = 8 < Z < 14$, $N_0 = 8 < N < 14$: $a = 0{,}042$, $R_0 = 2{,}91$, $b = 0$,
$Z_0 = 14 < Z < 20$, $N_0 = 14 < N < 20$: $a = 0{,}047$, $R_0 = 3{,}07$, $b = 0{,}025$.

For nuclei of the region $Z_0 = 8 < Z < 14$, $N_0 = 14 < N < 20$ the rms radii may be expressed by the formula:

$$<r^2>^{1/2} = 2{,}68 + (0{,}67 + 0{,}074(N - 14))(Z - 7)$$

and for $Z_0 = 14 < Z < 20$, $N_0 = 8 < N < 14$ by the formula:

$$<r^2>^{1/2} = 3{,}0 + (0{,}36 + 0{,}0047(N - 10))(Z - 11).$$

We carry out our analysis only for ground states of nuclei. With exclusion of isomeric states and the effect of staggering, that exists for few isotopes of Hg and Pd, the maximal deviations of calculated (according to formulas (9) and (10)) values of rms radii from experimental ones given in /17/ and /18/ do not exceed 0,01 Fm.

The general tendency in behavior of rms radii is a decrease of $\Delta R/\Delta Z$ and $\Delta R/\Delta N$ with increase of A and with that always $\Delta R/\Delta Z > \Delta R/\Delta N$ (the parameter a in (10) is larger than b). The local behavior of R(Z,N) is determined by the filling of proton and neutron shells. $\Delta R/\Delta Z$ decreases before and increases after filling the proton shells Z_m = 20, 28, 50 that is reflected in Figs.1 and 2 as a change of the slope of lines Similarly $\Delta R/\Delta N$ changes before and after filling of the neutron shells N_m = 20, 28, 50, 82, 126 that is reflected in Fig.2 as a condensation or divergence of lines

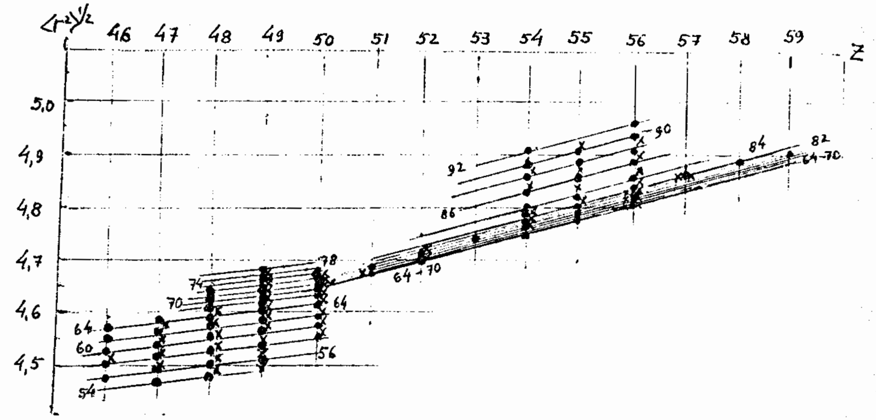

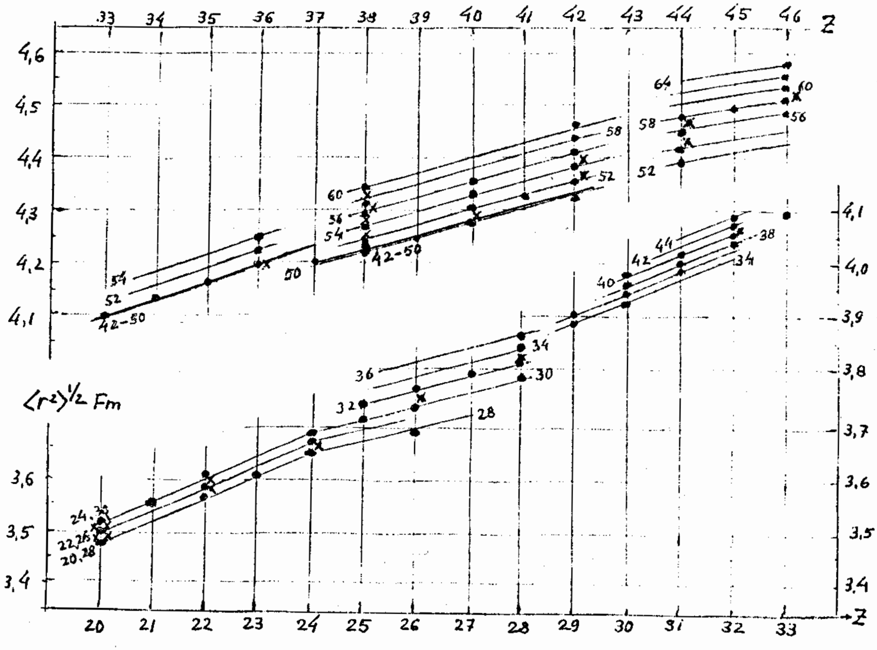

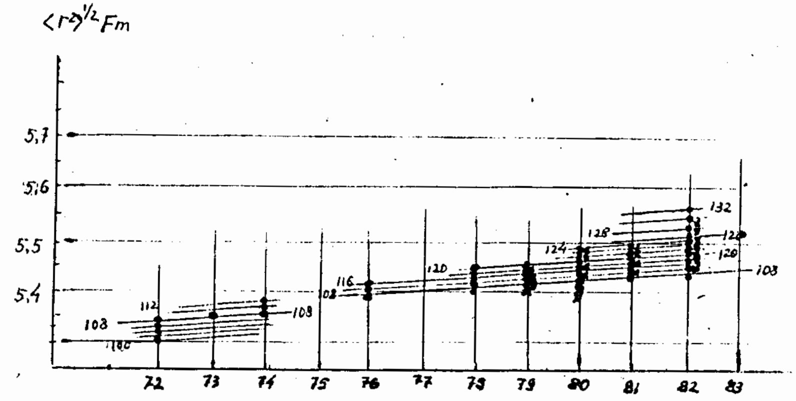

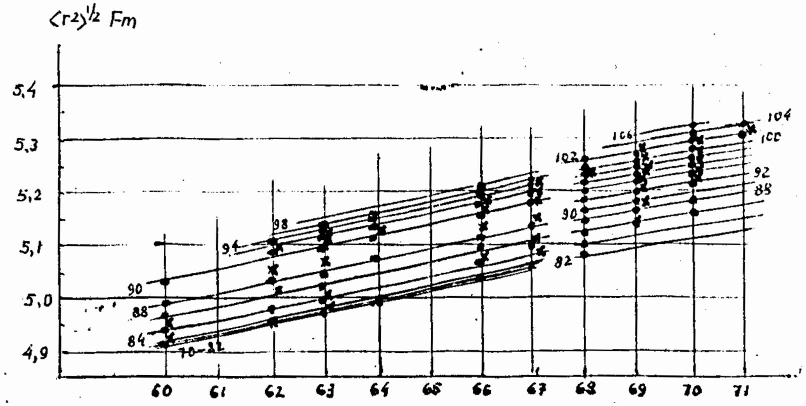

Fig.2. $\langle r^2 \rangle^{1/2}_{ch}$ from mu-atom spectra, electron scattering and optical measurements

x- odd N isotopes

corresponding to different N. Sometimes $\Delta R/\Delta N$ became even negative as for instance for nuclei with N = 24-28 at Z = 20-24 or for N = 42-50 at Z = 34-38 or for N = 70-82 at Z = 60-64. On the contrary as is seen in Fig.2 the space between lines increases after N equal to 50, 82 and 126, that is related with filling of neutron shells. This is observed also after N = 88 that is due to deformation of nuclei.

REFERENCES

1.I.Angeli, M.Csatlos, Nucl.Phys. A288, (1977), 480
2. 1; I.Angeli, Z.Phys.A334, (1989), 377; I.Angeli, M.Csatlos, Atomki Koslemengek. 20, (1976),
3.E.B.Shera et al. Phys.Rev. C14, (1976), 731
4.H.D.Wolfgang et al. Phys.Rev. C22, (1980), 264
5.N.N.Kolesnikov,V.S.Rostovsky, M.I.Starosotnikov,Ukr.J,Phys.31,(1986), 1131
6.N.N.Kolesnikov, M.I.Starosotnikov, Izv.vuzov, Fizika, N12, (1982), 84
7.D.R.Inglis, Rev.Mod.Phys. 25, (1953), 390
8.F.Hund, Z.Phys. 105, (1937), 202
9.H.A.Jahn, Proc.Roy.Soc. 201A, (1950), 516
10.D.Kurath, Phys.Rev. 101, (1956), 216
11.N.N.Kolesnikov,D.Amarasingam, V.I.Tarasov, Yad.Fiz. 35, (1982), 32
12.I.Talmi, Rev.Mod.Phys. 34, (1962), 704
13.J.P.Elliot, A.M.Lane, Phys.Rev. 46, (1934), 948
14.H.A.Jahn, H.W.Wieringen, Proc.Roy.Soc. 209A, (1953), 502
15.F.Feenberg,E.Wigner, Phys.Rev. 51, (1937), 95
16.H.de Vries, C.W.de Jager, C.de Vries, ADNDT, 36, (1987), 495
17.G.Fricke, C.Bernhardt, K.Heilig et al. ADNDT, 60, (1995), 177
18.E.G.Nadjakov, K.P.Marinova, Yu.P.Gangrsky, ADNDT, 56, (1994), 133
19.S.S.Vasiliev, N.N.Kolesnikov, L.Ya.Shevtvalov, Vestnik MGU, N5, (1969), 3
20.N.N.Kolesnikov, V.I.Tarasov, Izv.vuzov,Fizika, 40, (1997), 19
21.V.M.Strutinsky, Nucl.Phys. A95, (1967), 420
22.N.N.Kolesnikov, Izv.AN SSSR, 49, (1985), 2144
23.N.N.Kolesnikov, Int.Conf.on Nucl.Phys, St.Peterburg, 1999, p.384

Coherent Repopulation of Hyperfine Levels by Bichromatic Wave and Nuclear Spectroscopy

David F. Zaretsky and Stanislav B. Sazonov

Kurchatov Institute, Moscow, Russia.

In recent years a novel method of atomic spectroscopy based on coherent population trapping (CPT) in the case of bichromatic wave resonance interaction with three level atomic system has been developed. This method in the case of hyperfine structure is displayed on fig.1.

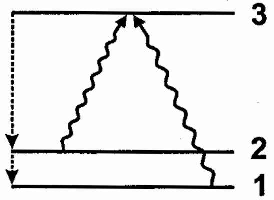

Fig. 1

In this case the hyperfine structure splitting ΔE_{12} is much less than the quanta energy: $\omega_1-\omega_2 \approx \Delta E_{12} << \omega_{1,2}$ The field of bichromatic wave has the form:

$$E = E_1 \cos(\omega_1 t - k_1 r) + E_2 \cos(\omega_2 t - k_2 r).$$

The population amplitude of level 3 is determined by the sum of amplitude corresponding to the transitions 1⇔3 and 2⇔3 and the result depends on the phase φ between the components of bichromatic wave. There may be the destructive interference of these amplitudes. These situation is named " population trapping". Normally the population of level 3 is investigated in the case of permanent lasers. But in the case of short time interaction of bichromatic wave with moving atoms or for non-stable atoms the pulsed laser regime may be preferable. Therefore we considered the population of level 3 in pulsed regime when the Rabi period is shorter than all other times. In this case to calculate the population amplitudes we may use the wave function formalism. As a result we obtained the time averaged difference of levels 1 and 2 populations P:

$$P = \overline{|a_2(t)|^2 - |a_1(t)|^2} = (V_1^2 - V_2^2)\left[(V_1^2 + V_2^2)/2 - 3V_1V_2\cos\varphi\right]\Omega^{-4},$$

where V_1 ,V_2 are the matrix elements for resonance 1⇔3 and 2⇔3 transitions; $\Omega = \sqrt{V_1^2 + V_2^2}$ is Rabi-frequency. The population of level 3 is zero at any time when the phase φ, V_1 and V_2 are up to the mark:

$$\cos\varphi = -(V_1^2 + V_2^2)/2V_1V_2.$$

It is clear that there is no polarization in the case $V_1^2 = V_2^2$. But when $V_1^2 \neq V_2^2$ these should be polarization. For example, let $V_2^2 = V_1^2/2$ and $\varphi = \pi$ we have P=0,64.

What are the preferences of bichromatic wave polarization in comparison with optical pumping?

1. This method is practically Doppler-free. Indeed for an atom moving with velocity v the resonance with atomic transition ω_{13} and ω_{23} will be achieved when $\omega_1 = \omega_{13} + k_1 v$; $\omega_2 = \omega_{23} + k_2 v$, where $k_{1,2}$ are the wave vectors of partial components of bichromatic wave. In the resonance case the difference between the frequency of components is $\omega_1 - \omega_2 = \Delta\omega_{12} + \Delta k_{1,2} v$.

   If $k_1 \| k_2$ then $\Delta k_{12} v \leq \Delta\omega_{12} v/c << \Delta\omega_{12}$. Therefore in resonance case $\omega_1 - \omega_2 \cong \Delta\omega_{12}$ and the hyperfine structure may be investigated when the Doppler width is larger than $\Delta\omega_{12}$. The possible idea to measure the difference $\Delta\omega_{12}$ is displayed on fig.2 These experiments correspond to the population trapping case.

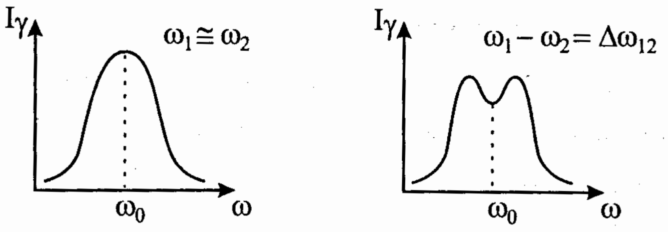

Fig. 2

2. The repopulation of hyperfine levels may be obtained during the time much shorter than the optical pumping time. This possibility is essential in the case when the time of life of nonstable atom is less than the time of optical

pumping. The second case is connected with the spectroscopy of fast moving atoms. D/v<<1/γ. D/v is the time of interaction atoms with the bichromatic wave; 1/γ is the relaxation time (fig.3).

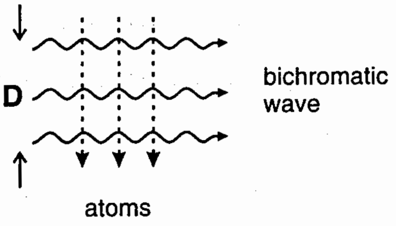

Fig. 3

3. There are difficulties for optical pumping when an atom has metastable states. But in the method proposed there is no problem with metastable states.

Referents:

1. Zaretsky, D.F., and Sazonov, S.B.,*Physics Letters A* **198,** 55-57 (1995)
2. Zaretsky, D.F., and Sazonov, S.B.,*Pis'ma Zh. Eksp. Teor. Fiz.* **60,** 682-685 (1994)

ELECTRIC DIPOLE MOMENTS AND ION STORAGE RINGS

I.B. Khriplovich

Budker Institute of Nuclear Physics, 630090 Novosibirsk, Russia

Upper limits on the electric dipole moments (EDM) of elementary particles and atoms are presented, and their physical implications are discussed. The bounds following from the neutron and atomic experiments are comparable. The nuclear EDMs can be studied at ion storage rings, with the expected sensitivity much better than 10^{-24} e cm. It would be a serious progress in the studies of the CP violation.

1. UPPER LIMITS ON ELECTRIC DIPOLE MOMENTS

Up to now, CP violation has been reliably observed only in the decays of the K^0 mesons. Recently, indications of CP violations were found in $B_d^0/\bar{B}_d^0 \to J/\psi K_S^0$ decays. Though the effects observed can be accomodated within the Standard Model, their true origin still remains mysterious.

Extremely important information on the origin of CP violation follows from the searches for electric dipole moments of the neutron, electron and atoms. The EDM of a nondegenerate quantum-mechanical system is forbidden by time-reversal symmetry T (and by parity conservation). T invariance and CP invariance are equivalent, due to the CPT theorem, which is based on very strong physical grounds. Detailed discussion of discrete symmetries (as well as of other problems touched upon in the talk) can be found, for instance, in book [1].

1.1 Elementary particles

The experimental upper limit on the neutron EDM is [2-4]

$$d_n < (6-10)\times 10^{-26}\ e\,\mathrm{cm}. \tag{1}$$

The sensitivity of these experiments can be, hopefully, improved by 2 – 3 orders of magnitude.

The best upper limit on the electron EDM

$$d_e < 4\times 10^{-27}\ e\,\mathrm{cm} \tag{2}$$

was obtained in atomic experiment with Tl [5]. Hopefully, this limit can be pushed well into the 10^{-28} e cm range.

I would like to quote here one more upper limit, that on the muon EDM [6]:

$$d_\mu < 10^{-18}\ e\,\mathrm{cm}. \tag{3}$$

An experiment was recently proposed to search for the muon EDM with the sensitivity of 10^{-24} e cm [7]. We will come back to this proposal in Section 3.

The predictions of the Standard Model are, respectively:

$$d_n \sim 10^{-32} \; - \; 10^{-31} \; e\,\mathrm{cm}; \tag{4}$$

$$d_e < 10^{-40} \; e\,\mathrm{cm}; \tag{5}$$

$$d_\mu < 10^{-38} \; e\,\mathrm{cm}. \tag{6}$$

1.2 Atoms and nuclei

The best upper limit on EDM of anything was obtained in atomic experiment with ^{199}Hg [8]. The result for the dipole moment of this atom is

$$d(^{199}\mathrm{Hg}) < 9 \times 10^{-28} \; e\,\mathrm{cm}. \tag{7}$$

Unfortunately, due to the electrostatic screening of the nuclear EDM in this essentially Coulomb system, the implications of the result (7) are somewhat less impressive. If one ascribes the atomic dipole moment to the EDM of the valence neutron in the even-odd nucleus ^{199}Hg, the corresponding upper limit on the neutron EDM will be an order of magnitude worse than the direct one (1).

It has been demonstrated, however, that the dipole moments of *nuclei* induced by the T- and P-odd nuclear forces can be about two orders of magnitude larger than the dipole moment of an individual *nucleon* [9]. In the simplest approximation of the shell model, where the nuclear spin coincides with the total angular momentum of an odd valence nucleon, while the other nucleons form a spherically symmetric core with the zero angular momentum, the effective T- and P-odd single-particle potential for the outer nucleon is

$$W = \frac{G}{\sqrt{2}} \frac{\xi}{2m_p} \boldsymbol{\sigma} \nabla \rho(r). \tag{8}$$

Here ξ is a dimensionless constant characterizing the strength of the interaction in units of the Fermi weak interaction constant G; $\boldsymbol{\sigma}$ and $\mathbf{r}$ are the spin and coordinate of the valence nucleon. Using the fact that the profiles of the nuclear core density $\rho(r)$ and the potential $U(r)$ are close, one can easily find now the perturbation of the wave function caused by the interaction (8). The characteristic value of the thus induced nuclear EDM is

$$d_{\mathrm{N}} \sim \; 10^{-21} \xi \; e\,\mathrm{cm}. \tag{9}$$

Being interpreted in terms of the CP-odd nuclear forces, the experimental result (7) leads to the following upper limit:

$$\xi < 2 \times 10^{-3}. \tag{10}$$

The Standard Model (SM) prediction for this constant is

$$\xi \sim 10^{-9}. \tag{11}$$

Thus, the theoretical predictions of the SM for dipole moments and CP-odd nuclear forces are about six orders of magnitude below the present experimental upper limits on them. But does this mean that the discussed experiments are of no serious interest for elementary particle physics, that they are nothing but mere exercises in precision spectroscopy? Just the opposite. It means that *the searches for electric dipole moments now, at the present level of accuracy, are extremely sensitive to possible new physics.*

1.3 Beyond the Standard Model

One could argue that the discussed experiments have ruled out more theoretical models than any other set of experiments in the history of physics. Still, theoretical models of CP violation surviving up to now, are to numerous to discuss all of them, and most of them have too many degrees of freedom. It is convenient therefore to proceed in a phenomenological way: to construct CP-odd quark-quark, quark-gluon and gluon-gluon operators of low dimension, and find upper limits on the corresponding coupling constants from the experimental results for d_n and $d(^{199}\mathrm{Hg})$. The analysis performed in [10,11], has demonstrated that the limits on the effective CP-odd interaction operators obtained from the neutron and atomic experiments are quite comparable. These limits are very impressive. All the constants are several orders of magnitude less than the usual Fermi weak interaction constant G. In particular, these limits strongly constrain some popular models of CP violation, such as the model of spontaneous CP violation in the Higgs sector, and the model of CP violation in the supersymmetric SO(10) model of grand unification.

2. NUCLEAR ELECTRIC DIPOLE MOMENTS AT ION STORAGE RINGS

The various upper limits on EDMs set so far constitute a valuable contribution to elementary particle physics and to our knowledge of how the Nature is arranged; the null results obtained so far are important. But it is only natural to think of essential progress in the field, of finding a positive result, of eventually discovering permanent electric dipole moment. So, let me add to the above rather old stories, a new one. It should be started with the discussion of new experiment.

2.1 Idea of new muon EDM experiment

A new experiment was recently proposed to search for the muon EDM [7]. The intention is to use a storage ring, with muons in it having natural longitudinal polarization. An additional spin precession due to the EDM interaction with external field should be monitored by counting the decay electrons, their momenta being correlated with the muon spin, due to parity nonconservation in the muon decay.

The frequency $\boldsymbol{\omega}$ of the spin precession with respect to the particle momentum in external magnetic and electric fields, $\mathbf{B}$ and $\mathbf{E}$, is

$$\begin{aligned} \boldsymbol{\omega} = & -\frac{e}{m}\left[a\mathbf{B} - a\frac{\gamma}{\gamma+1}\mathbf{v}(\mathbf{v}\mathbf{B}) - \left(a - \frac{1}{\gamma^2-1}\right)\mathbf{v}\times\mathbf{E}\right] \\ & -\eta\frac{e}{m}\left[\mathbf{E} - \frac{\gamma}{\gamma+1}\mathbf{v}(\mathbf{v}\mathbf{E}) + \mathbf{v}\times\mathbf{B}\right]. \end{aligned} \tag{12}$$

Here the anomalous magnetic moment a is related to the g-factor as follows: $a = g/2 - 1$ (for muon $a = \alpha/2\pi$); $\mathbf{v}$ is the particle velocity; $\gamma = 1/\sqrt{1-v^2}$. The last line in this formula describes the precession due to the EDM d, the dimensionless constant η being related to d as follows:

$$d = \frac{e}{2m}\eta \,.$$

Expression (12) simplifies in the obvious way for $(\mathbf{vB}) = (\mathbf{vE}) = 0$. Just this case is considered below.

The remarkable idea of [7] is to compensate for the usual precession in the vertical magnetic field $\mathbf{B}$ by the precession in a radial electric field $\mathbf{E}$, i.e., to choose $\mathbf{E}$ in such a way that the first line in (12) vanishes at all. Then the spin precession with respect to momentum is due only to the EDM interaction with the vertical magnetic field, and since electric fields in a storage ring are much smaller than magnetic ones, it reduces to

$$\omega = \omega_e = -\frac{e}{m}\eta\,\mathbf{v}\times\mathbf{B}. \tag{13}$$

In this way the muon spin acquires a vertical component which linearly grows with time. The P-odd correlation of the decay electron momentum with the muon spin leads to the difference between the number of electrons registered above and below the orbit plane.

In [7], it is stated that the limit on the muon EDM can be improved in the planned experiment by six orders of magnitude, to 10^{-24} e cm.

2.2 Nuclear dipole moments at storage rings

In the same way one can search for an EDM of a polarized β-active nucleus in a storage ring [15]. In this case as well, the precession of nuclear spin due to the EDM interaction can be monitored by the direction of the β-electron momentum.

β-active nuclei have serious advantages as compared to muon. The life-time of a β-active nucleus can exceed by many orders of magnitude that of a muon. The characteristic depolarization time of the ion beam is also much larger than the muon life-time, which is about 10^{-6} s. According to the estimates by I. Koop (to be published), the ion depolarization time can reach few seconds. Correspondingly, the angle of the rotation of nuclear spin, which is due to the EDM interaction and which accumulates with time, may be also by orders of magnitude larger than that of a muon. By the same reason of the larger life-time, the quality of an ion beam can be made much better than that of a muon beam.

However, necessary conditions here are also quite serious.

First of all, to make realistic the mentioned compensation of the EDM-independent spin precession by a relatively small electric field, the effective nuclear g-factor should be close to 2 (as this is the case for the muon). For a nucleus with the total charge Ze, mass Am_p, spin I, and magnetic moment μ, the effective anomalous magnetic moment is now

$$a = \frac{g}{2} - 1 = \frac{A}{Z}\frac{\mu}{2\mathrm{I}} - 1.$$

Fine-tuning of a is possible in many cases by taking, instead of a bare nucleus, an ion with closed electron shells. An accurate formula for the anomaly of an ion with the total charge z, is

$$a = \frac{A}{2z}\frac{\mu}{\mathrm{I}} - 1.00722 + \frac{\Delta}{Am_p} - \frac{z}{A}\frac{m_e}{m_p}. \tag{14}$$

As distinct from [15], we have included here the correction for the atomic mass excess Δ.

The ions which look at the moment promising from the point of view of the EDM searches are presented in Tables 1, 2. The isotope data are taken from the handbook [16]. The β-decaying excited states are marked in Table 1 by *.

The errors in the values of anomalous magnetic moments a, presented in Tables 1, 2, correspond to the experimental errors in values of μ. In fact, electron configurations, even with vanishing angular momentum J_e, produce a diamagnetic screening of nuclear magnetic moments. In most cases this correction, neglected here, is inessential indeed, but it is truly large for ${}^{24}_{11}$Na, changing its a-value from 0.0065, as presented in Table 1, to about - 0.1.

Table 1: Ion properties

	$I^\pi \to I^{\pi\prime}$	μ	z	$a \times 10^3$	$t_{1/2}$	Q (barn)	branching
${}^{24}_{11}$Na	$4^+ \to 4^+$	1.6903(8)	5	6.5(0.5)	15 h		99.944%
${}^{60}_{27}$Co	$5^+ \to 4^+$	3.799(8)	23	- 17(2)	5.3 y	0.44	99.925%
${}^{82}_{35}$Br	$5^- \to 4^-$	1.6270(5)	13	18.0(0.3)	35 h	0.75	98.5%
${}^{94}_{37}$Rb	$3^- \to 3^-$	1.4984(18)	23	12.5(1.2)	2.7 s	0.16	30.6%
${}^{110}_{47}$Ag*	$6^+ \to 5^+$	3.607(4)	33	- 6(1)	250 d	1.4	66.8%
${}^{118}_{49}$In*	$8^- \to 7^-$	3.321(11)	25	- 28(3)	8.5 s	0.44	1.4%
${}^{120}_{49}$In*	$(8^-) \to 7^-$	3.692(4)	27	17(1)	47 s	0.53	84.1%
${}^{121}_{50}$Sn	$3/2^+ \to 5/2^+$	0.6978(10)	28	2.9(1.4)	27 h	- 0.02(2)	100%
${}^{125}_{51}$Sb	$7/2^+ \to 5/2^+$	2.630(35)	47	- 9.0(1.3)	2.8 y		40.3%
${}^{131}_{53}$I	$7/2^+ \to 5/2^+$	2.742(1)	51	- 1.9(0.4)	8.0 d	- 0.40	89.9%
${}^{133}_{53}$I	$7/2^+ \to 5/2^+$	2.856(5)	53	16(2)	21 h	- 0.27	83%
${}^{133}_{54}$Xe	$3/2^+ \to 5/2^+$	0.81340(7)	36	- 6.37(9)	5.2 d	0.14	99%
${}^{134}_{55}$Cs	$4^+ \to 4^+$	2.9937(9)	51	- 24.9(0.3)	2.0 y	0.39	70.11%
${}^{136}_{55}$Cs	$5^+ \to 6^+$	3.711(15)	51	- 18(4)	13 d	0.22	70.3%
${}^{137}_{55}$Cs	$7/2^+ \to 11/2^-$	2.8413(1)	55	3.0(0.1)	30 y	0.051	94.4%

Table 2: Ion properties (continued)

	$I^\pi \to I^{\pi\,\prime}$	μ	z	$a \times 10^3$	$t_{1/2}$	Q (barn)	branching
$^{139}_{55}$Cs	$7/2^+ \to 7/2^-$	2.696(4)	53	2(1)	9.3 m	- 0.075	82%
$^{141}_{55}$Cs	$7/2^+ \to 7/2^-$	2.438(10)	49	- 6(4)	25 s	- 0.36	57%
$^{143}_{55}$Cs	$3/2^+ \to 5/2^-$	0.870(4)	41	3(5)	1.8 s	0.47	24%
$^{140}_{57}$La	$3^- \to 3^+$	0.730(15)	17	- 6±21	1.7 d	0.094	44%
$^{160}_{65}$Tb	$3^- \to 2^-$	1.790(7)	47	8(4)	72 d	3.8	44.9%
$^{170}_{69}$Tm	$1^- \to 0^+$	0.2476(36)	21	- 5±14	129 d	0.74	99.854%
$^{177}_{71}$Lu	$7/2^+ \to 7/2^-$	2.239(11)	57	- 15(5)	6.7 d	3.4	78.6%
$^{183}_{73}$Ta	$7/2^+ \to 7/2^-$	(+)2.36(3)	61	4±13	5.1 d		92%
$^{196}_{79}$Au	$2^- \to 2^+$	0.5906(5)	29	- 9.5(0.8)	6.2 d	0.81	8%
$^{198}_{79}$Au	$2^- \to 2^+$	0.5934(4)	29	5.4(0.7)	2.7 d	0.68	98.99%
$^{203}_{80}$Hg	$5/2^- \to 3/2^+$	0.84895(13)	34	6.31(0.15)	47 d	0.34	100%
$^{222}_{87}$Fr	$2^- \to 3^-$	0.63(1)	35	- 8± 16	14 m	0.51	55%
$^{223}_{87}$Fr	$3/2(^-) \to 3/2^-$	1.17(2)	87	- 7±20	22 m	1.2	67%
$^{224}_{87}$Fr	$1(^-) \to 1^-$	0.40(1)	45	- 11± 25	3.3 m	0.52	42%
$^{242}_{95}$Am	$1^- \to 0^+, 2^+$	0.3879(15)	47	- 8.4± 3.9	16 h	- 2.4	37%,46%

All isotopes presented in Tables 1, 2 are β^--active (their β^- branchings are indicated in the last column). Fortunately, many of them have allowed pure Gamow – Teller transitions ($|\Delta I| = 1$) where the magnitude of the needed correlation between the electron momentum and the initial spin is of the order of unity. Few isotopes in the tables have allowed mixed β^--transitions ($|\Delta I| = 0$). Here the magnitude of the needed asymmetry may change essentially from nucleus to nucleus. Obviously, for the allowed mixed transitions, as well as for forbidden transitions which are also presented in the tables, the values of the discussed asymmetry should be found experimentally.

On the other hand, if a sufficiently large EDM signal can be attained, if the angle of the spin rotation can reach, say, a milliradian, one could think about an experiment with stable nuclei or nuclei of a large life-time. Their polarization could be measured in scattering experiments (the idea advocated by Y. Semertzidis and A. Skrinsky). Among stable nuclei, the most suitable one seems to be $^{139}_{57}$La, with $a = -0.039$ for the bare nucleus and $a = -0.004$ for its helium-like ion.

The nuclear polarization can be obtained, for instance, starting with a hydrogen-like ion. For $Z \sim 50$, typical frequencies of hyperfine ground state transitions in these ions are close to the optical region. The ion can be polarized by optical pumping, and then stripped. A helium-like ion with polarized nucleus can be obtained from a polarized hydrogen-like one through the electron capture.

In principle, the demand $a \ll 1$ can be softened by going over to small velocities, $v/c \ll 1$. This would enhance the relative weight of the compensating electric field. However, in this case one looses in the magnitude of the EDM signal.

But how significant would be the discussed experiments with nuclei for elementary particle physics?

The typical value of a nuclear EDM, as induced by CP-odd nuclear forces, is roughly independent of A and Z, and can be estimated by formula (9). The upper limit (10) on ξ corresponds to the bound

$$d_N < 2 \times 10^{-24}\, e\,\mathrm{cm}, \tag{15}$$

and is at least as significant for elementary particle physics as the upper limit on the neutron EDM. So, even at the same sensitivity 10^{-24} e cm, as discussed in [7] for muons, the experiments with nuclei would compete with the best present EDM results. Certainly, progress in this direction well deserves serious efforts.

Acknowledgements

The work was supported by the Russian Foundation for Basic Research through Grant No. 98-02-17797 and by the Federal Program Integration–1998 through Project No. 274.

REFERENCES

1. I.B. Khriplovich and S.K. Lamoreaux, CP Violation without Strangeness, Springer, 1998.
2. K.F. Smith *et al*, Phys. Lett. B, 234, (1990) 191.
3. I.S. Altarev *et al*, Phys. Lett. B, 276 (1992) 242.
4. P.G. Harris *et al*, Phys. Rev. Lett., 82 (1999) 904.
5. E.D. Commins, S.B. Ross, D. DeMille, and B.C. Regan, Phys. Rev. A, 50 (1994) 2960.
6. J. Baily *et al*, Zs. Phys. G, 4 (1978) 345.
7. Y.K. Semertzidis, in Proceedings of the Workshop on Frontier Tests of Quantum Electrodynamics and Physics of the Vacuum, Sandansky, Bulgaria, June 1998.
8. S.K. Lamoreaux *et al*, Phys. Rev. Lett., 59 (1987) 2275.
9. O.P. Sushkov, V.V. Flambaum, and I.B. Khriplovich, Zh. Eksp. Teor. Fiz., 87 (1984) 1521; [Sov. Phys. JETP, 60 (1984) 873].
10. V.M. Khatsymovsky, I.B.Khriplovich, A.S. Yelkhovsky, Ann. Phys., 186 (1988) 1.
11. V.M. Khatsymovsky and I.B.Khriplovich, Phys. Lett. B, 296 (1992) 219.
12. P. Herczeg *et al*, to be published.
13. L. Wolfenstein, Nucl. Phys. B, 77 (1974) 375.
14. P. Herczeg, in Tests of Time Reversal Invariance in Neutron Physics, World Scientific, Singapore, 1987.
15. I.B.Khriplovich, Phys. Lett. B, 444 (1998) 98.
16. R.B. Firestone *et al*, Table of Isotopes, 8th Edition, John Wiley, 1996.

PERSISTENCE OF MAGIC NUMBERS FAR FROM THE BETA-STABILITY LINE

Z.Dlouhý
Nuclear Physics Institute ASCR, 250-68, Řež, Czech Republic
Collaboration GANIL - Orsay - Dubna - Řež - Bucurest

1. Introduction

The study of the properties of extremely neutron- or proton-rich nuclei of light elements is considered as an important and interesting research topic in modern nuclear physics. The interest in this field has been stimulated by the intriguing phenomenon that nuclei lying near the drip lines - the boundaries of the nuclear stability - have revealed "skin" or "halo" structure [1]. The synthesis and investigation of the properties of these nuclei are studied using the radioactive nuclear beams (RNB) produced at cyclotron facilities at GANIL - Caen (France) and FLNR - Dubna (Russia). RNB play an important role in this field of physics and cannot be substituted by other method.

In early 90's, the elastic scattering of RNB on different light targets has been used to study the nucleon halo in ^{11}Li [2] and ^{8}B [3]. The measurement of the dissociation, breakup and total reaction cross sections on the ^{28}Si target has established the halo structure in ^{11}Be and ^{8}B [4,5].

However, the fundamental question of nuclear structure near the drip line is whether the magic numbers are universal or are subjected to a change in certain regions far from stability or even disappear altogether. Such magicity breaking has been already observed at the N=20 shell closure for neutron-rich nuclei where "the island of inversion" has been pointed out [6]. The anomalous behaviour in the binding energy near the shell closure N=20 and 28 and the onset of the deformation in this region are closely connected to this question.

The aim of experiments was to study the particle stability of these nuclei, their masses, which constitutes the basic knowledge of the nucleus, and their spectroscopic characteristics. However, the inaccessibility of these short-lived nuclides means that very little is known about their spectroscopy. Spectroscopic measurements can reveal details of the underlying microscopic structures and have proved essential for understanding these unexpected properties as well as the precise location of the neutron drip line itself. Furthermore, they potentially provide a stringent test of the modern large scale shell model calculations applied to elucidate these problems [7].

2. Experiment

The experiment was carried out on a doubly achromatic spectrometer LISE3 [8] at GANIL. The fragmentation of a $^{36}S^{16+}$ (78.1 AMeV) beam of a mean intensity of 800 enA on the ^{181}Ta target (643 μm), followed by a C(102 μm) stripping foil to regroup the charge state has been used. This arrangement was expected to increase the production rate of the neutron-rich isotopes near $N = 20$ with respect to the former experiments. Reaction products have been focused and separated by a system of quadrupole lenses, two dipole magnets operated in an achromatic mode with rigidity 4.3 and 3.2 Tm, and a Wien filter. After passing through the spectrometer (total flight-path of 42m), the products were identified unambiguously by time-of-flight method, energy loss, and total kinetic energy (TKE) measurement. A detector telescope consisting of three planar surface barrier Si detectors with thickness of 300 μm, 300 μm, 500 μm and two 5 mm thick Si(Li) detectors, was mounted in a vacuum chamber at the achromatic focal point of LISE3. The time-of-light of the fragments was measured with respect to the radio-frequency signal derived from the cyclotron. The first three detectors allowed to make an independent Z identification of the ion. The masses (A) and atomic charges (Q) of the nuclei were derived from the total energy, time-of-light and magnetic rigidity measurements. The thickness of the detectors was chosen in the way to stop the neutron-rich fragments of the oxygen-neon region in the first 5 mm thick detector. One of the Si detectors was position-sensitive one and was used for spatial analysis of the secondary beam. The signals from each of the Si(Li) detectors were split into two branches; the first serves for residual energy measurements, the second for the detection of electrons from the β-decay following the implantation of a given ion. The implantation detectors were surrounded by 60 ^{3}He neutron counters and four 70% HPGe detectors for the measurement of $\beta - n$ and $\beta - \gamma$ coincidences and the search for microsecond isomeric states. The β-decay half-lives were obtained on an event-by-event basis using the measured time difference between the implantation of the ion of interest and the first β- particle subsequently detected in the same detector.

By correlating the implantation of the selected ions with their subsequent β-decay or β-delayed γ-decays, this highly selective experiment succeeded in identifying β-particles and γ-rays emitted by the previously unstudied nuclides.

3. Particle stability of heavy oxygen ions

The aim of the experiment was to establish the particle stability of nuclei in vicinity of the double magic nucleus ^{28}O. Most of theoretical models predicted stability for ^{26}O, while the ^{28}O nucleus was predicted to be particle unstable despite the fact that it is a double magic nucleus. In our experiment, no events corresponding to ^{26}O and ^{28}O have been observed. The identification matrix is shown in fig.1.

According to the experimental dependence of measured yield of light exotic nuclei with N=20 on their atomic numbers we could expect about 11 events of ^{28}O to be detected during 53 hour measurement. Thus the unbound character of both ^{26}O and ^{28}O nuclei was firmly established [8].

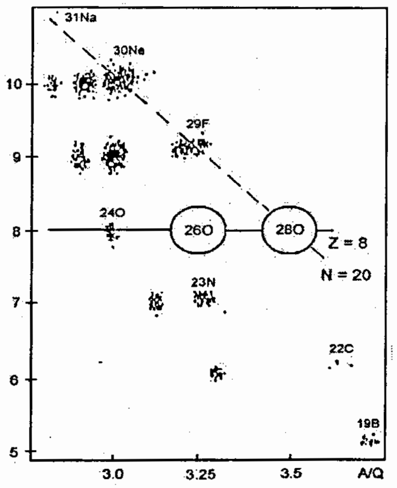

Fig. 1. Identification matrix.

Upper limits of the cross sections for the formation of the oxygen isotopes are estimated to be 0.7 pb and 0.2 pb for ^{26}O and ^{28}O, respectively. Our finding of particle unstability of ^{28}O could fairly support the idea that the nature of the onset of the deformation found in the Ne-Al region can influence the closure of the neutron shell N=20 in the ^{28}O nucleus.

4. β-decay half-lives

The deformation of nuclei close to this region could also result in effects which can influence the decay properties of these nuclei. The measurement of the β-decay of neutron-rich nuclei has been carried out using a Si semiconductor telescope mounted at the focal plane of the LISE3 spectrometer. The energy of the emitted β-particle E_b has been measured in two last Si(Li) detectors. The half-lives were determined on the basis of the time difference measured between the implantation of the ion in the residual E detector and the signal of the β-particle E_b. Thus an important information on the nuclear structure in this region has been obtained. The half-lives of β- decay of neutron-rich nuclei of fluorine, neon and sodium with N~20 are shown in the Table. Values for ^{26,27,29}F and ^{30}Ne were measured for the first time [9].

Table. Characteristics of β - decay of neutron-rich nuclei at N~20

	This work			Other works [10]		SM [11]	SM[a]
A/Z	Events	$T_{1/2}$[ms]	P_n[%]	$T_{1/2}$[ms]	P_n[%]	$T_{1/2}$[ms]	$T_{1/2}$[ms]
^{26}F	44 949	9.6(0.8)	11(4)			12.8	7.8
^{27}F	9 651	5.2(0.3)	90(30)			7.8	4.7
^{29}F	866	2.4(0.4)	100(80)			2.7	1.4
^{27}Ne	13 110	22(6)	0(3)	32(2)	2.0(0.5)		
^{28}Ne	112 877	20(3)	11(3)	17(4)	22(3)	16.9	12.9
^{29}Ne	7 955	15(4)	27(9)	200(100)		7.4	28.2
^{30}Ne	4 812	7.5(1.5)	9(17)			3.7	17.8
^{30}Na	40 632	50(4)		48(2)	30(4)	24.7	56
^{31}Na	97 011	16.9(1.5)		17.0(0.4)	37(5)	11.8	16.4

[a] we performed the shell-model calculation with the Strasbourg-Madrid SM code ANTOINE.

A relatively good overall agreement exists between our calculation and the experimental data. The calculations of Wildenthal et al. [10] are also presented in the Table.

5. β-delayed γ-decay

Since spectroscopic measurements can reveal details of the underlying microscopic structures, the in-beam γ-ray spectroscopy is a very effective tool for this study. Although the neutron drip line has probably been delimited for elements below neon and atomic masses of many of these nuclei have been measured, comparatively little is known about their radioactive decay characteristics or spectroscopy. Such measurement can probe important details of the underlying microscopic structures which give rise to the novel phenomena.

In our experiment, the correlation between the implantation of the selected ions and their subsequent β-delayed γ-decays measured by four tapered germanium detectors enable us to identify the γ-rays emitted by the previously unstudied nuclides ^{24}F, $^{25-27}$Ne and $^{27-29}$Na [12]. In the fig.2., one can see calculated and experimental energy levels built on the measurement of ^{24}F. Energy levels were calculated using the SM code OXBASH with a) USD interaction; b) the SDPOTA and c) interaction of Chung and Wildenthal [13]. The tentative partial level scheme deduced from our measurement of γ-ray transitions is shown as d). The low level of statistics has not allowed γ-γ coincidences to be studied and hampered the deduction of decay schemes.

However, having identified candidate transitions in the nuclides of interest it is possible, in next experiment, to gate on these to extract coincident γ-rays using more prolific production methods combined with a more efficient detector array.

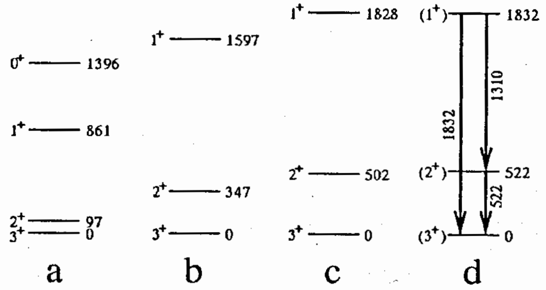

Fig. 2. Comparison of calculated and experimental energy levels of ^{24}F (see text).

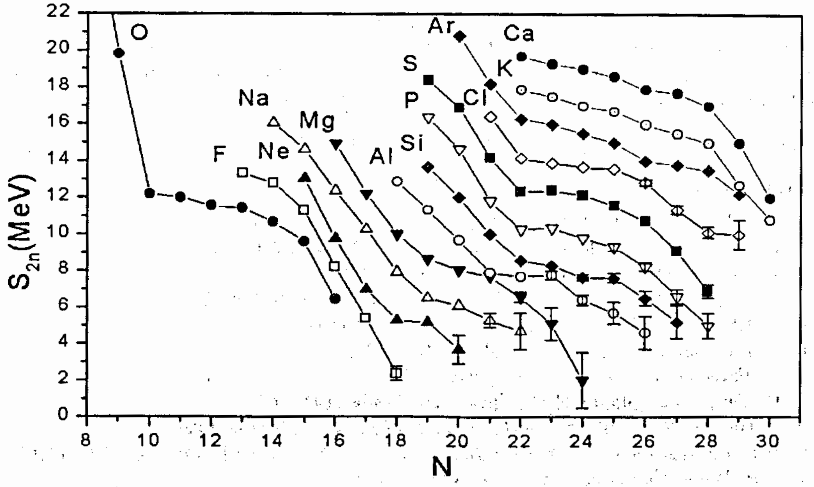

Fig. 3. Experimental S_{2n} values between the N=20 and N=28 shell closures.

6. Measurement of masses and separation energies

A present fundamental question for nuclear structure is whether the magic numbers are universal or whether they change in certain regions far from stability or even disappear altogether. To explain the behaviour of neutron shell closures N=20 and 28 the new mass measurements of 20 isotopes in the C-Cl range were performed.

Only a few masses of neutron-rich nuclei are known between the N=20 and N=28 shell closure. However, the measurements of these masses are direcly related to the binding energies and therefore constitute one of the most fundamental information one can get on these nuclei. In particular, the evolution of the binding energy of isotopes is illustrated by one of its derivatives, the separation energy of the two last neutrons S_{2n}.

$$S_{2n}(A,Z) = [M(A-2,Z) - M(A,Z) + 2M_n]c^2.$$

In the experiment done recently at GANIL [14] we succeeded in the measurement of the masses of the following heaviest isotopes of elements from F up to Cl, namely ^{27}F, ^{30}Ne, ^{33}Na, ^{39}Al, ^{41}Si, ^{43}P, ^{44}S and ^{46}Cl with the uncertainty better than +/- 1MeV, while in the lighter ones, the error bars are less than +/- 0.5MeV. In ^{35,36}Mg the errors are higher. These masses have been measured for the first time. In fig.3, the separation energies S_{2n} are plotted. Our new data are presented with error bars. In particular, the ^{43}P and ^{44}S, N=28 nuclei, appeared to be less bound than predicted which constitutes a new evidence of the weakening of the N=28 shell closure. This behaviour may result in a possible vanishing of the N=28 shell closure at least for these two elements. It seems very probable that the bounds of the neutron drip line can be shifted towards even more neutron-rich nuclei.

The synthesis and investigation of these extremely neutron-rich isotopes are crucial for better understanding of the nature of the nuclear interaction. The study of shell closures N=20 and 28 are particularly interesting since the vanishing of the latter one could be the first evidence of the weakening of the spin-orbit force in neutron-rich nuclei.

This work has been supported by Grant Agency of Czech Acad. Sci. N°. A 1048 605.

References

1. P.G. Hansen and B. Jonson, *Europhys. Lett.* **4** (1991) 275c.
2. M. Lewitowicz, Z. Dlouhý *et al., Nucl. Phys.* **A562** (1993) 301.
3. I. Pecina, Z. Dlouhý *et al., Phys. Rev.* **C52** (1995) 191.
4. F. Negoita, C. Borcea, Z. Dlouhý *et al., Phys. Rev.* **C52** (1995)
5. C. Borcea, Z. Dlouhý *et al., Nucl. Phys.* **A616** (1997) 231.
6. T. Motobayashi *et al., Phys. Lett.* **B346** (1995) 9.
7. A. Poves *et al., Z.Phys.* **A347** (1994) 227.
8. O. Tarasov, Z. Dlouhý et al., Phys. Lett. **B409** (1997) 64.
9. Z. Dlouhý, Yu. Penionzhkevich, *et al., J. of Phys. G* **25** (1999) 859.
10. R.B. Firestone and V.S. Shirley *Table of Isotopes 8th edn LBL, Univ. of Cal.* (1996)
11. B.H. Wildenthal *et al., Phys. Rev.* **C28** (1983) 1343.
12. A. Reed, O. Tarasov, C. Borcea, Z. Dlouhý, *et al., Phys. Rev.* **C** (1999) in press.
13. B.H. Wildenthal, *Progress in Part. and Nucl. Phys.* **11** (1984) 5.
14. F.Sarazin, D.Baiborodin, Z.Dlouhý *et al.: 37th Int.Wint. meet., Bormio,* (Jan.25-29.1999)

ONSET OF DEFORMATION IN NEUTRON-RICH N-ISOTOPES MEASURED BY A NEW β-LMR-NMR METHOD

G. Neyens, N. Coulier, D.L. Balabanski, R. Coussement, G. Georgiev, S. Ternier,
S. Teughels, K. Vyvey
University of Leuven, Instituut voor Kern-en Stralingsfysika, Celestijnenlaan 200 D, B-3001 Leuven, Belgium

M. Lewitowicz, W. Mittig, F. de Oliveira Santos, P. Roussel-Chomaz, N.A.Smirnova
GANIL, B.P. 5027, F-14076 Caen Cedex 5, France

W.F. Rogers,
Westmont College, 955 La Plaz Road, Santa Barbara, CA 93108 California USA

A. Lépine-Szily
Institute of Physics, University of Sao Paulo, C.P. 66318, 05389-970, Brazil

The electric quadrupole and magnetic dipole moments of the neutron rich nucleus ^{18}N ($I^\pi = 1^-$, $T_{1/2}$ = 624(12) ms) have been measured using a new β-NMR-LMR method. A quadrupole moment $|Q| = 2.7(4)$ efm^2 and a magnetic moment $|\mu| = 0.135(15)\ \mu_N$ have been deduced. The values are compared to shell model calculations using different cross-shell interactions in the *π0p-ν1s0d* model space.

The nucleus ^{18}N with Z=7 protons and N=11 neutrons, is a good probe to study the proton-neutron interaction between proton holes in the p-shell and valence neutrons in the sd-shell around the Z=N=8 shell closures. Very little is known experimentally on this nucleus, apart from its ground state spin I=1 and some excited levels from a mass measurement [1] and two beta-decay studies [2,3]. Until now, none of the existing shell models is able to calculate the experimentally determined spin I=1 [2] for the ^{18}N ground state: all theories result in I=2 [2,4-8]. In figure 1, the experimental level scheme of ^{18}N is compared to some shell model calculations in which different p-sd interactions were used.

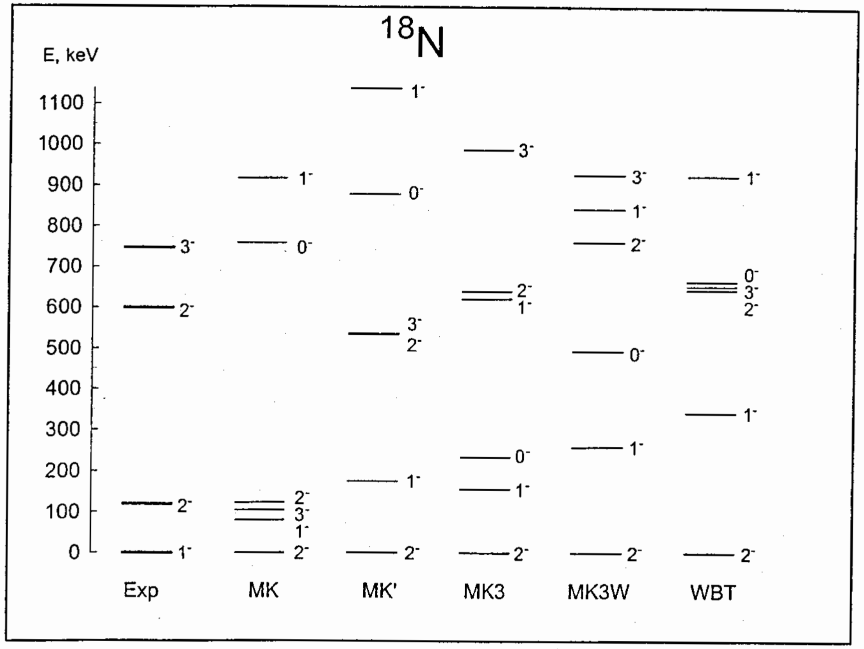

Figure 1 : Comparison of the experimental level scheme of ^{18}N to some calculated ones, using different interactions in the p-sd model space. The MK' and MK3 are taken from literature [5,6], while the MK, MK3W and WBT were calculated using standard interactions from the OXBASH package. Non of the models reproduces the ground state spin I=1.

The calculations have been performed using the OXBASH code in a *psd* model space (for MK) and *spsdpf* model space (for MK3W and WBT). Calculations were restricted to $1\hbar\omega$ excitations. The labels below each calculated scheme refer to the type of interaction and parametrisation that was used for the cross-shell matrix elements between *0p* holes and *1s0d* particles. While the MK-interaction of Millener and Kurath [2,8] works well to describe the main features of particle-hole spectra of the majority of nuclei between ^{11}Be and ^{16}O, it fails to reproduce the level schemes of ^{16}N and ^{17}N. Barker has modified the MK-interaction by adapting the $p_{1/2}^{-1}d_{5/2}$ and the $p_{1/2}^{-1}s_{1/2}$ matrix elements in such a way that the ^{16}N level scheme is well reproduced [4]. A similar modification has been made by Millener (MK'), who shows

that this modified interaction gives a good agreement for ^{17}N and an improved agreement for the ^{18}N level scheme [5]. Warburton and Millener used the G-matrix approach [6] and fitted the interaction parameters in order to reproduce the particle-hole spectrum of A=16 nuclei. This new interaction, named MK3, was a first step towards a good particle-hole interaction which is optimised to describe a wide range of data in the ^{16}O-region with multi-particle and multi-hole configurations. Again the ^{17}N level scheme is well reproduced, but still the ground state spin for ^{18}N is calculated to be I=2. The most recently developed interactions in this mass region are the WBT and WBP interactions of Warburton and Brown [7]. They are obtained by an approach similar to that of deriving the MK3 interaction, but with a more elaborate procedure of fitting two-body matrix elements (WBT) or two-body potential strengths (WBP), as well as *p* shell two-body matrix elements, to the binding and excitation energies of nuclei in the A=10-22 mass region. Besides that, a monopole term has been added to the cross-shell potential.

Each of the interactions however fails to reproduce the ground state spin and a few known excited levels of ^{18}N. It is clear that when going away from the stability line, more and more sophisticated interactions need to be taken into account.

By measuring the nuclear moments of the ground state, we hope to get a deeper insight in the structure of this nucleus. The experiments have been performed at the LISE3 spectrometer at the Grand Accelerateur National d'Ions Lourds in France. A 95% pure beam of ^{18}N fragments was obtained from the fragmentation of a ^{22}Ne (60.3 MeV/u) beam onto a ^{9}Be target. The experiments have been described in detail in previous publications [9-11]. The spin-alignment obtained by selecting fragments in the forward direction after the fragmentation reaction, was transferred to polarisation by means of a combined magnetic dipole and electric quadrupole interaction. From the resonant onset of polarisation, detected via the onset of asymmetry in the beta-decay of the ^{18}N-nuclei, the magnetic and quadrupole moment could be deduced.

In table 1 we compare the experimental values to the calculated values, using some of the above described interactions. For the magnetic moment, the free g-factors have been used for protons and neutrons. In order to compare the theoretical quadrupole moments to the experimental value Q_{exp}=2.7(4) efm^2, an effective charge has to be introduced. Calculations were performed with a proton effective charge $e_\pi=1.3e$, which reproduces well the quadrupole moment of ^{13}B (a pure proton configuration). A typical value for the neutron effective charge is $e_\nu=0.4e$ giving good agreement for the quadrupole moment of ^{17}O (assuming a pure $\nu d_{5/2}$ configuration). However, with this neutron effective charge, the quadrupole moment of the ^{18}N ground state is systematically underestimated for all interactions. Therefore, we have modified the neutron effective charge for each interaction in order to reproduce the experimental Q-moment: the effective charge has to be increased by more than 50% in order to reproduce the experimental quadrupole moment.

Table 1: Nuclear dipole and quadrupole moments of the ^{18}N, 1^- and the ^{19}O, $5/2^+$ ground states calculated with the OXBASH code using HO wave functions in a psd model space using different interactions. The magnetic moments are calculated using free g-factors, the quadrupole moments are calculated with $e_\pi=1.3e$ and e_ν adapted in order to reproduce the experimental quadrupole moments $|Q_{exp}(^{18}N)|=2.7(4)$ efm^2 and $|Q_{exp}(^{19}O)|=0.37(4)$ efm^2. Experimental values are taken from this work, and from [12] for ^{19}O.

Interaction	$\mu(^{18}N)(\mu_N)$	$e_\nu(^{18}N)$	$\mu(^{19}O)(\mu_N)$	$e_\nu(^{19}O)$
MK	-0.289	0.75(10)	-1.570	0.57(6)
MK3W	-0.156	0.74(9)	-1.566	0.83(8)
WBT	-0.117	0.77(10)	-1.568	0.97(10)
$\|\mu_{exp}\|$	0.135(15)		1.53195(7)	

Recently the quadrupole moment of the ^{19}O, I=5/2$^+$ ground state has also been measured [12]. This nucleus with closed proton shell, has 3 neutrons outside the neutron N=8 shell in the $\nu d_{5/2}$ orbit. In the ground state these 3 neutrons are coupled to I=5/2$^+$, and at 96 keV an isomeric state ($T_{1/2}$=1.37(4)ns) occurs with the neutrons coupled to I=3/2$^+$. The $\nu\left(d_{5/2}^3\right)_{3/2}$ configuration of the ^{19}O, 3/2$^+$ isomeric state, coupled to a $\pi p_{1/2}$ proton hole is the main component of the lowest ^{18}N, 1^- wave function. However, all calculations show that the wave function of this ^{18}N 1^- state is a mixture of several configurations, with main contributions $\pi p_{1/2}^{-1}\nu\left(d_{5/2}^3\right)_{3/2}$ (about 45%) and $\pi p_{1/2}^{-1}\nu\left(s_{1/2}d_{5/2}^2\right)$ (about 35%). The quadrupole moment of the ^{19}O,3/2$^+$ isomer has not yet been determined experimentally. We have compared the ground state quadrupole moment Q(^{19}O,5/2$^+$)=0.37(4) efm^2 to the calculated moments using the same models as for ^{18}N and again adapting the neutron effective charge to reproduce the experimental value. If this 5/2$^+$ state would have a pure $\nu\left(d_{5/2}^3\right)_{5/2}$ configuration, its Q-moment would be zero (half filled orbit). The experimental value is thus completely determined by configuration mixing, and thus a very sensitive probe to the influence of mixing. Similar as for ^{18}N, we find that a large effective charge is needed to reproduce the data, indicating that the shell model space used in the present models is too small. Higher order configuration mixing should be taken into account, such as xp-xh excitations, like the $(4p\text{-}4h)_{0^+}$ higly deformed ($\varepsilon \approx 0.75$) triaxial state found at low energy in ^{16}O [13, 14].

Another way to interpret the large quadrupole moment of these N=11 isotones is to describe these nuclei in a deformed Nilsson model. The interpretation of ^{19}O as a prolate rotor was presented by Sheline already in 1983 [15]. He shows that the level scheme of ^{19}O, studied rather in detail, can be interpreted as originating from a prolate rotor with a deformation $\varepsilon \approx 0.3$ (like for the ^{21}Ne isotone). The ground state band is described as the Nilsson orbital

3/2$^+$[211] Coriolis coupled to the ½$^+$[220] band at 1.472 MeV (so K=3/2). Apart from these two bands, also a ½$^-$[101] band at 3.11 MeV has been identified. Figure 2 shows the Nilsson orbits for this region [16].

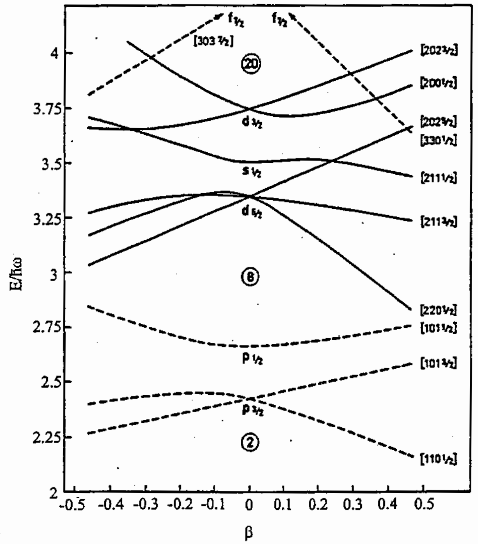

Fig. 2 : Nilsson orbits for single particle orbits in a deformed potential for nuclei with N,Z < 20, taken from [16]

If we consider ^{18}N in this context, the ground state would be described as the ½-[101] proton hole state in ^{19}O. The coupling of the ½-[101] proton hole orbit to the 3/2$^+$[211] neutron orbit, energetically favours the ν3/2$^+$[211]-π1/2$^-$[101] to give a 1$^-$ ground state [15]. So, in the context of a prolate rotor, the ground state of ^{18}N is indeed predicted as 1$^-$ in agreement with experimental observation. Further evidence for the deformed nature of ^{18}N is found in the systematics of the two-neutron separation energies, which shows an increase with neutron number around N=11 both for N and O isotopes [15]. Assuming that ^{18}N is a well-deformed rotor, one can deduce the proton deformation from the measured quadrupole moment using the relation between the spectroscopic and intrinsic moment, if we assume that axial symmetry is preserved. Then K is a good quantum number, and assuming K=I=1, the

intrinsic quadrupole moment is $Q_0(^{18}N,1^-) = Q_{exp}(2I+3)(I+1)/I(2I-1) = 27(4)$ efm^2. This value is directly related to the proton deformation as follows: $\beta_p = \frac{\sqrt{5\pi}}{3}\frac{Q_0}{ZR^2}$, with R=1.2A$^{1/3}$ resulting in $\beta_p(^{18}N)=0.52$ and a mass deformation β=0.20. For ^{19}O a similar calculation, assuming in this case K=3/2, gives a proton deformation $\beta_p(^{19}O)=0.42$ and a mass deformation $\beta(^{19}O)=0.176$.

Remark that in this workshop, another measurement of the nuclear moments of the ^{18}N ground state has been reported by Asahi et al. [17]. That experiment was performed on polarised ^{18}N fragments selected after fragmentation of a ^{22}Ne beam (at 110 MeV/u), using normal β-NMR (magnetic moment) and a multiple frequency β-NQR (quadrupole moment) technique. Their values differ considerably from our results, and are suggesting that the ^{18}N ground state is a normal spherical shell model state. At present, there is no clear evidence for the discrepancy of the two data sets. An explanation could be that one of the groups has seen the (LMR, NMR) resonance's induced by an isomer in ^{18}N, while the other group measured the ground state moments. This idea is supported by the result of the $^{18}C \rightarrow {}^{18}N$ beta-decay study, in which some missing gamma-intensity has been found at low excitation energy [3] which could be explained by the presence of an isomer. However, till now such an isomer has neither been observed, nor been searched for.

In conclusion, we have measured the magnetic and quadrupole moment of the ground state of ^{18}N, resulting in a large quadrupole moment. The moments have been compared to standard shell model calculations, using different *0p-1s0d* interaction parametrizations. A large neutron effective charge is needed to reproduced the E2-moments of the N=11 isotones ^{18}N and ^{19}O, indicating that the used model space is too small to describe these neutron rich nuclei near the proton shell closure. Both nuclei could be described in a deformed Nilsson model, allowing to give a good agreement for the level scheme of ^{19}O and a reproduction of the measured ground state spin of ^{18}N.

References

[1] G.D. Putt et al., Nucl. Phys. A399 (1983) 190

[2] J.W. Olness et al., Nucl. Phys. A373 (1982) 13

[3] M.S. Pravikoff et al., Nucl. Phys. A528 (1991) 225

[4] F.C. Barker, Austr. J. Phys. 37 (1984) 17

[5] D.J. Millener, AIP Conference Proceedings 163 (1988) 402

[6] E.K. Warburton and D.J. Millener, Phys. Rev. C39 (1989) 1120

[7] E.K. Warburton and B.A. Brown, Phys. Rev. C46 (1992) 923

[8] Xinhua Bai and Jimin Hu, Phys. Rev. C56 (1997) 1410

[9] G. Neyens et al., Phys. Lett. B393 (1997) 36

[10] G. Neyens et al., Heavy Ion Physics 7 (1998) 101

[11] G. Neyens et al., Phys. Rev. Lett. 82 (1999) 497

[12] T. Minamisono et al., Phys. Lett. B457 (1999) 9

[13] A. Aberg et al., Nucl. Phys. A391 (1982) 327, D. Auverlot et al., Phys. Lett. 149B (1984) 6

[14] F. Ajzenberg-Selove, Nucl. Phys. A281 (1977)1, A375 (1982) 1

[15] R.K. Sheline, Aust. J. Phys. 36 (1983) 825

[16] B.R. Mottelson and S.G. Nilson, Mat. Fys. Skr. Dan. Vid. Selsk 18 (1959)

[17] H. Ogawa, K. Asahi et al., Phys. Lett. B451(1999) 11 and this proceedings

---

TRACE AMOUNT LANTHANIDE AND ACTINIDE DETECTION BY PULSE LASER RADIATION

I.N.Izosimov
V.G.Khlopin Radium Institute, 194021 St.Petersburg, Russia

Abstract

The applications of the laser spectroscopy methods to lanthanide and actinide trace amount detection are discussed. The special attention is devoted to TRLIF method and it's modifications. It is pointed out that the enlargement of the number of actinide elements that can be detected by TRLIF method may be obtain by using the combinations of TRLIF with other laser spectroscopy methods and inside molecules energy transfer.

1. Introduction

Sensitive and direct detection of trace amounts of actinide and lanthanide elements in the different samples presents today major importance for ecology, radwaste handling and control, rehabilitation of contaminated areas and risk assessment. Despite the low spreading of these elements in the Earth lithosphere there is a great interest to their geochemical behavior. Nevertheless up to now our knowledge of lanthanide and actinide geochemistry is still limited in spite of a very large amount of work devoted to this subject. This peculiar situation mainly results from the difficulties in the assessment of these elements at very low environmental concentrations and the problems related to the complex formation with different organic and inorganic ligands present in natural aquifers and soils. The sensitivity of the methods which are presently used for direct location of actinide and rare-earth elements (REE) are often not high enough to detect the very low environmental concentration of these elements. Most of them require a pre-concentration or complete separation of each element before analysis, that may lower the detection limit and strongly perturb the initial states of the species in the environment. In this sense, the lasers fluorescence spectroscopy is very attractive, because in principle its theoretical sensitivity is limited only by the intensity of laser radiation.

In recent years in the element and isotope analyses of environmental samples the laser radiation is used more and more widely. The laser radiation can be tuned smoothly in the wide range of wavelength, has a high energy resolution and high power in comparison with usual light sources. These qualities of the laser radiation open new possibilities in determinating the element and isotope composition of different samples. It is necessary to indicate one principal difference of the nuclear radiation registration, on which many methods of isotope and element analyses of the samples are based, from the registration of the elements and isotopes by laser spectroscopy methods. In the first case the registration is based on nonreversible change of state of the researched object, for example by nuclear decay. That is why only one measurement can be done with each nuclear particle, it cannot be repeated. In the same time atom, ion or molecule after interaction with laser radiation can return into the primary state and so multiple measurements can be done. It opens new possibilities in study of presence in environmental samples of a very small concentrations of different elements and isotopes.

However the practical use of the methods of laser spectroscopy in the analysis of different samples encounters one essential difficulty, namely it is necessary to get the investigated element from the sample to a zone of interaction with laser radiation. That is why the most attractive from practical point of view is to use the solutions of investigated samples. But in this case , as a rule, one cannot determine the isotopic composition of a sample.

The main content of this report is connected with the application of laser spectroscopy methods for detection of trace lanthanides and actinides

concentration in the different solutions by Time Resolved Laser Induced Fluorescence (TRLIF) method.

2. Time Resolved Laser Induced Fluorescence (TRLIF) method

The practical limit of substance detection in solutions will be defined by luminescence of accompanying impurities and intensity of scattered light. In order to eliminate influence of scattered light one usually uses well constructed optical system with optimal collection of emission light, and also the choice of registration wavelength of luminescence determined by the best ratio of the intensity of useful fluorescence response to the intensity of scattered light. In order to diminish the influence of impurity luminescence one needs careful impurity removal of used solvents and reagents and, as well as in the case of scattered light, making choice of appropriate wavelength for excitation and registration of an emission, ensuring a maximum signal/noise ratio. The sensitivity of fluorescence technique is often limited by strong luminescence of aromatic impurity molecules, widespread in environment and difficult capable to removal. These impurities have absorption and emission spectra both in ultra-violet and visible spectral areas, therefore there is a lot of problems to increase considerably a signal/noise ratio by change of excitation and emission wavelength. Fortunately, for lanthanides and actinides this problem might be decided with the help of the time resolving fluorescence spectra [1-3]. The point is: the strong fluorescence of aromatic compounds emits from well-allowed $\pi - \pi^*$ molecular levels, measured lifetime of which makes $10^{-8} - 10^{-9}$ sec., whereas the emission of REE and actinides takes place from partial-forbidden levels and consequently their lifetimes are much longer ($\approx 10^{-3} - 10^{-6}$)sec. The time-resolved technique or time resolved laser induced fluorescence spectroscopy method (TRLIF) allows to separate useful long-lived fluorescence from impurity short-lived fluorescence and from scattered light, that enables to increase considerably the sensitivity of a method in the application to long-lived fluorescence of lanthanides and actinides.

The scheme of the experimental set-up is shown in fig.1. Analyzed solution in cuvette is irradiated by the pulsed (10 ns) laser source. The fluorescence spectra are detected after some (1 μs – 1ms) delay time relative to the excitation laser pulse. It allows to decrease considerably the background from laser pulse. Such a method is known as TRLIF and has a sensitivity up to 10^{-13} mol/l [4,5].

3. Lanthanides detection by TRLIF method

Now Eu^{+3}, Tb^{+3}, Gd^{+3}, Dy^{+3}, Sm^{+3}, Ce^{+3}, and Tm^{+3} ions can be detected by TRLIF method in solutions. For the TRLIF method application it is necessary to know the absorption spectrum, luminescence excitation spectrum , luminescence spectrum and luminescence lifetime for the detectable element. For many types of solutions such characteristics are well known [1,4,6]. The examples of above-mentioned spectra for Sm^{+3} are shown in figs.2–4 [7].

TRLIF method has resolution and selectivity on **four** parameters : *excitation wavelength (excitation spectrum), registration wavelength (luminescence spectrum), delay time for registration start after laser pulse and registration gate time.* The advantages of TRLIF method compared with usual spectroscopy are obviously demonstrated in fig.5, where the TRLIF and usual (without time resolution) luminescence spectrum examples for Eu^{+3} are shown.

The essential TRLIF method sensitivity increasing may be achieved by using special solutions with high extinction (absorption) coefficient of laser radiation in which excitation energy is transferred to the lanthanides ions. Such process takes place for example in so-called chelate complexes [8] but in this case we are loosing the selectivity on one parameter – excitation wavelength.

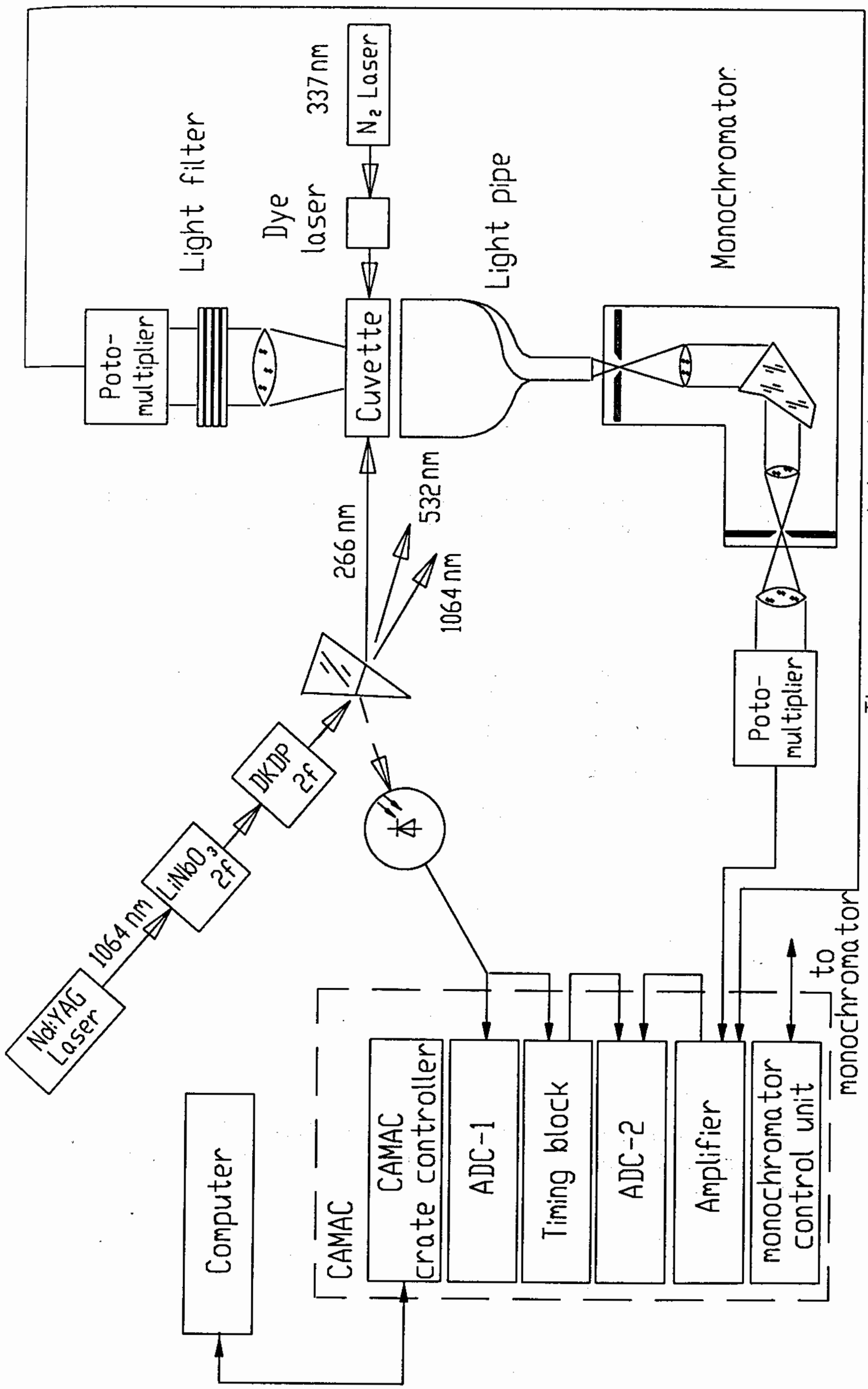

Fig. 1. The experimental set-up.

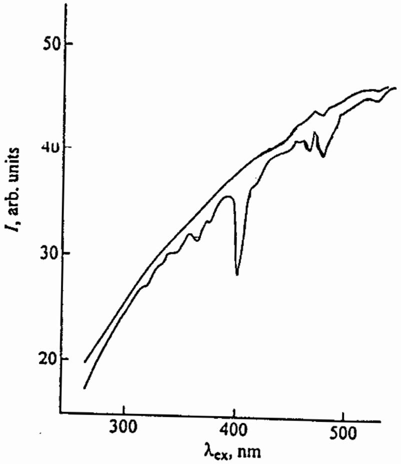

Figure 2. Transmission spectra of (1) solvent [10 ml D_2O + 1ml HCl (11M)] and (2) ^{154}Sm solution. The resolution on excitation wavelength λ_{ex} is $\delta\lambda_{ex}$=5nm.

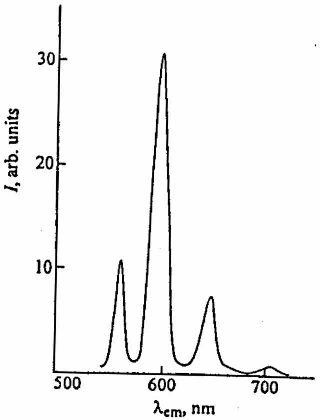

Figure 3. Luminescence spectra of $^{154}Sm^{3+}$ in D_2O solution. The excitation wavelength λ_{ex} =401nm, $\delta\lambda_{ex}$=5nm; resolution on registration wavelength is $\delta\lambda_{det}$=10nm.

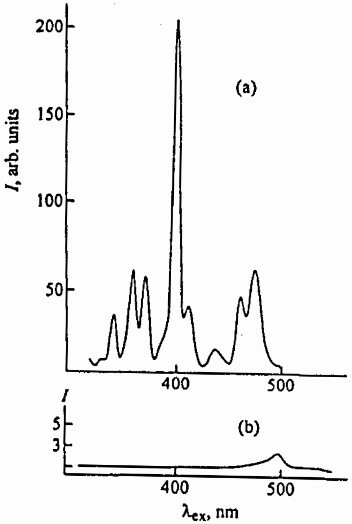

Figure 4. Luminescence excitation spectra of (a) $^{154}Sm^{3+}$ in D_2O solution and (b) solvent. The registration wavelength λ_{det} =595nm, $\delta\lambda_{det}$=5nm; resolution on excitation wavelength is $\delta\lambda_{ex}$=5nm.

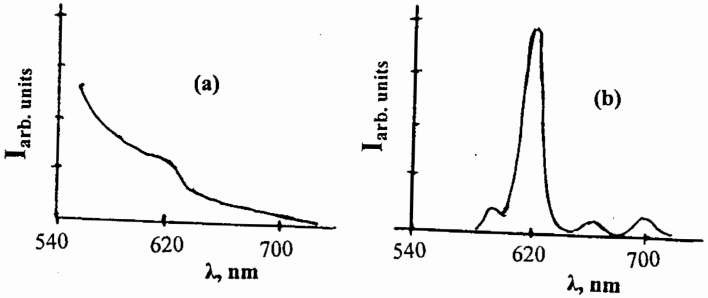

Figure 5. Luminescence spectra of Eu^{3+} in D_2O solution (a) without time resolution and (b) TRLIF spectrum with 10μs registration delay time.

The limits of detection (LOD) which are achieved now by TRLIF method [4] are summarised in Table 1. Of course the TRLIF method sensitivity can increase if the solutions with more low luminescence quenching and more effective energy transfer for lanthanides ions will be found. From this point of view the {polynucleotide}+{chelate}+{lanthanide ion} solutions are very interesting.

Table 1. Achieved limit of lanthanides detection (LOD) by TRLIF method.

Element	Eu^{3+}	Tb^{3+}	Gd^{3+}	Dy^{3+}	Sm^{3+}	Ce^{3+}	Tm^{3+}
LOD in mol/l (M)	10^{-12}	10^{-9}	10^{-8}	10^{-10}	10^{-10}	10^{-9}	10^{-6}

4. Actinides detection by TRLIF method

Now the following actinides can be detected by TRLIF method [2]: UO_2^{2+}, Cm^{3+}, Am^{3+}, Cf^{3+}, Es^{3+}, *and* Bk^{3+}. The most progress is achieved in UO_2^{2+}, Cm^{3+} *and* Am^{3+} TRLIF detection [2,5,9]. Examples of the luminescence excitation and luminescence spectra for uranium are shown in fig.6 and fig.7. The luminescence time scale is shown in fig.8, where the short-time (less than 0.1 μs) background luminescence is effectively separated from long-time (40 μs) uranium luminescence. The advantages of TRLIF over usual luminescence spectroscopy for trace amount detection are visible in fig.8, because without time resolution the background signal will exceed the detectable signal.

Limits of actinides TRLIF detection [2,5,9] and comparison with the radioactive counting methods are summarised in Table 2. The most impressive results of TRLIF applications is the uranium detection and now for trace amount uranium detection the TRLIF is one of the most effective method. For other actinides detection the TRLIF method development is necessary. The energy transfer effects in solutions with high laser radiation absorption coefficient may increase the TRLIF sensitivity.

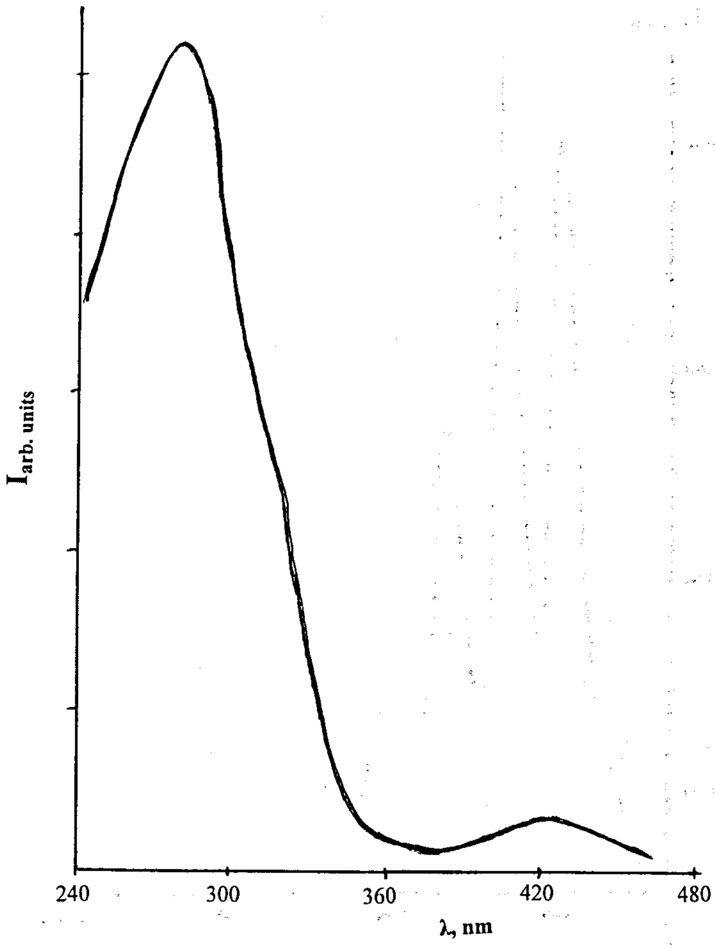

Figure 6. Uranium luminescence excitation spectrum. The $UO_2(NO_3)_2*6H_2O$ in 4.5M H_2SO_4 solution was studied.

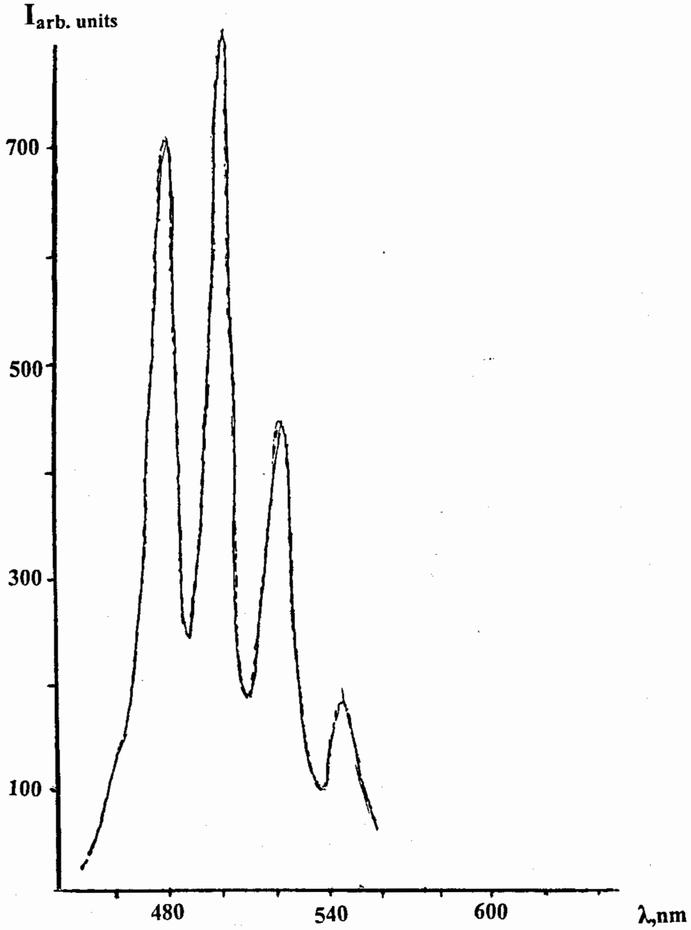

Figure 7. Uranium fluorescence spectrum. The $UO_2(NO_3)_2{*}6H_2O$ in 4.5M H_2SO_4 solution was irradiated by pulse nitrogen laser radiation.

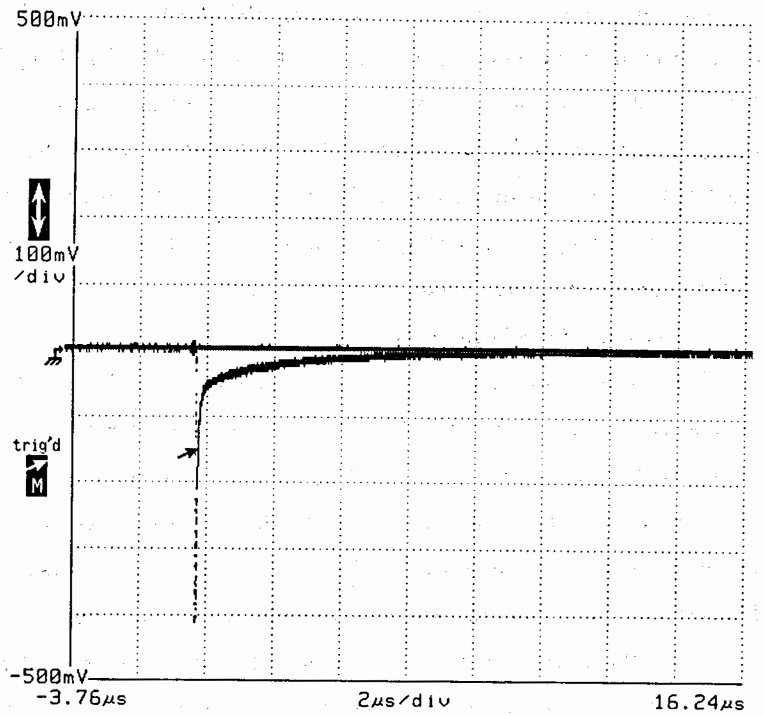

Figure 8. Time dependence of the photoluminescence intensity of the $UO_2(NO_3)_2{*}6H_2O$ in 4.5M H_2SO_4 solution. The pulse nitrogen laser was used for excitation.

Table 2. Limit of actinides detection (LOD) by TRLIF and by radioactive counting methods. For radioactive counting method the basis level 0.1Bq was taken.

Method	TRLIF			Radioactive counting		
Element	UO_2^{2+}	Cm^{3+}	Am^{3+}	^{238}U	^{244}Cm	^{241}Am
LOD	10^{-12}M (270pg/l)	10^{-13}M (24pg/l)	10^{-9}M (240ng/l)	8μg	0.03pg	0.8pg

Two laser spectroscopy methods used for Pu detection in solutions exist now. These are [10,11] Laser-Indused Photoacoustic Spectroscopy (LIPAS) and

Thermal –Lensing Spectroscopy (TLS). Pu(III), Pu(IV) and Pu(V) can be detected by these methods. The limit of detection (LOD) [10,11] by TLS and LIPAS is about 10^{-7}mol/l - and these LOD are not so good as by radioactive counting methods (10^{-13}mol/sampl for ^{239}Pu). It is very attractive to try to develop the TRLIF method modifications for Pu detection in solutions. From this point of view the study of the energy transfer effects both to Pu and from Pu in different solutions is very important.

5. Isotope effects in solutions

The isotope composition detection in solution must be based on some isotope effects (IEs) for detectable elements. At the same time, the isotope effects study in solutions is complicated, because the absorption and emission bands of various compounds in solutions are broader and no isotope effects on spectrum shape is observed. However, several characteristics such as fluorescence yield and the molar extinction (absorption) coefficient may depend on the differences in the interaction of isotopes of particular element with solutions components [7]. From this point of view the lanthanides and actinides are more suitable as the objects for isotope effects search in liquids. These elements have a partially occupied electrons *f* shell, transitions within the *f* shell are forbidden as the electric dipole E1 transitions and the small differences of two-isotopes interaction with solution compounds may change the intensity of electron transitions within *f* shall. The differences in molar extinction (absorption) coefficients for $^{144}Sm^{3+}$ and $^{154}Sm^{3+}$ ions in D_2O solutions have been observed in [7]. The detail study of such kind of isotope effects and especially its time scale characteristics may lead to TRLIF method applications for isotope composition detection in solutions.

6. Conclusion

The liquid systems are very attractive for trace lanthanides and actinides amount detection by pulse laser radiation. For direct determination of lanthanides and actinides in solutions the TRLIF method is currently the most appropriate. The development of different TRLIF method modifications is very essential for sensitivity increasing, possibility of isotope composition detection and the type of detectable elements expanding.

Acknowledgment

This work is supported by International Science and Technology Centre (ISTC), project ISTC 616-98.

References

[1]. T.Berthoud, P.Decambox, B.Kirsch, et.al., Analytica Chimica Acta, 1989, v.220, p.235.

[2]. R.Klenze, J.I.Kim, H.Wimmer, Radiochim. Acta, 1991,v.52/53,p.97.

[3]. G.Bernhard, G.Geipel, V.Brendler, H.Nitsche, Radiochim. Acta, 1996, v.74, p.87.

[4]. C.Moulin, P.Decambox, P.Mauchien, Journal de Physique IV, 1991, v.C7, p.677.

[5]. C.Moulin, P.Decambox, P.Mauchien, Anal.Chem., 1996, v.68, p.3204.

[6]. G.Bidoglio, P.N.Gibson, E.Halter, at.al., Radiochim.Acta, 1992, v.58/59, p.191.

[7]. I.N.Izosimov, V.V.Smirnov, V.M.Bakulev, Radiochemistry, 1998, v.40, p.204.

[8]. J.B.Lamture, B.Ivenson, M.E.Hogan, Tetrahedron Lett., 1996, v.37, p.6483.

[9]. P.Thouvenot, S.Hubert, C.Moulin, et.al., Radiochim.Acta, 1993, v.61, p.15.

[10]. G.Bidoglio, G.Tanet, P.Cavalli, et.al., Inorg.Chim.Acta, 1987, v.140, p.293.

[11]. S.Okajima, D.T.Reed, J.V.Beitz, et.al., Radiochim.Acta, 1991, v.52/53, p.111.

Ultrashort laser pulses in physics and chemistry

Ryszard Naskrecki
Quantum Electronics Laboratory, Institute of Physics, Adam Mickiewicz University,
Umultowska 85, 61-614 Poznan, Poland
e-mail: rysznas@main.amu.edu.pl

Abstract

Study of physical and chemical events accompanying light-matter interaction in pico- and femtosecond time scale has become possible with the use of ultrashort laser pulses. With the progress in generation of ultrashort laser pulses, the ultrafast optical spectroscopy, as a tool for dynamic study, is still evolving rapidly.

Introduction

The phenomenon of time and temporal change is one of the most fundamental concepts of science. Temporal changes investigated by scientific methods occur in time scale of 38 orders of magnitude, from 10^{18} s, which corresponds to the age of the universe to 10^{-20} s corresponding to the passage of a single photon across an elementary particle [1].

Many fundamental events in microscopic world proceed in time scales extending to ultrashort time scale. As ultrashort or ultrafast we call laser pulses or spectroscopic techniques whose duration or time resolution is in the time range $10^{-12} - 10^{-15}$ s.

The applications of ultrashort laser pulses have been historically concerned with spectroscopy and dynamics in physics, chemistry, biology and material sciences,and this aspect of ultrashort pulses applications we shall discuss here. But recently, potential applications have emerged in which ultrafast sources can be of importance in communication, metrology and medical therapeutics and diagnostics.

The remainder of this article comprises two main parts. The first one shortly describes how we can generate ultrashort laser pulses and the second describes the main ideas of ultrafast optical spectroscopy and three of the best known experimental techniques.

There are many ultrafast processes whose lifetime regions are in the ultrashort time scale and some of them are listed in the table. [1]

Table. *Lifetime regions of chemical and physical processes*

Photoionisation, photodissociation	$10^{-14} - 10^{-12}$ s
Vibrational motion	$10^{-14} - 10^{-12}$ s
Vibrational relaxation	$10^{-13} - 10^{-10}$ s
Vibrational dephasing	$10^{-14} - 10^{-12}$ s
Electronic relaxation	$10^{-12} - 10^{-8}$ s
Proton transfer	$10^{-12} - 10^{-10}$ s
Electron transfer in singlet states	$10^{-12} - 10^{-8}$ s
Energy transfer in singlet states	$10^{-13} - 10^{-10}$ s
Cage recombination	$10^{-13} - 10^{-12}$ s

The first scientific method for the study of fast physical and chemical phenomena was introduced in 1949 by George Porter, who developed the flash photolysis technique and by this initiated a "race against time". [4]. In this method two separate flash lamps were employed. The first one is used for the excitation of the sample, and when the sample is excited the short lived optical induced changes are probed by the analyzing flash pulse from the second lamp. This technique was designed for the spectroscopic study of free radicals and later, in the microsecond time scale for the measurements of absorption spectra in triplet excited states.

Soon after the invention of laser it became possible to generate light pulses of a few nanoseconds and replace the discharge lamps and hence to extend the time resolution by roughly 3 orders of magnitude.

The development of the first mode-locked picosecond laser sources was the motivation for development of the spectroscopy in picosecond time domain. But in contrary to the microsecond and nanosecond spectroscopy it was impossible to use the "classical" detection systems. The fastest electronics at that time were unable to detect picosecond events. It was the starting point for a completely new approach to the detection problems. The single pulse split into pump and probe pulses eliminated the problem of synchronization of two separate light sources and the need for a fast-response detection system. The time delay between the pump and probe pulses is achieved by an optical delay line using the constant propagation velocity of light in air equal 0.33 mm/ps. Therefore the time resolution of these pump-probe methods was only limited to a duration of picosecond pulses.

Additionally, Alfano and Shapiro showed that picosecond white-light pulses can be readily obtained by focusing a high-intense laser pulse in a dispersive medium and then the monochromatic beam is converted into a polychromatic pulse covering wavelengths throughout the UV, visible and IR regions [5]. The origin of this process is mainly governed by self-phase modulation and stimulated Raman scattering.

Therefore, to use effectively the pump-probe spectroscopy methods for direct investigation of ultrafast optical phenomena we need:

- ultrashort laser pulses, which interact with matter and then probe the induced changes as rapidly as possible
- optical detection system which records the information carried by the probe in the ultrashort time scale.

I. Femtosecond laser sources

The next step from picosecond to femtosecond time range was possible by progressive shortening the laser pulses. The development of colliding-pulse mode locked (CPM) dye lasers by Shank and his colleagues at Bell Laboratories, immediately reduced pulses well into the subpicosecond range [6]. A further pulse compression was achieved due to group velocity dispersion effect because red light travels faster than blue through a dispersive medium. The use of an anomalously dispersive grating or prism pair in the laser cavity enabled the generation of laser pulses up to 100 fs. Amplification of the CPM laser pulses in combination with fiber chirping and prism-grating compression techniques led to the generation of laser pulse as short as 6 fs [10].

Continued development of tunable, solid-state laser materials has resulted in the generation of more powerful and shorter laser pulses. An excellent example is titanium-doped sapphire or

$Ti:Al_2O_3$. The material characteristics of Ti:sapphire, namely a broad gain bandwidth, a large energy storage density, and excellent thermal properties make it one of the best candidates to be used in femtosecond lasers and amplification systems. The mode-locking mechanism of this laser is based on the Kerr non-linearity in Ti:sapphire crystal, in which the self-mode-locking is realized by a Kerr lens effect (Kerr lens mode-locking, KLM).

Thanks to the recent considerable progress in the field of generation of ultrashort laser pulses, pulses generation of duration below 100 femtosecond has become almost commonplace. Pulses as short as 7.5 fs can be generated directly in the laser oscillator and pulses of 4.8 fs by using an external compression [7]. In addition $Ti:Al_2O_3$ laser is tunable in the range from 680 to 1100 nm, which is much broader than that ensured by traditional organic dyes used in femtosecond oscillators.

For many applications it is necessary to amplify ultrashort laser pulses to the energy per pulse in mJ range. The idea of amplification of ultrafast laser pulses is very simple. A gain medium is pumped by an external source of radiation, which most often is another laser.

One of the most important techniques of ultrashort laser pulses amplification in solid state material is the chirped pulse amplification. The idea of temporary stretching pulses before their amplification was first demonstrated by Strickland and Mourou [8] in 1985 in Nd:glass laser and originated from the attempts at solving problems related to damage in the amplifier. A 1 mJ, 50 femtosecond pulse has a peak power of up to 20 GW and really only a few materials can resists to such a high power.

A typical amplifier system consists of a stretcher, regenerative amplifier and a pulse compressor. The fundamental concept is that the pulse duration is stretched by a factor of 1000-5000 before amplification and then compressed back to a duration as close as possible to its initial value. The processes of stretching and compression must be reversible, which is important demand of this method.

The laser pulse stretching is based on the dispersive properties of gratings or prisms. A typical stretcher set-up uses two gratings (arranged to provide positive velocity dispersion) and an afocal system. In such a system the optical path of the blue component of the pulse is longer than that of the red one, so the blue takes more time to travel through the system than the red. Since the blue part of the spectrum is delayed when compared to the red part and the output pulse is stretched and looks like a temporal rainbow.

The stretched pulse is then amplified in either a regenerative or a multipass amplifier. A typical regenerative amplifier configuration consists of an optical resonator that contains the gain medium, a Pockels cell and a thin-film polarizer. The pulse is allowed to make as many round-trips as necessary to fully deplete the gain. For the laser systems of pulse energy in up to 1J range either low repetition rate or multikilohertz, Ti:Al_2O_3 is the most-common amplifier material used. After amplification the pulse is recompressed by a grating or grating pair arranged to provide negative group velocity dispersion. Ideally, the dispersive characteristic of the compressor and stretcher should match all orders.

For instance, a femtosecond laser system of Spectra Physics (working in Institute of Physics, Adam Mickiewicz University, Poznan) [11] comprises of the Titanium-sapphire oscillator (Tsunami) pumped by a second harmonic from neodynium-doped yttrium vanadate Nd:YVO_4 laser (Millenia), regenerative optical amplifier on Ti:Al_2O_3 (Spitfire-F-1K), pumped by a second harmonic from Nd:YLF laser (Merlin) and a generator of the second and the third harmonics.

The beam leaving the oscillator is a train of femtosecond pulses at a repetition rate of 82 MHz, pulse duration of about 50 fs and a few nanoJules energy per pulse. These pulses are amplified inside the Spitfire based on the Chirped Pulse Amplification method. The pulses entering the amplifier are stretched to about 500 ps then undergo amplification to almost 10 000 times and then inside the compressor are restored as close as possible to the initial temporal duration.

At the output of the laser system the pulses have the following features: 1 kHz repetition rate, 80 fs time duration and energy in a single pulse reaching up to 1 mJ. The wavelength tuning falls in the range between 750 and 850 nm. The laser system also supplied with the second (375 – 425 nm) and the third (250 – 280 nm) harmonic generation incorporating KDP crystals 1.5 mm and 0.4 mm thick respectively.

II. Time-resolved optical spectroscopy

The main goal of the ultrafast time-resolved optical spectroscopy is to get a maximum spectral information as a function of time at a highest possible time resolution.

Three different but complementary time-resolved spectroscopic techniques based on the applications of ultrashort laser pulses will be presented:

- absorption spectroscopy, which can detect both radiation and radiationless processes
- fluorescence spectroscopy, connected to radiation processes

- Raman spectroscopy, for investigation of vibrational, i.e. structural information of transient species.

Although ultrashort laser pulses can be used in a variety of experimental configuration in most cases they are employed in the so-called pump-probe technique. The theoretical description relates the pump-probe spectroscopy to ordinary linear spectroscopy, however it is the linear spectroscopy of non-equilibrium electronic state produced by an intense pump pulse.

In a typical pump-probe experiment two incident ultrashort laser pulses spatially overlap in the sample. An intense, quasi-monochromatic pump pulse excites the sample and the induced optical changes are monitored, as a function of time, by measurements of the weaker probe pulse. The temporal evolution of the created transient species – response of the medium to the excitation – is obtained by the probe measurements for the different delay times between the pump and the probe pulses. This delay time may be varied continuously by using an optical delay line. An optical path difference of 1 micrometer is equivalent to a time delay of 3.3 femtosecond.

In spite of different detailed solutions, the pump-probe methods have some common characteristic features:

- every measured spectrum is a result of a different pair of laser pulses
- detection system reads an integrated photoelectric signal as a function of the delay time between the pump and the probe pulses so that it is not necessary to use the "ultrafast detection electronics".
- time resolution (response time) of the experimental set-ups is limited by the pulse duration, the smallest delay time between the pump and the probe pulses and the influence of group velocity dispersion effect.

II.1. Time-resolved transient absorption spectroscopy is a sensitive spectroscopy technique to study the time evolution of the excited states and the lifetimes of short living species by measuring the time-dependent transient absorption signal. The goal of the transient absorption experimental set-up is to extract the optical density of transient absorption from the measurements of the spectral intensity of the probe beam (quasi-monochromatic or with the broad spectrum) directly in front of the sample and then after passing through the sample

$$OD(\lambda,\tau) = \log \frac{I_o(\lambda)}{I(\lambda,\tau)} ,$$

where $I_o(\lambda)$ is the spectral intensity of the probe pulse in front of the sample, and $I(\lambda, \tau)$ is the spectral intensity of the probe pulse going through the sample measured at a time τ after excitation. If $I_o(\lambda) > I(\lambda,\tau)$ we observe transient absorption, if $I(\lambda,\tau) > I_o(\lambda)$ the probe beam is amplified in the sample and we observe transient gain.

This measurement is possible with the one-beam method or the two-beam method where the terms one-beam or two-beams refer only to the probe beam.

The one-beam method alternates measurements of the spectral intensity of the probe beam going through the unexcited sample and the spectral intensity of the probe beam going through the sample at a time τ after excitation. This procedure is performed several times for different delay times. The inconvenience of this method is the impossibility of elimination of intensity fluctuations of the probe beam.

The idea of the two-beam method is the separation of the white-light continuum into two beams: the probe and the reference. The probe beam is coaxial with the pump beam and is going through the excited volume of the sample when the reference beam is going through the unexcited volume of the sample. To get a desired excited frequency the pump pulses are frequency doubled or tripled mostly in BBO crystals. The probe pulses passed through a variable optical delay line are then focused into a valid medium to generate a white-light continuum which typically covers the visible range and near IR.

The blue/UV exciting and white-light continuum pulses spatially overlap into 0.1 - 0.5 mm flowing sample cell and then the probe and the reference beams are focused on the entrance slit of grating polichromator and the dispersed light is detected by a CCD camera.

With our experimental setup the optical density of transient absorption or transient gain can be measured in the spectral range from 330 to 700 nm, with a time resolution of 120 fs and with precision up to 0.003 OD.

II.2. Time-resolved Raman spectroscopy [12] is a spectroscopic technique to study the vibrational spectra of molecules in their excited states. The observation of the time evolution of the Raman spectra after perturbation brings structural information on transients of photophysical/photochemical processes as well as the sample structure.

The principle of the method is relatively simple. The pump pulse perturbs the sample when the probe pulse at frequency ω_p is incident on the sample at time τ after excitation and creates Raman scattering at frequencies $\omega_R = \omega_p \pm \sum \omega_{vi}$, where ω_{vi} are the frequencies of the

Raman modes of the sample. The frequency ω_p is close to one of the electronic transitions of the excited sample (in the resonance conditions the Raman scattering is much enhanced).

The Raman spectrum is recorded by a detection system consisting of a grating monochromator and a photomultiplier for traditional single-channel detection or a grating polichromator connected with PDA or CCD for multichannel detection and is studied as a function of time delay. It should be noted that Raman scattering even in resonance is a week effect. Detection of the signal therefore requires efficient collection of the scattered light.

The temporal resolution of this method is strongly connected with the spectral characteristic of the pulse. It means, that temporal resolution can only be improved at a compromise of spectral resolution. In the best case for both it is about 2 ps and 2 cm^{-1}, respectively.

II.3. Time-resolved emission spectroscopy [12] permits measurements of the emission dynamics of the sample (emission lifetime and spectral changes). Two kinds of methods have been developed to the study time resolved emission: the electronic methods using electronic devices and the optical methods based on a correlation between the exciting pulse and the emitted light.

The best time resolution is achieved using the optical methods so we will discuss in more detail the so-called up-conversion technique.

The pulse laser beam is divided into two parts. The first part excites the sample and induced sample emission is collected and then focused into a nonlinear crystal (LBO, BBO or $LiIO_3$). The second part of the laser beam (the "signal" or "gate" beam) is passed through an optical delay line and is also focused in the nonlinear crystal. When the emitted light and the signal beam are present simultaneously in the nonlinear crystal, the frequency mixing occurs and an up-converted signal is generated and then dispersed by a monochromator and detected by a single photon-counting detection system. Phase-matched nonlinear crystals play a role of the optical gate which is opened when the signal pulse is present in the crystal. Changing the optical delay between the pump and the signal pulses, the emission can be sampled at different time after excitation. This technique allows measurements of low level light signals which is particularly suitable for femtosecond lasers of low-energy per pulse and high repetition rate. The time resolution of the up-conversion technique is basically limited by the temporal width of the signal pulse and group velocity dispersion effect induced by nonreflective optics in the experimental set-up and nonlinear crystal itself, and consequently a time resolution of less than 70 fs can be achieved.

III. GVD effect

Propagation of the femtosecond laser pulses in homogenous optical media is strongly affected by the dispersive properties of these materials. Hence, the generation, diagnostic and applications of ultrashort laser pulses can be strongly perturbed by the dispersive properties of all optical elements and the sample itself.

For normal dispersion the refractive index is a monotonously decreasing function of the wavelength, i.e. the refractive index for the blue light is greater than for the red.. It means that the red light travels faster when compared to the blue one.

The group and phase refractive indices are related through the slope of the normal dispersion curve

$$n_g(\lambda) - n_\Phi(\lambda) = -\lambda \cdot \frac{\partial n_\Phi(\lambda)}{\partial \lambda},$$

where $n_\Phi(\lambda)$ and $n_g(\lambda)$ are a phase and group refractive indices of the medium, respectively.

A measure of dispersion can be the difference in time of passage of two laser pulses at two extreme wavelengths. In commonly used media, solid and liquid,this difference for the 266 nm and 800 nm pulses can be nearly 800 fs on 1 mm optical path.

Usually, a measure of dispersion is assumed to be a parameter known as the GVD factor, which represents dispersion properties of a given material and is defined as:

$$GVD \equiv -\frac{1}{\vartheta_g} \cdot \frac{d\vartheta_g}{d\omega} \equiv \frac{d^2k}{d\omega^2},$$

where v_g is the group velocity (velocity of the light pulse), k is a wave-vector and ω is the circular frequency.

In any optical material GVD ≠ 0 and each component of the pulse spectrum will propagate at a different velocity. This leads to the time broadening of the light pulses. It has been shown by Marcuse [9] that the Gaussian shaped laser pulse after a passage through a slab medium of thickness L will be chirped and temporally broadened to a new time duration τ (FWHM)

$$\tau = \tau_0 \sqrt{1 + \left(\frac{\tau_c}{\tau_0}\right)^2},$$

where

$$\tau_c = \sqrt{\frac{2 \cdot \ln 2 \cdot L \cdot \lambda^3}{\pi \cdot c^2} \cdot \frac{\partial^2 n_\Phi}{\partial \lambda^2}}$$

and τ_0 is the FWHM of the pulse before entering the material, λ is the central wavelength of the pulse, c is the speed of light in the vacuum and n_Φ represents the phase refractive index of the medium.

For the picosecond and subpicosecond pulses the effect of dispersion broadening is of little importance, however, it becomes significant for pulses shorter than 100 fs. For instance, laser pulses of 50 fs duration at a wavelength 266 nm propagating in an ethanol sample will double their duration over the optical path of 3 mm.

The influence of the group velocity dispersion effect in the time-resolved optical spectroscopy experimental set-ups causes a temporal broadening of laser pulses which can notably degrade the time resolution and inflict the dispersion of „time zero" position (i.e. an instant when the pump and probe pulses perfectly overlap inside the sample).

It is possible to remove the influence of the GVD effect for example by using gratings and to rephase all the spectral components of the probe beam. But this procedure is somewhat difficult and it is much easier to correct it numerically. This can be only done if the dispersion of the polychromatic probe beam is well known.

The simplest method to correct the „time zero" dispersion is based on the determination of the effective thickness of the optical materials (including the sample cell) traveled through by the laser pulses. Knowing the dispersion of the refractive index of the contributing media it is possible to calculate the influence of the GVD effect.

A more sophisticated, experimental method to determine the time resolution of the experimental set-up and the chirp of the „time zero" is based on two photon absorption involving absorption from the pump and from the probe in solid or liquid medium. Changing the delay time between the pump and probe pulses it is possible to determine at what time the maximum signal is reached. This is exactly the time at which the pump and probe perfectly overlap for a given wavelength. Having this dispersion curve, numerical correction of the measured spectra can be made. Additionally, the resulting signal as a function of time reproduces the pump-probe cross-correlation function and its temporal width determines the temporal resolution of the experimental setup.

In conclusion, we have discussed some general aspects of the ultrafast optical spectroscopy methods which permit observations of the dynamics of ultrafast events in real time making use of the light-matter interaction. But we should remember that the femtosecond spectroscopy is still rapidly an expanding field and a large number of novel, potentially fruitful applications are still developed and tested. Additionally, a combination of the ultrafast spectroscopy techniques and gas-phase molecular beam experiments permits observations of not only the elementary processes and reactions, but also various stages of these reactions. The molecular beam technique as a method of sample preparation offers the way of investigation of molecules not only in an isolated state but also in well defined (vibrationally cold) quantum states. This opportunity can bring essential information on the nature of the transitions states, energy redistribution in molecules and reaction dynamics which belong to the most fundamental areas of chemical physics.

Bibliography

1. *Application of time-resolved optical spectroscopy*, V. Bruckner, K.-H. Feller, U.-W. Grummt, Elsevier, Amsterdam ,1990.
2. *Ultrafast Phenomena X*, Ed. by P.F.Barbara, J.G.Fujimoto, W.H.Knox and W.Zinth (Springer-Verlag, Heidelberg, 1994.
3. *Femtosecond Chemistry*, edited by J.Manz and L.Woste , VCH, 1995.
4. G. Porter, Proc. Roy. Soc. (London) **A200**, 1950, 284.
5. R.R. Alfano, S.L. Shapiro, Phys. Rev. Lett., **24**, 1970, 592.
6. R.L. Fork, C.V. Shank, R.T. Yen, C. Hirlimann, IEEE J. Quant. Electr. **QE19**, 1983, 500
7. L.Xiu, Ch.Spielmann, F. Krausz, R. Szipocs, Opt.Lett, **21**, 1996, 1259 ; M. Nisoli, S.de Silvestri, O.Svelto, R.Szipocs, K.Ferençh, Ch.Spielmann, S.Sartania, F.Krausz, Opt.Lett, **22**, 1997, 522
8. D. Strickland, G. Mourou, Opt. Comm., **56**, 1985, 219
9. D. Marcuse, Appl.Opt., **19**, 1980, 1653
10. R.L. Fork, C.H. Brito Cruz, P.C. Becker, C.V. Shank, Opt. Lett., **12**, 1987, 483
11. R. Naskrecki, M. Lorenc, M. Ziolek, J. Karolczak, J. Kubicki, A. Maciejewski, M. Szymanski, submitted.
12. *Femtosecond laser pulses. Principles and experiments.* C. Rulliere (Ed.), Springer-Verlag, Berlin Heidelberg, 1998.

LOW-TEMPERATURE NUCLEAR ORIENTATION: POSSIBILITIES, RESULTS, PERSPECTIVES

J. Dupák[3], M. Finger[1,2;1], M. Finger, Jr.[1], A. Janata[1,4], T.I. Kracíková[1,2], M. Krmar[5], K. Kumar[6], J. Kvasil[2], M. Slunečka[1,2]

[1] *Laboratory of Nuclear Problems, JINR, 141980 Dubna, Russia*
[2] *Charles University, Faculty of Mathematics and Physics, V Holešovičkách 2, 180 00 Praha, Czech Republic*
[3] *Institute of Scientific Instruments, Academy of Sciences of the Czech Republic, Královopolská 147, 612 64 Brno, Czech Republic*
[4] *Nuclear Research Institute, 250 68 Řež, Czech Republic*
[5] *Institute of Physics, 21121 Novi Sad, Yugoslavia*
[6] *Department of Physics, Tennessee Technological University, Cookeville, Tennessee 38505, USA*

A new facility for low temperature nuclear orientation of radioactive nuclei far from stability line is proposed to be built at JINR Dubna - the SPIN Facility. This facility, based on the state of the art of technological achievements together with the existing and planned JINR radioactive beam complexes YASNAPP and DRIBs, will open new horizons for many new experiments with oriented nuclei in nuclear and solid state physics research. The possibilities and restrictions of the low-temperature nuclear orientation method are illustrated by some of our experimental and theoretical results such as the determination of the mechanismus of orientation of $\mathrm{Eu}\underline{\mathrm{Gd}}$ and $\mathrm{Yb}\underline{\mathrm{Gd}}$, the magnitudes of the magnetic dipole moments of the ^{147}Gd and ^{149}Gd ground states, the attenuation factors of orientation of the excited states in ^{171}Yb, the E2/M1 mixing ratios of γ rays in well deformed odd $^{167-173}$Yb which are excellently described by the quasiparticle-phonon model with Coriolis interaction, the E2/M1 mixing ratio sign change when going from ^{169}Yb to ^{171}Yb (observation of the space reflection property), and intensities of the components with different multipolarities in the β transition from $^{154}\mathrm{Eu}\underline{\mathrm{Fe}}$. Based on our nuclear orientation studies particularities in the properties of ^{166}Er, ^{160}Dy and ^{148}Gd are discussed. The results of measurements of the X and γ rays, $\gamma - \gamma$ coincidences, conversion electrons and positrons from the decay of 60 min ^{148g}Tb and of the low-temperature nuclear orientation of ^{166}Tm, $^{160g+m}$Ho and ^{148g}Tb in Gd are reported. Considerably enriched decay scheme of ^{148g}Tb is proposed. Particular interest is paid to the collective bands in ^{166}Er, ^{160}Dy and ^{148}Gd. The sign change of multipole mixing ratios of the $\Delta I = 0$ transitions between the levels of the γ- vibrational ($K^\pi = 2^+$) and ground-state ($K^\pi = 0^+$) bands in ^{166}Er and ^{160}Dy beginning from $I_i = 4_\gamma$ was observed. The effect seems to be present also in ^{164}Er which suggests the existence of an "island" of nuclei with "anomalous" γ- vibrational bands. The E2/M1 mixing ratios of the $\Delta I = 0$ transitions between the β- vibrational ($K^\pi = 0^+$) and ground-states ($K^\pi = 0^+$) bands in ^{160}Dy and ^{148}Gd were determined, and the magnitudes of the E0/E2 mixing ratios, $|q(E0/E2)|$, and the E0/E2 probability ratios, $X(E0/E2)$, were obtained. In general, all these values are consistent with systematics. The $|q(E0/E2)|$ and $X(E0/E2)$ values for the transition between the negative parity levels, $3^- \rightarrow 3^-$, in ^{148}Gd were firstly determined.

The mixing ratio sign change of the $\gamma \rightarrow g$ transitions with $\Delta I = 0$ is described at present by the dynamic deformation model only.

---

[1] E-mail: finger@mbox.troja.mff.cuni.cz

1 Introduction

The method of nuclear orientation (NO) is based on the interaction of the nuclear electromagnetic moments with the electromagnetic fields which results in the orientation of the ensemble of nuclear spins, if the temperature of the ensemble is sufficiently low, i.e. much lower than 1 K. Principially it is possible to produce the electromagnetic field required for NO in laboratory, however, much stronger fields often are experienced by nuclei from the unpaired electrons in atomic shells or from the localized environments of solid phase. This type of interaction is known as hyperfine interaction or, if we consider the atomic shells, as hyperfine structure. Thus, the low-temperature NO introduces the physical direction where the nuclear, atomic and solid state physics and the technology of low temperature are crossing among themselves. From the experimental point of view the low-temperature NO is very complicated, however, the results which may be obtained are very significant as the NO allows to solve directly many problems of the enumerated physical branches and also gives possibility to study some properties of fundamental interactions as, for instance, the violation of the space parity or time invariance in nuclear conversion processes.

We remind here the final expressions of the NO theory and their generalization which we made for the case of any number of initially oriented states [1]. These expressions will show the possibilities and also restrictions of the low-temperature NO which shall be illustrated by our experimental and theoretical results.

2 Possibilities

The developed theory of the low-temperature nuclear orientation (LTNO) for the description, analysis and interpretation of the experiments is probably one of the most worked out and graceful theories of nuclear phenomena and is based on the general principles of symmetry: space rotation and space reflection.

Directional distribution of γ rays following the decay of nuclei oriented at temperature T, see, for instance, Ref. [2], is written as

$$W(\Theta,T)=\Sigma_{\lambda even}B_\lambda(I,T)U_\lambda A_\lambda E_\lambda G_\lambda Q_\lambda P_\lambda(cos\Theta), \tag{1}$$

where Θ is the angle between the directions of the emitted radiations and external magnetic field B_{ext}. From (1), the possibilities, which the NO offers to solve, may be seen:

1) The B_λ are the orientation parameters which depend on (it means that they allow to determine):

1. spin of oriented nucleus, I;
2. temperature, T (nuclear thermometry);
3. μB_{hf}, where μ is the magnetic dipole moment of oriented nucleus and B_{hf} is the hyperfine magnetic field on the oriented nucleus;
4. eQV_{zz}, where Q is the electric quadrupole moment of the oriented nucleus and $V_{zz} = \partial^2 V/\partial z^2$ is gradient of the electric field on the oriented nucleus and e is charge of electron;
5. mechanism of the orientation of nuclei and the magnitudes of their interactions with the environment.

The orientation parameters are connected with the hyperfine interaction study, and in this case the nucleus is used as a tool for the investigation.

2) The U_λ are the deorientation coefficients and give information about preceding transitions and about interactions responsible for those transitions:

6. moment carried away by the β transition;
7. sometimes even the admixture of another multipole in this β transition;
8. relation of the matrix elements of various type of interactions caused the β transition and information about their symmetry.

3) The A_λ are the directional distribution coefficients:

$$A_\lambda=[F_\lambda(LLI_fI_i)+2\delta F_\lambda(LL'I_fI_i)+\delta^2F_\lambda(L'L'I_fI_i)](1+\delta^2)^{-1}, \tag{2}$$

where L is the multipolarity, $L' = L+1$ and
9. multipole mixing ratio,

$$\delta=<I_f\parallel L'\parallel I_i>/<I_f\parallel L\parallel I_i>, \tag{3}$$

is defined as the ratio of the emission matrix elements with the relative phase of these elements (sign of δ);
10. I_i and I_f are spins of the initial and final states connected by the observed transition;
11. if the experimental value of the internal conversion coefficient (ICC) is known, the magnitude of the E0/E2 mixing ratio, $|q(E0/E2)|$, may be determined using the correspondig δ (E2/M1) value and consequently the ratio of the E0 to E2 probability, X(E0/E2), may be evaluated;
12. if the E2 transition probability, B(E2), is known, the magnitude of the monopole transition matrix element, $|\rho(E0)|$, may be determined.

4) 13. The E_λ correct for incomplete magnetic saturation of the matrix.

5) 14. The G_λ are the factors of the directional distribution attenuation which appear when the observed radiation deexcites the state with long life-time τ. The elecromagnetic moments of the studied state interact directly with the hyperfine fields of surroundings and the orientation is reduced, i.e. reorientation is happened: $G_\lambda < 1$; $G_\lambda = 1$ means no attenuation.

The $P_\lambda(\cos\Theta)$ are the Legendre polynomials.

Thus, plenty of information may be obtained by the investigation of LTNO even if the γ radiation is only measured!

When the experimental NO data are analyzed, the problems are arised when the deorientation coefficients are calculated, because the knowledge of the γ-ray and conversion electron intensities, of the transition multipolarities and of the decay scheme is needed. The problem is even greater when there are several levels populated directly or via $\beta-\gamma$ and $\gamma-\gamma$ cascades from two or more initially oriented states. We have developed [1] the expressions needed for analysis of the experimental data for such cases. When the levels of daughter nucleus are populated from two initially oriented states: ground (g) and metastable (m), the directional distribution is

$$W(\Theta)=\sum_\lambda[B_\lambda(g)U_\lambda(g)+B_\lambda(m)U_\lambda(m)]A_\lambda Q_\lambda P_\lambda(cos(\Theta)). \tag{4}$$

For n isomeric states, we have

$$W(\Theta)=\sum_\lambda A_\lambda Q_\lambda P_\lambda(cos\Theta)\sum_n B_\lambda(n)U_\lambda(n). \tag{5}$$

It is seen from Eqs.(4,5) that the separate values of $B_\lambda(n)$ have to be determined from the experimental anisotropies for pure transitions and the values of $U_\lambda(n)$ have to be calculated using the existent decay scheme. For n=g, we have

$$U_\lambda(g)=\frac{I^\beta U_\lambda^\beta(g)+\sum_i^{N-1}I_{\gamma i}^{(to)}(g)U_{\lambda i}^l(g)U_{\lambda i}^\gamma(g)}{\sum_j^M I_{\gamma j}^{(out)}}, \tag{6}$$

where $I_i^{(to)}$ and $I_j^{(out)}$ are the total (γ plus corvension electron) intensities of transitions populated (to) and depopulated (out) the observed level, I^β is total intensity of β transition to this level,

$$I^\beta=\sum_j I_{\gamma j}^{(out)}-\sum_i I_{\gamma i}^{(to)}, \tag{7}$$

$U^{\beta}_{\lambda}(g)$ are the deorientation coefficients of the β transition to the observed level, and $U^{l}_{\lambda i}$ and $U^{\gamma}_{\lambda i}$ are the orientation coefficients of the i-th intermediate level and of its depopulating transition. The $U_{\lambda}(m)$ coefficients are calculated using Eq.6, where the symbol g is replaced by m and appropriate values of the intensities, mixing ratios and U_{λ} coefficients are taken.

The most possibilities offered by the LTNO study were used, and hundreds of spin values, I, I_i and I_f, thousands of the E2/M1, M2/E1, E3/M2 (isomers) and E0/E2 mixing ratios, $|\mu|$, $|Q|$, $|B_{hf}|$, G_2, admixtures of other multipoles in the β transitions and some mechanisms of orientation were determined.

The IBA model, the quasiparticle-phonon model and the latter included a Coriolis interaction and the dynamic deformation model (DDM) were used to interprete our experimental results, (see, for instance, Refs. [3-6]).

3 Advantages and restrictions

The advantages and restrictions of the LTNO facility are flowing out from the technical possibilities of the SPIN facility and also in general from the physical phenomenon of the LTNO [2].

1. After one has the ensemble of oriented nuclei, the study of the directional distribution of γ radiation following the decay of these nuclei is simple. The question is to measure the singles γ-ray spectra which allows to study sufficiently small activities (~0.003 -0.3MBq) and to obtain quite precise results even in the short time measurements. Moreover, the normalized intensities of γ rays are measured ($W(\Theta)=S_{cold}/S_{warm}$) which means that the knowledge of the detector efficiencies is not needed.

2. Very small quantity of the radioactive nuclei, which dissolves in the matrix material, practically excludes the disturbance of the hyperfine interactions by mutual effect of the admixed ions.

3. Great significance has the LTNO for the investigation of nuclear properties. It provides one of the most precise methods for determination of spins of the nuclear levels and of multipole mixing ratios of the γ transitions, gives an opportunity to establish the admixtures of other multipoles in β transitions, the attenuation factors of the directional distribution for transitions from the long-lived states, the electromagnetic moments of the ground states of the oriented nuclei, etc.

4. There is limitation of the allowed spin values for the initially oriented nucleus which has to have $I \geq 1$ (if the parity is conserved). However, the isotropic radiation gives the information that spin of the nucleus is $I \leq 1/2$.

5. The LTNO is based on the hyperfine interactions of the nuclei admixed into the matrix environment. There is the advantage - possibility to determine the magnitudes of μ, Q, B_{hf}, V_{zz} and T, but also the difficulties - the necessity to exclude any perturbation of the hyperfine interactions. Moreover, the form of the anisotropy dependence on the sum of the hyperfine interaction parameters, a_M and P, contains the danger of the systematic errors.

6. The necessity to measure the temperature dependence of the anisotropy (uncertainties in the anisotropies of the studied nuclei and also in those of the thermometer nuclei) which magnitudes are decreasing with the increase of the temperature puts the limit at the accuracy of the a_M and P values.

In general, the method of the low-temperature NO allows to determine with high accuracy the quantities independent of the hyperfine interactions (nuclear properties), however the quantities connected with hyperfine interaction are determined with much lower accuracy.

7. Basical technical and technological limitation is determined by the region of the nuclei which are accessible to study by the SPIN facility. The time needed for the sample preparation and for its cooling puts limit on the half-life of the nuclei which can be measured. The half-life $T_{1/2} \geq 1$ h is the limit for the SPIN facility.

4 Future development

This is clear from the facts given above: SPIN-2 - the on-line experiment is needed to supplement the off-line facility. We have a beam of the monoisotopic nuclei, but we need a new refrigerator and so on. The on-line experiment was planned as having a facility with orientation before implantation (cold matrix), i.e. the measurement of half-lives up to $T_{1/2} > 1$s would be possible. The limits put the spin-lattice relaxation time. With the ferromagnetic matrixes, the half-lives of 1-100s would be possible to measure. The laser induction orientation would decrease the half-life limit up to $T_{1/2} > 1$ns.

However, there are possibilities much to do even with the off-line SPIN-1 facility. For instance:

1. Measurements of the β and α radiations and coincidences from oriented nuclei.

2. The fission of oriented nuclei to study the parity violation which was predicted theoretically (Novosibirsk) to have higher effect at least by an order of magnitude than with γ radiation, which was already measured.

3. Laser spectroscopy with oriented nuclei.

4. New regions of deformation below $A = 100$.

5. The plasma source for mass-separator is in construction. This will give the possibilities to study (i) the end of the deformed nuclei region and the transition $\subset\supset\rightarrow\bigcirc$. This end seems to be not so sharp as in the A~150 region. There is no proper study of this problem yet. (ii) The nuclei around the Pb with the doubly closed shells and (iii) the transuranium elements which are produced in very small quantities.

5 Some results

About 70 nuclides (isotopes of more than 20 elements from Mn up to Np) with half-lives from about 50 min to several years (^{167}Lu, $T_{1/2}$=51.5 min, ^{148}Tb, $T_{1/2}$=60 min and ^{154}Eu, $T_{1/2}$=8.5y) were investigated using the off-line SPIN-facility. Examples of the multipole mixing ratios of γ rays following the decay of various nuclei oriented in Fe nad Gd are shown in Table 1.

The ability of the Gd and Fe matrices were studied. As a result our samples in Gd have superior quality (with approximately complete substitution in the lattice sites). Our results show that for the nuclear structure studies, Fe is a good matrix for the majority of nuclei (the γ-ray anisotropies up to 50%). It was shown on ^{146}Eu, that saturation of the Fe matrix is the same at implantation voltage of 35 and 65 kV. Examples of the γ-rays anisotropies for Eu and Yb oriented in Fe and Gd are shown in Table 2.

1. *Mechanism of orientation:* the low-temperature nuclear orientation of Eu and Yb in gadolinium [14].

It is known that europium and ytterbium do not dissolve in gadolinium being the exceptions from the rare-earth elements. We did this using the decays of the parent nuclei [14]: $^{147}\mathrm{Gd}\underline{\mathrm{Gd}} \rightarrow {}^{147}\mathrm{Eu}\underline{\mathrm{Gd}} \rightarrow {}^{147}\mathrm{Sm}\underline{\mathrm{Gd}}$ and $^{169}\mathrm{Lu}\underline{\mathrm{Gd}} \rightarrow {}^{169}\mathrm{Yb}\underline{\mathrm{Gd}} \rightarrow {}^{169}\mathrm{Tm}\underline{\mathrm{Gd}}$.
In the first case, the anisotropies up to 10% for $^{147}\mathrm{Gd}\underline{\mathrm{Gd}}$ and up to 20% for $^{147}\mathrm{Eu}\underline{\mathrm{Gd}}$ were observed. In the case of the $^{169}\mathrm{Yb}\underline{\mathrm{Gd}}$, the picture was quite different, and we provided the NO of ^{169}Yb in iron, see Table 2.

Systematic study of the hyperfine interactions shows that the eQV_{zz} interaction is about 10% from the μB_{hf} one. The magnetic hyperfine interaction cannot change the sign of the orientation parameter which is always positive. However, in the case of ^{169}Yb the anisotropies from $^{169}\mathrm{Yb}\underline{\mathrm{Gd}}$ have opposite signs to those from $^{169}\mathrm{Yb}\underline{\mathrm{Fe}}$. It seems that there is unique case of electromagnetic hyperfine interaction when $P > a_M$, where

$$P = 3/4\ e\,QV_{zz} / I(2I-1) \quad \text{and} \quad a_M = \mu B_{hf}/kI$$

are parameters of the hyperfine electric quadrupole and magnetic dipole interactions, respectively. The calculations for $P\uparrow\uparrow a_M$ and $P\uparrow\downarrow a_M$ confirm our supposition.

2. *Magnetic dipole moments of the ^{147,149}Gd ground states.* Magnetic dipole hyperfine splitting

SPIN–YASNAPP–2 FACILITY: AVAILABLE EXPERIMENTS

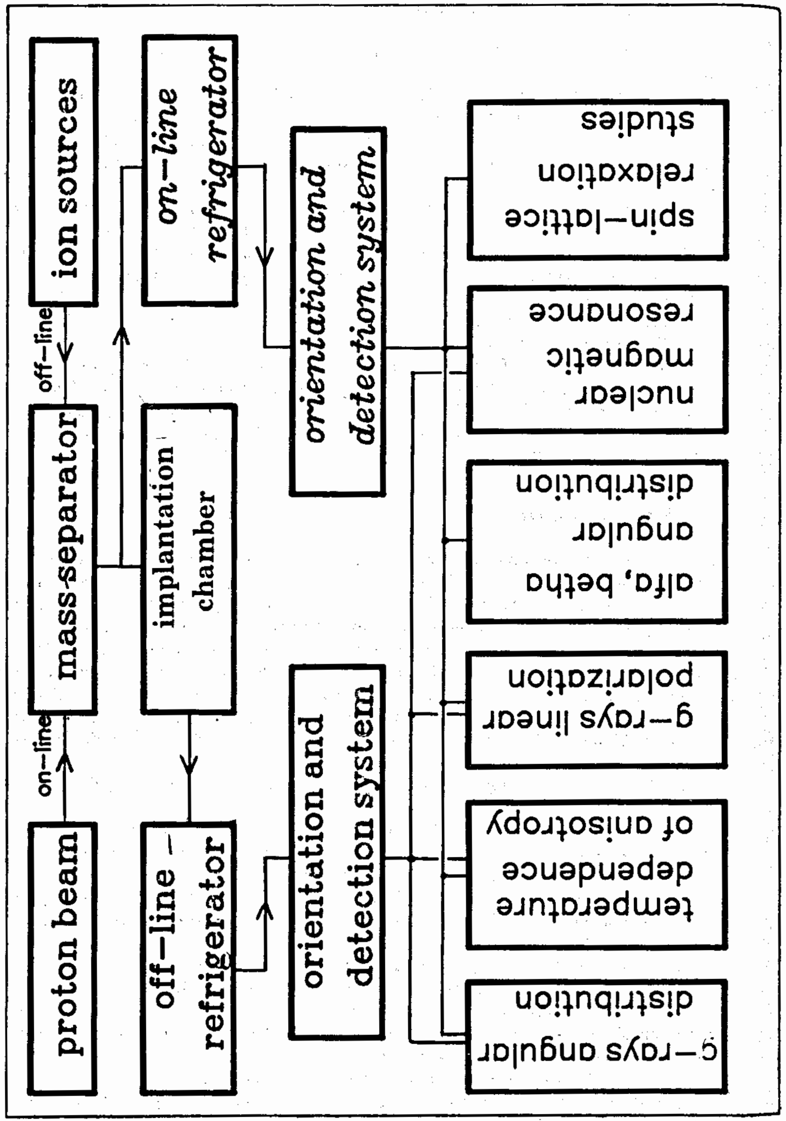

Table 1. Examples of the E2/M1, M2/E1, E3/M2 and E0/E2 mixing ratios of transitions in ^{145}Sm, ^{155}Tb, ^{167}Yb, ^{169}Yb, ^{239}Np, ^{150}Gd and ^{172}Yb measured by the decay study of ^{145}Eu<u>F</u>e, ^{155}Dy<u>G</u>d, ^{167,169}Lu<u>G</u>d, ^{239}Np<u>G</u>d, ^{155}Tb<u>G</u>d and ^{172}Lu<u>G</u>d, Fe, respectively

Nucleus	E_{level} (keV)	I_i^{π}	E_{γ} (keV)	I_f^{π}	δ	$\lvert q(E0/E2)\rvert$	Multipolarity
$^{145}\mathrm{Sm}^{a}$	1547	$3/2^+$	111	$1/2^+$	-1.98(6)		E2+M1
			1547	$7/2^-$	0.62(+12,-10)		M2+E3
	2426	$5/2^-$	1532	$3/2^-$	-0.40(+4,-5)		M1+E2
$^{155}\mathrm{Tb}^{b}$	271	$5/2^+$	271	$3/2^+$	0.52(+8,-7)		M1+E2
	761	$3/2^+$	761	$3/2^+$	-0.74(+31,-4) -2.5(+42,-17)	3.8(+34,-10) 2.5(+191,-21)	E2+M1+E0
	1062	$5/2^-$	835	$5/2^-$	-0.35(+20,-17) 4.7(+172,-21)	1.9(+26,-12) 1.0(+82,-9)	E2+M1+E0
$^{167}\mathrm{Yb}^{c}$	302	$11/2^-$	243	$9/2^+$	0.20(14)		E1+M2
	308	$7/2^-$	230	$7/2^-$	-0.39(+24,-20)		M1+E2
	1948	$9/2^-$	1227	$7/2^-$	0.39(+11,-9) 4.8(+34,-16)		E2+M1
$^{169}\mathrm{Yb}^{d}$	191	$5/2^-$	191	$7/2^+$	-0.058(9)		E1+M2
	887	$9/2^+$	816	$9/2^+$	-0.80(20)		M1+E2
	1071	$7/2^+$	1071^{h}	$7/2^+$	-0.74(+13,-11) 10(+50,-5)	5.8(+9,-7) 3.55(17)	E0+M1+E2 E0+M2 (+M1)
	1708	$7/2^-$	1517	$5/2^-$	-5.9(+9,-7)		E2+M1
	1869	$7/2^-$	1498	$5/2^-$	0.238(64)		M1+E2)
	1909	$5/2^+$	1339	$5/2^-$	-0.043(34)		E1+M2
$^{239}\mathrm{Pu}^{e}$	285	$5/2^+$	278	$3/2^+$	0.165(2)		M1+E2
	330	$7/2^+$	254	$7/2^+$	-0.159(12)		M1+E2
	392	$7/2^-$	334	$5/2^+$	0.006(4)		E1+M2
$^{150}\mathrm{Gd}^{f}$	1134	3^-	496	2^+	0.05(2)		E1+M2
	1518	2^+	880	2^+	-7(+3.-1)	0.83(3)	E2+M1+E0
	2787	2^+	2149	2^+	≤0.1 2.1(4)		E2+M1
$^{172}\mathrm{Yb}^{g}$	1172	3^+	912	4^+	-2.36(15)		E2+M1
	1466	2^+	1387	2^+	-5.17(+16,-11)	0.22(+16,-22)	E2+M1+E0
	1641	4^-	265	5^+	-0.092(63)		E1+M2
	1658	4^+	1398	4^+	-1.10(+46,-23) 42(+∞,-36)	0.44(+13,-22) ≤0.40	E2+M1+E0

[a] Ref.[7]. [b] Ref.[8]. [c] Ref.[9]. [d] Ref.[10]. [e] Ref.[11]. [f] Ref.[12]. [g] Ref.[13].

[h] As example,we give the probability ratios $X(EO/E2) = \left\{ \begin{array}{l} 2.75(95) \\ 1.04(10) \end{array}\right.$, and the multipole compositions, $\left\{ \begin{array}{l} 92.2(+27,-73)\%E0 + 2.8(+11,-6)\%E2 + 5.0(+63,-20)\%M1 \\ 92.6(8)\%E0 + 7.4(4)\%E2 + 0.1(+2,-1)\%M1 \end{array}\right.$, possible for this γ ray,and written in the same order as δ and $|q|$.

Table 2. Experimental anisotropies of several γ rays from the decay of ^{147}Eu and ^{169}Yb oriented in iron and gadolinium

Nucleus	E_γ (keV)	Anisotropy [%] Fe	Anisotropy [%] Gd
		T=13.6(1)mK	T=13.7(1)mK
^{147}Eu	197	-8.12(32)	-4.47(34)
	799	-11.50(28)	-7.10(43)
	856	-32.51(51)	-18.86(80)
		T=13(2)mK	T=13(2)mK
^{169}Yb	63	-7.88(49)	1.8 (39)
	198	13.44 (9)	-0.7 (3)
	308	-7.18(16)	0.6 (4)

parameters,$| \mu B_{hf} |$, for the $^{147}Gd_{83}$ and $^{149}Gd_{85}$, both having $I^\pi = 7/2^-$, in iron and gadolinium were evaluated from the experimental B_2 parameters. Electric quadrupole hyperfine interaction, expected to be small for the studied nuclei, was neglected. The values of $| \mu(^{147}Gd) | = 1.02(9)\mu_N$ and $| \mu(^{149}Gd) | = 0.88(4)\mu_N$ were evaluated [15] and they follow the systematics of the $7/2^-$ state magnetic moments of the odd-A nuclei in this region.

3. *Attenuation of the directional distribution of γ rays following the decay of oriented ^{171}Lu<u>Gd</u>.* Two low-lying states in ^{171}Yb have long half-lives [16]: 95 keV, $T_{1/2}$ = 525 μs and 122 keV, $T_{1/2}$ = 0.265 μs. The 95 keV state is only deexcited by the 19 keV γ ray, but its anisotropies have not been measured. However, the 67 and 76 keV states are strongly populated from the 95 and 122 keV states. Using the orientation parameter of the ^{171}Lu ground state, $B_2 = 0.636(15)$, determined from the anisotropies of the intense 740 and 781 keV transitions which deexcite unperturbed states, and the calculated deorientation coefficients, the attenuation factors of orientation of the 67, 76 and 122 keV states were determined from the anisotropies of the 67, 76 and 57 keV transitions with the M1+E2, E2 and M1+E2 multipolarities, respectively, see Ref. [17]. The results are presented in Table 3.

Table 3. Attenuation factors, G_2, for long-lived states in ^{171}Yb excited in the decay of oriented ^{171}Lu<u>Gd</u>

E_i (keV)	$T_{1/2}(\mu s)$	E_γ(keV)	I_i^π	I_f^π	G_2
66.7	a	66.7	$3/2^-$	$1/2^-$	0.32(2)
75.9	a	75.9	$5/2^-$	$1/2^-$	0.18(5)
122.4	0.265	56.7	$5/2^-$	$3/2^-$	1.0(6)

[a] Strong population from the states at 95 keV ($T_{1/2}$ = 525 μs) and 122 keV.

For the 57 and 67 keV transitions, the $| \delta(\alpha_K) |$ values calculated from the ICC data were used. The deorientation coefficients of the 9 and 19 keV transitions with the M1+E2 and E1+M2 multipolarities, respectively, were calculated using the values [18] of δ^2(9 keV) = $3.4x10^{-4}$ and δ^2(19 keV)$\leq 1.5x10^{-5}$.

4. *Experimental illustration of the symmetry principle action.* The structure of odd isotopes $^{167-173}$Yb was studied by NO of $^{167-173}$Lu<u>Gd</u> [17,9,10,19]. There is very interesting rotational band, $1/2^-[521]$, which is observed in all these isotopes of Yb. This band has irregular energy spacing and this is clearly reflected in the δ(E2/M1) values: the transitions connecting the levels furthest apart have large E2 admixtures ($\geq$15%), while the close-lying levels are connected by nearly pure M1 transitions (E2$\leq$1%). The most interesting fact [19] is that signs of δ(E2/M1) are suddenly changed when going from ^{169}Yb to ^{171}Yb, see Table 4.

Table 4. Comparison of the experimental and calculated multipole mixing ratios for the intraband transitions between the levels of the $1/2^-[521]$ band in ^{169,171}Yb

Nucleus	E_γ(keV)	I_i^π	I_f^π	Mixing ratio δ(E2/M1)	
				Exp	Theor
^{169}Yb	62.7	3/2	1/2	0.64(6)	0.42
	12.3	5/2	3/2	|0.06(2)|	0.03
	144.6	7/2	5/2	$0.52(^{+12}_{-9})$	0.55
	20.4	9/2	7/2	|0.08(3)|	0.05
	222.7	11/2	9/2	$0.15\leq \delta \leq 0.40$	0.45
^{171}Yb	66.7	3/2	1/2	-0.696(13)	-0.50
	9.2	5/2	3/2	|0.018(3)|	-0.04
	154.8	7/2	5/2	|0.62(12)|	-0.39

The explanation of the jump in properties is in the filling of the $1/2^-[521]$ shell which becomes the ground state in ^{171}Yb. Thus, there is a transition from the particle states to the hole states: $\bullet \rightarrow \circ$, i.e. there is experimental observation of the space reflection property.

5. *Admixture of another multipole in the multipolarity of β transition.* Multipole mixing ratios deduced for the 757 and 1005 keV γ rays from the decay of oriented ^{154}Eu<u>Fe</u> [3], δ (757 keV) = $-7.0^{+0.8}_{-1.0}$ and δ (1005 keV) = $-7.1^{+0.4}_{-0.5}$ agree with the most precise results of the γ-γ correlation measurements [14], $\delta = -6.1 \pm 0.2$ and $\delta = -7.8^{+0.2}_{-0.3}$, respectively, only if the $3^- \rightarrow 3^+$ β transition to the 1128 keV level in ^{154}Gd contains the $\Delta j_\beta = 1$ and 61.5(65)% $\Delta j_\beta = 0$ components.

6 Particularities in the properties of ^{166}Er, ^{160}Dy and ^{148}Gd

6.1 Introduction

In last few years we have been studying the low-temperature nuclear orientation (LTNO) of ^{148,153,155}T ^{155}Dy, ^{158,160}Ho and ^{166}Tm in Gd. Final results were already obtained on the ^{148}Tb and ^{160}Ho.

In this report we shall show some (far from all) results which we received of late and which seem to be interesting. They are connected with "anomalous" properties of the γ- vibrational bands in ^{166}Er (preliminary results in [20,21]) and ^{160}Dy [6] and with collective properties of ^{148}Gd (preliminary results in [22,23]).

6.2 Experimental details

As all samples were prepared by our usual way, we only mention some details.

Activities, samples: The radioactive sources were produced in a spallation reaction on tantalum making use of the 680 MeV proton beam of the Dubna phasotron. Chemical separation of the Yb, Er and Tb fractions were carried out from the irradiated target, and each of ^{160}Er and ^{148}Tb was mass-separated and simultaneously implanted into Gd. The ^{160}ErGd ($^{160g+m}$HoGd, equilibrium) and ^{148}TbGd samples were thermally treated. After 24 h, the Yb fraction decayed and ^{166}Tm was melted with the piece of Gd resulting into the ^{166}TmGd sample. All samples were formed as the disks of diameter ≈ 5-6 mm and were soldered to the cold finger of a top-loading ^{3}He-^{4}He dilution refrigerator.

Note: (i) about ten times stronger activity of ^{166}Tm is needed due to strong flying ability of Tm at high temperatures during melting and soldering; (ii) the Er isotope ($I^\pi = 0^+$, $T_{1/2}$ = 29 h, EC-decay, practically no γ-rays) decays to $^{160g+m}$Ho and (iii) the half-life of ^{148}Tb, $T_{1/2}$ = 60(1) min, is short, a top speed is needed in all procedures. (By the way, ^{148}Tb and ^{167}Lu, $T_{1/2}$ = 51.5 min, are the most short-lived isotopes measured by the off-line LTNO.)

"Cold" samples were maintained at 14-15 mK, "warm" states were at ≈ 1.0 - 1.2 K.

The γ-ray spectra were taken at 0° and 90° relatively to external magnetic field direction, B_{ext} = 1.0 - 1.2 T, by Ge(Li) detectors.

6.3 Experimental results

6.3.1 ^{166}TmGd $\rightarrow ^{166}$ErGd

The level structure of the well-deformed even-even ^{166}Er [6] nuclide may be studied through the β^- decay of $^{166g+m}$Ho and through the β^+ and electron capture (EC) decay of ^{166}Tm. The high-spin levels (up to I = 8) with $E_{level} \angle$ 1.9 MeV are excited in the decay of the metastable state of ^{166}Ho ($I^\pi = 7^-$, $T_{1/2} = 1.2x10^3$ y), whereas the states with the lower spins (I = 1-4), but up to $E_{level} \approx$ 3.0 MeV are seen in the decay of ^{166}Tm ($I^\pi = 2^+$, $T_{1/2}$ = 7.7 h).

Multipole mixing ratios of the transitions in ^{166}Er were studied by the $\gamma - \gamma$ angular correlations from both decays [24] and by the LTNO of ^{166}HoHo [25].

We have measured directional distributions, [W(0°)-1] up to 70 % and [1-W(90°)], for 30 γ rays following the decay of oriented ^{166}TmGd.

The anisotropies of the 786 and 876 keV transitions both **having pure E2 multipolarity, and** the E1(+M2) transition at 215 keV (our value of mixing ratio is δ(M2/E1) = -0.07(9)) were used to evaluate the orientation parameters. The weighted mean values obtained are B_2 = 0.254(22) and $B_4 \leq$ 0.07. These B_λ values and calculated U_λ coefficients were used to determine δ for all mixed transitions, see Table 5.

Table 5. Examples of present experimental results on the E2/M1 and M2/E1 mixing ratios of transitions in ^{166}Er

E_{lev} (kev)	I_i^π	E_γ (kev)	I_f^π	δ	E_{lev} (keV)	I_i^π	E_γ (keV)	I_f^π	δ
786	2^+	705	2^+	$-6.7^{+3.4}_{-22.8}$	2123	3^+	215	3^-	-0.04 ± 0.8
859	3^+	594	4^+	-12 ± 2			1868	4^+	$+3.6^{+2.4}_{-1.2}$
		779	2^+	$-6.2^{+0.8}_{-1.0}$			2052	2^+	$+6.0^{+7.7}_{-2.4}$
956	4^+	691	4^+	$+5.5^{+2.8}_{-1.4}$	2160	3^+	1374	2^+	$-0.34^{+0.12}_{-0.17}$
2021	2^-	1235	2^+	+0.05(10)			2080	2^+	$+9.7^{+\infty}_{-6.1}$

Particular interest was paid to the E2/M1 mixing ratios of the γ-vibrational to ground-state band transitions, see Table 6. It is seen that mixing ratios of the $4^+ \rightarrow 4^+$, $6^+ \rightarrow 6^+$ and $8^+ \rightarrow 8^+$ γ-vibrational transitions, see Table 1 and Ref. [25], are changing the sign inside the band!

6.3.2 $^{160g+m}$HoGd $\rightarrow$ ^{160}DyGd

A number of studies have been carried out in the past to determine the level structure of ^{160}Dy from the β^- decay of ^{160}Tb and from the β^+ + EC decay of $^{160g+m}$Ho. The previous results on γ rays, conversion electrons, $\gamma - \gamma$ coincidences, internal conversion coefficients (ICC) and multipolarities of many transitions in ^{160}Dy are summarized in the Nuclear Data Sheets [28]. Multipole mixing ratios of γ rays have been investigated extensively by the LTNO and $\gamma - \gamma$ angular correlation measurements from the decay of ^{160}Tb [29] and by the (α, 2n) reaction and Coulomb excitation, see [28].

We have studied the LTNO of both decaying nuclei, ^{160}Tb [30] and $^{160g+m}$Ho [6], and the latter was studied by LTNO for the first time. Note that the ^{160}Ho was measured using the decay: ^{160}Er ($I^\pi = 0^+$, $T_{1/2}$ = 29 h) $\rightarrow ^{160}$Ho. The decay study of oriented $^{160g+m}$Ho gave an excelent posibility to investigate the high-spin members (up to I = 6) of collective bands as well as the low-spin states (I = 1).

The anisotropies, [W(0°)-1] up to 80 % and [1-W(90°)], of 29 γ rays were measured. [Note: since resolution of the HPGe detector (20 cm^3, at 0°) is much better than that of a coaxial Ge(Li) detector (33 cm^3, at 90°), 1.9 and 4.5 keV at 1.3 MeV, respectively, the uncertainties in W(0°) and W(90°) are different, i.e. $\Delta W(90°) \gg \Delta W(0°)$.]

Table 6. Reduced E2/M1 mixing ratios, Δ(E2/M1) = δ(E2/M1)/ E_γ(MeV), of the γ-vibrational to ground-state transitions in ^{166}Er obtained by the LTNO are compared with previous results and with theoretical values calculated using the dynamic deformation model (DDM) [8]

$I_i^+ \rightarrow I_f^+$	Δ^{exp}				Δ^{th}
	Present^a TmGd	Krane et al.^{b} HoHo(1981)	Present^c TmGd(1985)	Hamilton et al.^{d} HoHo(1990)	Hamilton^d et al. (1990)
			ΔI = 0		
2 → 2	-10^{+5}_{-8}		-7^{+4}_{-20}		-16
4 → 4	$+8^{+2}_{-4}$	$-23^{+13}_{-\infty}$	$-12 \leq \delta \leq +10$	$+819^{+891}_{-755}$	+6.3
6 → 6		$+15^{+3}_{-2}$		$+37^{+10}_{-26}$	+4.3
8 → 8			$+8^{+2}_{-4}$	+3.8	
			ΔI = -1		
3 → 2	-8 ± 1	-26^{+5}_{-3}	-19^{+8}_{33}	-57^{+16}_{-10}	-63
5 → 4		-26 ± 3		-26^{+3}_{-2}	-59
7 → 6		-28 ± 5		-21 ± 2	-384
			ΔI = +1		
3 → 4	-20^{+8}_{-49}	-9^{+4}_{-12}	-60^{+54}_{-19}	-59	
5 → 6		-117^{+32}_{-75}		-81^{+14}_{-10}	-90
7 → 8		$-110^{+45}_{-\infty}$		-512^{+688}_{-329}	+16

^{a} Reference [20]. ^{b} Reference [27]. ^{c} Reference [21]. ^{d} Reference [25].

It may be seen that the produced ^{160}Ho source contains an equilibrium mixture of the ground-state, ^{160g}Ho, and the first metastable state, ^{160m}Ho, activities. As there is no posibility to separate

Table 7. Orientation parameters of the ground and metastable states of ^{160}Ho oriented in Gd

E_γ(keV)	I_i^π	I_f^π	B_2	$B_4{}^a$
		^{160g}Ho, $I^\pi = 5^+$		
728.2	4^+	2^+	1.372(77)	0.97 (12)
753.1	5^+	3^+	1.41 (11)	0.62 (29)
1069.1	4^+	2^+	1.30 (17)	0.72(121)
Weighted average:			1.374(60)	0.92 (11)
		^{160g}Ho, $I^\pi = 2^-$		
2184.7	2^-	2^+	1.02 (45)	
2674.8	1^-	0^+	1.17 (17)	
2735.1	1^-	0^+	1.21 (44)	
Weighted average:			1.16 (15)	

[a] Theoretical value of B_4 = 0.24(3) was used for the ^{160m}Ho 2^- state, see text.

these activities sufficiently well, a precise establishment of two separate decay schemes is impossible. Thus, the β-decay spin sequence and intensity balance for each level were used to deduce the intensity of any particular β^+ + EC transition and to separate the ^{160g}Ho decay scheme.

Naturally, the population of the ^{160}Dy levels from ^{160g}Ho, ^{160m}Ho and $^{160g+m}$Ho must be considered and corresponding B_λ and U_λ values must be determined. The appropriate expressions, which we have evaluated [1] for any number of isomeric states, were used. The orientation parameters for the ground and metastable states of ^{160}Ho, evaluated from the anisotropies of the E2 and E1(+M2) transitions, are presented in Table 7. The values of the B_λ obtained are very close to saturation values: $B_2(g) = 1.698$, $B_4(g) = 1.177$ and $B_2(m) = 1.195$, so we concluded that the theoretical value of $B_4(m) = 0.24(3)$ corresponding to our $B_2^{exp}(m)$, with similar uncertainty, is a good estimate.

Mixing ratios of the transitions in ^{160}Dy are illustrated by Table 8.

As is seen from Table 9, the collective bands in ^{160}Dy are very interesting.

And the most interesting results concern the $4_\gamma \rightarrow 4_g$ 872 and $6_\gamma \rightarrow 6_g$ 857 keV transitions. There are two solutions of Eq. for the A_2 coefficient [6]: $\delta = 5.0^{+2.2}_{-1.1}$ or $-0.70^{+0.08}_{-0.09}$ and $\delta = 5.1^{+5.8}_{-1.6}$ or $-1.06^{+0.17}_{-0.25}$. The ICC data give $|\ \delta(\alpha_K)\ | = 4^{+\infty}_{-1}$ and $2.5^{+1.9}_{-0.6}$, respectively, in agreement with the larger positive values in both cases.

Thus, the sign change of mixing ratios was observed for the $\Delta I = 0$ transitions between the γ-vibrational and ground-state bands beginning again, as for ^{166}Er, at the $4_\gamma \rightarrow 4_g$ transition.

It should be pointed out that in 1979, when our results of the LTNO studies of ^{160}Tb$\underline{\text{Gd}}$ were published, nothing was known about the mixing ratio sign change for the $\gamma \rightarrow g$ transitions. On the contrary, systematic study of these δ (E2/M1) have indicated the dependence which is looking like this:

before ○ →⊂⊃ transition	affer ○ →⊂⊃ transition
N = 88-90	N = 88-90
γ band $+\delta$	γ band $-\delta$
β band $-\delta$	β band $+\delta$

for the $4_\gamma \rightarrow 4_g$ 872 keV transition, the negative value of δ was chosen from two solutions [30]: $\delta = -0.70 \pm 0.10$ or $5.0^{+2.4}_{-1.3}$. The ICC data were not known since the 872 keV γ ray is quite weak (let us compare:

$$I_{765} : I_{872} : I_{879} : I_{962} = \left\{ \begin{array}{l} 18 : 30 : 100 : 90 - Ho \\ 7 : 0.73 : 100 : 33 - Tb \end{array} \right\})$$

and is affected by the close and intense 879 keV γ ray. Ten years later, the same conclusion was made by Marshak et al. [29], who also preferred

Table 8. Examples of the A_λ coefficients and mixing ratios for the E2, M1+E2 and E1+M2 transitions in ^{160}Dy

E_{level} (keV)	I_i^π	E_γ (keV)	I_f^π	A_2	A_4^a	δ^a
966	2^+	$879^{b,c}$	2^+	0.222(26)	-0.17(18)	$-12.5^{+2.9}_{-5.0}$
		966	0^+	-0.597(40)	-1.13(33)	
1156	4^+	$872^{b,c}$	4^+	0.109(48)	0.20(60)	$+5.0^{2.0}_{-1.1}$
		1069	2^+	-0.408(52)	-0.10(56)	
1289	5^+	1005	4^+	0.142(48)	0.35(26)	$-13.2^{+3.3}_{-6.7}$
1399	3^-	1312	2^+	0.21 (10)		$+0.071 \pm 0.052$
1438	6^+	857	6^+	0.178(67)	0.02(21)	$+5.1^{+5.8}_{-1.6}$
1519	2^+	1432	2^+	-0.31 (18)		$+2.9^{+2.1}_{-1.0}$
1694	4^+	$539^{b,c}$	4^+	0.205(64)	-0.03(12)	$+12.1^{+141.3}_{-6.0}$
		728	2^+	-0.446(32)	-0.48(25)	
1703	4^+	1419	4^+	-0.13 (28)		$2.1^{+4.6}_{-1.0}$
2675	1^-	2588	2^+	0.16 (28)		0.1 ± 0.3
		2675	0^+	0.74 (23)		

[a] Theoretical values of A_λ coefficients for pure E2 and E1 transitions are: A_2 ($2 \rightarrow 0$) = -0.598, A_4 = -1.07; A_2 ($4 \rightarrow 2$) = -0.448, A_4 = -0.304 and A_2 ($1 \rightarrow 0$) = 0.707, A_4 = 0.

[b] A_λ coefficients are determined independently on B_λ and U_λ values using the anisotropies of pure E2 transition from the same level.

[c] The A_2 coffecients for the 539, 872 and 879 keV transitions determined using B_λ and U_λ values are A_2 = 0.204(64), 0.100(44) and 0.221(26), respectively.

the negative value of $\delta = -0.953^{+0.081}_{-0.105}$ for the 872 keV γ ray from the oriented ^{166}Tb$\underline{\text{Tb}}$(sc), see Table 9.

Thus, the results of the LTNO measurements of $^{160g+m}$Ho$\underline{\text{Gd}}$ and ^{160}Tb$\underline{\text{Gd}}$ show that the multipole mixing ratios of the $2_\gamma \rightarrow 2_g$, $3_\gamma \rightarrow 2_g$, $3_\gamma \rightarrow 4_g$ and $5_\gamma \rightarrow 4_g$ transitions and the $4_\gamma \rightarrow 4_g$ and $6_\gamma \rightarrow 6_g$ transitions differ in both magnitude and sign.

Two $K^\pi = 0^+$ bands are excited, but very weakly, in the decay of $^{160g+m}$Ho, and the first band is even weaker than the second one. The anisotropies of $2 \rightarrow 2$ and $4 \rightarrow 4$ transitions at 1419 and 1432 keV, respectively, between the second β_2-vibrational ($K^\pi = 0^+$) and ground- state ($K^\pi = 0^+$) bands were measured. The larger values of δ, see Table 9, were preferred since the E0 admixtures were assumed on the basis of the ICC data which means that

$$\alpha_K^{exp} = [\delta^2(1+q^2)\alpha_K(E2) + \alpha_K(M1)]/(1+\delta^2), \tag{8}$$

where $|q(E0/E2)|$ is the magnitude of the E0/E2 mixing ratio for $\Delta I = 0$ transition and α_K^{exp}, α_K(E2) and α_K(M1) are experimental and theoretical K-conversion coefficients. The E0/E2 probability ratio is

$$X(E0/E2) = 2.56 \cdot 10^9 \frac{A^{4/3} q^2 \alpha_K(E2) E_\gamma^5}{\Omega_K(Z,k)}, \tag{9}$$

where E_γ is the transition energy in MeV and Ω_K(Z,k) is the electronic factor in s^{-1}. This factor is related to the E0 conversion coefficient, A(E0), as

$$\Omega_K(Z,k) = 8\pi\alpha k A(E0), \tag{10}$$

Table 9. Present E2/M1 mixing ratios δ for the γ-vibrational ($K^{\pi}=2^+$) and β_2-vibrational ($K^{\pi}=0^+$) to the ground state ($K^{\pi}=0^+$) band transitions in ^{160}Dy are compared with previous results obtained by NO of ^{160}Tb

$I^+_{\gamma} \rightarrow I^+_g$	E_{γ} (keV)	Present[a] HoGd	Fox et al.[b] TbGd(74)	Our prev.w.[c] TbGd(82)	Krane[d] TbTb(82)	Marshak et al.[e] TbTb(sc)(89)
				$K^{\pi}=2^+$, γ-vibr.		
$2 \rightarrow 2$	879	-12^{+3}_{-5}	-18^{+4}_{-8}	-13 ± 2	-17^{+1}_{-2}	-16.6 ± 0.5
$3 \rightarrow 2$	962	-13^{+2}_{-4}		-12 ± 1	-11 ± 1	-13.8 ± 0.3
$3 \rightarrow 4$	765	-13^{+4}_{-10}	$-7.7^{+0.6}_{-0.7}$	-9^{+5}_{-5}	$-8.3^{+0.7}_{-0.9}$	-13.7 ± 0.9
$4 \rightarrow 4$	872[f]	5^{+2}_{-1}		$+5^{+2}_{-1}$ -0.70 ± 0.10		$+21^{+\infty}_{-10}$ -0.95 ± 0.10
$5 \rightarrow 4$	1005					
$6 \rightarrow 6$	857					
				$K^{\pi}=0^+_3$, β_2-vibr.		
$2 \rightarrow 2$	1432	3^{+2}_{-1}				
$2 \rightarrow 2$	1419	2^{+5}_{-1}				

[a] Reference [6]. [b] Reference [31]. [c] Our previous work [30]. [d] Reference [32]. [e] Reference [29]. [f] By analogy with the sign of the δ values for the γ-vibrational transitions in the even-even deformed nuclei, the negative values were preferred in Refs.[30] and [29]. Comparison with the ICC value determined from the ^{160}Ho data gives the positive value for this transition.

where α is the fine structure constant and k is transition energy in the mc^2 units. The values of $|q(E0/E2)|$ and $X(E0/E2)$ determined are presented in Table 10.

Though uncertainties in $|q|$ and $X(E0/E2)$ are large due to large experimental errors in α_K^{exp}, the $|q(E0/E2)|$ and $X(E0/E2)$ values are generally consistent with the systematics: values for the $\gamma \rightarrow$ g transitions are by an order of magnitude smaller than those for the $\beta \rightarrow$ g transitions.

Our experimental results allow for more precise, and in many cases unique, spin assignments of several levels in ^{160}Dy, especially as compared to the multiple spins allowed by the previously available data. We shall show one example only.

The 2271.3 keV level, $I^{\pi} = 2^-$. The E1 multipolarity of the 2185 keV transition to the 2^+ state indicates negative parity and I = 1, 2 or 3. For $I^{\pi} = 1^-$ and 3^-, the M2 admixtures of (22^{+8}_{-15})% and of $(7.5^{+2.4}_{-2.1})$%, respectively, obtained from the anisotropy of the 2185 keV γ ray, are too large for the E1+M2 transition. Thus, the 1^- and 3^- assigments are ruled out.

6.3.3 ^{148}TbGd $\rightarrow$ ^{148}GdGd

The even-even $^{148}_{64}$Gd nuclide is of particular interest as it is lying near by the transition from the spherical to deformed nuclei (N = 88-90) and the $^{146}_{64}Gd_{82}$ nuclide, treated as a doubly magic nucleus, is a core for ^{148}Gd.

We have studied the X and γ rays, $\gamma-\gamma$ coincidences, conversion electrons and positrons from the decay of 60 min ^{148}Tb. Preliminary results of these studiues were only published [22] in the years 1975 and 1979. However, after we measured the nuclear orientation of ^{148g}Tb in gadolinium [23], the decay scheme of ^{148g}Tb became to be needed for the analysis of the experimental NO data.

Before our investigations, in the year 1973, Vylov et al.[33] measured 49 γ rays, 4 K-conversion lines and 7 $\gamma-\gamma$ coincidences and proposed the decay scheme of ^{148g}Tb with 34 γ rays placed among 18 levels in ^{148}Gd. After our previous results [22] were reported, Tidemand-Petersson (in 1985) measured [34] 67 γ rays and 52 $\gamma-\gamma$ coincidences, and after this Tidemand-Petersson et al.[35] determined decay energy of ^{148g}Tb, Q, and the E2/M1 mixing ratio of the 1079 keV transition, $\delta = 4.6\ ^{+3.5}_{-1.4}$, by the $\gamma-\gamma$ angular correlation measurement. The value of δ was chosen from two solutions by comparison with our value of $|\ \delta(\alpha_K)\ |$. The decay scheme was proposed [34] with 55 γ rays placed among 26 levels.

Table 10. Magnitudes of the E0/E2 mixing ratios and the relative E0/E2 probabilities of the $\Delta I = 0$ transitions from the γ-vibrational ($K^{\pi} = 2^+$) and second β-vibrational ($K^{\pi} = 0^+$) bands to the ground-state ($K^{\pi} = 0^+$) band

$I^+_i \rightarrow I^+_f$	E_{γ} (keV)	E_{level} (keV)	$\|q(E0/E2)\|$	$X(E0/E2)$
		γ-vibrational ($K^{\pi} = 2^+$) band		
$2 \rightarrow 2$	879	966	$0.24^{+0.09}_{-0.16}$	0.043 ± 0.038
$4 \rightarrow 4$	872	1156	$0.15^{+0.18}_{-0.15}$	$0.016^{+0.064}_{-0.016}$
$6 \rightarrow 6$	857	1438	$0.32^{+017}_{-0.32}$	$0.072^{+0.079}_{-0.072}$
		β_2-vibrational ($K^{\pi} = 0^+$) band		
$2 \rightarrow 2$	1432	1519	$0.63^{+0.36}_{-0.63}$	$0.78^{+1.13}_{-0.78}$
$4 \rightarrow 4$	1419	1703	0.85 ± 0.22	$1.40^{+0.79}_{-0.62}$

We measured 129 γ rays, 38 $\gamma-\gamma$ coincidences, conversion lines of 14 γ transitions and 3 β^+ transitions. On the basis of our results and all data available [33-36] we propose the decay scheme of 60 min ^{148}Tb which contains 39 levels in ^{148}Gd up to 5400 keV based mostly on the $\gamma-\gamma$ coincidence results with 90 γ rays placed among these levels. Together with our previous results [4], 20 new levels were proposed.

The LTNO of ^{148g}TbGd was measured for the first time. The anisotropies, [W(0°)-1] up to 25%, for 35 γ rays were measured. For instance, the anisotropies of the 489, 784, 1089 and 1863 keV transitions are [W(0°)-1] = 28.1(33), -25.0(31), 8.7(35) and -24.5(50)%, respectively.

The orientation parameters were determined from anisotropies of pure E2 transitions at 632, 784 and 1863 keV. Weighted mean values are $B_2 = 1.039(81)$ and $B_4 = 0.10(8)$. Examples of directional distribution coefficients and multipole mixing ratios of transitions in ^{148}Gd, determined from the transition anistropies using above B_{λ} and calculated U_{λ} values, are presented in Table 11.

Using our values of δ and α_K^{exp} the values of $|q(E0/E2)|$ and $X(E0/E2)$ for the $\Delta I = 0$ transitions in ^{148}Gd were determined, see Table 12.

The most interesting is the $|q|$ value for the $3^- \rightarrow 3^-$ 960 keV γ ray which is consistent with the values for the β- vibrational transitions ($\beta \rightarrow$ g) which indicates the collective character of the 3^- state at 2234 keV. This is the first such value for the transition between the levels with negative parities!

6.3.4 Discussion

The dynamic deformation model [8], where large configuration space is employed for the microscopic part of the calculation and a numerical integration method is used for the collective (band-mixing) part, has been applied to calculate the low-energy structure of ^{166}Er and ^{160}Dy. Two model parameters, the proton- and neutron-pairing strengths, were adjusted to fit the energy and magnetic moments of the first 2^+ states.

The structural properties of the ground-state, γ- and β-vibrational bands of ^{166}Er and ^{160}Dy were calculated. The quadrupole- and pairing-deformations were averaged over the β- and γ-

Table 11. Directional distribution coefficients and multipole mixing ratios of transitions in ^{148}Gd

E_{level} (keV)	I_i^π	E_γ (keV)	I_f^π	A_2	δ or A_2^{th}
784	2^+	784	0^+	-0.564(93)^a	A_2^{th}=-0.598
1274	3^-	489	2^+	0.472(69)	-0.068±0.039
1416	4^+	632	2^+	-0.430(71)	A_2^{th}=-0.448
1835	2^+	1050	2^+	-0.33(26)	$+2.7^{+3.7}_{-1.2}$
	3^+	1050	2^+	-0.27(21)	$+12.6^{\infty}_{-7.8}$
1863	2^+	1079	2^+	-0.057(56)	$+6.9^{+2.9}_{-1.6}$
		1863	0^+	-0.66(17)^a	A_2^{th}=-0.598
2189	2^+	1404	2^+	0.38(13)	$-4.1^{+21.}_{-5.4}$
		2188	0^+	-0.70(21)	A_2^{th}=-0.598
2234	3^-	960	3^-	-0.435(99)	$+1.31^{+0.34}_{-0.30}$
2700	2^+	1426	3^-	0.16(24)	+0.03±0.19
		1916	2^+	-0.56(18)	$+1.66^{+0.79}_{-0.59}$ or $+0.12^{+0.23}_{-0.16}$
5400	3^-	842	1^-	-0.44(12)	A_2^{th}=-0.495
	4^+	842	2^+	-0.50(14)	A_2^{th}=-0.448

^{a} The A_2 coefficient is calculated using the weighted mean values of B_λ without the B_λ parameters of this transition.

dependent wave functions for each nuclear state. Several of these deformations are not constant but vary by 10-30%. Mixing of all K-values allowed for each spin I were taken into account. It was shown that the K-mixing increases with I and with the excitation energy. Such variations play a crucial role in the values of the E2/M1 mixing ratios, since the M1 transitions are much weaker than the E2 transitions among collective bands. Hence, even minute variations in deformations and in the K-mixing can have dramatic effect on the mixing ratios.

The calculated reduced mixing ratios, $\Delta(E2/M1) = \delta(E2/M1)/E_\gamma$ (MeV), of the transitions in ^{166}Er and ^{160}Dy are presented in Tables 2 and 9 where they are compared with the experimental data. The experimental and theoretical values of X(E0/E2) for ^{160}Dy are also given in Table 13. Considering the sensitivity of the mixing ratios, the sign change of the Δ(E2/M1) values is described by theory correctly for ^{166}Er, though the experimental and theoretical magnitudes of Δ differ appreciably, whereas in ^{160}Dy, the calculated Δ(E2/M1) values are remarcably close to the experimental mixing ratios, except that the sign change for the theoretical $\gamma \rightarrow$ g E2/M1 mixing ratios (with $\Delta I = 0$) is shifted from $I_i = 4_\gamma$ to $I_i = 10_\gamma$.

It is not easy to interprete the levels of ^{148}Gd as (i) the data are not sufficiently precise and they are far away from the completeness, and (ii) even in the case when the data are quite accurate, there are doublets of levels which are not observed in neighbouring nuclei.

As regards the X(E0/E2) values, such ratios for $\Delta K = 2$ transitions are predicted to vanish in the lowest order, since the E0 transitions are forbidden. The latter are allowed for the ΔK = 0 transitions, which is an important signature of a β-vibrational band. This is indicated by the relatively large X(E0/E2) values for the $\beta \rightarrow$ g transitions in the studied nuclei. The large value of X(E0/E2), firstly observed for the transition between the levels with negative parity, the $3^- \rightarrow 3^-$ transition in ^{148}Gd, also indicates the collectivity of this 3^- level.

Table 12. The values of δ(E2/M1), α_K^{exp}, |q(E0/E2)| and X(E0/E2) for the $\Delta I = 0$ transitions in ^{148}Gd

E_{level} (keV)	E_γ (keV)	Transition	δ	α_K^{exp}	|q(E0/E2)|	X(E0/E2)
1835	1050	$2_2^+ \rightarrow 2_g^+$	$2.7^{+3.7}_{-1.2}$	2.3(8)	$0.11^{+0.57}_{-0.11}$	$0.002^{+0.054}_{-0.002}$
1863	1079	$2_3^+ \rightarrow 2_g^+$	$5.8^{+2.2}_{-1.0}$	1.6(1)	~0	~0
2189	1404	$2_4^+ \rightarrow 2_g^+$	$-4.1^{+2.1}_{-5.4}$	2.0(4)	$0.81^{+0.27}_{-0.30}$	$0.13^{+0.10}_{-0.08}$
2424	1008	$4_2^+ \rightarrow 4_g^+$	$1.0^{+0.4}_{-0.5}$	3.3(8)	$0.2^{+0.8}_{-0.2}$	$0.004^{+0.096}_{-0.004}$
2522	1106	$4_3^+ \rightarrow 4_g^+$	$1.3^{+0.6}_{-0.5}$	2.3(7)	$0.4^{+0.5}_{-0.4}$	$0.02^{+0.08}_{-0.02}$
2334	960	$3_2^- \rightarrow 3_1^-$	1.3±0.3	4.4(10)	$0.83^{+0.38}_{-0.44}$	$0.065^{+0.072}_{-0.050}$

6.3.5 Conclusions

The X and γ rays, $\gamma - \gamma$ coincidences, conversion electrons and positrons from the decay of 60 min ^{148g}Tb were measured. Considerably enriched decay scheme of 60 min ^{148}Tb is proposed with 90 γ rays placed among 39 levels (20 of them are new) with energy up to 5400 keV. Directional distributions of γ rays following the decay of ^{166}Tm, $^{160g+m}$Ho and ^{148g}Tb oriented in gadolinium were measured and multipole mixing ratios were determined.

Sign change of the E2/M1 mixing ratios of transitions from the γ- vibrational ($K^\pi = 2^+$) band to the ground-state band in ^{166}Er and ^{160}Dy was observed: mixing ratios of the $\Delta I = 0$ transitions differ in magnitude and sign from the negative values of δ for all other $\gamma \rightarrow$ g transitions. The mixing ratio sign change was probably observed also in ^{164}Er (the uncertainties are large), and in all three cases, ^{160}Dy, ^{164}Er and ^{166}Er, the effect begins at $I_i = 4_\gamma$, i.e. the mixing ratio of the $4_\gamma \rightarrow 4_g$ transition changes sign first. The available data also show that positive mixing ratios occur in all three nuclei and are smaller in magnitude (larger M1) than the negative values of δ. This suggests that the mixing ratio sign change of the $\gamma \rightarrow$ g transitions is a more general and significant phenomenon. It seems that there is an "island" of nuclei with "anomalous" γ-vibrational bands and also with very weakly excited β-vibrational bands as compared with lighter (Sm, Gd) and heavier (Yb) even-even nuclei.

The anisotropies of the transitions between the β-vibrational ($K^\pi = 0^+$) and ground-state ($K^\pi = 0^+$) bands were also measured and the E2/M1 mixing ratios were determined in ^{160}Dy and ^{148}Gd. The magnitudes of the E0/E2 mixing ratios and consequently the E0/E2 probability ratios for the $\Delta I = 0$ transitions were obtained, including the |q(E0/E2)| and X(E0/E2) values for the transition between the negative parity levels in ^{148}Gd determined firstly. In general, all these values are consistent with the systemstics: the E0/E2 probability ratios of the $\gamma \rightarrow$ g transitions are by an order of magnitude smaller than those for the $\beta \rightarrow$ g transitions.

The mixing ratio sign change (in the same nucleus and for the same initial and final bands) is described at present by the dynamic deformation model only.

Table 13. Theoretical and experimental reduced mixing ratios for the $\gamma \to g$ and $\beta_2 \to g$ transitions in ^{160}Dy

$I_i \to I_f$	E_γ(keV)	E_i(keV)	$\Delta(E2/M1)(MeV^{-1})$		X(E0/E2)	
			Theor.	Exp.	Theor.	Exp.
$\gamma \to g,\ \Delta I = 0$						
$2 \to 2$	879.4	966.2	-19.0	$-14.2^{+3.3}_{-5.7}$	0.00058	0.043 ± 0.038
$4 \to 4$	872.0	1155.8	-14.3	$5.7^{+2.3}_{-1.3}$	0.0064	$0.016^{+0.064}_{-0.016}$
$6 \to 6$	856.9	1438.3	-17.4	$6.0^{+6.8}_{-1.9}$	0.0017	$0.072^{+0.079}_{-0.072}$
$8 \to 8$	834.2	1801.2	-61.6			
$10 \to 10$	794.1	2222.8	55.2			
$\gamma \to g,\ \Delta I = +1$						
$3 \to 4$	765.3	1049.1	-11.2	$-16.7^{+5.1}_{-12.7}$		
$5 \to 6$	707.6	1288.6	- 8.3			
$7 \to 8$	650.4	1617.4	- 8.9			
$9 \to 10$		2022.0	-11.7			
$\gamma \to g,\ \Delta I = -1$						
$3 \to 2$	962.4	1049.1	-14.1	$-13.3^{+2.4}_{-3.7}$		
$5 \to 4$	1004.7	1288.6	- 8.8	$-13.1^{+3.3}_{-6.7}$		
$7 \to 6$	1036.6	1617.4	- 9.6			
$9 \to 8$	1055.4	2022.0	-23.1			
$\beta_2 \to g,\ \Delta I = 0$						
$2 \to 2$	1432.0	1518.8	160.2	$2.0^{+1.5}_{-0.7}$	0.70	$0.78^{+1.13}_{-0.78}$
$4 \to 4$	1419.0	1703.2	-7.0	$1.5^{+3.2}_{-0.7}$	3.22	$1.40^{+0.79}_{-0.62}$

7 Conclusions

A new facility for low-temperature nuclear orientation of radioactive nuclei far for stability line is proposed to be built at JINR Dubna - the SPIN Facility. This facility, based on the state of the art of technological achievements together with the existing and planned JINR radioactive beam complexes YASNAPP and DROBs, will open new horizons for many new experiments with oriented nuclei in a broad range of atomic and mass numbers and nuclear half-lives. The SPIN program will lead to rich program in nuclear and solid state physics research.

References

[1] M. Krmar, T.I. Kracíková, and M. Finger: Yad. Fiz. **61** (1998) 797. [Phys. At. Nucl. **61** (1998) 717.]; Proceedings of the International Workshop "Symmetry and spin" Prague, August 31 - September 5, 1998, Eds. M.Finger, E.Kolganova, Czech. J. Phys. Vol. 49 (1999) S2.

[2] W.D. Hamilton: in *The Electromagnetic Interaction in Nuclear Spectroscopy* (Ed. W.D. Hamilton), North-Holland, Amsterdam, 1975.

[3] P.O. Lipas, J. Kumpulainen, E. Hammarèn, T. Honkaranta, M. Finger, T.I. Kracíková. I. Procházka, and J. Ferencei: Phys. Scripta **27** (1983) 8.

[4] T.I. Kracíková, M. Finger, S. Davaa, V.M. Tsupko-Sitnikov, V.M. Deryuga, and W.D. Hamilton: Nucl. Phys. **A408** (1983) 45.

[5] J. Kvasil, T.I. Kracíková, S. Dava, M. Finger, and B. Choriev: Czech. J. Phys. **B31** (1981) 1376; **B33** (1983) 626; **B35** (1985) 1084; **B36** (1986) 581.

[6] T.I. Kracíková, M. Fimger, M. Krmar, K. Kumar, A. Janata, N.A. Lebedev, V.N. Pavlov, and E. Šimečková: Phys. Rev. **C58** (1998) 1986.

[7] V.A. Deryuga, T.I. Kracíková, M. Finger, J. Dupák, A.I. Vdovin, and W.D. Hamilton: Izv. AN SSSR, Ser. Fiz. **46** (1982) 860.

[8] T.I. Kracíková, M. Finger, N.A Lebedev, M. Lyablin, V.N. Pavlov, I. Procházka, D.E. Shabalin, E. Šimečková, M. Slunečka, and Yu.V. Yushevich: in *The 46-th Annual Conf. on Nucl. Spectroscopy and Structure of At. Nucleus.* Nauka, Moscow, 1996, p. 64.

[9] T.I. Kracíková, M. Finger, S. Davaa, J. Dupák, V.N. Pavlov, N.A. Lebedev, W.D. Hamilton, and C. Girit: Czech. J. Phys. **B31** (1981) 527.

[10] S. Davaa, T.I. Kracíková, M. Finger, J. Kvasil, V.I. Fominykh, and W.D. Hamilton: J. Phys. G **8** (1982) 1585.

[11] E. Šimečková, P. Čížek, M. Finger, J. John, P. Malinský, and V.N. Pavlov: JINR Preprint E6-89-799, Dubna 1989.

[12] W.D. Hamilton, R.A. Fox, D.D. Warner, M. Finger, T.I. Kracíková, V.N. Pavlov, and A.F. Shchus: J. Phys. G **4** (1978) 1871.

[13] T.I. Kracíková, S. Davaa, M. Finger, M.I. Fominykh, W.D. Hamilton, P.O. Lipas, E. Hammarèn, and P. Toivonen: J. Phys. G **10** (1984) 1115.

[14] T.I. Kracíková, S. Davaa, M. Finger, V.N. Pavlov, and V.M. Tsupko-Sitnikov: Hyp. Int. **34** (1987) 127.

[15] T.I. Kracíková, S. Davaa, and M. Finger: Hyp. Int. **34** (1987) 69.

[16] V.D. Vorobiev, T.M. Usypko, and S.A. Shestopalova: in *Skhemy raspada radioaktivnykh yader A=171-174* (Ed. B.S. Dzhelepov), Nauka, Leningrad, 1977.

[17] T.I. Kracíková, S. Davaa, J. Kvasil, M. Finger, J. Koníček, and W.D. Hamilton: Nucl. Phys. **A440** (1985) 203.

[18] B.S. Dzhelepov: in *Svojstva deformirovannykh yader* (Ed. A.I. Muminov), Fan, Tashkent, 1983, p. 3.

[19] T.I. Kracíková, S. Davaa, M. Finger, N.A. Lebedev, V.N. Pavlov, M. Slunečka, Yu.V. Yushkevich, and J. Kvasil: Nucl. Phys. **A621** (1997) 639; T.I. Kracíková et al.: Hyp. Int. **15/16**(1983)37; S. Davaa et al.: JINR Report R6-84-556, Dubna, 1984.

[20] S. Davaa, T.I. Kracíková, J. Ferencei, M. Finger, N.A. Lebedev, and V.N. Pavlov: in *Proc. of 34th Annual Conf. on Nucl. Spectroscopy and Structure of At. Nuclei*, Leningrad, 1985. Nauka, Leningrad, 1985, p. 123.

[21] T.I. Kracíková, M. Krmar, M. Finger, A. Janata, N.A. Lebedev, V.N. Pavlov, I. Procházka, D.E. Shabalin, and E. Šimečková: in *Proc. of the Int. Conf. on Exotic Nuclei and At. Masses (ENAM 95)*, Arles, France, 1995 (M.de Saint Simon and O.Sorlin, eds.), Frontieres, Gif-sur-Yvette Cedex, Erance, 1995, p. 615; *Proc. of the Int. Conf. on Physics of Nucleus*. Moscow, 1996 (PIYaF, ed.), St-Peterburg, 1996, p. 67.

[22] A.E. Shchus, Ts. Vylov, K.Ya. Gromov, M.Ya. Kuznetsova, M.I. Fominykh, and Yu.V. Yushkevich: in *Proc. of 29th Annual Conf. on Nucl. Spectroscopy and Structure of At. Nuclei*, Riga, 1979, Nauka, Leningrad, 1979, p. 90; L.Puszok, M.Finger, and A.F.Shchus: in *Proc. of 25th Annual Conf. on Nucl. Spectroscopy and Structure of At. Nuclei*, Leningrad, 1975, Nauka, Leningrad, 1975, p. 107.

[23] T.I. Kracíková, M. Finger, A.F. Shchus, P. Tlustý, and A. Janata: in *The IXth Int. Conf. on Hyp. Int.*, Osaka, Japan, 1992, p. A-015.

[24] A.E. Ignatochkin, E.N. Shurshikov, and Yu.F. Jaborov: Nucl. Data Sheets **52** (1987) 365; E.N.Shurshikov and N.V.Timofeeva: Nucl. Data Sheets **67** (1992) 45.

[25] W.D. Hamilton, H. Marshak, and K. Kumar: J. Phys. G **16** (1990) L219.

[26] K. Kumar: in *Nuclear Models and Search for Unity in Nuclear Physics*, Universitetsforlaget, Bergen, 1984; Hyp. Int. **75** (1992) 43.

[27] K.S. Krane and J.D. Moses: Phys. Rev. C **24** (1981) 654.

[28] C.W. Reich: Nucl. Data Sheets **68** (1993) 405; **78** (1996) 547.

[29] H. Marshak, W.D. Brewer, and P. Roman: Phys. Rev. C **40** (1989) 1759.

[30] I.I. Gromova, J. Dupák, J. Koníček, T.I. Kracíková, N.A. Lebedev, B.S. Neganov, V.N. Pavlov, I. Procházka, M. Finger, V.M. Tsupko-Sitnikov, A.F. Shchus, A. Machová, W.D. Hamilton, and R.A. Fox: Izv. Akad. Nauk SSSR, Ser. Fiz. **43** (1979) 53 [Bull. Acad. Sci. USSR, Phys. Ser. **43** (1979) 422].

[31] R.A. Fox, W.D. Hamilton, and D.D. Warner: J. Phys. A **7** (1974) 1716.

[32] K.S. Krane: Nucl. Phys. **A377** (1982) 176.

[33] Ts. Vylov, K.Ya. Gromov, I.I. Gromova, G.I. Iskhakov, V.V. Kuznetsov, M.Ya. Kuznetsova, A.V. Potempa, and M.I. Fominykh: Izv. Akad. Nauk SSSR, Ser. Fiz. **37** (1973) 43 [Bull. Acad. Sci. USSR, Phys. Ser. **37** (1973) 36]; 37 (1973) 48 [**37** (1973) 41].

[34] P. Tidemand-Petersson: Z. Phys. **A320** (1985) 655.

[35] P. Tidemand-Petersson, E.Runte, W.D.Schmidt-Ott, and U.J.Schrewe: Z. Phys. **A320** (1985) 405.

[36] L.K. Peker: Nucl. Data Sheets **59** (1990) 393.

ON THE POSSIBILITY TO PRODUCE A POLARIZED RADIOACTIVE BEAM USING A LASER ION SOURCE

G.Neyens, R.Coussement, G.Georgiev, B.Bruyneel, M.Huyse, K.Kruglov,
Yu.Kudryavtsev, N.Severijns, P.Van Duppen, J.Van. Roosbroeck, L.Vermeeren,
L.Weissman

*University of Leuven, Instituut voor Kern-en Stralingsfysika, Celestijnenlaan 200 D,
B-3001 Leuven, Belgium*

We suggest to use the element selective two-step laser ionization process in an ion guide based laser ion source (IGLIS) not only to produce very efficiently and selectively a beam of radioactive nuclei, but also to polarize the spins of these nuclei during the ionization process. For this it is sufficient to use circularly polarized laser light in the first step (the resonant excitation) of the ionization process. Polarized beams of radioactive nuclei open the way to perform nuclear moment measurements or fundamental interaction studies on nuclei far from stability, without the need for an external spin-polarization process. The principle and possible problems are being discussed.

Since the discovery of parity nonconservation in weak interactions [1] this property of beta-decay of radioactive nuclei has been used widely for nuclear physics, solid state physics and fundamental interaction studies. It causes an asymmetry in the beta-decay of a spin-polarized ensemble of nuclei, the on-set or destruction of which - due to interaction of the nuclei with surrounding electromagnetic fields - is a signature to obtain information on, e.g., nuclear moments, electric field gradients, hyperfine fields or asymmetry parameters in beta-decay. Several techniques have been developed over the years to polarize radioactive nuclei. The first technique, also used by Wu et al. in their experiment which revealed the parity nonconservation [1], is the low temperature nuclear orientation (LTNO) method [2]. This technique requires lifetimes of the order of seconds or more for the radioactive nuclei, and is thus less suited for most nuclei near the border of stability. However, very high amounts of polarization can be obtained. A complementary technique to LTNO is the optical pumping method [3,4], in which a beam of radioactive nuclei is interacting with a circularly polarized laser beam over a flight path of several meters. The polarized laser beam will polarize the electron spins, and via the hyperfine interaction between the nuclear spin I and the electron spin J, the atomic spin polarization is transferred to the nuclear ensemble. In order to obtain sufficient polarization in the ground state, the atoms need to be pumped into an excited electron state, from which they decay back to the ground state, and this process has to be repeated several times. This requires the interaction time between the laser and the atoms to be typically of the order of ms. However, recent developments have shown that also isomeric states with lifetimes as short as microseconds can be spin-polarized using an optical pumping technique [5]. With optical pumping nuclear polarizations of the order of 30-40% can easily be achieved. A method which can be applied to very short-lived nuclei (down to μs half-lives), but which in general yields spin-polarizations of a few percent only, is tilted foil polarization [6,7]. Finally a nuclear spin-polarization can relatively easy be obtained also by using the nuclear reaction mechanism in which the radioactive nuclei are produced. Till now, spin-polarization has been measured for light recoiling fusion-evaporation residues [8] and for projectile fragments selected after a high-resolution in-flight mass spectrometer [9]. In both cases nuclear polarizations up to 10-15% have been observed. The fragmentation reaction allows to produce a pure beam of oriented radioactive nuclei far from stability, both on the proton and neutron rich side of the line of stability. The fact whether or not a spin-polarization can be obtained in projectile fragmentation is probably related to the difference in

mass number between the projectile and the fragment, but a systematic study on this has not yet been performed.

An alternative technique to produce a pure beam of radioactive nuclei far from stability is by using an element selective laser ion source in combination with an on-line mass separator [10]. This production and selection technique has recently been developed at the Leuven Isotope Separator On Line (LISOL) facility at the CYCLONE cyclotron in Louvain-la-Neuve. Pure beams of ^{54,55}Ni and ^{54}Co have been obtained in a light-ion induced fusion-evaporation reaction. The fusion-evaporation residues are neutralised and stopped in a high-pressure gas cell (typically 500 mbar) and submitted to an element selective resonant two-step laser ionization process. The basic principle of this two-step ionization is shown in figure 1. In the first step, the atoms are resonantly excited to an intermediate level by the first laser beam. This step is highly element selective. In the second step the atom is ionized, either resonantly (into an autoionization or a Rydberg state) or nonresonantly into the continuum.. The ionized atoms are then extracted from the ion source and sent through a mass separator, after which an isobaric pure beam is obtained.

The idea we suggest here is to use at least for the first step of the ionization process, circularly polarized laser light [11]. Due to the high power of a pulsed laser, it is possible to orient the atomic spins (and thus the nuclear spins) very fast in a single step by Rabi-oscillation. The idea was presented already in 1980 by Zaretsky et al. [12], who developed the formalism for optical spin-alignment. In a recent paper we have used similar ideas to calculate the amount of both spin-alignment and spin-polarization that can be obtained in a single-step resonant excitation of an atom with a circularly polarized laser beam [11]. By measuring the resonance fluorescence radiation of ^{23}Na atoms excited by short pulses of polarized laser radiation, Gangrskii et al. [13] have shown that it is indeed possible to obtain polarizations of the order of 10-20% with this technique.

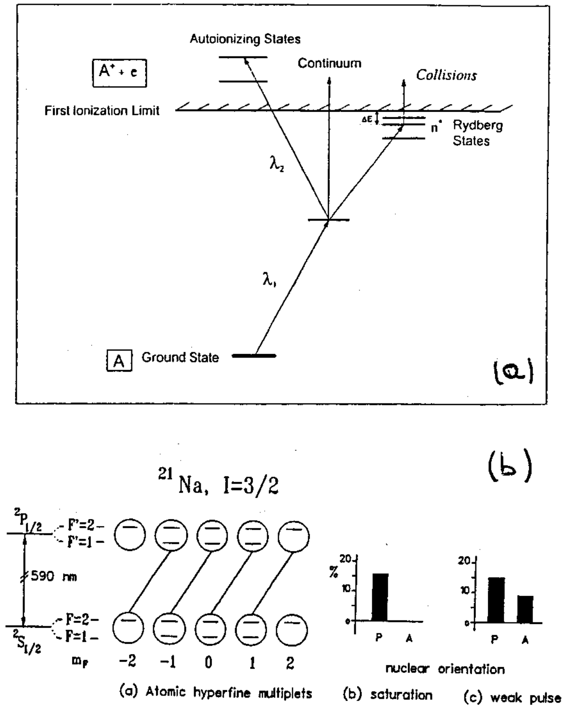

Figure 1: (a) Basic principle of the two-step laser ionization process [10]. (b) By using circularly polarized light in the first step of the process, a nuclear polarized radioactive beam can be obtained [11].

Now it remains to be proven, that the spin-orientation induced on atoms in the high-pressure medium of a laser ion source is still present after the atoms have been evacuated from the gas cell, transported through a short radiofrequency structure [15], accelerated to 50 keV and mass separated using a dipole magnet. Several causes for deorientation can occur between the moment of ionization and the moment of detection of the spin-oriented mass-separated radioactive nuclei. The most important ones are due to collisions with the buffer gas atoms

and the interactions with random magnetic fields that are noncollinear with the polarization direction. Once the atoms are oriented and ionized, the atomic spin-orientation has to survive in the high pressure of the gas cell: typically a pressure of 200-500 mbar of He or Ar gas is needed to stop the radioactive nuclei after the production reaction. As far as we know, studies of the maintenance of spin-polarization in a gas pressure have been performed only at low pressures (up to 40 mbar), showing that 50-80% of the polarization is maintained [14]. It is mainly the evacuation time from the gas cell which might play a crucial role. As this evacuation time can be fast (order of 5 ms) for atoms ionized using a transverse laser beam [10], there is a reasonable chance that atomic polarization is maintained. Another important possible cause for loss of atomic polarization is the passage through the SPIG (sextupole ion guide) [15], which is used to optimize the extraction efficiency. In the SPIG, an oscillating voltage is applied to 6 rods placed in a hexagonal configuration along the beam path. This oscillating electric field assures radial confinement of the ion beam. It is not clear whether or not the SPIG can induce loss of orientation. Finally the dipole field of the mass separator could still cause loss of spin-orientation. To avoid this, we have placed the circularly polarized laser beam vertically, thus parallel to the dipole field of the mass separator. Such parallel dipole field will induce a Larmor precession of the atomic spin around its symmetry axis, thus causing no loss of spin-orientation. However, small stray fields at the entrance and exit of the separator magnet, which are randomly oriented, might cause loss of orientation. Therefore a carefull measurement of the separator stray field should be performed. If that field is oriented in the same direction of the main field (which might be expected), the possible loss of orientation due to this interaction can be neglected.

In conclusion, we suggest to use circularly polarized light in the first step of a two-step resonant laser ion source, in order to obtain a pure beam of polarized short-lived radioactive nuclei. Such beams could be used for nuclear moment studies or fundamental interaction investigations. A feasibility test using ^{55}Ni ($T_{1/2} \sim 200$ ms) produced in a ^{54}Fe(^{3}He,2n) reaction is underway.

References

[1] C. Wu et al., Phys. Rev. C 105 (1957) 1413

[2] "Low Temperature Nuclear Orientation", eds. H. Postma and N.J. Stone (Norht Holland, Amsterdam, 1986)

[3] R. Neugart et al., Z. Phys. 261 (1973) 237

[4] E. Arnold et al., Z. Phys. A331 (1988) 295

[5] J. Mackin et al., Phys. Rev. Lett. 66 (1991) 1681

[6] W.F. Rogers et al., Phys. Lett. B 177 (1986) 293

[7] M. Lindroos et al., Nucl. Instr. And Meth. In Phys. Res. A361 (1995) 53

[8] R.L. Williams et al., Phys. Rev. C2 (1970) 1219

[9] K. Asahi et al., Phys. Lett. B251 (1990) 488 and contribution to this proceedings

[10] Y. Kudryavtsev et al., Nucl. Instr. And Meth. In Phys. Res. B114 (1996) 350

[11] G. Neyens et al., Nucl. Instr. And Meth. In Phys. Res. B122 (1997) 121

[12] D.F. Zaretskii and A.V. Kozlinskii, Sov. J. Nucl. Phys. 31 (1980) 461

[13] Yu. P. Gangrskii et al., Sov. Phys. JETP 71 (1990) 857

[14] R.A. Lasell et al., Phys. Rev. A50 (1994) 423

[15] P. Van Den Bergh et al., Nucl. Instr. And Meth. In Phys. Res. B126 (1997) 194

Optogalvanic ionization of recoil atoms into the plasma of the ion guide source

G. V. Mishinsky, V. I. Zhemenik,
Joint Institute for Nuclear Research, Flerov Laboratory of Nuclear Reactions,
141980 DUBNA, MOSCOW REGION, RUSSIA
e-mail: laser@cv.jinr.ru
G. Petrov, S. Atanassova, D. Zhechev.
Institute of Solid State Physics, Bulgarian Academy of Sciences
72 Tzarigradsko Chaussee Blvd., BG-1784 SOFIA, BULGARIA
e-mail: spectron@gateISSP.issp.bas.bg

INTRODUCTION

Atomic and molecular spectroscopy makes wide use of what is known as the optogalvanic effect. Initially discovered into the glow-discharge [1, 2] and flame plasma [3], this effect based on the enhanced rate of the collisional ionization of the analyzed element, due to its resonant laser photoexcitation. The laser excited atoms have a lower ionization potential than a ground state atoms and are more efficiency ionized in thermal collisions. The ionization rate constant in the Maxwellian plasma is governed by the so-called Arrhenius factor - exp(-I/kT), where I is an ionization potential of analyzed atom in a given state, T is a plasma temperature, k - Boltzmann constant. In result at the temperature of 2.500 K the ionization rate constant increases by two order for each eV optical excitation[4].

A similar process may also occur in the plasma produced by irradiation of a gaseous media with ionizing radiation, for example in the Ion Guide Ion Source (IGIS). But production mechanism and conditions are quite different in this case, so special investigation of this effect in such media is required.

Present paper is a step simulating the IGIS properties. The Electron Energy Distribution Function (EEDF) and the most important processes are analysed and discussed. The model is based on solution of the electron Boltzmann equation accounting for the ionization with the high energy heavy ion beam and creation of secondary electrons. The results obtained allow one to estimate conditions, favourable for Laser Enhanced Ionizations (LEI) into IGIS environment.

1. ION GUIDE ION SOURCE

The principle of the operation for IGIS is based on use of recoils, which knock out from the target by a projectile beam. The ions produced in such a way are stopped in gas and are transported by a gas flow through the exit hole to vacuum chamber, where ions are separated from the buffer gas and usually directed to mass-separator unit (Fig. 1). The main defect of such source is the strong dependence of ion output on intensity and charge of projectiles. The output begins to decrease from some value of density of plasma, formed as a result of ionization of gas by beam of projectiles (plasma effect)/5/. The last circumstance compelled to use this source only for relatively poorly ionizing particle, such as p, d, a, and limited the area of effective application of a source, as a rule, the production of neutron-reach nuclides in reactions of induced fission of U, Th. However, last time one used multistep multicolor resonant laser ionization in a gas flow. It is possible to compensate the decreasing of the output of ions as a result of their neutralization in a large density plasma/6/.

Another way to avoid plasma effect can be the usage of LEI in the IGIS plasma. A continuous day laser tuned at suitable optical transition excites selectively the recombined atoms of interest. Usually the absorbing transition lies high enough in order to ensure the following ionisation by the thermal electrons. The chosen optical transition and A-A , A-e interactions in the IGIS medium determine the degree of the necessary interatom selectivity and LEI efficiency. Therefore, the physical characteristics of IGIS are of exceptional importance.

2. MAIN PROCESSES IN IGIS

The cyclotron charged particles beam bombards the target on the inside surface of the IGIS. Really all projectiles penetrate into IGIS, ionize the buffer gas atoms *B*, creating a specific medium, which distinguishes the known types of plasma. There are few data about this kind of medium.

At the very beginning, the IGIS medium consists of the neutrals first of all and ions of buffer gas, electrons, recoil-products and heavy projectiles losing their initial energy. The latter is redistributed from high energetic cyclotron projectiles to the other particles. The main part of this loss $-dE/dx$ is the process of buffer gas atoms ionisation. For a particle of mass M and energy $E << (M/m_e)Mc^2$:

$$-\frac{dE}{dx} = \frac{4\pi N_e z^2 e^4}{m_e v^2}\left\{\ln\frac{2m_e v^2}{I} - \ln(1-\beta^2) - \beta^2 - \delta - U\right\} , \qquad \textbf{(1)}$$

where I, N_e are the average ionisation potential for the atoms, and the electron density in the target material, respectively; Z is the projectile charge, $\beta = v/c$; δ and U, the members accounting for the influence of the density and the consistency of the *K*- and *L*-electrons. Thus, generally, the characteristics and behaviour of such type of plasma follow those of particles B and B$^+$, i.e. their ionization and recombination.

The main part of losses in Eq (1) are transferred to the lighter particles - the electrons. Their energetic state is of importance for the step like ionization as well as in describing the IGIS medium at all.

2.1. ELECTRON ENERGY DISTRIBUTION FUNCTION

The Electron Energy Distribution Function (EEDF) is an essential characteristic of the plasma kinetics. The knowledge of the EEDF is important to evaluate several plasma characteristics (electron density, mean energy, etc.) and to estimate the role of different elementary processes. The EEDF has been obtained by solving the time independent and spatially averaged electron Boltzmann equation using two-term expansion in Legendre polynomials/7/. The following processes have been accounted: elastic scattering, excitation and ionization from the ground state of the buffer gas, diffusion, recombination (dissociative and three-body) and a source term describing the appearance of secondary electrons due to ionization with the fast ion beam. The solution method and the terms appearing in the electron Boltzmann equation are similar to e-beam plasmas, described in detail elsewhere/7/. Only the ionization differential cross section in the source term is different (since it describes ionization with ion beam), for which an analytical formula derived in Garcia /8/ has been used.

The EEDF $f^0(U)$ is calculated for Ar, Ne and He buffer gases (50 - 150 torr) in case of He^{++} projectiles of energy E=40 MeV and intensity I=10^9-10^{17} part./s·cm^2. At these conditions the production and loss of electrons into the IGIS buffer gas *A* have been calculated:

i) the ionization by the ion beam

$$A + \text{ion-beam} \Rightarrow A^+ + e\ ;$$

ii) the ionisation by electrons

$$A + e \Rightarrow A^+ + 2e\ ;$$

iii)dissociative recombination

$$A_2^+ + e \Rightarrow A + A;$$

iv)three body-recombination with electron as a third particle

$$A_2^+ + e + e \Rightarrow 2A^* + e;$$

v) three body-recombination with atom as a third particle

$$A_2^+ + A + e \Rightarrow 3A^*;$$

vi) electron diffusion to the wall

Recombination without molecular ion formation is important for low gas pressure only (less then 10 torr).

The corresponding EEDFs are calculated by solving Boltsmann equation under energy up

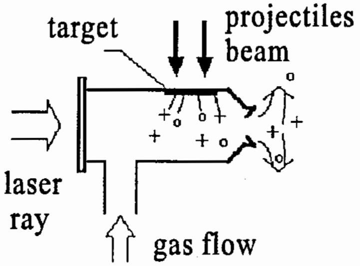

Fig. 1.

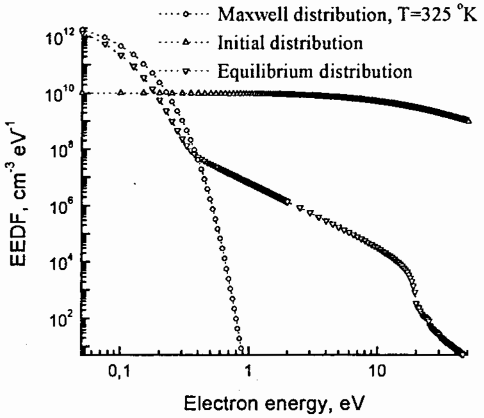

Fig. 2.

to 100 eV. For higher energy the solution is not correct but these energies do not contribute to the rate constants value. As an example, at Fig. 2 is shown the initial energy distribution function of secondary electrons according to Rudd model[/9/], the calculated equilibrium EEDF and the Maxwellian distribution function at temperature of 325 K, which corresponds to temperature of the equilibrium distribution, for 150 torr He buffer gas.

Equilibrium EEDFs in the case of Ar and He buffer gas have essential distinctions. It's a result of the different dependence of the electron-atom elastic collision cross section on incident energy for Ar and He and different mean energy loss in one collision due to their mass ratio.

For the He buffer gas the EEDF consists of the Maxwellian distribution with some high-energetic tile, which is almost constant for projectile beam intensity up to 10^{11} pps/cm^2 and then rises up with the intensity growth (Fig. 3). The temperature of the electron subsystem is almost independent of beam intensity up to 10^{16} pps/cm^2 (Fig. 5).

For the Ar buffer gas the EEDF consists of the Maxwellian, Druvestin distribution and a high-energy tile (Fig. 4). The Druvestin contribution has developed a tendency to grow from the beam intensity of 10^{12} pps/cm^2. This fact leads to the rapid growth of the electron subsystem temperature (Fig. 5). The atomic subsystem still be cold in both cases.

The ionization of the buffer gas by plasma electrons accounts for about 22% of the total number of ionization (by projectiles beam and by plasma electrons) for Ar and about 8.5% for He.

Different recombination channels weight for this gases and diffusion loss for the projectile propagated region of 1 cm diameter versus projectile beam intensity are shown on Fig. 6. For He, the diffusion loss dominance at low projectile intensity results in the

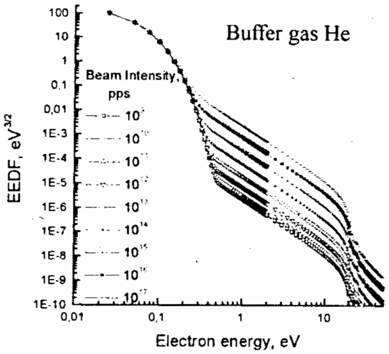

Fig. 3.

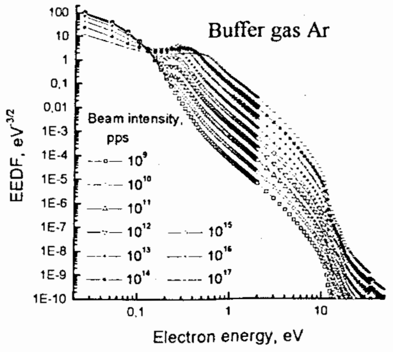

Fig. 4.

independence of the free electron mean lifetime on the plasma density. So the free electrons mean lifetime is almost constant up to projectile intensity of 10^{11} pps/cm^2 (Fig. 7), when the pure neutralization rate rises up dramaticaly. It can be an important point to understand a "plasma effect" in IGIS[/5/]. Because of longer free electrons lifetime, the He plasma has a higher density in comparishion with Ar plasma, if projectile intensity is higher than 10^{10} pps/cm^2 (Fig. 8). But variation of projectile propagation region diameter and gas pressure can change situation for He plasma in low beam intensity region.

In spite of its low mean energy, the plasma produced contains electrons whose energy is sufficient to ionise atoms of most the chemical elements.

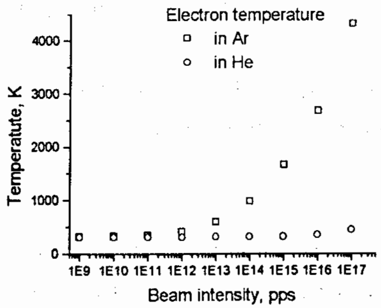

Fig. 5.

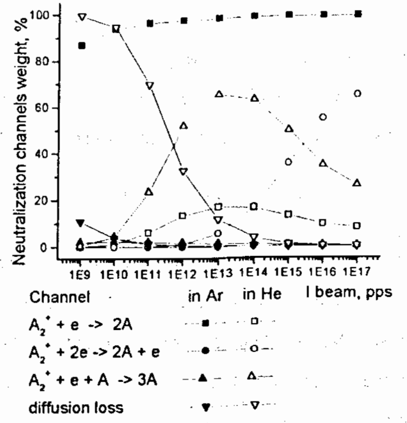

Fig. 6.

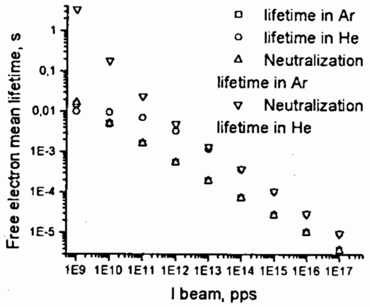

Fig. 7.

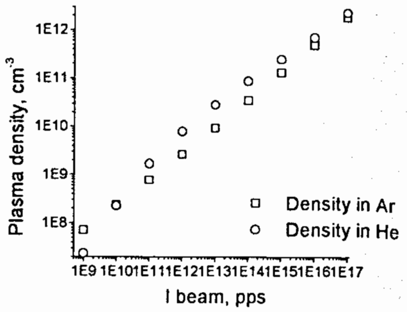

Fig. 8.

2.2. SELECTIVE IONISATION OF ANALYZED ATOMS IN IGIS

What a signal-to-background ratio may be expected at selective laser excitation of the recoil atoms in IGIS? Usually the laser excites the atom to a high enough level near to the potential of ionisation. The electron impact ionisation dominates for such atoms in enough dense plasma. According to the improvements of Gruzinski[10], Deutsch and Mark[11], Thomson's classical expression for single ionization cross-section σ_i near the ionization threshold may be written as:

$$\sigma_i = 4\pi r^2 N \frac{R}{I \cdot t} \cdot \left(\frac{t-1}{t+1}\right)^{3/2} \cdot \left\{1+\frac{2}{3}\left(1-\frac{1}{2 \cdot t}\right) \cdot \ln\left(2.7+(t-1)^{1/2}\right)\right\}$$

where r is the radius of the outer electron sublevel belonging to the atomic state, N and I the number of electrons and ionization energy in the valent subshell, respectively, R the Rydberg energy, $t = E/I$, E is the energy of the incident electron.

Let us analyse the ionization of atom with two energy levels - a ground state and an excited state. The ionization rate constant k_{ji} for an arbitrary j-state is defined as:

$$k_{ji} = \int_{I_j} f(E) \cdot \sqrt{E} \cdot \sigma_j(E) dE,$$

where f(E) is the energy distribution of the electrons, $\sigma_j(E)$ the cross section for the ionization of the j-state atom by an electron of energy E, I_j the ionization threshold for this state. Hence it follows that the ionization rate constant for the excited state atom is significantly higher than that for the ground state atom. The ratio of the ionization rate constants for excited and ground state atoms $\alpha = k_{*i}/k_{0i} = \alpha_0 \cdot (r^*/r_0)^2$, where r_0, r^* are the radii of the outer electron subshells for the ground and excited states, and α_0, according to our calculation, is almost independent of the projectiles intensity, but strongly depends on the buffer gas type. In the table one present the calculation for the atoms with the ground state ionization threshold of 6 eV and with the excited state ionization threshold of 4 eV or 2 eV:

Excited state ionization thresholds	α_0 in:		
	He	Ne	Ar
4 eV	2.9	4.0	7.7
2 eV	11.5	22.9	98.1

From the table one sees that the Ar is the most suitable buffer gas for LEI.

For laser-performed excitation, the ratio of the numbers of excited state atoms and ground state atoms is the ratio of the populations of these states, and, according to Travis et al[3], is as follows:

$$\xi = \frac{n^*}{n_0} = \frac{B_{0*} \cdot E_\nu + k_{0*}}{B_{*0} \cdot E_\nu + A_{*0} + k_{*0}},$$

where B_{0*}, A_{*0}, B_{*0} are the Einstein coefficients for absorption, emission and simulated emission, k_{0*}, k_{*0} the collision rate constant for the excitation and deexcitation of the upper level, respectively, E_ν the laser spectral irradiance. The j-level ionization rate is equal to $k_{ji}n_j$, where n_j is the number of atoms at the corresponding j energy level. In two level atom approximation, for laser-irradiated plasma $n_0+n^* = (1+\xi)n_0 = N_a$, whereas, when plasma is not irradiated, we assume that all the analyzed atoms are in the ground state - $n_0' = N_a$, where N_a is the total number of analyzed atoms. Then, the total ionization rate during laser irradiation increases by a factor

$$F = (k_{*i}\xi n_0 + k_{0i}n_0)/k_{0i}N_a = n_0(\alpha k_{0i}\xi + k_{0i})/k_{0i}(1+\xi)n_0 = (\alpha\xi+1)/(\xi+1)$$

In the case of optical transition saturation the value of ξ equals $B_{0*}/B_{*0} = g^*/g_0$, where g_j is the statistical weight of the j-state. Therefore, the F cannot exceed the value $(\alpha g^*+g_0)/(g^*+g_0)$, which is equal to $\alpha/2 + 0.5$, when $g^* = g_0$.

Thus, the usage of laser radiation results in the fact that for the ion-guide source plasma, the ionization factor of the analyzed element $K = N_i/(N_i+N_a)$ reaches the value

$$K_{irr} = K_0F/(1+K_0(F-1)),$$

where K_0 is the ionization factor in the absence of laser radiation, N_i the number of ions of the analyzed element. If we assume that F = 20, then for K_0 = 1% we can expect the K_{irr} growth to 17%, and for K_0 = 10% - growth to 70%. It can be sufficien improvement for efficiency of the IGIS.

CONCLUSIONS

A new kind of optogalvanic medium - IGIS plasma, formed by heavy ion beam propagated through the noble gases - Ar, Ne, He, was analyzed.

EEDF, free electron density and temperature, lifetime and different neutralization channels contribution, including diffusion, were calculated for such mediums.

The possibility of LEI in IGIS was demonstrated and its difference from conventional LEI was investigated.

The efficiency of IGIS can be increased by using the optogalvanic effect in plasma, especially for conditions, where the "plasma effect" is important.

The proposed ion source is element selective.

This source allows one to obtain information about isotope shift of an optical transition, where it's possible.

The experimental check up of above calculations is required.

REFERENCES

1. Smyth K.C., Schenck P.K., Chem. Phys. Lett. 55, 466 (1978)
2. Zalewski E.F., Keller R.A., Engleman R., J. Chem.Phys. 70, 1015 (1979)
3. Travis J.C. et al., Anal. Chem. 51, 1516 (1979)
4. Travis J.C., Turk G.C., Green R.B. Anal. Chem. 54, 1006A (1982)
5. Dendooven P., Nucl. Instr. and Meth. B 126, 182 (1997)
6. Kudryavtsev Yu. et al., Nucl. Instr. and Meth. B 114, 350 (1996)
7. Bretagne J., Godart J. and Puech J., J.Phys. D 15, 2205 (1982)
8. Garcia J.D., Phys.Rev. 177, 223 (1969)
9. Rudd M.E., Phys. Rev. A 38, 6129 (1988)
10. Gryzinsky M., Phys. Rev. 138, 336 (1965)
11. Deutshc H. and Mark T. D., Int. J. Mass Spectr. Ion. Proc. 70, R1 (1987)

High-Selective High-Temperature Target — Laser Ion Source Unit for the Short-Lived Isotope Production

V.N. Panteleev, A.E. Barzakh, D.V. Fedorov, F.V. Moroz, A.G. Polyakov, S.Yu. Orlov,
M.D. Seliverstov and Yu.M. Volkov

188350, Petersburg Nuclear Physics Institute RAS, Gatchina, Leningrad district, Russia
Corresponding author: vnp@hep486.pnpi.spb.ru

Abstract. A high temperature refractory target specially designed for the suppression of the thermoion background coming from the target volume to the laser ion source has been tested. The use of the potential of the heating current in the target temperature range 2200–2800 C° gave the possibility to lock ions in the target volume and reduce considerably unselective thermal current of the laser ion source. The value of the Ba, Eu, Sm, Yb and Tm thermal ion suppression obtained in off-line and on-line experiments was about 20. A high selectivity of the method was shown by direct measurements of the photoion current of the radioactive ^{163,162,160,158}Tm isotopes on the background of Yb isobars.

1. Introduction

As has been shown by latest ten years in the trend of ISOL (Isotope Separator On-Line) facilities, an idea of the refractory high temperature cavity use to construct a high efficient selective laser ion source [1, 2] turned out to be a very productive one.

A high efficiency and selectivity of the laser ion source (LIS) have been proved for isotopes of some rare earth elements [3] and for many other elements [4, 5] of the periodical table. Futhermore, as has been shown during latest experiments, the LIS construction may be used without any modifications for the spectroscopic purposes [6, 7, 8].

One of the main problems seriously limiting the application of the LIS when it is coupled with a high temperature refractory target (HTRT) is the problem of a high thermoionic current background supplied by the ions produced in the process of the surface ionization not only in the cavity of the laser ion source but in the volume of a target connected with it.

When a high temperature refractory metal target is being used for the rare earth nuclide on-line production, the target temperature is considerably higher than the temperature of the laser ion source cavity and therefore a high temperature refractory target contribution to the thermoion current is noticeably higher (more than 100 times) than the contribution of laser ion source itself [3]. So one of the main tasks, when a high temperature refractory target coupled with the LIS is used, turns out to be the suppression of the thermoion current from the target volume.

For that purpose at IRIS facility a special construction of the high temperature refractory target was developed and tested in off-line and on-line experiments. The thermoion current suppression value for a HTRT with tantalum-tungsten foils as a target material coupled with a LIS made of niobium tube proved to be around 20 in the target temperature range 2200–2700 C° for different kinds of stable and radioactive ions.

2. High temprature target–laser ion source unit selectivity

As has been shown by on-line and off-line experiments with the laser ion source the selectivity of an on-line used high-temperature target-laser ion source unit is strongly influenced by the parameters of the target coupled with the LIS. The target-laser ion source unit selectivity value can be expressed as

$$S = K_B \cdot \frac{I_L}{I_T},$$

where K_B is the ratio of the period of laser pulses to the duration of ion bunches produced by the laser light and extracted from the ion source. The value of K_B achieved so far with used 10 kHz pulsed lasers varies in the range of $4 \div 10$ [9, 10].

I_L is the current of the investigated isotope ions produced by the laser ionization (selective signal) and I_T is the current of the same isotope and its isobar thermoions produced by the surface ionization inside the volume of the laser ion source and in the target volume (nonselective signal).

If the target temperature is rather low (<2200 C°), or the target container and target substance are prepared from the material with a low workfunction, it does not deliver a noticeable ion current to the laser ion source. In that case $\frac{I_L}{I_T} \equiv K_S \approx 100 \div 200$ for Tm and Yb isotopes in a niobium tube of the LIS at its working temperature 1800–2000 C° [3]. But when the LIS is being coupled with a high temperature target, and the target container and the target material have considerably higher workfunctions and temperature, the HTR target supplies the thermoion current of the isotope being investigated (nonselective ion current) two orders of magnitude higher than the laser ion source itself and the value of selectivity drops down to the value ~ 1. In Fig. 1 the K_S value for stable Yb versus a tungsten-tantalum target temperature is represented. As a laser ion source cavity, the niobium tube was used at a temperature 1800 C°. It could be seen from Fig. 1, the target temperature rise in the region $1800 \div 2700$ C° causes the K_S drop from 120 to 1. It is worth to note that in the process of the target temperature change the LIS cavity temperature permanently has to be controlled.

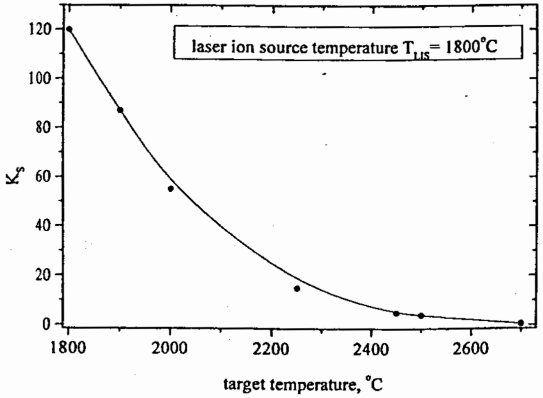

Fig. 1. Target temperature dependence of the K_S value for Yb ions.

The LIS temperature rise, when the target temperature had been changed from 1800 C° to 2700 C°, was about 20 C° and could not give noticeable contribution to the fall of the K_S value.

The above considerations bring us to the conclusion that one of the main tasks when one uses a HTR target coupled with the laser ion source is to suppress a nonselective thermal ion current from the high temperature target volume. In order to have a noticeable selective ion signal, the suppression coefficient value should be about 10 or even higher.

3. Selective high-temperature target – laser ion source unit construction

In Fig. 2 a schematic drawing of a selective high-temperature refractory target – laser ion source unit developed at IRIS facility is shown.

The target consists of a tungsten cylindrical container with a wall thickness $0.2 \div 0.3$ mm connected through the front end with the cavity of LIS by a thin tungsten tube about 2 mm in diameter. Small plates or tapes cut from tantalum and tungsten foils 20μm thick are placed along or perpendicular to the incoming proton beam in the target container. The target mass is $4 \div 20$ g/cm^2.

The target was heated by direct or alternating current flowing through the target container. The potential drop of the target heating current on the target container was $3 \div 4$ V. The target container had a hole 0.5 mm in diameter in the back end to remove positive ions from the target volume when it was heated by direct current. The cavity of the LIS was constructed as a tube rolled from niobium foil with a wall thickness $0.2 \div 0.3$ mm. The LIS tube was being heated by direct current with the potential drop on the tube about 3 V. The sign of the potential, as it is shown in Fig. 2, was chosen to direct ions produced in the volume of the ion source to the extraction electrode of the mass-separator. The LIS tube had the length 55 mm and diameter 2 mm.

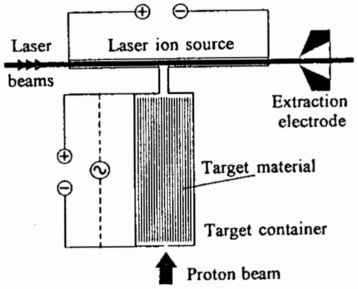

Fig. 2. Schematic drawing of a selective high-temperature refractory target – laser ion source unit.

4. Ion locking, bunching and accumulation effect

During off-line and on-line tests of the HTR target,the ion bunching effect of alkali element ions escaping from the target has been found. This effect takes place when the target is being heated by alternating 50 Hz current. Ions are bunched by the voltage of alternating heating current flowing through the target container and target material. As the ionization efficiency of alkali element atoms inside the target volume is close to 100%, for these ions with thermal energy about 0.4 eV the target closing-opening potential (3 - 4 V) of alternating current is effective enough to lock and accumulate them inside the target during the positive half-cycles of the target heating voltage. During the negative half-cycles the ions freely pass from the target to the ion source. In Fig. 3 the ion bunches of Li, Cs and Yb are represented (the HTR target has been heated by alternating 50 Hz current). The ion current was measured at the mass-separator collector by the electron multiplier. All curves were normalized in their maximum value. As could be seen from Fig. 3, the efficiency of the ion blockade during the positive half-cycles was very high for all kinds of ions. Additionally, a very essential accumulation effect of alkali atom ions was observed.

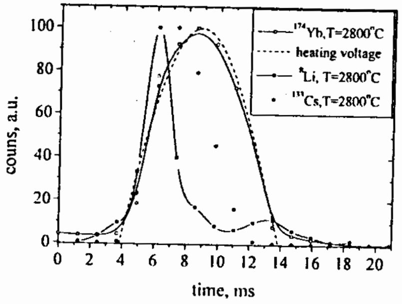

Fig. 3. Integrated ion bunches of Li, Cs and Yb.

It follows from the fact that the half-width of Li and Cs bunches is considerably shorter than the half-width of a sinusoid half-cycle. At the same time there is no noticeable effect of Yb ion accumulation, since the form of Yb bunches exactly follows the sinusoid form of the heating current voltage. That kind of experiments carried out not only with ions of stable isotopes but with radioactive ^{8}Li and ^{80}Rb have clearly demonstrated that a high value of the positive ion suppression during positive half-cycle can be obtained for any element positive ions produced in the HTR target. Let us determine the suppression coefficient as the ratio of the ion current value when the target is open to the direction of the ion source (i.e. during negative half-cycle of the heating current) to the ion current value when the target is closed (i.e. during positive half-cycle of the heating current). As was measured at a temperature 2800±50°C,the ion suppression coefficient does not depend on element being investigated and had a value around 20. It is clear that if the ions produced by the laser light are being counted in time gates during a positive half-cycle, when thermal ions are blocked in the target, the selectivity of the LIS will be approximately twenty times higher than in normal regime of the ion counting without time gates. In Fig. 4 the temperature dependence of the selectivity value K_S of the LIS has been shown when the HTR target is heated by alternating current.

As one can see from Fig. 4 the rise of the K_S value for Yb ions in the temperature range 2500 – 2700 °C is from 5 to25. It's in good agreement with a value of the suppression coefficient obtained for stable ytterbium ions at a target temperature 2800°C.

Ions inside the HTR target also may be blocked by the potential drop of the dc heating. In that case the suppression coefficient is the ratio of the ion current measured, when the voltage polarity at the target end connected with the ion source is negative to the ion current of the same isotope, when the voltage polarity at the target end is positive.

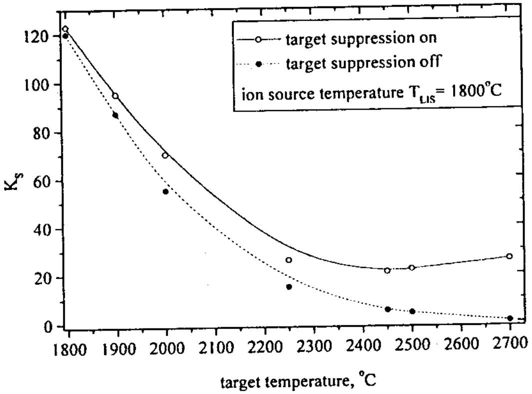

Fig. 4. Temperature dependence of the K_S value for Yb ions.

In Fig. 5 the temperature dependence of the suppression coefficient for stable Ba and Tm isotope ions is shown. From the comparison of two methods of the thermal ion locking by the potential of alternating or direct heating current flowing through the target it's possible to come to a preliminary conclusion: the way of the thermal ion closing by the potential of direct heating current is more efficient and gives effect at considerably lower temperature than the target locking by the alternating current potential.

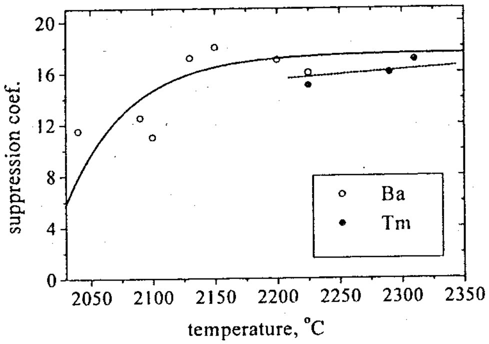

Fig. 5. Effect of the target thermoion current suppression.

As one can see from Fig. 5 the suppression coefficient values are very close for Ba and Tm and in the temperature range 2250–2350°C are about 16. In the case of the target heating by direct current a construction of the HTR target with a hole in the back end was used (see Fig. 2).

5. The suppression of Sm and Eu thermal ion background produced in the HTR target for selection of Gd isobars

On-line run has been carried out to measure the suppression coefficient for Sm and Eu radioactive isotopes produced inside the HTR target coupled with a niobium tube of the ion source. The target was heated by direct current,and ions produced in the target were locked by the permanent potential on the target. The target temperature was about 2500°C, the temperature of niobium tube was 1800÷ 1900°C.

The activity produced by the decay of isobars with the mass number 143 was collected on the tape and delivered to the X-ray detector for X-ray spectra measurements. The main task of the experiment was the suppression of Sm and Eu current to select ^{143}Gd, as from ordinary high temperature target the yields of Sm and Eu isobars are considerably higher than of Gd ones.

In Fig. 6 one of the X-spectra measured on the mass number 143 is shown. In the upper part of the figure the X-ray spectrum which is produced in an ordinary HTR target is shown. In the lower part similar X-ray spectrum of the isobars in the HTR selective target with ion locking potential and a hole at the back end is shown. It is a clear indication that the use of a selective HTR target gives the possibility to select ^{143}Gd by suppressing Sm and Eu isobars. The suppression coefficient for Sm and Eu for the experimental condition specified above was about 30. The possible reason of the fact that in the on-line experiment the suppression coefficient was 50% higher than it was measured during off-line tests was a very long time (about four days) of the target outgasing that ensures a low level of impurity ions inside the target volume. It was shown in the off-line tests that the efficiency of the ion locking inside the target is strongly influenced by the amount of impurities with low ionization potentials (Na and K ions) in the target volume.

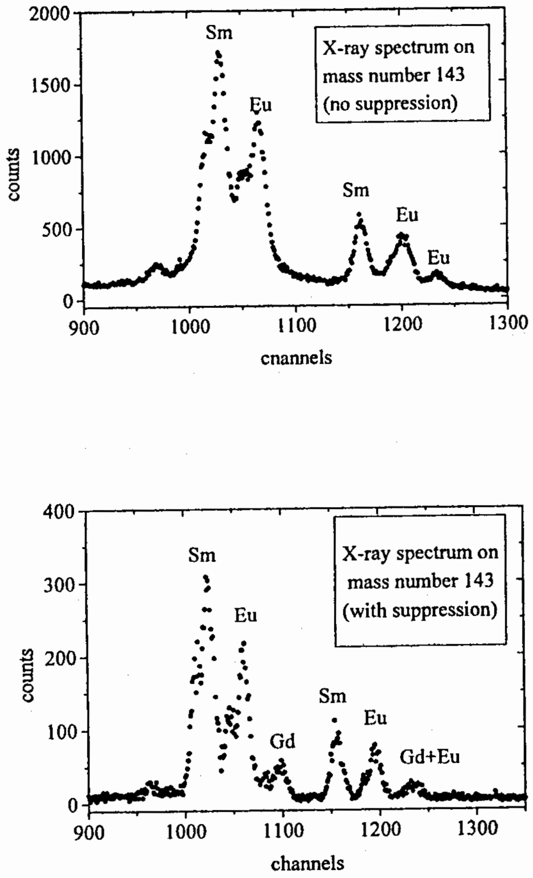

Fig. 6. The X-spectra measured on the mass number 143.

6. Experimental set-up

The scheme of the experimental installation is presented in Fig. 7. Neutron deficient isotopes were produced in the target of the mass-separator by 1 GeV protons. Atoms of the isotopes under investigation were ionized in the ion source by the beam of three laser rays. Frequencies of the lasers were tuned to the resonance transitions of the chosen excitation scheme (Fig. 8). The radiation frequency of the two broadband lasers (bandwidth 30 GHz) were fixed on the second and the third step frequencies correspondingly. Wavelength of the narrow band laser (bandwidth 1 GHz) was scanned around the first transition frequency. When the laser frequency coincided with the first step frequency, resonance ionization occurred and the photoion current on the mass-separator collector arose. So the experimental spectra represent a dependence of ion current on the scanned laser frequency.

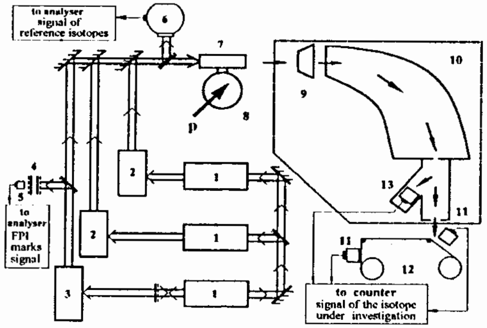

Fig. 7. Experimental installation.

1 – Cu-vapour lasers; 2 – broadband dye lasers; 3 – narrowband scanning dye laser; 4 – Fabry-Perot interferometer; 5 – photodiod; 6 – reference chamber; 7 – laser ion source; 8 – target; 9 – extraction electrod; 10 – mass-separator; 11 – α-detectors; 12 – tape-driving device; 13 – electron multiplier.

In the experiment two registration modes have been applied:

1) direct registration of the ion current by the electron multiplier, which was used for ^{158,160,162,163}Tm measurements;
2) registration of the α – particles from the decay of the isotopes under investigation by α – detector, which was used for ^{154,154m}Tm measurements.

In the first case selectivity was determined by the relation of the photoion current of the isotope under investigation to its thermoion current and to the current of its isobars. In the second case selectivity depends only on the ratio of the photoion and the thermoion currents of the isotope under consideration.

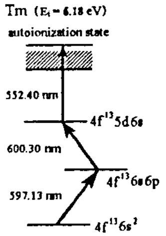

Fig. 8. Scheme of the Tm atoms photoionization.

7. Experimental results

As was shown by the on-line experiments as well the new method can provide very efficient background suppression. The isotope shifts for the chain of the neutron deficient thulium isotopes $^{158-163}$Tm were measured on-line by using the electron multiplier as a detector. The experimental spectra are represented in Fig. 9. The measured isotope shifts for these isotopes are in good agreement with the previous results, obtained by the photoionization spectroscopy in atomic beam [11].

8. Conclusion

In the process of the high-temperature target tests, a new locking, accumulation and bunching effect of positive ions escaping from the target volume has been observed.

The use of the positive ion locking effect when the HTR target was coupled with a laser ion source allowed to suppress considerably (about 20 times) an unselective thermal current from the target and to rise in the same ratio the HTR target – laser ion source selectivity. Application of the new method of the background suppression enables one to extend essentially the range of application of the resonance ionization spectroscopy technique (preserving its high efficiency) for short-lived isotopes when the registration methods based on the radioactive decay detection are not sensitive enough. The selectivity of the HTR target – laser ion source unit does not fall down with the target temperature rise.

The HTR target – laser ion source unit selectivity can be rised 4 ÷10 times more, making use of the time structure of selective ion current from the laser ion source.

The observed ion bunching and accumulation effect can facilitate the separation of the isobars with essentially different ionization potentials and volatility, that's true for pairs of elements such as Li–Be, Na–Mg, K–Ca, Rb–Sr, Cs–Ba, Fr–Ra and probably In–Sn and In–Ag.

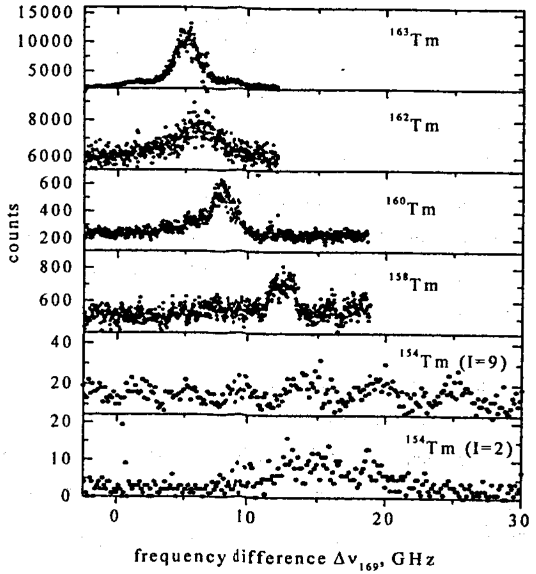

Fig. 9. Experimental spectra of the neutron deficient Tm isotopes.

References

[1] G.D Alkhazov, E.Ye. Berlovich and V.N. Panteleev, Pisma v Zh. Tekh. Fiz. 14(1988)1109.

[2] G.D Alkhazov, E.Ye. Berlovich and V.N. Panteleev, Nucl. Instr. and Meth. A280(1989)141.

[3] G.D Alkhazov, L.Kh. Batist, A.A. Bykov, V.D. Vittmann, V.S. Letokhov, V.I. Mishin, V.N. Panteleev, S.K. Secatsky and V.N. Fedoseyev, Nucl. Instr. and Meth. A306(1991)400.

[4] T. Kautzsch, I. Kloeckl, K.-L. Kratz, E. Kugler, J. Lettry, V.I. Mishin, H.L. Ravn, Y. Jading, R. Catherall, V.N. Fedoseyev, A. Jokinen, O.C. Jonsson, F. Schecrer, O. Tengblad, P. Van Duppen, W.R. Walters, A. Woehr and ISOLDE Collaboration, Nucl. Instr. and Meth. B126(1997)76.

[5] A. Jokinen, A.-M. Evensen, E. Kugler, J. Lettry, H. Ravn, P. Van Duppen, N. Erdmann, Y. Jading, S. Koehler, K.-L. Kratz, N. Trautman, A. Woehr, V.N. Fedoseyev, V.I. Mishin, V. Tikhonov and ISOLDE Collaboration, Nucl. Instr. and Meth. B126(1997)95.

[6] G.D Alkhazov, A.E. Barzakh, V.P. Denisov, K.A. Mezilev, Yu.N. Novikov, V.N. Panteleev, A.V. Popov, E.P. Sudentas, V.S. Letokhov, V.I. Mishin, V.N. Fedoseyev, S.V. Andreev, D.S. Vedeneev and A.D. Zyuzikov, Nucl. Instr. and Meth. B69(1992)517.

[7] A.E. Barzakh, I.Ya. Chubukov, D.V. Fedorov, F.V. Moroz, V.N. Panteleev, M.D. Seliverstov and Yu.M. Volkov, Eur. Phys. J. A1(1998)3.

[8] A.E. Barzakh, I.Ya. Chubukov, D.V. Fedorov, V.N. Panteleev, M.D. Seliverstov and Yu.M. Volkov, in: *Proc. Exotic Nucl. and Atom. Mass. Conf.*, Shanty Creek 1998, B.M. Sherrill, D.J. Morrissey, C.N. Davids, eds. American Institute of Physics, Woodbury, New York, 1998, p. 94.

[9] A.E. Barzakh, V.P. Denisov, D.V. Fedorov, S.Yu. Orlov and M.D. Seliverstov, Nucl. Instr. and Meth. B126(1997)85.

[10] J. Lettry, R. Catherall, G.J. Focker, O.C. Jonsson, E. Kugler, H. Ravn, C. Tamburella and ISOLDE Collaboration, Rev. of Sci. Instr. 65(1998)761.

[11] G.D Alkhazov, A.E. Barzakh, I.Ya. Chubukov, V.P. Denisov, V.S. Ivanov, V.N. Panteleev, V.E. Starodubsky, N.B. Buyanov, V.N. Fedoseyev, V.S. Letokhov, V.I. Mishin and S.K. Sekatskii, Nucl. Phys. A477(1988)37.

Fluorescence lifetimes of Uranium (VI) species in hydrolyzed solutions

Zdzisław Stryła

Quantum Electronics Lab., Institute of Physics, A. Mickiewicz University
Umultowska 85, 61-614 Poznań, Poland
e-mail: zetes@main.amu.edu.pl

ABSTRACT

Fluorescence lifetimes and relative emission intensities of uranium species UO_2^{2+}, $(UO_2)_2(OH)_2^{2+}$ and $(UO_2)_3O(OH)_3^{+}$ have been determined for a set of samples characterized by different concentrations of the species. Single- and double-exponential decays have been observed.

1. Introduction

The interest in physical and chemical properties of uranium stems mainly from the fact that it is the prevalent component of radioactive wastes and occurs in the contaminated areas near former uranium mines. In the natural aquatic systems it occurs mainly in the hexavalent form U(VI) as uranyl ion UO_2^{2+} (species I), which is almost ideally linear. The hydrated form is pentagonally coordinated by 5 water ligands in the equatorial position. Depending on the concentration and pH of the solution, also higher oligomers appear, particularly the dimer $(UO_2)_2(OH)_2^{2+}$ (species II) and trimer $(UO_2)_3O(OH)^{3+}$ (species III) entities.

The absorption spectra of uranyl ion reveal a weak band in the range 370-520 nm, showing a characteristic structure, and a strong band in the UV range. The emission spectrum shows a clearly marked structure with the maxima at 473, 488, 509, 534, 560 and 588 nm. This character of the spectra can be explained as a consequence of the coupling of electronic transitions to a symmetric stretching vibration of uranyl (VI).

The spectra of the higher oligomeric forms $(UO_2)_2(OH)_2^{2+}$ and $(UO_2)_3O(OH)^{3+}$ are similar although somewhat shifted with respect to those of hydrated uranyl (VI). Molar absorption coefficients for these species are an order of magnitude higher than those for UO_2^{2+}. The emission bands considerably overlap, which hinders analysis of the relationships obtained. The fluorescence lifetimes of particular species are different and equal about 1μs for UO_2^{2+}, ~3μs for $(UO_2)_2(OH)_2^{2+}$ and ~7μs for $(UO_2)_3O(OH)^{3+}$ [1].

The fluorescence lifetimes of uranyl (VI) significantly depend on many factors including temperature, presence of quenchers, relative contribution (speciation) of particular oligomeric forms. Speciation depends on the concentration and pH of the solution. The recognition of the influence of these factors on the lifetimes of exited states of uranyl is far from satisfactory.

2. EXPERIMENTAL

Working solutions were prepared from the stock one obtained by dissolving $(UO_3)x\ 2H_2O$ in 0.1 M perchloric acid, which weakly coordinates with U(VI). Twenty samples were prepared of total uranyl concentration from $3x10^{-4}$ M to $3x10^{-3}$ M. The values of pH were adjusted by addition of 0.1M NaOH solution, so that the final value was in the range 3.5–4.5.

The speciation of the samples [2, 3] was determined by the method, based on deconvolution of UV-VIS absorption spectra using the factorial analysis (Meinrath [4]).

All the samples were excited by 5ns, 1mJ light pulses at the wavelength of 440 nm, generated in an optical parametric generator (Surelite-OPO) pumped with a III harmonics of an Nd-YAG laser (Surelite). The fluorescence was observed using a standard photomultiplier - monochromator (M3 - COBRABiD) setup and recorded by a digital oscilloscope Tektronix TDS 620 in the range 480 – 580 nm. The curves of fluorescence decay were fitted by the mono- and biexponential model curves using the Levenberg-Marquardt algorithm.

3. RESULTS

The content of the species I in the samples studied changed from about 25 to 100% wt. For the samples containing only species I, the fluorescence lifetime changed with the wavelength of the emission light, reaching ca. 5μs in the centre of the emission line. It should be mentioned however, that the intensity of emission of these samples was very low, which leads to a significant error in determination of the decay constant. For many samples for which speciation indicated a possibility of multiexponential decay curves, only a single time constant was observed, see Fig.1. This testifies to the prevalence of the contribution of one of the forms in the emission. However, the emission decay of another sample in which relative concentration of strongly emitting form II has been reduced almost twice, is clearly two-exponential (Fig. 2.), with one of the times of ~9μs and the other ~3μs.

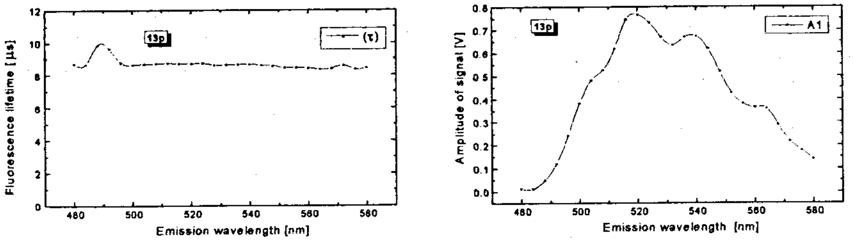

Fig.1. Fluorescence lifetime and amplitude for the sample containing: $1.05*10^{-3}$ M species I, $1.82*10^{-4}$ M species II, and $9.6*10^{-5}$ M species III.

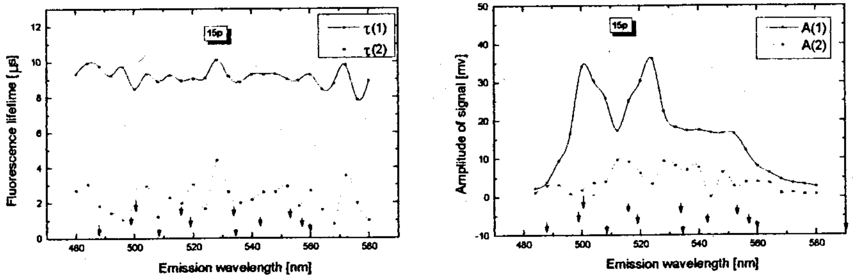

Fig.2. Fluorescence lifetime and amplitude for the sample containing: $1.68*10^{-3}$ M species I, $1.05*10^{-4}$ M species II, and $8.11*10^{-5}$ M species III.

Deconvolution of the obtained spectrum of the sample characterized by very strong fluorescence and clearly single -exponential decay of 9 μs shows evidently that apart from the expected four maxima at 499, 515, 536 and 563 nm another very broad peak centered at 556 nm appears (Fig.3.). Results of the deconvolution are collected in the Table.

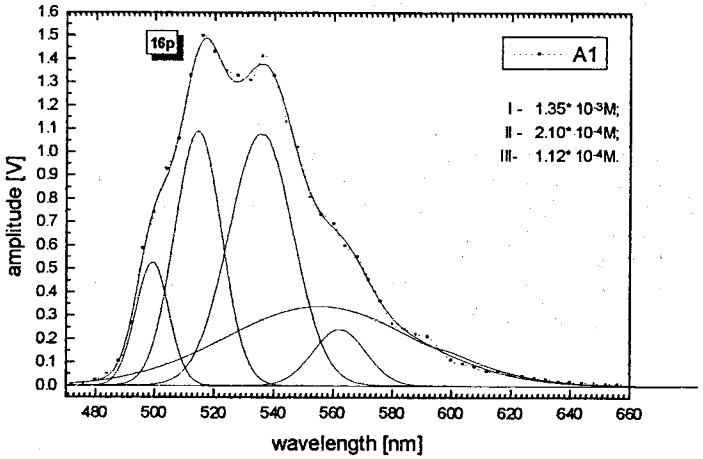

Fig.3. Deconvolution of fluorescence spectrum of the sample containing: $1.35*10^{-3}$ M species I, $2.10*10^{-4}$ M species II, and $1.12*10^{-4}$ M species III. Dotted curve - measured spectrum; solid lines - components and their sum.

Table. *Numerical results of deconvolution of fluorescence spectrum shown in Fig. 3.*

Center wavelength [nm]	Width of the line [nm]	Amplitude [V]
499.4	11.3	0.42
514.8	15.3	0.91
536.1	21.91	0.86
562.8	17.2	0.20
556.0	**63.4**	**0.27**

4. CONCLUSIONS

The dominant components in the fluorescence spectra of uranyl (VI) ions are due to the emission of the higher oligomeric forms $(UO_2)_2(OH)_2^{2+}$ and $(UO_2)_3O(OH)^{3+}$. The increase in the lifetime of uranyl in the samples in which the presence of only monomer form was expected, suggests the occurrence of an unrecognised individuum in the solution, whose presence was not taken into regard in the speciation analysis and which masks the emission of the main form. This suggestion is also supported by the results of analysis of the measured spectra.

ACKNOWLEDGMENTS

I would like to thank Dr. G. Meinrath for preparation of samples and providing with speciation data and Mr. M. Bińkowski for his help in experiment.

References

1. G. Meinrath, J. Radioanal. Nucl. Chem. 220 (1997)119-126,
2. G. MEINRATH, S.LIS, Z.STRYŁA, C.NOUPACTEP.: "Life Time and Fluorescence Quantum Yield of Uranium(VI) Species in Hydrolyzed solution", 3rd International Winter Workshop on Spectroscopy and Structure of Rare Earths Systems, Szkalrska Poreba 27.04-1.05.1999, Abstracts O1, 1999.
3. G. Meinrath : private communication,
4. G. Meinrath : Aquatic chemistry of uranium , Freiberg On-line Geoscience v.1. (www.geo.tu-freiberg\fog)

A New and Versatile Deposition Method of Metallic Particles at Room Temperature

Isao Sugai

High Energy Research Organization
Tanashi, Midoricho, 3-2-1, Tokyo, Japan

We have discovered a new deposition method, which is based on the vibrational motion of microparticles in the electrostatic field between parallel electrodes. This method is straight forward and does not require any complicated mechanism. It has been found that this deposition technique is useful for the target preparation of foils, in both the backed and unbacked condition. The uniformity in thickness is excellently good compared to that obtained using conventional deposition methods. It is a dry method used at room temperature. Furthermore, the deposited materials show strong adhesion.

1. Introduction

In target preparation for nuclear physics experiments a variety of techniques are used. These involve vacuum evaporation / condensation using electron beam and laser heating including AC arc discharge, ion beam sputtering, electroplating, electrospraying, centrifugal precipitation, rolling and electrophoresis. Among these, the electron beam evaporation / condensation and heavy-ion beam sputtering (HIBS) have been the conventional and the predominant techniques used to prepare target foils for high-resolution nuclear spectroscopy. The focused electron-beam technique is based on the high-temperature thermal evaporation of material in high vacuum. The HIBS technique, on the other hand, uses atomic collisions between inert gas ions and the source and does not depend on heating of the source and raising its vapor pressure to transport the material. In particular, the HIBS method has been long used as an excellent technique for the production of high melting materials targets, such as Mo, Hf and W (1).

As mentioned above, HIBS is basically a cold method. However, enough power can be deposited into the source by the ion beam that the temperature can rise to 400-1200℃, depending upon the beam conditions and the materials to be sputtered.

At these temperatures, contamination from the supporting materials can occur. So, the purity of targets produced by both the electron beam evaporation and the HIBS techniques can be compromised.

Target thickness uniformity can also be a problem because the source to substrate distance must be kept small for isotropically enriched materials.

We have recently investigated the phenomenon of vibrational motion of metallic microparticles in a static electric field (2 and 3). Through this study, we discovered a new deposition method which is turned out to be an excellent deposition method, overcoming many of the problems associated with electron beam and HIBS deposition. This paper describes the preliminary experiments carried out with this new method.

2. Experimental deposition method with particles

It is well know that metallic particles placed between parallel plate electrodes in vacuum vibrate randomly between the plates when DC voltage is applied (2 and 3). This principle can be explained as follows: particles placed on the lower plate are charged by an applied voltage, and accelerated toward the upper plate, where their charge becomes opposite. They are then accelerated back toward the lower plate. In this manner, the particles move back and forth continuously between the electrodes. The possibility of applying this continuous vibration of particles to deposit a substrate has been explored, since we expect that a number of particles can obtain the kinetic energy required to be deposited onto the electrode plate if a sufficiently high voltage is applied. Fig.1 is a schematic drawing of the experimental setup of our home made apparatus. It is very simple, consisting of two parallel metallic disks of 3 cm diameter placed in vacuum. These disks serve as electrodes.

Brass and Aluminum have both been used successfully as electrode materials. The distance between the two electrodes is 10-15 mm in normal operation. A hollow cylinder made of Lucite or glass inserted between the disks confines the particles to the electrostatic field region. The motion of the particles was monitored by inspection of YAG laser light scattered by the particles. The high voltage between the electrodes was turned on after the vacuum in the surrounding chamber was better than 1×10^{-2} Pa. Deposition by this method took a few hours. After the high voltage was turned off, the electrodes were immediately removed. Because, this process was performed at room temperature.

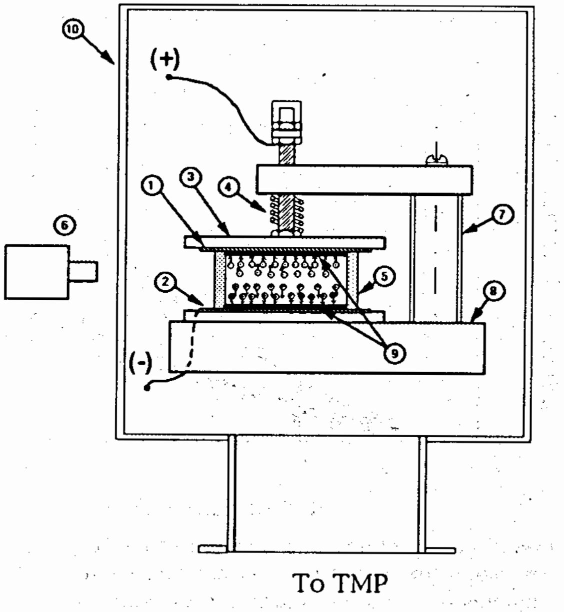

Fig.1 Schematic drawing of experimental set up;
1: backing foil (upper electrode: anode), 2: backing foil (lower electrode: cathode), 3: press plate, 4: spring for the press plate, 5: glass pipe, 6: He-Ne laser, 7: strut, 8: Teflon holder, 9: deposited layer, 10: glass vacuum chamber.

3. Results and discussion

We have applied this method to various materials under different conditions. The metallic elements examined were Mn, Mo, Os and Ni, and the nonmetallic ones were B, C and Si. These elements were successfully deposited onto substrates, but Pt, Au and Cu elements were not successfully deposited. The particle sizes examined ranged from 0.1 to 100 mm in diameter. Discs of Fe, Cu, brass and Al of 1 to 5 mm in thickness were examined as substrate materials. The following results were obtained from the present studies of the new deposition method. A threshold voltage at which the particles start the vibrational motion exists. This motion occurs at approximately 3 KV for most of the metallic materials and 6 KV for the nonmetallic elements that we studied. The deposition rate strongly depends on the applied voltage between the electrodes. Thus, the deposition thickness was easily controlled by changing either the applied voltage or the operation time. In Fig.2, the deposition thickness (mg/cm^2) of Pd on Cu plate is plotted against the applied voltage. As shown in the figure, the rate increases in proportion to the voltage increase.

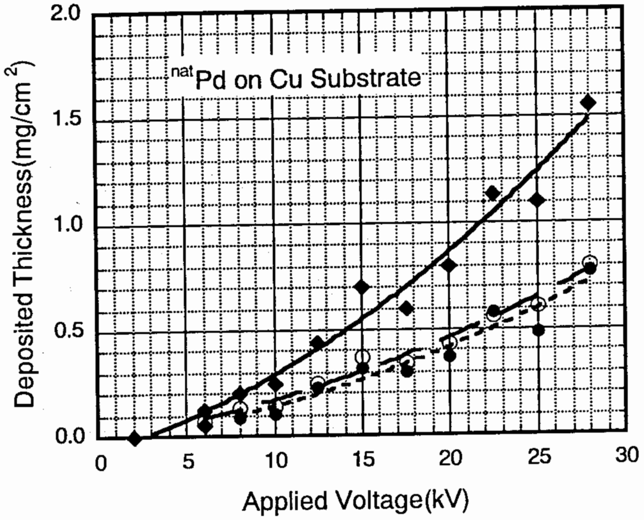

Fig.2 Deposited thickness versus applied voltage for a 3 h run. The open and solid circles are the data for the cathode and anode. The solid squares represent the sum of two.

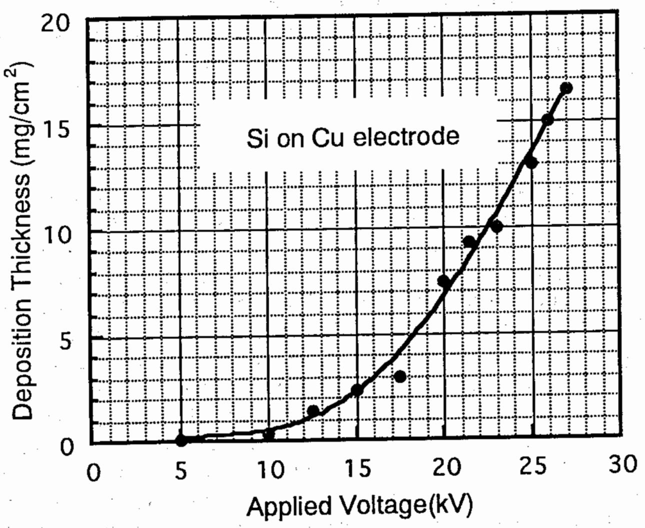

Fig.3 A characteristic performance of non-metallic Si element (MP:1410℃) Showing a relation ship between a finally applied voltage and an average thickness (mg/cm^2)

The thickness of the deposited layer on both electrodes was almost the same as shown in the figure. Fig.3 shows the characteristics of the Si deposition at various applied voltages.

The thickness uniformity of the prepared foils was measured with an alpha-ray thickness gauge using a ^{241}Am source (4) and a MINITEST 3001 (ELECTRO=PHYIK KÜLN) electromagnetic coating thickness gauge. In the uniformity measurements, target foils of self-supported enriched isotopic ^{106}Pd and Mn were examined. The measurements were carried out at 1 mm intervals using the 1.2 mm aperture of the gauge. FIg.4 (a) shows the thickness data for a ^{106}Pd target foil along the perpendicular direction to (a). A maximum deviation of 8 % (50 μg/cm^2) from the thickness at the center position (0.62 μg/cm^2) was obtained. Fig.5 shows the uniformity of a Mn coated on an Fe substrate. In this case, the substrate was not removed, and we measured the deposited layer thickness with the MINITEST gauge, assuming good uniformity of the substrate. In this case, a maximum deviation of 4% of the central thickness 2.05mg/cm^2 was obtained. Therefore, the deposition of metallic target material can be said to be fairly uniform.The uniformity of this target compared favorably with targets made by means of the electron beam heating and HIBS methods when the source -to -target distance was 4 cm.

Fig.6 shows various targets deposited on copper backing substrate by present method.

The temperature of the substrate during the deposition is nearly constant at 30±5℃ for 24h at 20 kV and 100 μA, and does not depend on the substrate material being tested. Fig.7 shows an example of a characteristic curve of temperature vs applied voltage. The temperature of the substrate (cathode) was measured every 10 minutes using a CA thermocouple. It can be clearly seen that the maximum temperature of the copper electrode was 33℃ at 27 KV of applied voltage (33℃ was classified as room temperature for this experiment).

The adhesion strength of Mo and Mn to the electrodes was examined by peeling off the deposition layer with gummed tape. No peeling was observed from the Al and the brass substrates, and no changes were observed on the surface. Furthermore, we attached the side of a brass rod of 10 mm in diameter x 20 mm in length to the deposited surface using an Araldite bidending agent. After drying, the deposited layers were tested by pulling the rod by a spring balance with a maximum tensile strength of 70 kg/cm^2. None of the deposited layers mentioned above were detached from the substrates during this peeling test.

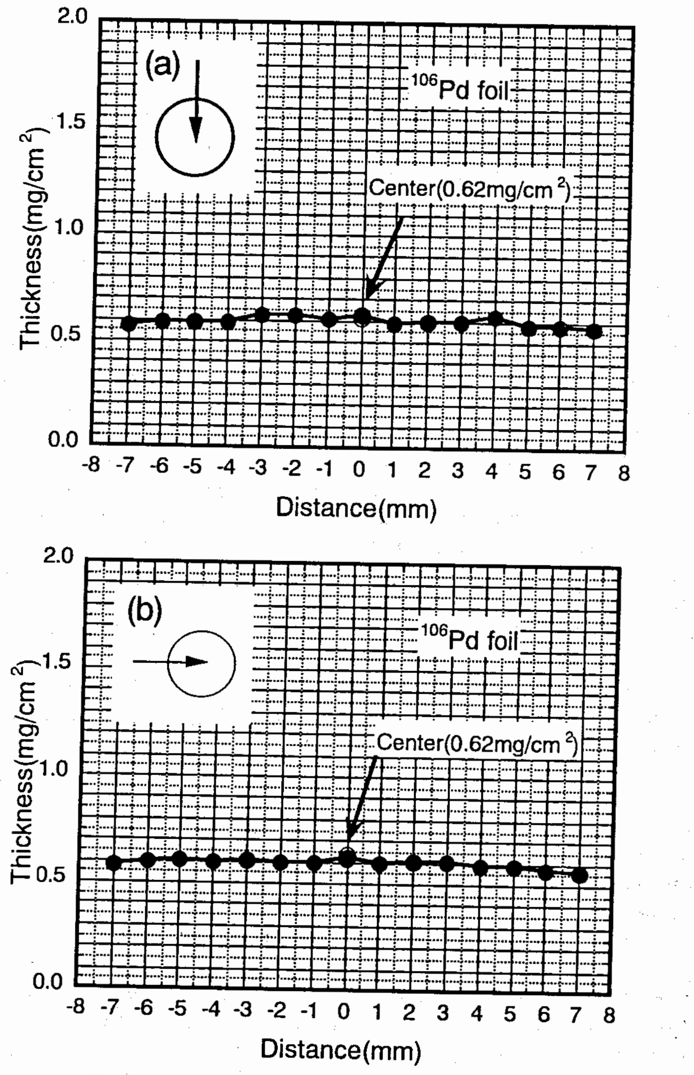

Fig.4 Thickness uniformity of desited foil. (a)and (b) for enriched isotopic ^{106}Pd.

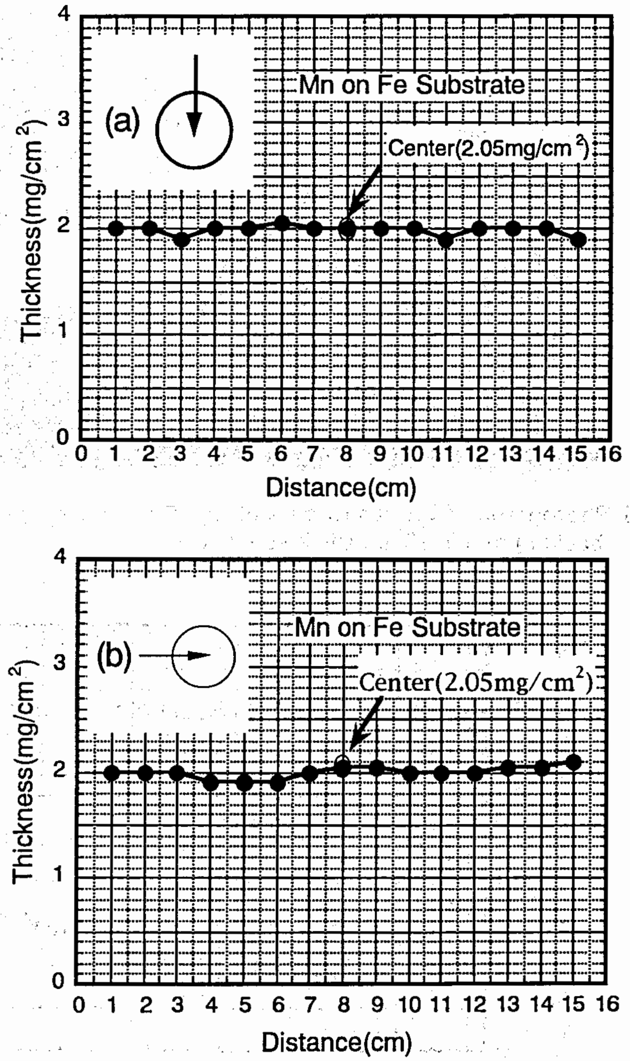

Fig.5 Thickness uniformity of deposited layer on a Fe substrate. (a) and (b) for Mn.

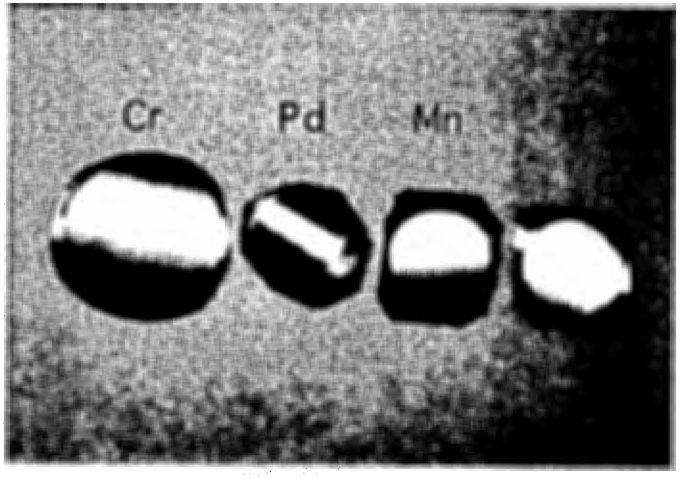

Fig.6 Photograph of various targets of Mo, Pd, Mn and Cr on copper backing of 10-30 μm thick substrate.

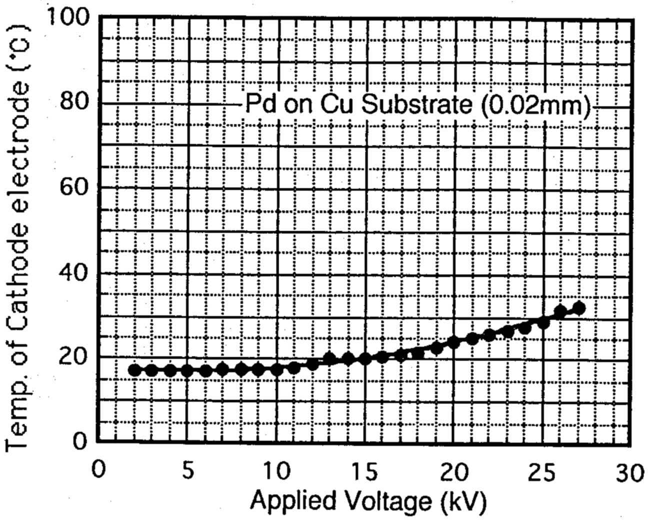

Fig.7 Characteristics of the temperature on a copper substrate of deposited Pd.

4. Conclusion and Summary

In conclusion, we have discovered a very interesting behavior of metallic and nonmetallic microparticles under high-static electric fields, and found an excellent and new deposition method through careful investigation of this phenomena. The present method is based on a new phenomenon of deposition using high kinetic energy-particles deposited onto substrates.
It is a dry-powder method performed at room temperature.
Furthermore, this method is independent of melting temperature of the element material.

References

(1) G. Sletten . P. Knudesen,Nucl. Instr. and Meth. 102(1972)459.
(2) T. Tanabe, I. Sugai M. Yasue,Nucl. Instr. and Meth. A256(1987)439.
(3) J . F. Fruchituchit :Rev. Sci. Instrum. 33(1962)209.
(4) I. Nonaka, I. Sugai, INS-J-132,1971.

4th INTERNATIONAL WORKSHOP "LASER SPECTROSCOPY ON BEAMS OF RADIOACTIVE NUCLEI"

May 24-27, 1999, Poznan, Poland

PARTICIPANTS LIST

B.Arcimowicz
Chair of Atomic Physics, Poznan University of Technology,
Piotrowo 3, 60-965, Poznan, Poland.
Tel. +48-61-878-23-25, +48-61-878-23-43
Fax: +48-61-878-23-24.
E-mail: arcimow@phys.put.poznan.pl

K.Asahi
Department of Physics, Tokyo Institute of Technology,
Oh-okayama 2-12-1, Meguro-ku, Tokyo 152-8551, Japan
Tel: +81-3-5734-2455
Fax: +81-3-5734-2751
E-mail: asahi@yap.ap.titech.ac.jp

G.Auger
GANIL, BP 5027, F-14021 Caen Cedex
France
Tel:
Fax:
E-mail: auger@ganil.fr

J.Billowes
Department of Physics and Astronomy, University of Manchester, Schuster Laboratory,
Manchester M13 9PL, UK.
Tel: +44-161-275-4104
Fax: +44-161-275-5509
E-mail: j.billowes@man.ac.uk

Z.Blaszczak
Institute of Physics, Adam Mickiewicz University,
ul. Umultowska 85, 61-614 Poznan, Poland.
Tel: +48-61-827-30-03
Fax: +48-61-825-77-58
E-mail: zetbe@main.amu.edu.pl

B.Bruyneel
IKS KU Leuven,
Celestijnenlaan 200 D, B-3001 Leuven, Belgium.
Tel: +32-16-32-72-71
Fax: +32-16-32-79-85
E-mail: bart.bruyneel@fys.kuleuven.ac.be

P.Campbell
Department of Physics and Astronomy, University of Manchester,
Schuster Laboratory, Brunswick St., Manchester M13 9PL, UK.
Tel: +44-161-275-4157
Fax: +44-161-275-5509
E-mail: pc@mags.ph.man.ac.uk

S.Chojnacki
Institute of Physics, Pedagogical University of Kielce,
ul. Konopnickiej 15, 24-406 Kielce, Poland.
Tel./Fax: +48-41-362-64-52
Heavy Ion Laboratory, Warsaw University
Poland, 02-097 Warsaw, Pastuera 5A
Tel:+48-22-822-21-23 ; +48-22-658-20-21
Fax: +48-22-659-27-14
E-mail: schojn@pu.kielce.pl
or inamura@slcj.uw.edu.pl

E.Cochrane
School of Physics and Astronomy, The University of Birmingham,
Edgbaston, Birmingham, B31 2HX, UK
Tel: +44-121-414-4580
Fax: +44-121-414-4580
E-mail: ec@np.ph.bham.ac.uk.

T.Czosnyka
Heavy Ion Laboratory, Warsaw University,
ul. Pasteura 5A, 02-093 Warszawa, Poland.
Tel: +48-22-8-22-2123
Fax: +48-22-8-659-2714
E-mail: czosnyka@slcj.uw.edu.pl

J.Dembczynski
Chair of Atomic Physics, Poznan University of Technology,
Piotrowo 3, 60-965, Poznan, Poland.
Tel: +48-61-878-23-43
Fax: +48-61-878-23-24.
E-mail: dembczyn@phys.put.poznan.pl

P.Dendooven
Department of Physics, University of Jyväskylä,
P.O. Box 35, (Y5) Jyväskylä, Finland.
Tel: +358-14-602-430
Fax: +358-14-602-351
E-mail: dendooven@phys.jyu.fi

Z.Dlouhy
Nuclear Physics Institute of Czech Academy of Science,
250-68 Rez (near Prague), Czech Republic.
Tel: +420-2-66-17-2382
Fax: +420-2-20-94-1130
E-mail: dlouhy@ujf.cas.cz

Ch.Droste
Institute of Experimental Physics, Warsaw University,
ul. Hoza 69, 00-681 Warsaw, Poland.
Tel:
Fax: +48-22-621-09-85
E-mail: droste@xfja-gate.fuw.edu.pl

M.Drozdowski
Institute of Physics, Poznan University of Technology,
Piotrowo 3, 60-965, Poznan, Poland.
Tel: +48-61-878-25-97
Fax: +48-61-878-23-24
E-mail: mirdrozd@phys.put.poznan.pl

M.Finger
Laboratory of Nuclear Problems, JINR,
Joliot Curie str.6, 141980 Dubna, Moscow Region, Russia.
Tel: +7-096-21-62610
Fax: +7-096-21-66666
E-mail: finger@nusun.jinr.ru

B.Furman
Chair of Atomic Physics, Poznan University of Technology,
Piotrowo 3, 60-965, Poznan, Poland.
Tel: +48-61-878-23-43
Fax: +48-61-878-23-24
E-mail: -

Yu.P.Gangrsky
Flerov Laboratory of Nuclear Reactions, JINR,
Joliot Curie str.6, 141980 Dubna, Moscow Region, Russia.
Tel: +7-09621-
Fax: +7-09621-65-083
E-mail: gangr@cv.jinr..ru

F.A.Gareev
Bogoliubov Laboratory of Theoretical Physics, JINR,
Joliot Curie str.6, 141980 Dubna, Moscow Region, Russia.
Tel:
Fax:
E-mail:

Marek Halas
Institute of Physics, Adam Mickiewicz University,
ul. Umultowska 85, 61-614 Poznan, Poland.
Tel: + 48-61-827-30-08
Fax: +48-61-825-77-58
E-mail: halas@main.amu.edu.pl

K.Heilig
Schelling str. 5,
D-68165 Mannheim, Germany
Tel:
Fax:
E-mail:

C.Hradecny
Nuclear Physics Institute
CAS, 250-68 Rez (near Prague), Czech Republic.
Tel: +420-2-66-17-2105, +420-2-66-17-2132, +420-2-66-17-2133
Fax: +420-2-20-94-1130
E-mail: hradecny@vax.ujf.cas.cz
or czholo@holo.cz

T.T.Inamura
Heavy Ion Laboratory, University of Warsaw
02-093 Warsaw, ul.Pasteura 5A, Poland
Tel: +48-22-658-2021 ext.213 (Office)
Tel: +48-22-822-2123 ext.213 (Laboratory)
Fax: +48-22-659-2714
E-mail: inamura@slcj.uw.edu.pl
or inamura@itak.slcj.uw.edu.pl

Iwona Iwaszkiewicz-Kostka
Institute of Physics, Adam Mickiewicz University,
ul. Umultowska 85, 61-614 Poznan, Poland.
Tel: +48-61-827-30-08
Fax: +48-61-825-77-58
E-mail: kostka@main.amu.edu.pl

I.N.Izosimov
V.G.Khlopin Radium Institute,
194021 St.-Petersburg, 2nd Murinski av. 28, Russia.
Tel: +812-247-80-95
Fax: +812-247-80-95
E-mail: izosimov@mail.dux.ru

Z.Janiak
Institute of Physics, Adam Mickiewicz University,
ul. Umultowska 85, 61-614 Poznan, Poland.
Tel: + 48-61-827-30-10
Fax: +48-61-825-77-58
E-mail: -

J.Kaszynska
Institute of Physics, Adam Mickiewicz University,
ul. Umultowska 85, 61-614 Poznan, Poland.
Tel: + 48-61-827-30-08
Fax: +48-61-825-77-58
E-mail: -

M.Koizumi
Japan Atomic Energy Research Institute (JAERI),
Watanuki 1233, Takasaki-shi, Gunma 370-1292, Japan
Tel: +81-27-346-9677,
Fax: +81-27-346-9690,
E-mail: koizumi@taka.jaeri.go.jp

N.N.Kolesnikov
Moscow State University, Faculty of Physics,
117234 Moscow, Russia
Tel: +095-143-37-29
Fax:+095-143-37-29
E-mail: stepan@theor.phys.msu.su.

J.Kownacki
Heavy Ion Laboratory, Warsaw University,
ul. Pasteura 5A, 02-093 Warsaw, Poland.
Tel:
Fax: +48-22-659-27-14
E-mail:

L.M.Lazarev
Russia Federal Nuclear Centre - VNIIEF
607190 Sarov, N.Novgorod region, Russia
Tel: +831-30-45-770
Fax: +831-30-45-569
E-mail: lazarev@expd.vniief.ru.

A.Leliwa-Kopystynska
Institute of Experimental Physics, Warsaw University,
ul. Hoza 69, 00-681 Warsaw, Poland.
Tel: +48-22-621-09-85
Fax: +48-22-625-64-06
E-mail: akopyst@fuw.edu.pl

P.Lojewski
Institute of Physics, Adam Mickiewicz University,
ul. Umultowska 85, 61-614 Poznan, Poland.
Tel: + 48-61-827-30-08
Fax: +48-61-825-77-58
E-mail: -

K.Maciejna
Institute of Physics, Adam Mickiewicz University,
ul. Umultowska 85, 61-614 Poznan, Poland.
Tel: +48-61-827-31-00
Fax: +48-61-825-77-58
E-mail: -

B.N.Markov
Flerov Laboratory of Nuclear Reactions, JINR,
Joliot Curie str.6, 141980 Dubna, Moscow Region, Russia.
Tel: +7-09621-64-586
Fax: +7-09621-65-083
E-mail: markov@flnr.jinr.ru.

K.P.Marinova
Faculty of Physics, Sofia University,
J.Bouchier Blvd. 5, BG-1164 Sofia, Bulgaria.
Tel:
Fax: +359-2-962-52-76
E-mail: nadjakova@uni-sofia.bg

L.M.Melnikova
Flerov Laboratory of Nuclear Reactions, JINR,
Joliot Curie str.6, 141980 Dubna, Moscow Region, Russia.
Tel: +7-09621-64-502
Fax: +7-09621-65-083
E-mail: melnikov@u400.jinr.ru

G.V.Mishinsky
Flerov Laboratory of Nuclear Reactions, JINR,
Joliot Curie str.6, 141980 Dubna, Moscow Region, Russia.
Tel: +7-09621-63-659
Fax: +7-09621-65-083
E-mail: laser@cv.jinr.dubna.ru

B.Mroz
Institute of Physics, Adam Mickiewicz University,
ul. Umultowska 85, 61-614 Poznan, Poland.
Tel. +48-61-8273291
Fax: +48-61-8257758
E-mail: bmroz@main.amu.edu.pl

R.Naskrecki
Institute of Physics, Adam Mickiewicz University,
ul. Umultowska 85, 61-614 Poznan, Poland.
Tel: +48-61-827-30-15
Fax: +48-61-825-77-58
E-mail: rysznas@main.amu.edu.pl

W.Nawrocik
Institute of Physics, Adam Mickiewicz University,
ul. Umultowska 85, 61-614 Poznan, Poland.
Tel. +48-61-827-32-02
Fax: +48-61-825-77-58
E-mail: nawrocik@main.amu.edu.pl

G.Neyens
University of Leuven and GANIL,
GANIL, BP 5027, F-14076 Caen Cedex 5, France
Tel: +33-231-45-46-46
Fax: +33-231-45-46-65
E-mail: neyens@ganil.fr
or gerda.neyens@fys.kuleuven.ac.be

V.K.Novikova
Joint Institute for Nuclear Research,
Joliot Curie str.6, 141980 Dubna, Moscow Region, Russia.
Tel: +7-096-21-65170
Fax: +7-096-21-65599, +7-096-21-65891
E-mail: novikova@cv.jinr.ru

V.Panteleev
St.-Petersburg Nuclear Physics Institute,
188350 Gatchina, Leningrad region, Russia.
Tel: +7-812-271-46208
Fax: -
E-mail: vnp@hep486.pnpi.spb.ru

A.Pasternak
A.F.Ioffe Physical-Technical Institute of RAS,
194021 St.-Petersburg, Russia
Tel: +812-247-91-22
Fax: +812-247-10-17
E-mail: alexander@alpas.ioffe.rssi.ru.

M.Pearson
State University of New York at Stony Brook,
NY 11794-3800, USA
Tel: +1-516-632-8119
Fax: +1-516-632-8573
E-mail: pearson@sbnslk.physics.sunysb.edu.

Yu.E.Penionzhkevich
Flerov Laboratory of Nuclear Reactions, JINR,
Joliot Curie str.6, 141980 Dubna, Moscow Region, Russia.
Tel: +7-09621-64-857
Fax: +7-09621-65-083
E-mail: pyuer@nrsun.jinr.dubna.ru

J.R. Persson
Department of Physics, Karlstadt University
SE-65188 Karlstadt, Sweden
Tel: + 46-54-700-2175
Fax: + 46-54-700-1449
E-mail: jonas.persson@kau.se

W.Pierzchalski
Institute of Physics, Adam Mickiewicz University,
ul. Umultowska 85, 61-614 Poznan, Poland.
Tel: + 48-61-827-30-18
Fax: + 48-61-825-77-58
E-mail: uluru@main.amu.edu.pl

J.Pinard
Laboratory of Aime Cotton,
CNRS, 91405 Orsay Cedex, France.
Tel:
Fax: +33-169-352-100
E-mail: pinard@lac.u-psud.fr
or jacques.pinard@lac.u-psud.fr

M.Prazmo
Institute of Physics, Adam Mickiewicz University,
ul. Umultowska 85, 61-614 Poznan, Poland.
Tel: + 48-61-827-30-08
Fax: +48-61-825-77-58
E-mail: -

P.Przybylski
Institute of Physics, Adam Mickiewicz University,
ul. Umultowska 85, 61-614 Poznan, Poland.
Tel: + 48-61-827-30-08
Fax: +48-61-825-77-58
E-mail: -

A.A.Rimski-Korsakov
V.G.Khlopin Radium Institute,
194021 St.-Petersburg, 2nd Murinski av. 28, Russia.
Tel:
Fax: +812-247-80-95
E-mail:

M.Sewtz
Institute of Nuclear Physics, University Mainz
J.J.Becher Weg 45, D-55099 Mainz, Germany
Tel:
Fax: +49-61-31-395-199
E-mail: sewtz@kph.uni-mainz.de

V.V.Smirnov
V.G.Khlopin Radium Institute,
194021 St.-Petersburg, 2nd Murinski av. 28, Russia.
Tel: +812-346-11-11
Fax: +812-247-57-81
E-mail:

A.A.Solnyshkin
Laboratory of Nuclear Problems, JINR,
Joliot Curie str.6, 141980 Dubna, Moscow Region, Russia.
Tel:
Fax:
E-mail:

G.Sprouse
Department of Physics, SUNY, Stony Brook,
New York 11794-3800, USA
Tel:
Fax: +1-516-632 8176
E-mail: gene.sprouse@sunysb.edu

E.Stachowska
Chair of Atomic Physics, Poznan University of Technology,
ul. Piotrowo 3, 60-965, Poznan, Poland.
Tel: + 48-61-878-27-24
Fax: + 48-61-878-23-24
E-mail: stachows@phys.put.poznan.pl.

Z.Stryla
Institute of Physics, Adam Mickiewicz University,
ul. Umultowska 85, 61-614 Poznan, Poland.
Tel: + 48-61-827-30-06
Fax: + 48-61-825-77-58
E-mail: zetes@main.amu.edu.pl

I.Sugai
High Energy Accelerator Research Organization
Tanashi Midori-cho, 3-2-1 Tokyo, Japan
Tel: +81-424-69-2221
Fax: +81-424-68-5844
E-mail: sugai@tanashi.kek.jp

N.I.Tarantin
Flerov Laboratory of Nuclear Reactions, JINR,
Joliot Curie str.6, 141980 Dubna, Moscow Region, Russia.
Tel: +7-09621-64-580
Fax: +7-09621-65-083
E-mail: tarantin@cv.jinr.ru

D.Verney
Institute of Nuclear Physics,
IN2P3-CNRS, 91406 Orsay Cedex, France.
Tel: +33-169-154-489
Fax: +33-169-157-196
E-mail: verner@inpo.in2p3.fr

M.Wakasugi
Hirosawa 2-1, Wako-shi,
Saitamana, 351-0198, Japan.
Tel:
Fax:
E-mail: rikaxp@riken.ga.jp

B.Wawrzyniak
Institute of Physics, Adam Mickiewicz University,
ul. Umultowska 85, 61-614 Poznan, Poland.
Tel: + 48-61-827-30-08
Fax: +48-61-825-77-58
E-mail: -

L.Weissman
IKS KU Leuven,
Celestijnenlaan 200 D, B-3001 Leuven, Belgium.
Tel: +32-16-32-72-71
Fax: +32-16-32-79-85
E-mail: leonidweissman@fys.kuleuven.ac.be

E.Wesolowski
Heavy Ion Laboratory, Warsaw University,
ul. Pasteura 5A, 02-093 Warsaw, Poland.
Tel:
Fax: +48-22-659-27-14
E-mail:

A.Wojtasiewicz
Institute of Experimental Physics, Warsaw University,
ul. Hoza 69, 00-681 Warsaw, Poland.
Tel: +48-22-628-30-31 ext.128
Fax: +48-22-625-14-96
E-mail: wojtasie@zfyavs.fuw.edu.pl

D.F.Zaretsky
Russian Research Centre "Kurchatov Institute",
123182 Moscow, Russia.
Tel: +95-196-93-35, +95-196-96-37
Fax: +95-194-19-94
E-mail: zaretsky@imp.kiae.ru.

S.G.Zemlyanoi
Flerov Laboratory of Nuclear Reactions, JINR,
Joliot Curie str.6, 141980 Dubna, Moscow Region, Russia.
Tel: +7-09621-64-502
Fax: +7-09621-65-083
E-mail: zemlya@nrsun.jinr.dubna.su

J.Zylicz
Institute of Experimental Physics, Warsaw University,
ul. Hoza 69, 00-681 Warsaw, Poland.
Tel: +48-22-621-3810
Fax: +48-22-622-6154
E-mail: zylicz@fuw.edu.pl.

IV Международное рабочее совещание
«ЛАЗЕРНАЯ СПЕКТРОСКОПИЯ НА ПУЧКАХ РАДИОАКТИВНЫХ ЯДЕР»

IV International Workshop
LASER SPECTROSCOPY ON BEAMS OF RADIOACTIVE NUCLEI

E15-2000-75

Ответственный за подготовку сборника к печати
Б.Н.Марков

Обложка Е.А.Минина

Редактор Э.В.Ивашкевич. Макет Р.Д.Фоминой

Рукопись сборника поступила 10.04.2000. Подписано в печать 23.06.2000
Формат 60 × 90/16. Офсетная печать. Уч.-изд. листов 24,89
Тираж 150. Заказ 52099

Издательский отдел Объединенного института ядерных исследований
Дубна Московской области